REPORT DOCUMENTATION PAGE

Form Approved
OMB NO. 0704-0188

Public Reporting burden for this collection of information is estimated to average 1 hour per response, including the time for reviewing instructions, searching existing data sources, gathering and maintaining the data needed, and completing and reviewing the collection of information. Send comment regarding this burden estimates or any other aspect of this collection of information, including suggestions for reducing this burden, to Washington Headquarters Services, Directorate for information Operations and Reports, 1215 Jefferson Davis Highway, Suite 1204, Arlington, VA 22202-4302, and to the Office of Management and Budget, Paperwork Reduction Project (0704-0188,) Washington, DC 20503.

1. AGENCY USE ONLY (Leave Blank)	2. REPORT DATE October 15, 2004	3. REPORT TYPE AND DATES COVERED Final Progress Report 01 Jun 01 - 31 May 04

4. TITLE AND SUBTITLE
Hybrid Metal/Electrolyte Monolithic Low Temperature SOFCs

5. FUNDING NUMBERS

6. AUTHOR(S)
Joe Cochran, Jim Lee, Meilin Liu, Dave McDowell, Tom Sanders

DAAD19-01-1-0649

7. PERFORMING ORGANIZATION NAME(S) AND ADDRESS(ES)
Georgia Institute of Technology
Office of Sponsored Programs
Atlanta, GA 30332-0420

8. PERFORMING ORGANIZATION REPORT NUMBER

9. SPONSORING / MONITORING AGENCY NAME(S) AND ADDRESS(ES)

U. S. Army Research Office
P.O. Box 12211
Research Triangle Park, NC 27709-2211

10. SPONSORING / MONITORING AGENCY REPORT NUMBER

42645.1-CH-DRP

11. SUPPLEMENTARY NOTES
The views, opinions and/or findings contained in this report are those of the author(s) and should not be construed as an official Department of the Army position, policy or decision, unless so designated by other documentation.

12 a. DISTRIBUTION / AVAILABILITY STATEMENT Approved for public release; distribution unlimited.	12 b. DISTRIBUTION CODE

13. ABSTRACT (Maximum 200 words)

The program objective is to develop SOFCs, operating in the 500-700°C range, based on Metal/Electrolyte square cell honeycomb formed by simultaneous powder extrusion of electrolyte and metal interconnects on alternate layers. The alloy interconnect is being formed as an oxide powder mixture which will be reduced to the metal and then co-sintered with the electrolyte during hydrogen thermal treatment. Goals include power density of 5 KW/liter, alternative fuels, designed thermal management, and low fabrication cost. The project is divided into electrolyte/electrode development, fabrication of hybrid and electrolyte monoliths, and thermo-mechanical stress modeling and heat transfer. Honeycomb fuel cells offer a great potential for high-power density and low-cost manufacturing. Also, producing multiple layers simultaneously forms a gas-tight high temperature seal in a single step, minimizing or eliminating difficulties encountered in other designs (planar or tubular) of SOFCs. The unique honeycomb cell geometry, however, poses some challenges in application of electrodes with desired microstructures to the honeycomb channels. However, near the end of the program, success was obtained in reduction and co-sintering of crack free, hermetic SOFC platform with alternating layers of metal interconnect and YSZ electrolyte. The structures were electroded and operated as fuel cells at modest powder levels. In, monolithic, all YSZ, honeycomb fuel cells, power levels of 0.09 W/cm^2 of electrolyte area, 0.30 W/cm^3 of call volume, and 0.15 W/g was achieved in the program.

14. SUBJECT TERMS Solid oxide fuel cells, Layered stack extrusion,	15. NUMBER OF PAGES 140
	16. PRICE CODE

17. SECURITY CLASSIFICATION OR REPORT UNCLASSIFIED	18. SECURITY CLASSIFICATION ON THIS PAGE UNCLASSIFIED	19. SECURITY CLASSIFICATION OF ABSTRACT UNCLASSIFIED	20. LIMITATION OF ABSTRACT UL

NSN 7540-01-280-5500

Standard Form 298 (Rev.2-89)
Prescribed by ANSI Std. 239-18

298-102

Final Progress Report for the Period 06/1/2001 – 05/31/2004

**Hybrid Metal/Electrolyte Monolithic Low Temperature SOFCs
ARO Grant DAAD19-0101-0649**

Joe Cochran, Jim Lee, Meilin Liu, Dave McDowell, Tom Sanders
Schools of Materials Science and Mechanical Engineering
Georgia Institute of Technology, Atlanta, GA 30332-0245
(404) 894-6104 or joe.cochran@mse.gatech.edu

ARO Monitor: Dr. Richard Paur

(1) Statement of Problem

Overview - The program objective is to develop SOFCs, operating in the 400-600°C range, based on Metal/Electrolyte square cell honeycomb, formed by simultaneous powder extrusion of electrolyte and metal interconnects on alternate layers. The alloy interconnect is being formed as an oxide powder mixture which will be reduced to the metal and then co-sintered with the electrolyte during hydrogen thermal treatment. Goals include power density of 5 KW/liter, alternative fuels, designed thermal management, and low fabrication cost. The project is divided into electrolyte/electrode development, fabrication of hybrid and electrolyte monoliths, and thermo-mechanical stress modeling and heat transfer.

This program is divided in to developmental areas of (A) Low Temperature Fuel Cell Development, (B) Alloy Interconnect Design and Fabrication (C) Fabrication of Hybrid and Monolithic Electrolyte Linear Structures, (D) Co-sintering of Electrolyte and Interconnect Materials, and (E) Design and Thermo-mechanical Analysis of LCMs for Fuel Cell Applications. The results are summarized in section(5) below and detals of the results are presented in Appendices A-E.

(2) Summary of Important Results

(A) Electroding and Demonstration of Honeycomb Fuel Cells

Composition and processing conditions for high-performance electrolyte and cathodes fabricated by extrusion is being optimized for low-temperature SOFCs. Significant efforts are (1) development of procedures for preparation of fuel cell electrode slurries with or without fibers, (2) application of electrodes to honeycomb cells by slurry coating, (3) conductivity measurement of monolithic and hybrid honeycomb cells, and (4) development of new electrode materials and microstructures to further reduce the interfacial resistance at low temperatures.

Honeycomb fuel cells offer a great potential for high-power density and low-cost manufacturing. Also, producing multiple layers simultaneously forms a gas-tight high temperature seal in a single step, minimizing or eliminating difficulties encountered in other designs (planar or tubular) of SOFCs. The unique honeycomb cell geometry, however, poses some challenges in application of electrodes with desired microstructures to the honeycomb channels. For instance, the electroding process is limited primarily to slurry- or solution-based processes. Various unique electroding processes have been explored to optimize the electrode composition and microstructure. In particular, the uniformity and adhesion of electrode layers to electrolyte have been significantly improved to demonstrate reasonably high power densities. Current efforts are focused on further process improvements in order to produce durable and functionally graded electrodes of high performance at low temperatures. Methods of producing ceramic and metal foams are being developed to aid in current collection and add turbulence to the gases to enhance fuel utilization. Special attention is directed to critical issues in manufacturability, reliability, and durability of electrodes in honeycomb channels.

Performance evaluation of the monolithic honeycomb fuel cells is showing power density near the anticipated levels for YSZ based systems. Further, initial results indicate that the compatibility of electrodes with the interconnect compositions is very encouraging, implying that the electroding processes developed for monolithic cells may be applied to the hybrid cells without much difficulty.

(B) Alloy Development for SOFC Interconnects

A unique approach to produce a SOFC was based upon co-extruding layers of electrolyte (YSZ) and interconnects which in this case is an oxide mixture of transition metal oxides. The interconnect material is then reduced in a hydrogen atmosphere resulting in the metal interconnect and the layered fuel cell platform is co-sintered to an impervious state. The choice of the alloy system for the interconnect is based on four factors. First, the alloy must be resistant to high temperature oxidation. To improve the oxidation resistance, chromium and aluminum are usually added to either iron base or nickel base alloys. Since the oxide powders must be capable of being reduced at reasonable oxygen partial pressures, this negates the use of aluminum because of the inherent stability of aluminum oxide. Furthermore, the addition of aluminum to the alloy has a profound effect of increasing the resistance of the oxide film. A second requirement is that the thermal expansion characteristics during the processing of the interconnect and the electrolyte stack must match.

The Ni-Fe-Cr system is perfect for this application because of the ability to affect changes in thermal expansion by controlling the nature of the phase present over the operating range of the fuel cell.   Not only is it possible to control thermal expansion with the normal FCC to BCC transformations but it is possible to significantly reduce expansion by controlling magnetic transformations that occur in this system. The decision to select an alloy from the Ni-Fe-Cr system is based upon the third requirement that the interconnect must have the best combination of low strength and high ductility so that mismatch between the interconnect and the ceramic can be accommodated by the plastic metal interconnect.   To this end composition along the Ni-Cr, the Fe-Cr and the Ni-Fe binary systems were prepared by reducing oxides of the required compositions. Alloys were also prepared from ternary Ni-Fe-Cr compositions. Thermal expansion, thermal gravimetric analysis (TGA) and strength data were collected on 34 alloys in this system. Based on all the data the alloy with the best combination of thermal expansion characteristics, thermal stability and strength was 47.5Ni-47.5Fe-5Cr. However, if the maximum oxidation resistance requirement is relaxed, 46Ni-54Fe provides the best thermal expansion match. At the time of this report, this composition is providing a hermetic sintered hybrid platform. The structure does still contain strains that can lead to delayed cracking in the electrolyte and this is being investigated currently.

(C) Fabrication of Hybrid and Electrolyte Monoliths

In an effort to produce low cost SOFC stacks, layered structures are being fabricated by extruding square cell honeycomb with alternating layers of electrolyte and metal

interconnect. The extruded alloy interconnect layers are metal oxide mixtures which are hydrogen reducible to the alloy. Hydrogen thermal treatment does not affect electrochemical properties of the electrolyte. Techniques are being developed to fully reduce the interconnect oxide layers at lower temperatures and then co-sinter the entire structure (alloy and electrolyte layers) to an impervious stack at higher temperatures, all in a hydrogen atmosphere. Accomplishments for this year include (1) developing the process for forming the layered structure in a single step extrusion, (2) providing the basis for characterizing, modeling and matching the rheology of the pastes sufficiently to permit extrusion of compositionally layered structures, and (3) characterizing the defect pore structure present in current extrusions and consider ways to eliminate them. Designing and fabricating a multi-chamber extruder that could hold pastes of different compositions in five cylindrical cavities and then morph the pastes into closely spaced layers was used to accomplish layered extrusion. The layered paste is fed directly into a square cell honeycomb die to form the SOFC stack. This arraignment keeps pastes separated until the layers are joined in the honeycomb die land. Successful extrusion requires that the rheological properties (i.e., paste shear strength) be matched to prevent excessive mixing of layers. Applying the Dougherty-Kreiger model to predict paste properties has facilitated paste rheology matching and this allows rapid formulation of new compositions to a specific yield stress. Microstructural characterization of the sintered structures revealed isolated porosity in the 10-50 micron size range that was traced to polymer segregation in the extrusion pastes. Polymer-derived porosity was significantly reduced with higher shear rate mixing and increased mixing time in both the dry mixing and paste compounding stages of paste preparation.

(D) Co-sintering of Electrolyte and Interconnect Materials

Construction of Non-Contact Dilatometer: To allow efficient characterization of co-sintering efforts, a non-contact dilatometer was developed in year 1 of the contract and has been fully operational since September 2002. This apparatus is constructed for studying sintering behaviors of hybrid SOFC structure consisting of an electrolyte and metallic interconnect simultaneously. With this tool a sintering curve, which usually requires multiple individual runs for each and every data point (one per day) and two weeks to complete, can now be generated in one day. Quality of data has improved dramatically too since the data are now acquired with the same specimen. The precision of this dilatometer is far better (approaching +/- 0.01%, typical: +/- 0.02%) than had been anticipated (+/- 0.1%), so CTE measurement of SOFC components can also be conducted with this instrument. This capability is also being utilized to monitor the thermal cycling ability of a hybrid structure. This unit contributed to development of a hermetic hybrid stack SOFC in late 2003 and early 2004.

Summary of Co-Reduction & Sintering of Hybrids -Process know-how gained thru studies with non-contact dilatometer in the past two years have enabled co-reduction and sintering of certain hybrid honeycomb structures. Hybrid honeycomb (YSZ-Fe50Ni Interconnect) has been successfully sintered in regular length (2") and in long section

(>8"). Main material compatibility criteria of whether a hybrid structure can be co-sintered are the sintering shrinkage of both components, the closeness of their CTE match, and extrudate quality. Process controls that are critical to the success are dynamic sintering profile matching and stress relaxation dwell at critical temperature around 650C during cooling. Carefully controlled cooling reduces the residual stress in the hybrid honeycomb. Over-coat treatment with YSZ of the free ends and angular termination of the interface provide improved yields of the process (from 30% to over 70% success rate). The process has been successfully scaled up to an industrial-sized (3 feet x 3 feet x 3 feet working volume) vacuum furnace. Production runs can be conducted on a routine basis with an automatic control of all important process parameters.

(E) Process Modeling, Thermal Analyses/Design and Thermomechanical Stresses of Hybrid Stacks
Three principal activities in the modeling program support realization of a functional stack to achieve the Palm Power performance objectives:
- Development and implementation of constitutive models for metal oxide reduction/sintering/plasticity and ceramic viscoelasticity/sintering that permit simulation of the fabrication process for hybrid metallo-ceramic fuel cell stacks, including development of stresses at joints during cooling and residual stresses in the assembly as a function of cell size/shape and stack geometry (LeMasters, Eisele, Wang, and McDowell). This work is being performed in collaboration with the effort on non-contact dilatometry (Lee) and an in-line hygrometer (Eisele) to measure dimensional changes (former) and water vapor indicative of the reduction process (latter) during various phases of the processing. Supporting mechanical property experiments have been conducted on a sample Fe39Ni8Cr / ScSz system.
- Modeling and simulation of steady state heat transfer and temperature distribution in externally insulated hybrid LCA fuel cell stack as a function of stack geometry, and air/fuel flow rates, taking into consideration constraints for processing the stack, sufficient flow conditions to driven reactions, and temperature dependent electronic performance and heat dissipation (Dempsey). A complete model has been developed to analyze operating temperature distribution and power production for a given configuration of the LCM SOFC stack. Approximate models have been developed for electronic performance (Liu's group) and heat generation/dissipation (Dempsey, McDowell). In-house finite difference analyses have been developed that compare within 10% of FLUENT CFD models to enable more efficient preliminary design. A parallel thermal stress analysis capability has been developed by transferring temperature distributions to an ABAQUS finite element input mesh (LeMasters).
- Thermal stresses arise locally from CTE mismatch and globally within the structure due to temperature gradients. As a function of cell type and stack geometry, modeling of thermal stresses is being pursued along three lines: (i) effects of temperature gradients on stress fields at metal-ceramic joints, the "weak links" in the system, (ii) effects of temperature gradients on driving locally debonded metal ceramic joints or other extrusion defects to lengthen/propagate, and (iii) determination of the stress fields arising from temperature gradients during steady state operation and start-up/shutdown phases of fuel cell operation (LeMasters and Dempsey).

(3) Publications, Presentations, Personnel, Patents

(a) Lists of Manuscripts, Peer-Reviewed Journals

1. C. Xia and M. Liu, "Novel Electrode Materials for Low-Temperature Solid Oxide Fuel Cells", *Advanced Materials* 14 521-523 (2002)

2. X. Lu, P. W. Faguy, and M. Liu, "In-Situ Potential Dependent FTIR Emission Spectroscopy: A Novel Probe for High Temperature Fuel Cell Interfaces", *J. Electrochem. Soc.* , 149(10) A 1293-1298 (2002)

3. C. Xia, W. Rauch, F. Chen, and M. Liu, "Sm $_{0.5}$ Sr $_{0.5}$ CoO $_3$ Cathodes for Low-Temperature SOFCs", *Solid State Ionics* , 149, 11-19, (2002)

4. C. Xia, W. Rauch, W. Wellborn, and M. Liu, "Functionally Graded Cathodes for Honeycomb SOFCs", *Electrochem. and Solid State Letters* , 5, A217 (2002).

5. C. Xia and M. Liu, "Microstructures, Conductivities, and Electrochemical Properties of GDC and GDC-Ni Anodes for Low-Temperature Sold Oxide Fuel Cells, *Solid State Ionics,* 152-153 (C), pp. 423-430, (2002).

6. Jason H. Nadler, T.H. Sanders, Jr., and Robert F. Speyer, "Oxidation, Reduction and Sintering of Fe-Cr Alloy Honeycombs, Journal of Materials Research, 18, 8, 1787-1794, (2003)

7. C. Xia, Y. Zhang, and M. Liu, "A Composite Cathode Based on Yttria Stabilized Bismuth Oxide for Low-Temperature SOFCs", *Appl. Phys. Lett.,* **82,** 901-903, (2003).

8. K. M. Hurysz and J. K. Cochran, "Application of high solids content suspension models to pastes," Journal of European Ceramic Society**, 23**, 2047-2052, (2003).

9. Kevin M. Hurysz and Joe K. Cochran, " Modeling paste properties with minimum experimentation", Journal of Ceramic Processing Research, Accepted, December (2003)

10. Kumar, R.S. and McDowell, D.L., "Design of Rectangular Linear Cellular Materials for Maximum Heat Transfer," AIAA Journal, March 2003, accepted for publication.

(b) Papers published in conference proceedings

1. X. Lu, P. Faguy, and M. Liu, "In-Situ FTIR Emission Spectroscopy of Cathodes for SOFCs", *Solid State Ionic Devices III,* Edited by E. Wachman et al, The Electrochemical Society, Pennington, NJ, (2002).

2. C. Xia, B. Rauch, J. Cochran, J. Lee, and M. Liu, "Recent Advances in Design and Fabrication of Low-Temperature SOFCs", in Proceedings of Symposium on Fuel Cells: Bridging Processing and Performance, The First International Conference on Materials Processing for Properties and Performance, Singapore, August 1-3, (2002).

3. J. K. Cochran, K. J. Lee, D. L. McDowell and T. H. Sanders, Jr., "Multifunctional Metallic Honeycombs by Thermal Chemical Processing," 3rd Global Symposium on

Materials Processing and Manufacturing proceedings, Feb 17-21, , A. Ghosh, T. H. Sanders, Jr., and D. Claar, eds., p.127-136, (2002)

4.   Joe Cochran, Kevin Hurysz, Kon Jiun Lee, and Tom Sanders, "Extrusion and Thermo-chemical Processing of Layered Linear Cellular Alloys", Materials Science Forum, 426-**432**, 4295-4300, (2003)

5.   M. Liu, X. Lu, P. Faguy, "In-situ Characterization of Electrode Reactions in Solid Oxide Fuel Cells", in Proceedings of *The 8th International Symposium on SOFCs*, Editor, S. C. Singhal and M. Dokiya, The Electrochemical Society, Pennington, NJ, **PV 2003-07**, pp.1132-1146, 2003.

6.   W. Rauch, K. J. Lee, J. Cochran, M. Liu, "Low Cost Solid Oxide Fuel Cell Stack Design Using Extruded Honeycomb Technology", 203rd Meeting Electrochemical Society, SOFC VIII, Paris, France, 6 pp., (2003).

7.   E. Koep, W. Rauch, and M. Liu, "Investigation of Electrode Kinetics Using Patterned Electrodes", *Solid State Ionic Devices III,* Edited by E. Wachman, K. Swider-Lyons, M. F. Carolan, F.H. Garzon, M. Liu, and J. R. Stetter, The Electrochemical Society, Pennington, NJ, PV 2002-26, pp.319-328 (2003).

8.   J. L. Clark, T. McCoy, R. Oh, K. M. Hurysz, and J. K. Cochran, "Improving Binder Distribution in Extruded Ceramic Paste", Innovative Processes/Synthesis: Ceramics, Glasses, and Composites VII Ceramic Transactions, **154,**131-140, (2003).

9. R. Oh, K. M. Hurysz, and J. K. Cochran, "Effects of Die Geometry and Paste Rheology on Extrusion Pressure", Innovative Processes/Synthesis: Ceramics, Glasses, and Composites VII, Ceramic Transactions, **154,**153-163, (2003).

10. K. M. Hurysz and J. K. Cochran, "Bulk Shear Stress Modeling of Pastes Made from Low Maximum Solids Content Raw Materials", Innovative Processes/Synthesis: Ceramics, Glasses, and Composites VII, Ceramic Transactions, **154**, pp.165-175, (2003).

11. Jason H. Nadler, Thomas H. Sanders, Jr., and Joe K. Cochran, "Microstructural Evolution of Direct Reduced Iron-Chromium Alloys", Proceedings 2nd International Conference on Thermal Process Modeling and Computer Simulations, Nancy, France, Mar 31-Apr 2, (2003) In Press

(c) Papers presented at meetings but not published in proceedings

1.   Joe Cochran, Jim Lee, Meilin Liu, Dave McDowell, Tom Sanders, "Hybrid Metal/Ceria Monolithic Low Temperature SOFCs, DARPA Palm Power Program Review, Panama City, FL, March 12, 2002

2.   J. K. Cochran, Jim Lee, Meilin Liu, Dave McDowell, T. H. Sanders, Jr., "Solid Oxide Fuel Cells Based on Hybrid Metal/Electrolyte Monoliths," DARPA Palm Power Program Review, Washington, DC, June 6, (2002).

3.   J. K. Cochran, Jim Lee, Meilin, Dave McDowell, T. H. Sanders, Jr., "Hybrid Solid Oxide Fuel Cells from Layered Extrusions," CIMTEC 2002, Florence, Italy, July 13-19, (2002).

4. J. H. Nadler, T. H. Sanders, Jr., J. K. Cochran, R. F. Speyer, "Oxide Reduction and Sintering of Fe-Cr Alloy Honeycombs, "NATO ASI: Thermodynamics, Microstructures, and Plasticity, Frejus, France, September 2-13, (2002).

5. Kumar, R. and McDowell, D.L., "Design of Multifunctional Materials," 9th AIAA/ISSMO Symposium on Multidisciplinary Analysis and Optimization, Mini-Symposium on Simulation-Based Design of Materials for Affordability, Atlanta, Georgia, Sept. 5-6, 2002.

6. J. K. Cochran, Jim Lee, Meilin Liu, Dave McDowell, T. H. Sanders, Jr., "Solid Oxide Fuel Cells Based on Hybrid Metal/Electrolyte Monoliths," DARPA Palm Power Program Site Visit, MSE, Georgia Tech, Atlanta, GA, October 18, (2002).

7. J. K. Cochran, Jim Lee, Meilin Liu, Dave McDowell, T. H. Sanders, Jr., "Solid Oxide Fuel Cells Based on Hybrid Metal/electrolyte Monoliths," DARPA Palm Power Program Review, San Diego, CA, February 3-6, (2003).

8. J. H. Nadler, T. H. Sanders, Jr., J. K. Cochran, and R F Speyer, "Oxide Reduction and Sintering of Fe-Cr Alloy for SOFC Interconnects," Poster Presentation, DARPA Palm Power Program Review, San Diego, C, February 3-6, (2003).

9. Kevin Hurysz, Tammy McCoy, Raymond Oh, Jim Lee, and Joe Cochran, "Fabrication and Characterization of SOFC Extruded Layered Stacks", Poster Presentation, DARPA Palm Power Program Review, San Diego, CA, February 3-6, (2003).

10. S.Zha, W. Rauch, C. Xia, and M. Liu, Novel Electrodes for Low-Temperature SOFCs", Poster Presentation, DARPA Palm Power Program Review, San Diego, CA, February 3-6, (2003).

11. W. Rauch, R. Williams, and M. Liu, "Design and Performance Prediction of Honeycomb SOFCs", Poster Presentation, DARPA Palm Power Program Review, San Diego, CA, February 3-6, (2003).

12. X. Lu, H. Abernathy, and M. Liu, "Electrode Properties Using *In-Situ* FTIR/Raman Spectroscopy", Poster Presentation, DARPA Palm Power Program Review, San Diego, CA, February 3-6, (2003).

13. K.J. Lee and Raymond Oh, "Co-Reduction and Sintering of Hybrid Honeycomb SOFCs", Poster Presentation, DARPA Palm Power Program Review, San Diego, CA, February 3-6, (2003).

14. Scott Eisele and Dave McDowell, "Process Modeling of Integrated Metallo-Ceramic LCMs", Poster Presentation, DARPA Palm Power Program Review, San Diego, CA, February 3-6, (2003).

15. B. Dempsey, A. Wang, J. LeMasters, and D. Mcdowell, "Transport Mechanisms and Integrety of LCM Fuel Cells", Poster Presentation, DARPA Palm Power Program Review, San Diego, CA, February 3-6, (2003).

16. 16. R. Kumar, C.Seepersad, B. Dempsey, and D. McDowell, "Multifunctional Design of Linear Cellular Materials, Poster Presentation, DARPA Palm Power Program Review, San Diego, CA, February 3-6, (2003).

17. Aijun Wang, Jennifer Totty, and Dave McDowell, "Mechanical Properties of Linear Cellular Arrays", Poster Presentation, DARPA Palm Power Program Review, San Diego, CA, February 3-6, (2003).

18. J.K. Cochran, K.M. Hurysz, K.J. Lee, M. Liu, D.L. McDowell, W.L. Rauch, and T.H. Sanders, "Extruded SOFC Stacks, Processing and Performance", International Symposium of SOFC Materials and Technology, American Ceramic Society, Cocoa Beach, FL, Jan. 27-29, 2004 (Invited)

19. Joe Cochran, Jim Lee, Meilin Liu, Dave McDowell, Tom Sanders, "Extruded SOFC Stacks, Processing and Performance", DARPA Palm Power Program Review, Orlando, FL, February 9-11, (2004).

20. Ben Church, T H Sanders, and J K Cochran, "Alloy Development for Solid Oxide Fuel Cells (SOFC) Interconnects", Poster Presentation, DARPA Palm Power Program Review, Orlando, FL, February 9-11, (2004).

21. Joe Cochran, K.J. Lee, Tammy McCoy, and Raymond Oh, "Fabrication and Sintering of Hybrid Monolithic SOFCs", Poster Presentation, DARPA Palm Power Program Review, Orlando, FL, February 9-11, (2004).

22. Joe Cochran, Kon Juin Lee, Dave McDowell, Tom Sanders, "Co-Sintering and Joining of Direct Reduced Alloys to Ceramics for SOFC Packages", Steven Fishman Honorary Symposium, American Ceramic Society, Indianapolis, IN, April 21, 2004 (Invited)

(d) Scientific Personnel

Principal Investigators

Joe Cochran, B. Mifflin Hood Professor and Associate Chair, MSE, Georgia Tech, Atlanta, GA; *Project Direction Area - Hybrid Monolith Fabrication*

Jim Lee, Senior Research Engineer, MSE, Georgia Tech, Atlanta, GA; *Project Direction Area - Hybrid Reduction, Sintering, Joining*

Meilin Liu, Professor and Co-Director, Center for Fuel Cell & Battery Technology, MSE, Georgia Tech, Atlanta, GA; *Project Direction Area - Electrolyte and Electrode Development*

David L. McDowell, Regents' Professor and Carter N. Paden, Jr. Distinguished Chair in Metals Processing, Director, Mechanical Properties Research Laboratory, ME &MSE,

Georgia Tech, Atlanta, GA; *Project Direction* Area - Thermal/Mechanical Modeling/Design

Thomas H. Sanders, Jr., Regents' Professor and Director of Graduate Programs, MSE, Georgia Tech, Atlanta, GA; *Project Direction Area* - Metal Interconnect Development

Post Doctoral Students

Kevin Hurysz, MSE, Hybrid Monolith Fabrication
Rajesh Kumar, ME, Cell Structure Modeling/Design
Bill Rauch, MSE, Electrolyte and Electrode Development/Cell Testing
Aijun Wang, ME, Thermal/Mechanical Modeling/Design
Changrong Xia, MSE, Electrolyte and Electrode Development
Shaowu Zha, MSE, Electrolyte and Electrode Development/Electrode Fabrication

Doctoral Students

Robert Williams, MSE, Performance Modeling and Fabrication of Electrodes
Rupak Das, MSE, Chemical/Electrochemical Modeling/Performance Prediction
Harry Abernathy, MSE, In-situ Characterization of Electrode Reactions
Justin Clark, MSE, Metal Interconnect Development, **Graduated - 05/2004**
Ben Church, MSE, Metal Interconnect Development, **Graduated - 09/2004**
Ben Dempsey, ME, Thermal/Mechanical Modeling/Design
Xinyu Lu, MSE, Electrolyte and Electrode Development
Tammy McCoy, MSE, Hybrid Reduction, Sintering, Joining
Jason Nadler, MSE, Metal Interconnect Development, **Graduated - 09/2003**
Ray Oh, MSE, Hybrid Monolith Fabrication

Masters Student

Jason LeMasters, ME, Coupled Thermo-mechanical Stress Analysis, **Graduated 4/2004**
Scott Eisele, ME, Thermal/Mechanical Modeling/Design, **Graduated 4/2004**

Undergraduate Student

Scott Eisele, ME, Thermal/Mechanical Modeling/Design, **Graduated - 4/2002**
Charles Dellinger, Layered SOFC Fabrication

(e) Report of Inventions

1. Joe Cochran, Jim Lee, Meilin Liu, and Bill Rauch, "Hybrid Solid Oxide Fuel Cells from Linear Cellular Materials", Invention Disclosure ID 2412, January 2001, US Patent Application, January 2002, International filing, July 2003.

2. Meilin Liu, Joe Cochran, and Shaowu Zha, "Mixed Ionic-Electronic Conducting Membrane with Honeycomb Structure for Gas Separation and Purification and for Reforming of Hydrocarbon Fuels", Invention Disclosure ID 3026, GTCR, OIT, Georgia Tech, October 2003.

Appendix A
Electroding and Demonstration of Honeycomb Fuel Cells

1. Objectives

- Investigate new materials (mainly electrolyte and cathode) that can satisfy the low-temperature operation of functional fuel cells.
- Develop unique electroding approaches and testing techniques for honeycomb fuel cells.
- Demonstrate functional honeycomb fuel cells running at reduced temperatures.

2. Development of Fuel Cell Materials for Low-temperature Operation

The internal resistances of a fuel cell mainly consist of two parts, i.e., bulk resistance of electrolyte and polarization resistance in the cathode and electrolyte interface, which limit the performance of SOFCs. This is extremely true when running a fuel cell below 700°C in order to substantially increase the life of an SOFC, widen the selection of electrode, interconnect and manifold materials and reduce the cost of the materials processing and cell fabrication. In order to decrease the operation temperature, one important approach is to develop new electrolyte materials to alleviate the contribution of bulk resistance. Another main method is to adopt novel cathode materials and/or unique microstructures which have lower interfacial resistance interacted with electrolyte component, especially when the fuel cell operates below 550°C.

2.1. Electrolyte

Scandia stabilized zirconia is investigated as an alternative to ceria for a low temperature electrolyte because conductivities may be comparable, it is much stronger than ceria, the expansion is lower, and a reliable, reasonable cost, powder supply is available for extrusion fabrication.

To determine conductivities of scandium-stabilized zirconia (ScSZ), 4×4 square cell honeycomb was fabricated from commercial powder by extrusion and sintered at 1350°C and 1400°C. Cathodes of LSM/YSZ were fabricated by coating the slurry on the surfaces of an ScSZ honeycomb. To form a uniform slurry, strontium doped lanthanum manganite ($La_{0.85}Sr_{0.15}MnO_3$, LSM) was ball milled with YSZ (LSM:YSZ= 60:40 in weight), an organic binder, and acetone. The cathodes were finally fired in air at 1100°C for 4 hours. The electrical conductivities of the ScSZ and the interfacial resistances of the LSM/YSZ cathode were measured using impedance spectrum. Shown in Fig. A1 are the electrical conductivities of ScSZ in honeycomb form. The conductivities of an YSZ honeycomb are also shown in the figure for comparison. It is very clear that scandium stabilized zirconia is much more conductive than yttrium stabilized zirconia, the conductivity of ScSZ at 600°C is higher than those of YSZ at 700°C, implying that fuel cells based on ScSZ can be operated at least 100°C lower than those on YSZ with the similar microstructures. The conductivities of ScSZ in hydrogen with 3% H_2O are almost

the same as those measured in air, implying that ScSZ is stable under the fuel cell operating conditions. The small differences in conductivities of ScSZ as measured in air and in hydrogen are within experimental error. Interfacial resistances are measured as a function of temperature for the LSM/YSZ cathode on the ScSZ electrolyte. At temperatures above 650°C, the interfacial resistances are much smaller than that for the same cathode on YSZ.

2.2.Cathode

As the operation temperature drops below 700°C, the interfacial resistance between the cathode and electrolyte will dominate the overall polarization of fuel cell. Thus, development of new cathode materials and optimization of the cathode microstructures are two critical issues in order to decrease the cathodic overpotential, and hence improve the fuel cell performance at low temperatures. In this work, BICUVOX and Ag-YDB were originally developed as novel cathode materials. Moreover, functionally graded materials were also intensively investigated as potential cathodes for honeycomb fuel cells.

BICUVOX

BICUVOX ($Bi_2V_{0.9}Cu_{0.1}O_{5.35}$) represents one of the most attractive oxygen-ion conducting ceramics at temperatures below 600°C. Its reported oxygen-ion conductivity is about 10^{-2} S cm^{-1} at 350°C and 10^{-1} S cm^{-1} at 600°C, much higher than the conductivities of GDC at similar temperatures. This material cannot be used as electrolyte for fuel cells because it is not stable under reducing conditions (e.g., in fuel). However, its stability may be adequate for use as the cathode in a SOFC since the cathode is exposed to the oxidant (e.g., air). Thus, we have initiated our investigations into this material to evaluate its suitability for cathode in low-temperature SOFCs. Samples of BICUVOX were prepared using a repeated solid-state reaction and calcinations, starting from Bi_2O_3 (99.9%), V_2O_5 (99.6%) and CuO (min.99%), all from Aldrich chemicals. The Bi_2O_3 was previously heated at 600°C for 6 hrs in order to eliminate any trace of carbonate. The stoichiometric amounts of oxide powders were mixed and ground in an agate mortar. Part of the powder was then heated for 12 hrs successively at 600, 700 and 800°C and, finally, cooled down to room temperature at 20°C per hour rate. The other powder was heated and cooled at the same procedure as the former one, but it was ground before increasing the heating temperature. X-ray powder diffraction analysis indicates that the samples prepared by different routes have the same structure, an orthorhombic structure as reported in the literatures. Shown in Fig. A2 are the cathode-electrolyte interfacial resistances as a function of cell operating temperature, together with the total cell resistances and the electrolyte resistances.

Ag-YDB

Our SOFC honeycomb design with alternating layers of electrolyte and interconnect is an elegant way of cell stacking, offering the advantages of not only high power density but also easy manifolding and sealing. The new cathode of Ag-YDB offers a significant

advancement to our system and increases the probity of allowing us to meet our performance goals. The cathode is a composite consisting of silver and yttria doped bismuth oxide (YDB), which is an excellent oxygen ion conductor. YDB was synthesized using a co-precipitation method. Silver oxide was then mixed with YDB by ball milling with organic binders and acetone to form slurry, which was subsequently coated onto the inner channels of YSZ honeycombs. The coated layers were then dried, fired, and characterized in air using impedance spectroscopy. Each impedance spectrum was taken about 30 minutes after the system reached equilibrium when the conditions were stabilized.

The interfacial polarization resistances of several cathodes (as determined from the impedance spectra) are compared including an Ag-YDB composite, a recently developed functionally graded cathode, and a composite consisting of lanthanum strontium manganite (LSM) and gadolinium doped ceria (GDC). Clearly, the polarization resistances of the Ag-YDB composite cathode are far smaller than those of other cathodes. This newly-developed Ag-YDB composite cathodes for low temperature solid oxide fuel cells (at temperatures below 700°C) has interfacial polarization resistances about one order of magnitude (or 10 times) smaller than those reported in the literature. In other words, the catalytic activity of the electrode is about 10 times higher than those reported in recent literature.

Functionally Graded Cathodes

Cathodes graded in microstructure (particle size) and compositions were fabricated on stabilized zirconia (YSZ and ScSZ) honeycombs using the combination of a sol-gel process (the first layer) and a slurry coating process. Shown in Fig. A3 are the cross-sectional views of a graded cathode. The composition was gradually changed from GDC+LSM (the electro-catalytically active layer) to LSCF (the current-collecting layer), as indicated on the side of the figure. The GDC-LSM layer was prepared using a sol-gel process with GDC sol and fine LSM powder fabricated by a glycine-nitrate process (GNP). The subsequent layers were prepared by a slurry-coating process with powders that were prepared by solid state reaction and a glycine nitrate method. Fig. A3 shows that the top layer (current-collecting layer) consists of grains much bigger than those of the intermediate layers. Further, the sizes of the grains in the intermediate layers are bigger than those in the catalytically active layer. The BET specific area of the powder prepared by the sol-gel process is about 47 m^2/g, ten times greater than that prepared by the glycine-nitrate process. Shown in Fig. A4 are the interfacial resistances of the graded cathodes prepared by different methods, and the resistance of LSM-GDC cathodes prepared by the glycine-nitrate method. The graded cathodes show much better electrochemical performances than the LSM-GDC composite. However, the performance of the cathode graded in both composition and particle size is not as good as the one graded in composition, implying that the microstructure of the cathode is yet to be optimized.

2.3. Anode

Several material sources were used to understand the impact of the various materials. The nickel oxide used for this process was all derived form the glycine-nitrate process and then post treated at either 500$^{\text{o}}$C (NiO [1]) or 800$^{\text{o}}$C (NiO [2]). Likewise, the GDC was derived from glycine-nitrate, but the same powder was used in all samples. Finally, two samples contained YSZ, which was derived from either glycine-nitrate (GN) or commercial YSZ (Comm). Sample 1, composed of 65 wt% NiO [1] 8 wt% GDC and 27 wt% YSZ (GN). Sample 2 was composed of 65 wt% NiO [1] and 35 wt% GDC. The third sample is identical to sample 2, except that it substitutes the coarser NiO [2] for the NiO [1]. Finally, the fourth sample was the same as sample 1, except with commercial YSZ powder.

Fig. A5a shows the data attained for the interfacial resistance of the four samples during symmetric anodic testing. The general trend indicates reasonable performance with higher levels of GDC in place of YSZ and an unexpected result in that courser YSZ enhances performance over a finer variety. These results are a combination of the electrochemical measurements and physical measurement to deduce the specific sample area. Fig. 5b, showing the ohmic resistance associated with each sample, including the electrolyte resistance the bulk resistance of the electrode and the wires. It is clear that compositions 2 and 3 are superior performers overall and are currently being applied to ScSZ/YSZ monolithic hybrid extrusions for complete evaluation.

3. Development of Electroding and Fuel Cell Testing Techniques

3.1. Slurry Coating

Slurry coating is a typical electroding process developed in this work to fabricate both anode and cathode for honeycomb fuel cells. Fig. A6 shows a schematic diagram of slurry coating process. A sample of this electroding method is described in detail as following.

YSZ honeycombs were fabricated by extrusion, followed by sintering at 1350$^{\text{o}}$C for 12 hours both in air or in a reducing atmosphere (7% H_2 balanced with Ar). Strontium doped lanthanum manganate, $La_{0.8}Sr_{0.15}MnO_3$ or LSM, was synthesized by a glycine-nitrate process. The amorphous LSM powder derived from the GNP was then annealed at 800$^{\text{o}}$C for 4 hours to form the perovskite structure, as determined by X-ray diffraction analysis. The perovskite LSM powder was then ball milled with YSZ in weight ratio of LSM:YSZ= 60:40, together with proper amount of an organic binder (V006) and acetone, to form a slurry for a composite cathode consisting of LSM and YSZ. The electrode slurry was subsequently applied to the YSZ honeycombs by slurry coating and followed by firing at 1150$^{\text{o}}$C for 4 hours. Shown in Fig. A7 are the surface and cross-sectional views of the composite electrode as revealed using a scanning electron microscope (SEM).

3.2. Ceramic Fiber Filling

The slurry coating process, while allowing excellent tailoring of microstructure and composite structures, leads to dramatic variations in thickness of the electrodes in the corners compared to flat surface. This macrostructural detail, while seemingly harmless, is likely a large source of the cracking and delamination difficulties to which we currently attribute the less than ideal cell performance. Several new approaches are being pursued from a macroscopic perspective to attain a compatible electroding system, which will create the necessary structure while maintaining suitable performance. The system needs to be easily applicable in the honeycomb structure and provide the necessary porosity for gas transport, sufficient surface area, and electronic/ionic conductivity for electrochemical reactions. New methods being investigated include organic templating, creation of ceramic foams, and the use of fibers.

Initial work with fibers appears to hold some promise. The advantages of fibers include the ability to make open structural networks, long avenues of phase continuity, and substantially lowered theoretical percolation limits. Fibers of YSZ are commercially available and relatively inexpensive. Producing pastes or slurries is relatively straightforward and the fibers are less prone to drying shrinkage than similar powder based slurries. Pastes are easily injected into the green honeycomb and fired to yield the structures seen below. Fig. A8 shows a section of honeycomb that underwent complete channel fill. Partial fill options can be produced through different slurries and application techniques. Two other options are seen in Fig. A9. The edge fill seen in Fig. A9a, will allow easy gas flow through the channel, whereas the surface coating only seen in A9b is designed as a structural support for of subsequent slurry coating.

3.3. Testing Set-up

Efforts were made to reduce the fluctuating combustion within the furnace through the use of a hard ceramic seal, produced using Acoustic cement and adding a third quartz tube to contain and remove the waste hydrogen gas. Our typical test configuration can be seen in Fig. A10. Silver wires were added into each channel to serve as current collectors and platinum paste was applied to both ends to attach platinum wires. Quartz tubes were sealed to the monolithic cell. Temperature was increased to $550^{\circ}C$ and held for 10 hours. Potentiodynamic measurements were performed to evaluate the power generated by the cell. Temperature was increased in increments, up to $750^{\circ}C$. At each step, the voltage was allowed to stabilize and power measurements were performed.

4. Demonstration of Functional Honeycomb Fuel Cells

4.1. Monolith Fuel Cells

Monolithic zirconia structures were electroded and tested by using the set-up as shown in Fig. A10. Efforts were made to eliminate cracking and shrinkage through the use of thinner coatings and more firings per electrode. The payoff is seen in increased power from each successive cell, though not to the degree desired. The performance of one

functional honeycomb fuel cell is shown in Fig. A11. This cell contained alternating layers of YSZ and ScSZ and was ported to utilize only layers 2 and 4 of the 5 layered structure.

Electrodes were applied using traditional slurry coating procedures as described previously. The extrusion was plugged, ported and fired before electrode application. The anode consisted of nickel oxide-YSZ cermet with 8 percent ceria. The cathode consisted of a 40/60 (wt%) composite of YDB and Ag_2O. The cells were mounted in the normal manner on quartz tubes and supplied with moist (3%) hydrogen and air. AC and DC measurement techniques were performed to evaluate the cell. The estimated active area is about 3.2 cm^2. Peak performance of the cell was about 90 mW/cm^2 at 700°C. Impedance spectroscopy indicated that the resistance is evenly split between the bulk resistance and the electrode-electrolyte interfaces.

After testing, the cell was broken and electrodes were observed using SEM. The anode, seen in Fig. A12, shows reasonable coverage. Fig. A12a shows a complete anodic cell with sufficiently thick and coherent coverage across all of the wall surfaces. The inset (A12b) shows the minimum thickness observed in the anode to be more than 10 microns. The anode is easier to observe during coating since it is the first coating applied and the honeycomb is translucent. The cathodic channels show similar microstructure as that of anode, with much thinner electrode thickness in the wall area compared with the honeycomb corners.

4.2. Hybrid Fuel Cells

A hybrid structure based on the interconnect 54Fe-46Ni and YSZ as the electrolyte was extruded. Fourteen samples, 5 cm in length, were ported and hydrogen sintered. Twelve of the samples were crack free after sintering. These hybrid cells can be seen as "real" fuel cell stacks with alternate three interconnect and two electrolyte layers.

The hybrid cell was plugged by ceramic sealant and was examined to be gas-tight in green state. Platinum paste was applied to all honeycomb channels acting as either anodes or cathodes. The cell was then mounted to testing set-up and heated slowly to 600 and 700°C at a rate of 1°C/min. Both sealant and electrodes were fired in-situ. Pure H_2 and O_2 were fed as fuel and oxidant.

Shown in Fig. A13 are the cell voltages and power output as a function of electrical currents. The open circuit voltage shows a small increase when heating from 600 to 700°C (1.48 vs 1.51 V), which may be due to the electrode calcination. The short current increased from 8 to 50 mA correspondingly. The cell stability was also evaluated at 700°C. The OCV drops from 1.51 V to 1.32 V after the continuous operation at a terminal potential of 1 V for 5 hours.
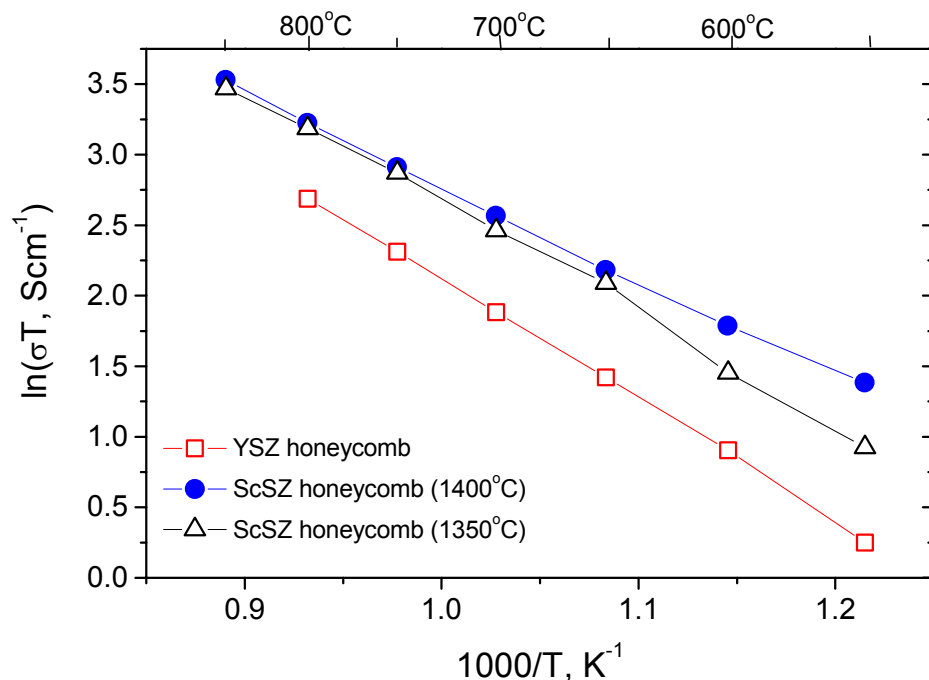
Figure A1. Conductivities of ScSZ and YSZ honeycombs versus temperature.
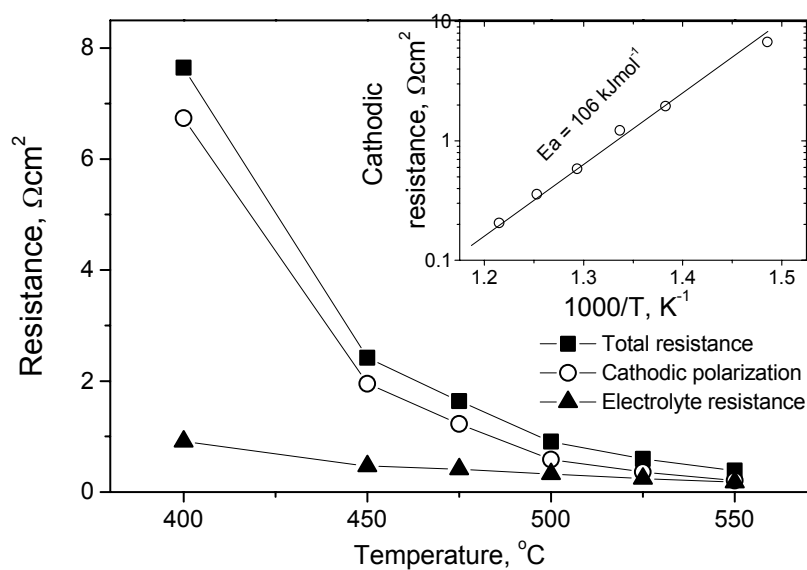
Figure A2. Total cell resistances, cathode-electrolyte interfacial resistances, and electrolyte resistances as determined from impedance spectra for a fuel cell consisting of an Ag-BICUVOX composite cathode, a GDC electrolyte, and a Ni-GDC composite anode.

LSCF (Solid state rection)

GDC+LSCF (Glycine, Solid State)

GDC+LSM+LSCF, Glycine

GDC+LSM (Sol-Gel)

ScSZ
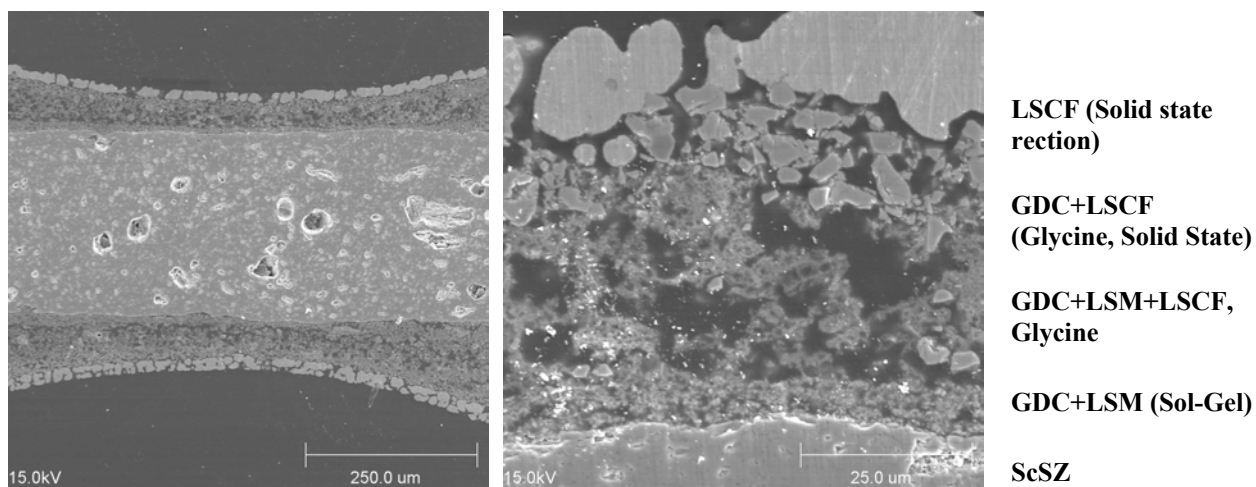
Figure A3. Cross-sectional views of a composite cathode prepared by the combination of a sol-gel process and a slurry coating process using powders prepared by glycine-nitrate process or solid state reaction.
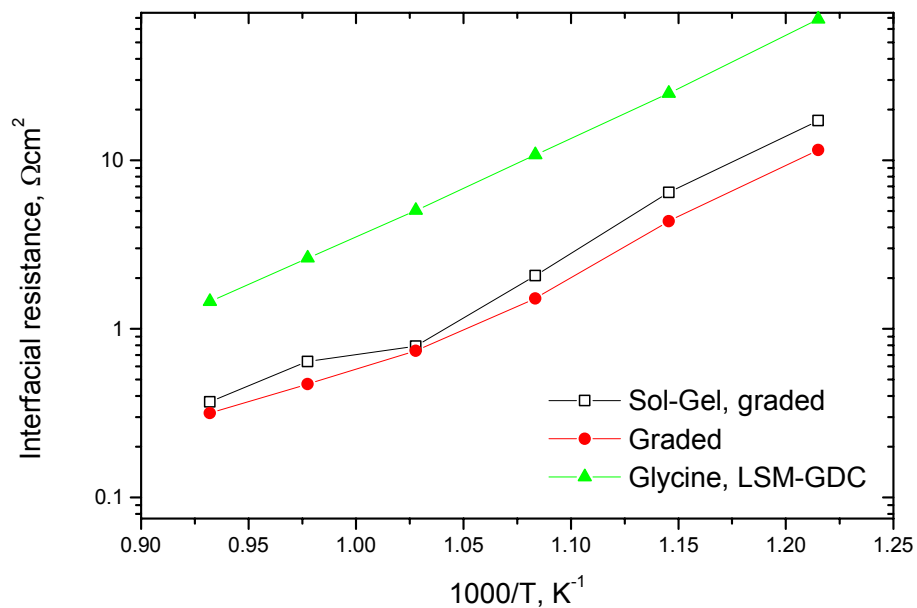
Figure A4. Interfacial polarization resistances of several cathodes measured at different temperature.
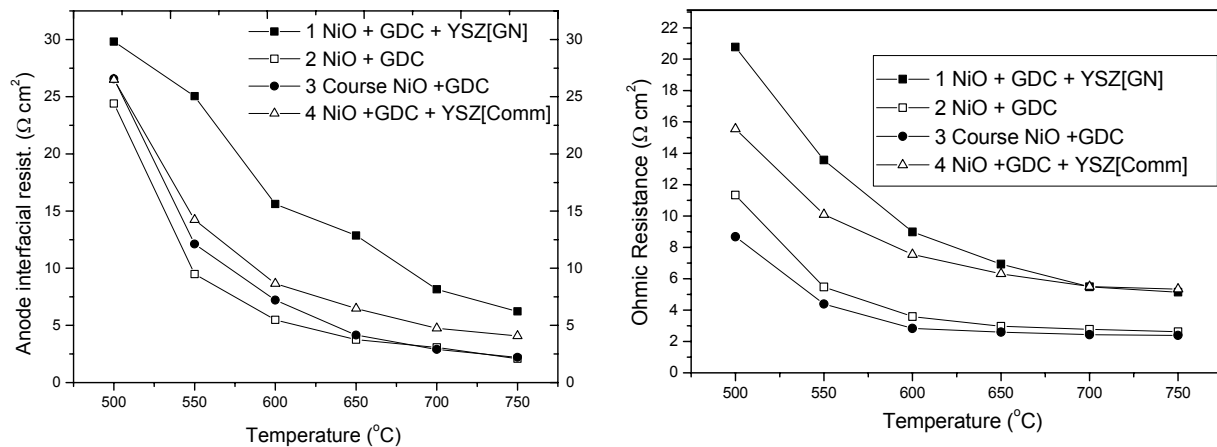
Figure A5. Interfacial and Ohmic resistances of anodes applied to honeycombs with different anodic materials.
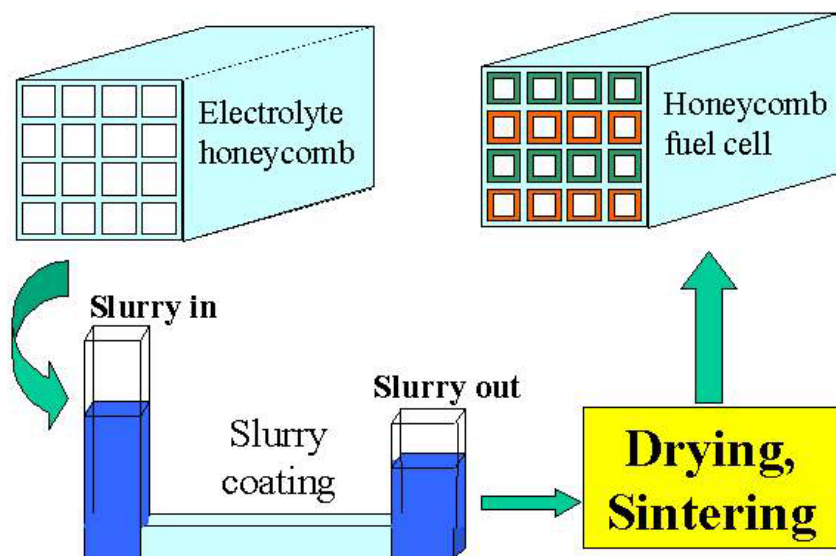
Figure A6. A schematic diagram of slurry coating process for electroding honeycomb fuel cells.
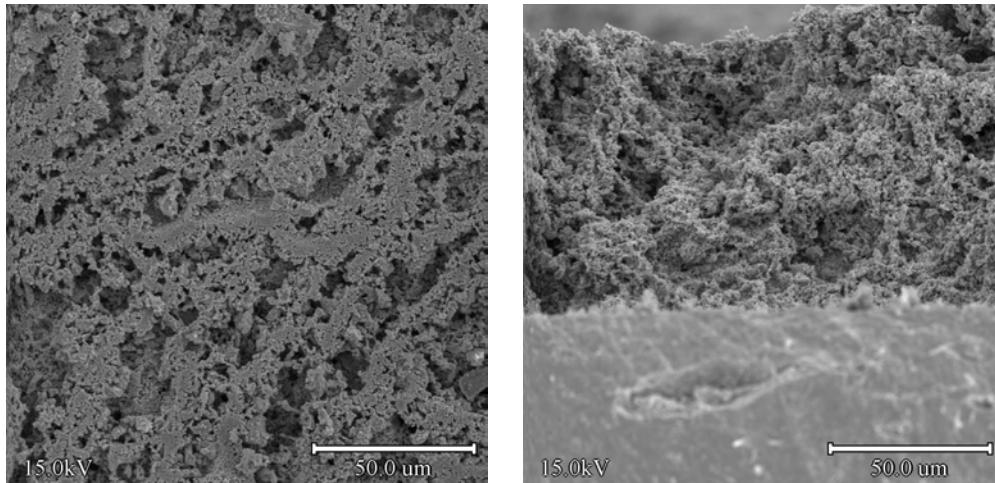
Figure A7. (a) Surface and (b) cross-sectional views (SEM micrographs) of a composite cathode consisting of LSM and YSZ prepared by slurry coating.
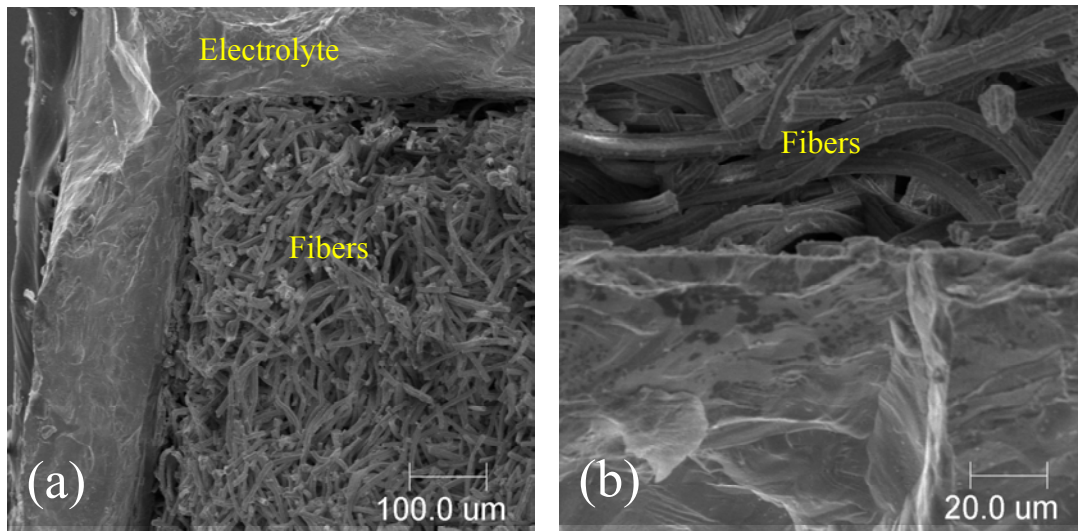
Figure A8. Micrographs of YSZ fiber filled honeycomb channels.
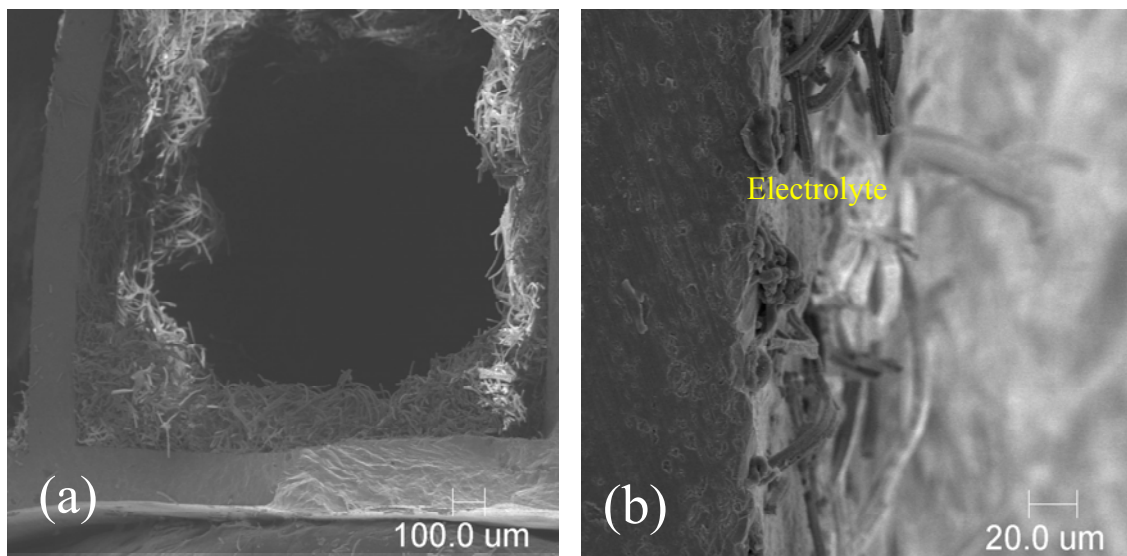
Figure A9. Partial filling options for fibrous networks in honeycomb channels include (a) partial filling and (b) surface modification.
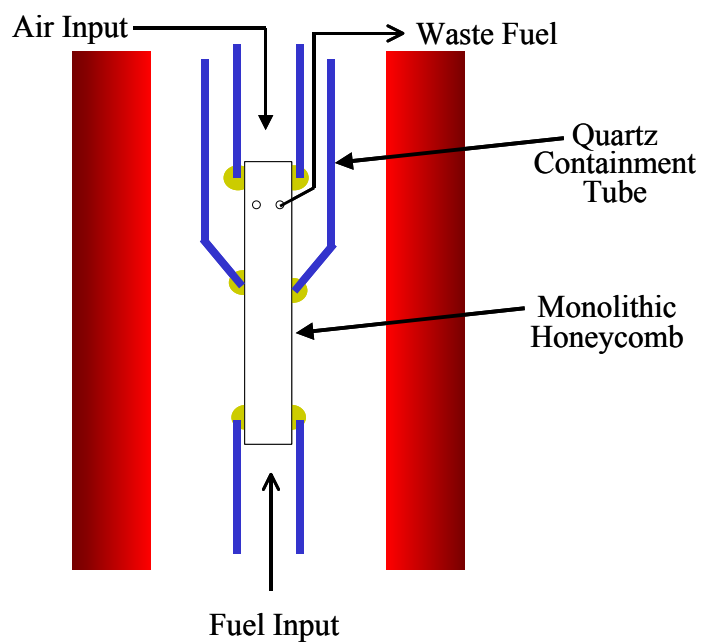
Figure A10. A typical test configuration for monolithic honeycomb fuel cells.
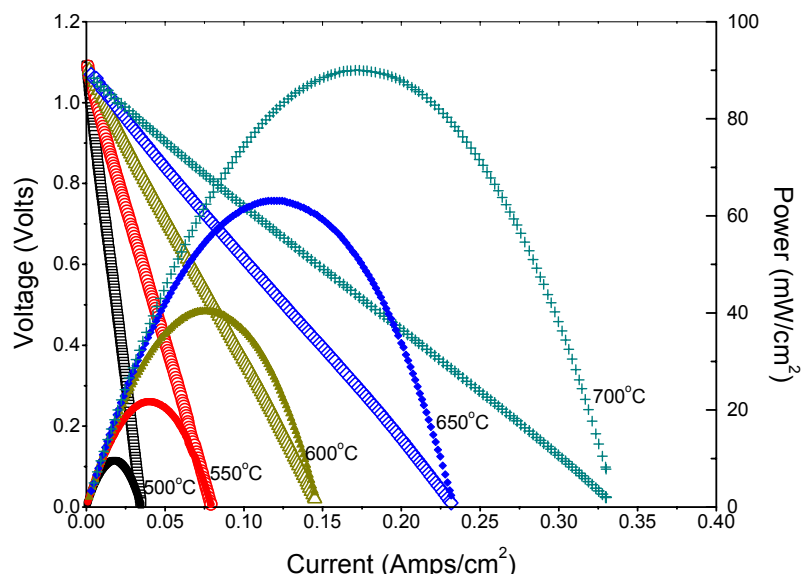
Figure A11. Power and I-V plots for HC-18 monolithic zirconia hybrid cell.
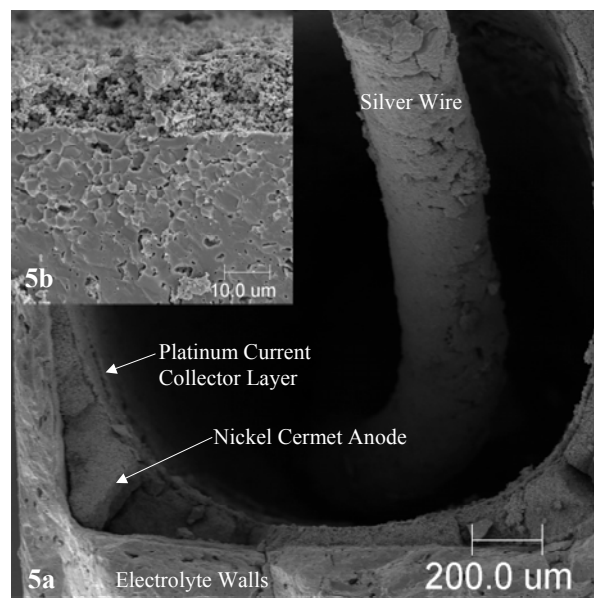
Figure A12. Section of honeycomb cell showing anodic channel with nickel cermet anode, Pt current collection layer, and current collecting wire. Inset shows close up of anode structure.
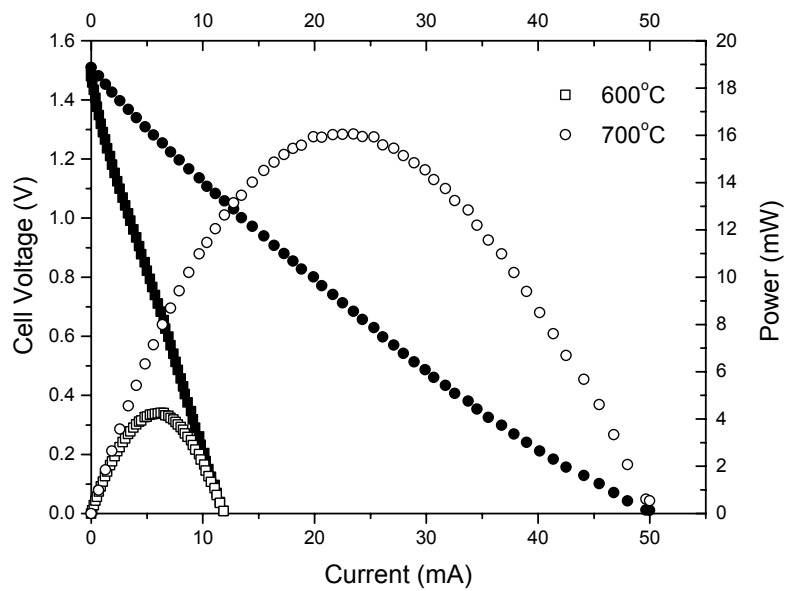
Figure A13. Cell voltages and power output for a honeycomb fuel cell stack as a function of currents at 600 and 700°C.

Appendix B
Interconnect Thermal Expansion Matching to Solid Oxide Fuel Cells

1. Abstract

A method for the rapid fabrication of homogeneous potential interconnect alloys from metal oxide precursors and evaluation of their thermal expansion mismatch to solid oxide fuel cells is described. Pastes of metal oxide powders were extruded into honeycomb geometries and sintered in hydrogen. Thermal expansion mismatch was evaluated based on heating with a zero-mismatch at room temperature, and on cooling with zero-mismatch temperatures at 600 or 1100 °C. The non-linear expansion behavior of Fe-Ni invar alloys resulted in different compositions being optimum, based on the assumed zero-mismatch temperature.

2. Introduction

A solid oxide fuel cell (SOFC) is a device that generates electric power through the oxidation of a fuel such as hydrogen or methane. There has been significant recent activity in developing new SOFC designs and incorporating new materials with the general goals of increasing efficiency, lowering production cost, and increasing reliability. The recent ability to operate a SOFC at relatively low temperatures (<700 °C) has made it possible to economically employ metal alloys as interconnects. This is widely seen as a method to reduce cost and improve manufacturability, since metal alloys are less expensive and more formable than traditional $LaCrO_3$ interconnects. The properties that a metal interconnect should exhibit for a planar SOFC design have been recently discussed by Linderoth, *et al.* [i] and Zhu and Deevi [ii]; the two most critical properties are a close thermal expansion match with the electrolyte, and oxidation resistance at the operating temperature of the SOFC. Reviews of potential alloys suitable for this application have recently been made by Quadakkers, *et al.* [iii] and Yang, *et al.* [iv]. Research on SOFC interconnect alloys has tended to concentrate on oxidation behavior; several commercial and experimental ferritic Fe-Cr alloys have been identified as oxidation resistant in these reviews.

The traditional SOFC fabrication method consists of assembling alternating layers of anode, interconnect, electrolyte and cathode at room temperature [v]. The layers are stacked to create the desired cell height and seals, such as compression, glass, or cement, are applied to the edges of the plate to make the stack hermetic. Certain types of seals require a high-temperature heat-treatment during which the layers become rigidly joined while other seals become rigid upon application at room temperature. Recently, Rauch, *et al.* [vi] have described a method for producing hybrid SOFC stacks by means of a paste extrusion technique. An example of a SOFC structure making use of this technique is shown schematically in Figure 1. The SOFC structure is comprised of alternating layers of electrolyte and metal interconnect (Figure 1), made from the co-extrusion of two pastes. The interconnect paste is comprised of metal oxides blended in proportion to yield the desired metal alloy composition. After co-extrusion, the SOFC stack is heat-treated in a hydrogen atmosphere in which the metal oxides that constitute the interconnect layers reduce, densify and homogenize. The yttria-stabilized zirconia (YSZ)

electrolyte is chemically stable in the reducing atmosphere and only undergoes densification. The anode, cathode, gas manifolds, and contacts are added in post-heat-treatment stages. In service, SOFCs of various designs will not typically be exposed to temperatures in excess of roughly 700 °C, which is the operating temperature of the fuel cell.

Eisele [vii] has recently modeled the stresses that develop during the reduction and sintering stages of the extruded hybrid stack and observed defects associated with processing. It was noted that severe cracking can result from even slight changes in heat-treatment schedules. Cochran, *et al.* [viii] showed that while total shrinkage of the YSZ portion of the hybrid SOFC stack can be similar to that of the metal interconnect, the shrinkage of the different components occurs to different extents at different temperatures during the reduction/sintering heat-treatment, which then leads to cracking and delamination of the YSZ/metal interface. These defects will result in a structure that is neither hermetic nor mechanically reliable. It was also shown that the sintering profile of the metal interconnect layer can be modified to match more closely the sintering profile

☐ Metal Interconnect

☒ Ceramic Electrolyte
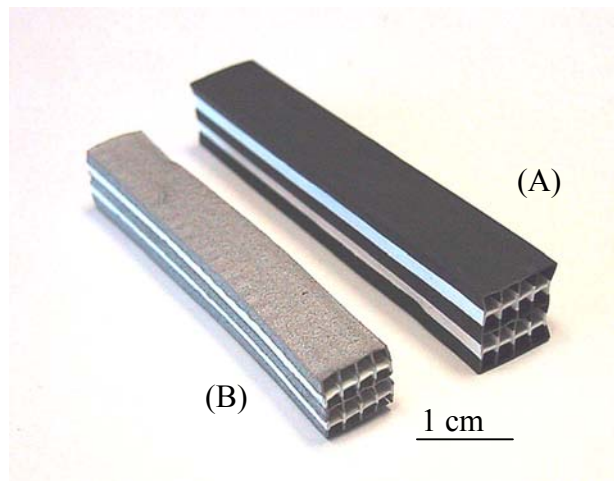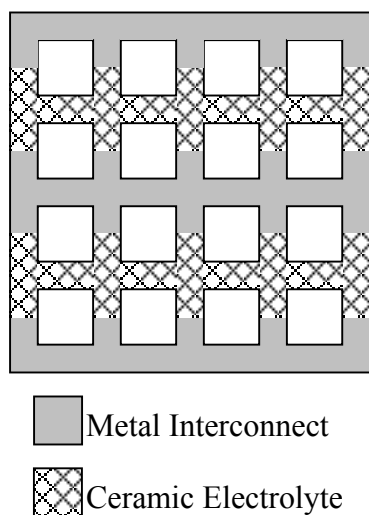
Figure 1. Schematic of a hybrid fuel cell stack (left) comprised of alternating layers of interconnect and electrolyte. Photos of (A) as-extruded hybrid stack and (B) after heat-treating in hydrogen. (After Rauch, et al.

of YSZ by making changes to the raw material (i.e. particle size and distribution) or changing the sintering heat-treatment schedule. However, the contraction of the metal upon cooling can only be modified by changing the metal composition. Furthermore, using a metal with a closer thermal expansion match to the electrolyte reduces the likelihood of failure due to thermal cycling during service. Therefore, the thermal

expansion behavior of the metal interconnect must be tailored to match that of the electrolyte.

Allowable mismatch in thermal expansion between SOFC materials has been mentioned [i, ix], though the proposed design limits are not generally in agreement. For traditional SOFCs, the evolution of stress due to thermal expansion mismatch would depend on the fabrication method; stress would evolve on heating for stacks rigidly joined at room temperature or on cooling for stacks joined during the high-temperature heat-treatment required for certain types of seals. For hybrid SOFCs, interfacial stress initiates upon cooling at a temperature below which atomic diffusion, plastic flow, and microstructural recrystallization processes in the metal layers can relieve interfacial stresses.

The current work details a method for rapidly fabricating interconnect alloy compositions from metal oxide precursors and characterizing their thermal expansion behavior. Extrusions of interconnect alloys can be tested independently for properties such as thermal expansion, sintering characteristics, and oxidation resistance. Potential interconnect alloys that show superior properties can then be incorporated into the more complex hybrid structure for further evaluation.

As pointed out previously, the focus of most alloy development programs for interconnect materials has been on ferritic stainless steels because the thermal expansion of ferrite is less than austenite. However, austenitic Fe-Ni alloys were selected for initial examination because of the interesting thermal expansion behavior of near-invar compositions. These alloys have been used historically for low temperature (< 200 °C) applications; the thermal expansion behavior at temperatures in the operating range of a SOFC has not been well documented. In this paper, the thermal expansion matching between selected Fe-Ni alloys and YSZ are compared with a commonly-recommended [iv, x] interconnect alloy, Fe 20 wt% Cr. Binary Fe-Ni alloys would likely suffer severe oxidation in the operating environment of a SOFC. This work considers only thermal expansion and is thus a first-step in the process of designing novel ternary (or greater) alloys for hybrid SOFC interconnects.

3. Experimental Procedure

Metal oxides [Fe_2O_3 (Pea Ridge, 2-8 μm, 99.7%), NiO (Ceramic Color, 6 μm, 99.9%) and Cr_2O_3 (Fisher Scientific, 2-5 μm, 99.9%)] were mixed in proportion to produce the desired alloy compositions after complete reduction. The metal oxide powders were first dry-mixed with Methocel A4M (Dow Chemical), which acts as a binder when hydrated. A solution of deionized water with 2.5 wt% Pegosperse 100S (Lonza), a lubricant, was then added to the dry powder mixture in a commercially available food blender. Solids loading was kept constant at 50.5 vol% for each composition. Binder contents were tailored to meet particular paste properties using equations and techniques described by Hurysz [xi]. A granulated powder mixture was produced after mixing for 30 s the blender. Next, the granulated powder was pugged in a Buss kneader to form a homogeneous paste. The paste was then formed into a honeycomb structure using a Loomis extruder with custom-made extrusion dies of various cross-sections. The

extrudate was allowed to dry at room temperature for ~24 h. Extrusions were reduced and sintered in flowing H_2 in a closed-ended tube furnace heated at a rate of 2 °C/min and held at 1300 °C for 10 h. Ultra high purity grade hydrogen was backfilled three times after mechanical pump evacuation and then continuously flowed through the furnace, exiting through a bubbler to prevent back diffusion of air. Honeycomb made of 8 mol% yttria-stabilized zirconia was formed using this same process, with the exception that the solids content was 40 vol% and sintering was carried out in static air in a bottom-loading $MoSi_2$ resistance element furnace.

The honeycomb samples were cut from the green extrusions prior to reduction and sintering to form a 2x3-type cell structure, as shown in Figure 2. Samples were then cut to length (34.7 mm) and ground to ensure parallel ends. Dilatometry experiments were performed in a dual pushrod dilatometer using alumina pushrods / casing and a sapphire reference. A flowing argon atmosphere was used to prevent excessive oxidation of the samples. Three pump-down / backfill cycles were performed prior to each run. All experiments used a 3 °C/min heating rate up to 1300 °C. Data were not collected during cooling. Sample temperature was measured using a thermocouple junction floating ~ 1 mm above the sample.
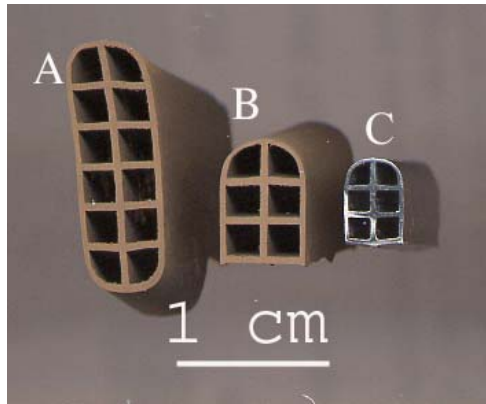
Figure 2. Cross-sections of honeycomb samples A) as-extruded and dried, B) cut into 2x3 cell geometry, and C) as-reduced.

The coefficient of thermal expansion (CTE), α_T, was calculated from the displacement versus temperature data and is given in Equation 1

$$\alpha_T = \frac{dl/l_0}{dT} = \frac{1}{l_0}\frac{dl}{dT} \tag{1}$$

where T is temperature in °C, l_0 is the length at room temperature, and l is the length at a given temperature. It should be noted that the values of α_T may vary from other calculated values of CTE, as has been described recently by James, *et al*. [xii]. With the

$\Delta l/l_0$ versus T data, values of α_T were calculated by linear regressions over small temperature intervals, as shown in Equation 2,

$$\alpha_T = \frac{n\sum x_i y_i - \sum x_i \sum y_i}{n\sum x_i^2 - \left(\sum x_i\right)^2} \tag{2}$$

where x_i represents a T datum point, y_i represents a $\Delta l/l_0$ datum point, and n is the range over which each regression is performed. The value of $n = 41$ was used in all calculations which roughly equates to a 20 °C temperature range. The value of α_T calculated for each regression was assigned to the median temperature for each particular regression range. A averaged CTE over a designated temperature range was calculated using Equation 3.

$$\alpha_m = \frac{1}{l_0}\frac{\Delta l}{\Delta T} \tag{3}$$

α_m is more commonly reported than α_T; in this work, values of α_m are based on a reference temperature of 20 °C.

The thermal expansion mismatch between an alloy and YSZ upon heating from the zero-mismatch point of room temperature to a temperature T, $\Delta E_{T, heating}$, was calculated from the raw expansion data using Equation 4.

$$\Delta E_{T,heating} = \left[\frac{\Delta l}{l_0}\right]_{metal,T} - \left[\frac{\Delta l}{l_0}\right]_{YSZ,T} \tag{4}$$

The thermal expansion mismatch between an alloy and YSZ from a zero-mismatch temperature of T_S (600 or 1100 °C) to a lower temperature T was calculated from Equation 5.

$$\Delta E_{T,cooling} = \left(\left[\frac{\Delta l}{l_0}\right]_{metal,T} - \left[\frac{\Delta l}{l_0}\right]_{metal,T_S}\right) - \left(\left[\frac{\Delta l}{l_0}\right]_{YSZ,T} - \left[\frac{\Delta l}{l_0}\right]_{YSZ,T_S}\right) \tag{5}$$

This equation is based on the assumption that there is a zero-stress state between the metal and YSZ at and above T_S, due to plastic flow in the metal at all higher temperatures.

Lattice parameters were calculated using the Nelson-Riley method for x-ray diffraction (XRD) data taken with a Philips PW1800 diffractometer using Cu Kα radiation. The compositions of the metal alloys were determined by first calculating the lattice parameter and then determining the composition based on literature data of lattice parameter versus composition [xiii]. The conversion equations used were

$$C \;=\; 2862.1 - 7838.8 \cdot a, \quad 43 < C < 100 \text{ wt\% Ni} \tag{6b}$$

where C represents the calculated composition in wt% Ni and a represents the measured lattice parameter in nm. Diffraction and microscopy samples were in the form of extruded strip of roughly 0.5 mm thickness. Metallographic samples were prepared using standard techniques and were observed using a Leica optical microscope.

4. Results

A representative microstructure of Fe-Ni alloys made from reduced metal oxides is shown in Figure 3. The unetched sample taken from extruded Fe 50 wt% Ni honeycomb reveals the porosity commonly observed in these materials. Pores tended to be well-rounded and had average diameters on the order of 5 μm. Porosity levels, measured by calculating the area fraction of pores from optical micrographs, ranged between 3 and 5 vol%, and showed no discernible trend with alloy composition.

Lattice parameter calculations for several Fe-Ni alloys made from reduced oxides are shown in Figure 4 and are compared with literature values [xiii]. The x-values for extruded and reduced honeycomb in Figure 4 were assigned based on the as-batched compositions, in which complete reduction and homogenization were assumed. Lattice parameter measurements made from the extruded and reduced strip fall in line with the literature values. The lattice parameter increased from 25 to 40 wt% Ni, after which it decreased linearly to 100% Ni. All samples examined were single-phase γ Fe,Ni with the exception of the Fe 30 wt% Ni sample which showed trace levels of α Fe,Ni in addition to the γ phase. None of the XRD scans revealed the presence of any metal oxide, even in trace amounts.
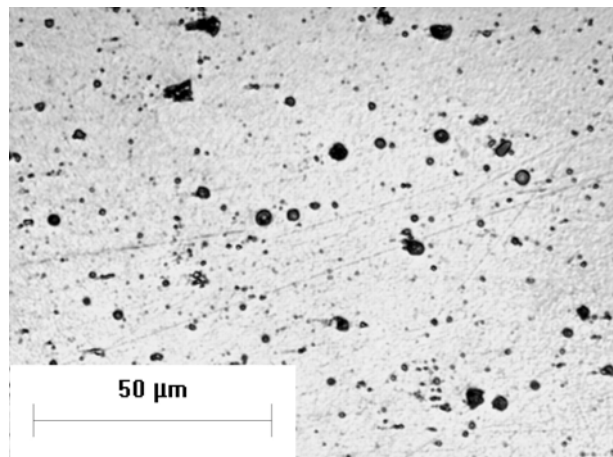
Figure 3. As-polished transverse section of Fe 50 wt% Ni metal honeycomb.
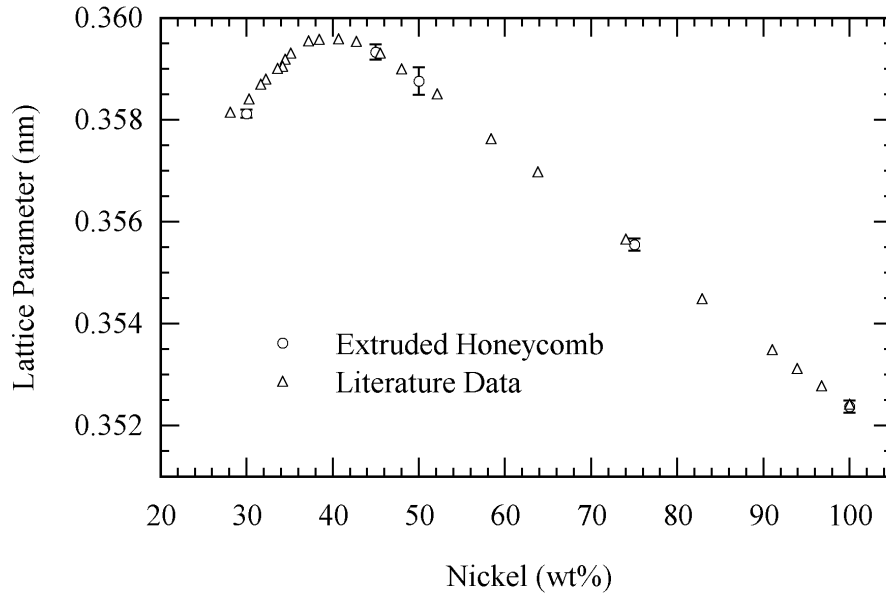
Figure 4. Lattice parameter measurements for Fe-Ni alloys made from reduced oxide precursors compared to literature composition-lattice parameter data [13]. Error bars, based on a 95% confidence interval, represent uncertainty in the lattice parameter calculation.

The linear thermal expansion of YSZ extruded honeycomb was measured and the CTE (α_T) was calculated. As shown in Figure 5, the α_T increases linearly between 200 and 1000 °C and ranges from roughly $8.5 \cdot 10^{-6}$ K^{-1} at room temperature to nearly $12 \cdot 10^{-6}$ K^{-1} at 1000 °C. Using Equation 3, the CTE (α_m) was calculated to be $10.39 \cdot 10^{-6}$ K^{-1} between room temperature and 1000 °C. This compares well to other α_m values for YSZ in the literature of 9.8 [ix], 10.5 [iii], and $10.9 \cdot 10^{-6}$ K^{-1}[i].
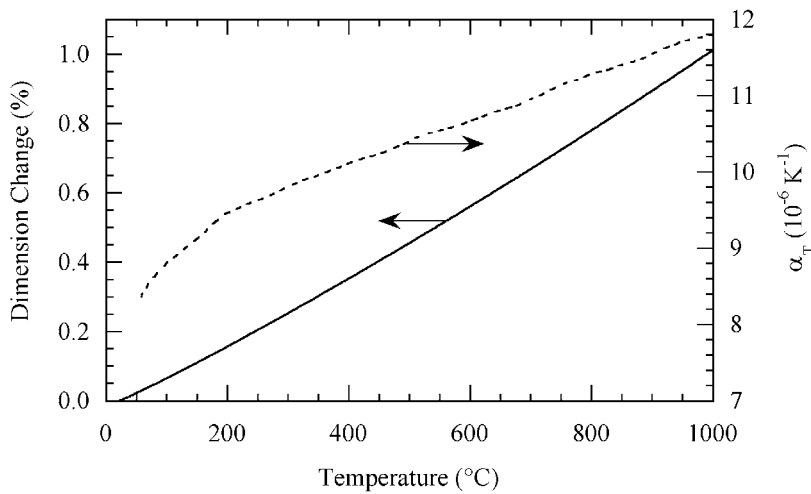
Figure 5. Linear thermal expansion and CTE (α_T) of YSZ extruded honeycomb.

The measured linear expansion and α_T, for a Fe 50 wt% Ni alloy, are shown in Figure 6. The CTE decreases slightly from ~75 °C up to the Curie temperature of the alloy, (473 °C) after which there is a prominent increase. The Curie temperature effect is also visible in the measured expansion curve but it is not pronounced

The α_T values for each Fe-Ni alloy tested are shown at several temperatures in Figure 7. The low-temperature invar effect tends to lessen in intensity and shift towards higher nickel contents with increasing temperature. Above 600 °C, there is no apparent invar effect across the composition range.

As seen in Figure 6, the Fe 50 wt% Ni alloy goes through the Curie transformation at ~ 473 °C. The Curie temperature effectively represents the end of the magnetic influence on the CTE, and above it the alloy experiences a dramatic increase in CTE over a short temperature interval. Figure 8 shows a comparison between Curie temperatures from the literature [xiv] and as measured from extruded honeycomb samples. The measured data show good agreement with literature data, which were measured using dilatometry.
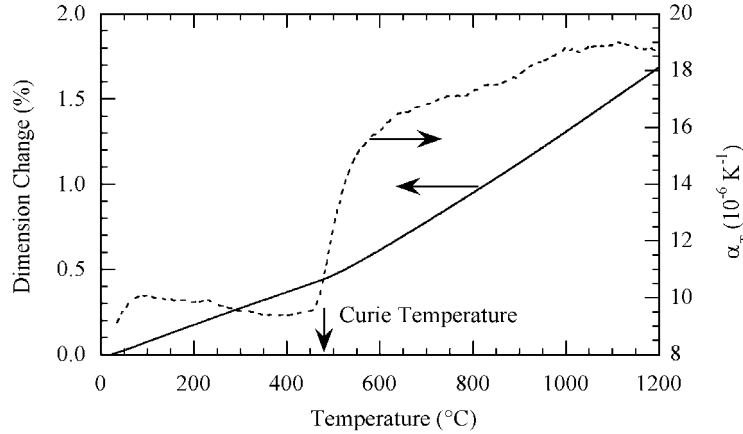
Figure 6. Linear thermal expansion and CTE (α_T) of Fe 50 wt% Ni honeycomb alloy. The indicated Curie temperature of 473 °C was measured from the intercept of linear extrapolations of the (nearly) horizontal and vertical portions of the CTE vs. temperature curve.
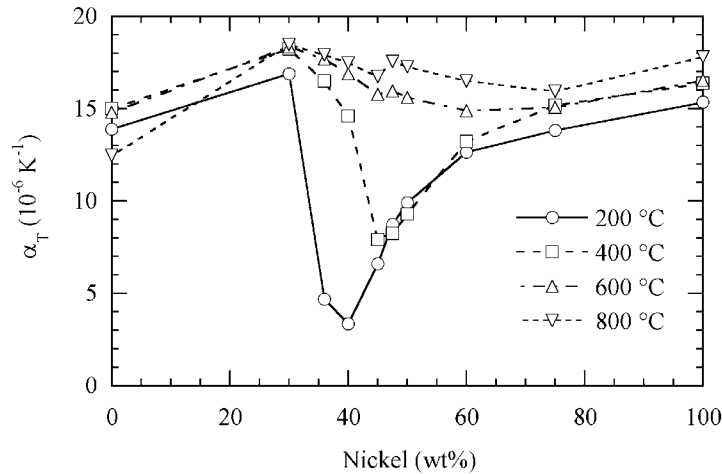
Figure 7. CTE (α_T) of Fe-Ni alloys at several temperatures.

Thermal expansion mismatch values between a given metal alloy and extruded YSZ upon heating from room temperature, calculated using Equation 4, are shown in Figure 9. Both Fe 50 wt% Ni and Fe 47.5 wt% Ni have a lower magnitude mismatch with YSZ compared with Fe 20 wt% Cr up to roughly 1000 °C. While the Fe 45 wt% Ni alloy has no net mismatch with YSZ at 650 °C, the mismatch between room temperature and 650 °C is generally higher in magnitude than the Fe 20 wt% Cr and the Fe 50 and 47.5 wt% Ni alloys.

Thermal expansion mismatch values, calculated using Equation 5, are shown in Figure 10. In this case, the materials are assumed to initially be in a stress-free state at 1100 °C. Results of thermal mismatch calculations assuming the stress-free state at 600 °C are shown in Figure 11.
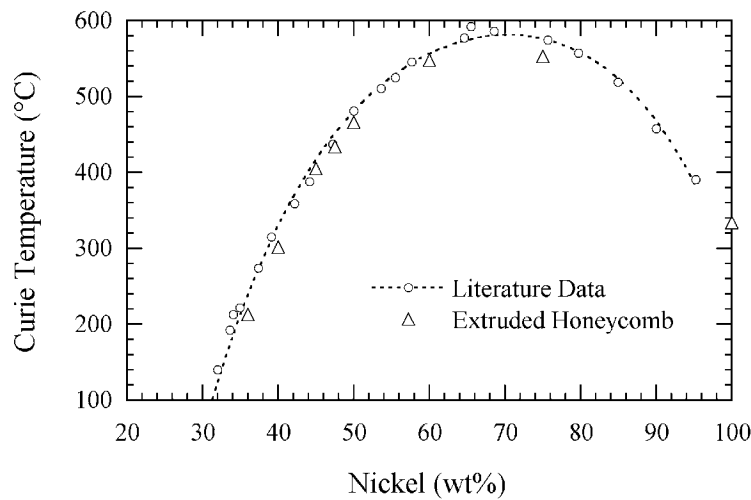
Figure 8. Curie temperature versus composition for Fe-Ni extruded honeycomb samples compared with literature [14] data. Literature data [14], shown with a 4th-order polynomial curve-fit, were measured using dilatometry.
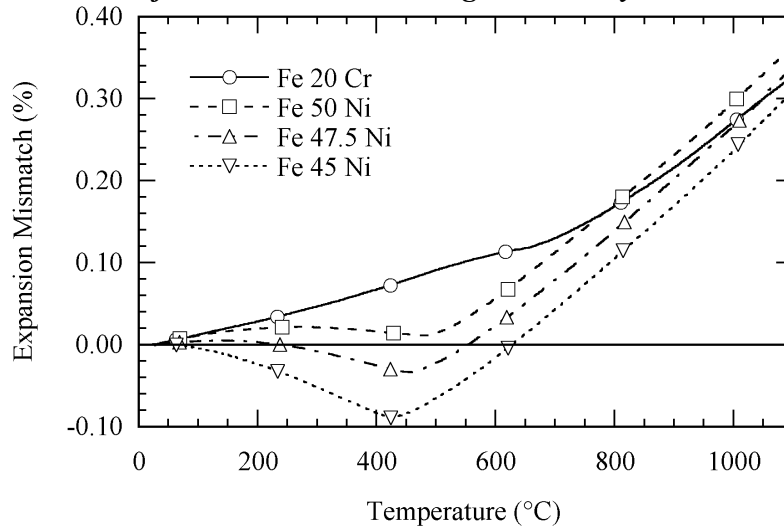
Figure 9. Expansion mismatch between metal alloys and YSZ upon heating from room temperature as calculated using Equation 4. Symbols are used to denote data sets and do not represent individual datum pairs (also true for Figures 10 and 11).
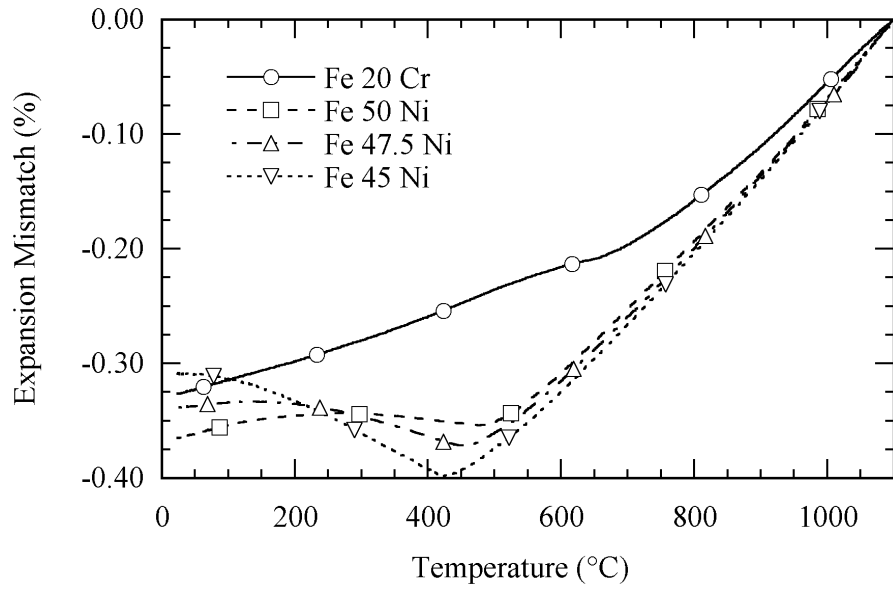
Figure 10. Expansion mismatch due to cooling from 1100 °C to room temperature as calculated using Equation 5.
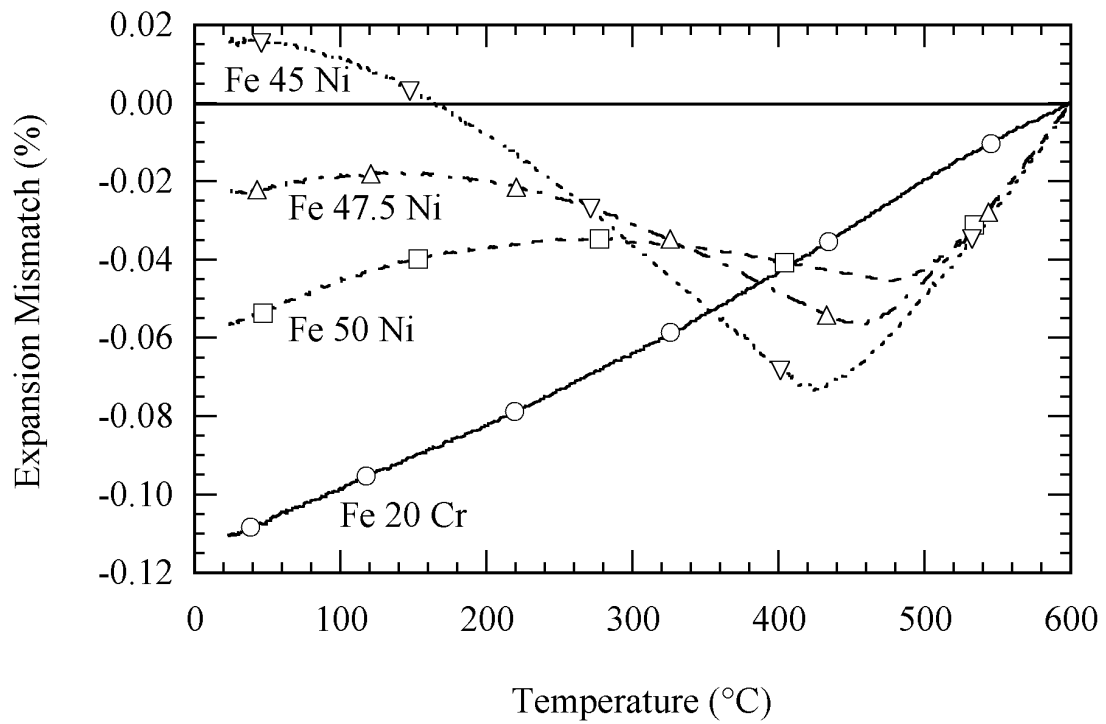
Figure 11. Expansion mismatch due to cooling from 600 °C to RT as calculated using Equation 5.

5. Discussion

Producing metals directly from oxide precursors may be problematic if complete chemical reduction and homogenization are not achieved. If the sample were homogenized poorly, the XRD pattern would tend to have broad peaks implying a compositional variation. In addition, a larger error would be expected in calculated lattice parameter values. The XRD peaks of all Fe-Ni samples had widths similar to those taken from pure Ni or Fe samples made from the same process. Also, the error in the lattice parameter calculations was typically on the order of 0.1% and did not vary significantly between pure and alloyed samples. Another consideration would be the potential for compositional variation between batches of extruded material. While not systematically studied for all compositions, limited data suggest there was very little variation in properties from batch to batch.

Many studies of potential SOFC interconnects rely on the availability of commercial alloys [i, x, xv, xvi, xvii] which tends to limit the ability of researchers to explore a wide range of compositions in a given system. A select few studies have used samples produced in-house by means of vacuum induction melting and subsequent hot forging of ~ 10 kg melts [xviii] or arc-melting of small buttons for oxidation tests [xix]. The honeycomb extrusion process used in this work is relatively simple, rapid, cost-effective and allows the researcher to produce a wide range of compositions including Fe-Ni, Fe-Cr [xx], and Fe-Ni-Cr, among others. The primary limitation of this fabrication technique is the inability to incorporate low nobility elements such as Al, Mg, or Si.

Of the samples tested using XRD, all were observed to be single-phase austenitic (γ) Fe,Ni with the exception of the Fe 30 wt% Ni sample which showed trace amounts of the ferritic (α) phase. The γ to α transition temperature for a Fe 30 wt% Ni alloy was shown by Jones and Pumphrey [xxi] to be approximately 50 °C, and decreased with increasing nickel content. This makes the presence of the ferritic phase improbable in alloys prepared in this work containing greater than 30 wt% Ni.

The degree of alloy-YSZ thermal mismatch upon heating from room temperature, shown in Figure 9, is pertinent to SOFC designs that are rigidly joined at room temperature. The Fe 50 wt% Ni and Fe 47.5 wt% Ni alloys have a remarkably low mismatch with YSZ from room temperature up to roughly 500 °C, after which the mismatch begins to increase. At the target operation temperature of 700 °C, the Fe 45 wt% Ni sample has the lowest mismatch. An open question is whether the more extensive expansion mismatch at 425 °C for this composition will cause inter-layer bowing or buckling delamination during heating to the service temperature.

Expansion mismatch values calculated using Equation 5, shown in Figures 10 and 11, are applicable to the process by which the hybrid SOFC stack is produced. In this case, the stack is co-fired at high (>1200 °C) temperatures. At some point during cooling from the reduction/sintering heat-treatment, a last stress-free state temperature between the YSZ and the metal is assumed. If the cooling rate from the processing temperature were sufficiently slow to allow for plastic flow, the zero-stress temperature could reasonably

assumed to be on the order of 0.4 to 0.5 of the absolute melting temperature (T_M) [xxii]. This ratio is generally considered the temperature above which stress relaxation, creep, and other thermally-activated processes can occur. Iron-nickel alloys with between 40 and 50 wt% Ni have melting temperatures in the range of 1725 to 1775 K. Thus a zero-stress temperature is estimated to be 600 °C. If, on the other hand, the cooling rate from the processing temperature (~ 1200 °C) were not sufficiently slow to allow for plastic flow, the zero-stress temperature could be much higher than 600 °C. For this case, 1100 °C was used as the zero-stress temperature.

Assuming a stress-free temperature of 1100 °C, the Fe 20 wt% Cr alloy yields a lower magnitude of expansion mismatch upon cooling to roughly 100 °C. Below 100 °C, the Fe 45 wt% Ni alloy has a slightly lower magnitude of mismatch with the YSZ. When considering the entire range of temperatures during cool-down from 1100 °C, Fe 20 wt% Cr in general has less mismatch with YSZ. The situation changes when the assumed stress-free temperature is changed to 600 °C, as shown in Figure 11. In this case, the Fe-Ni alloys containing between 45 and 50 wt% Ni have a lower expansion mismatch with YSZ upon cooling to room temperature when compared with Fe 20 wt% Cr.

Of course, the Fe-Ni binary alloys would not possess other desirable properties such as oxidation resistance that the Fe 20 wt% Cr alloy would have. However, these data provide starting points for the development of oxidation-resistant, expansion-matched Fe-Ni-Cr alloys.

6. Conclusions

Metal honeycomb alloys made from reduced oxides can be screened rapidly for potential application as a SOFC interconnect. Chemical composition of the Fe-Ni alloys made via the extrusion and subsequent reduction of metal oxide pastes matched the molar ratios of the mixed oxides based on XRD lattice parameter measurements. Thermal expansion behavior of several Fe-Ni binary alloys was measured and the identified Curie temperatures compare well with literature values. The fabrication method of the SOFC stack must be considered when comparing the expansion behavior potential interconnect alloys. For a hybrid SOFC design, the stress-free temperature must be determined prior to comparing potential interconnect alloys. It was shown that a Fe 50 wt% Ni material has a lower thermal expansion mismatch with YSZ compared with Fe 20 wt% Cr, upon heating from room temperature to 1000 °C.

8. References

[1] S. Linderoth, P.V. Hendriksen, M. Mogensen and N. Langvad: Investigations of metallic alloys for use as interconnects in solid oxide fuel cell stacks. *Journal of Materials Science* **31**, 5077 (1996).

[2] W.Z. Zhu and S.C. Deevi: Development of interconnect materials for solid oxide fuel cells. *Materials Science and Engineering* **A348**, 227 (2003).

[3] W.J. Quadakkers, J. Piron-Abellan, V. Shemet and L. Singheiser: Metallic interconnectors for solid oxide fuel cells - a review. *Materials At High Temperatures* **20** (2), 115 (2003).

[4] Z. Yang, K.S. Weil, D.M. Paxton and J.W. Stevenson: Selection and evaluation of heat-resistant alloys for SOFC interconnect applications. *Journal of The Electrochemical Society* **150** (9), A1188 (2003).

[5] N.Q. Minh: Ceramic fuel cells. *Journal of the American Ceramic Society* **76** (3), 563 (1993).

[6] W. Rauch, K.J. Lee, J. Cochran and M. Liu, in Solid Oxide Fuel Cells VIII Proceedings of the International Symposium, edited by S.C. Singhal and M. Dokiya (The Electrochemical Society, Paris, 2003) p. 1090.

[7] S. Eisele: Characterization of material behavior during the manufacturing process of a co-extruded solid oxide fuel cell. Thesis, Georgia Institute of Technology, (2004).

[8] J. Cochran, K. Hurysz, K.J. Lee and T. Sanders: Extrusion and thermo-chemical processing of layered linear cellular alloys. *Materials Science Forum* **426-432**, 4295 (2003).

[9] C.S. Montross, H. Yokokawa and M. Dokiya: Thermal stresses in planar solid oxide fuel cells due to thermal expansion differences. *British Ceramic Transactions* **101** (3), 85 (2002).

[10] S. Linderoth and P.H. Larsen, in *New materials for batteries and fuel cells*, edited by D.H. Doughty and L.F. Nazar, (Materials Research Symposium Proceedings Volume 575, San Fransisco, CA 1999) p. 325.

[11] K.M. Hurysz and J.K. Cochran: The application of models for high solids content suspensions to pastes. *Journal of the European Ceramic Society* **23**, 2047 (2003).

[12] J.D. James, J.A. Spittle, S.G.R. Brown and R.W. Evans: A review of measurement techniques for the thermal expansion coefficient of metals and alloys at elevated temperatures. *Measurement Science and Technology* **12**, R1 (2001).

[13] W.B. Pearson, <u>Lattice Spacings and Structures of Metals and Alloys</u>, Permagon Press, New York, (1958) p. 639.

[14] P. Chevenard: Alliages de fer, de nickel, et de chrome. T*ravaux et Memoires du Bureau International des Poids et Mesures* **17** (1927).

[15] T. Horita, Y. Xiong, K. Yamaji, N. Sakai and H. Yokokawa: Evaluation of Fe-Cr alloys as interconnects for reduced operation temperature SOFCs. *Journal of the Electrochemical Society* **150** (3), A243 (2003).

[16] K. Huang, P. Hou and J. Goodenough: Characterization of iron-based alloy interconnects for reduced temperature solid oxide fuel cells. *Solid State Ionics* **129**, 237 (2000).

[17] W.A. Mullenberg, S. Uhlenbruck, E. Wessel, H.P. Buchkremer and D. Stover: Oxidation behaviour of ferrous alloys used as interconnecting material in solid oxide fuel cells. *Journal of Materials Science* **38**, 507 (2003).

[18] T. Uehara, A. Toji, K. Inoue, M. Yamaguchi and T. Ohno, in *Solid Oxide Fuel Cells VIII Proceedings of the International Symposium*, edited by S.C. Singhal and M. Dokiya (The Electrochemical Society, Pennington, N.J. 2003) p. 915.

[19] L. Mikkelsen and S. Linderoth: High temperature oxidation of Fe-Cr alloy in O_2-H_2-H_2O atmospheres. microstructure and kinetics. *Materials Science and Engineering* **A361**,198 (2003).

[20] J.H. Nadler, T.H. Sanders and R.F. Speyer: Oxide reduction and sintering of Fe-Cr alloy honeycombs. *Journal of Materials Research* **18** (8), 1787 (2003).

[21] F.W. Jones and W.I. Pumphrey: Free energy and metastable states in the iron-nickel and iron-manganese systems. *Journal of the Iron and Steel Institute* **163**, 781 (1949).

[22] R.W. Evans and B. Wilshire, <u>Creep of Metals and Alloys</u>, The Institute of Metals, London (1985) p.4.

Appendix C
Fabrication of Hybrid and Electrolyte Monoliths

1. Fabrication Approach and Highlights

As stated above the overall goal of this project was to fabricate a layered SOFC stack using a single step honeycomb extrusion where metal interconnects and electrolyte would be extruded on alternating layers. This structure would be manifolded as shown in Fig C1, and then cosintered to an impervious state. After sintering, electrodes would be applied as described above using the manifolded structure. Manifolding consisted of plugging alternate rows at one end for fuel and also plugging opposite rows at the other end for oxidizer. Exit holes next to plugs provide exhaust gas for that row and power results from fuel and air at opposite ends. A schematic is shown for this approach in Figure C1.

Extrusion of the interconnect layers would be from an aqueous based paste consisting principally of mixtures of iron oxide, nickel oxide, and chromium oxide powders in 1-5 micron range. The electrolyte would be extruded from high surface area stabilized zirconia powders to match sintering of metal. Thermal treatment and sintering of the extruded layered structure would be in hydrogen which would reduce the oxide powders in the interconnect layers leaving a powder metal composition in the 400-1000°C range and at higher temperatures in the 1100-1300°C range, both the interconnect and electrolyte layers would be co-sintered to an impervious state as described below in the co-sintering section.

Hermetic YSZ
Cell = 1900 μm
Wall = 280 μm
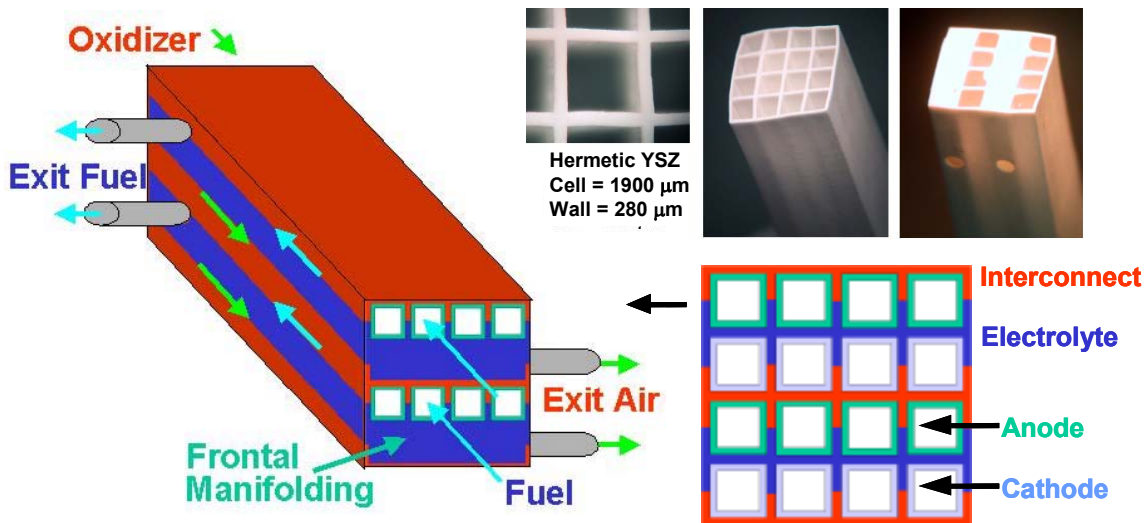
Figure C1. Schematic of counter current manifolding for hybrid SOFC and photo of a manifolded all YSZ electrolyte cell demonstrating the manifolding concept.

2. Fabrication of Electrolyte Monoliths

Early in the program, extrusion efforts concentrated on producing YSZ honeycomb (square cell, 4 x 4) for measurement of electrolyte conductivity and to develop techniques for slurry deposition of electrodes. For this, a small batch compounder with 50c capacity was use for compounding paste. Using this facility, a number of YSZ-8% batches were compounded and the paste rheology was systematically characterized with a capillary rheometer. As a result of the batch variations, a paste was developed which extruded well from the coarsest of our 4 x 4 square cell honeycomb dies. Several pieces of these were sintered to 1400°C and the wall density was 5.65 g/cc or 94% of theoretical density, Fig. C2. The resulting walls were 280 μm in thickness, which is much thicker than allowable for fuel cell operation and this was reduced later. The wall porosity was in the form of discontinuous pores remaining from paste preparation. Thus, the honeycomb walls were impervious and suitable for fuel cell construction. In the unfired state, plugging alternating rows of the square cell arrays with YSZ-8% paste in as shown in Fig. C2 was used to manifold several pieces of honeycomb. Holes were then drilled through the cell wall adjacent to the plugs to provided gas connectivity. Thus gas entering these cells at the opposite end will exit through the holes. The shrinkage of the paste plugs was too high and some plug cracking occurred. This was corrected in the later structures. These samples were given the Dr. Liu's group to develop the electroding process for honeycomb in the manner described above.

YSZ-8%
Cell = 1900 μm
Wall = 280 μm
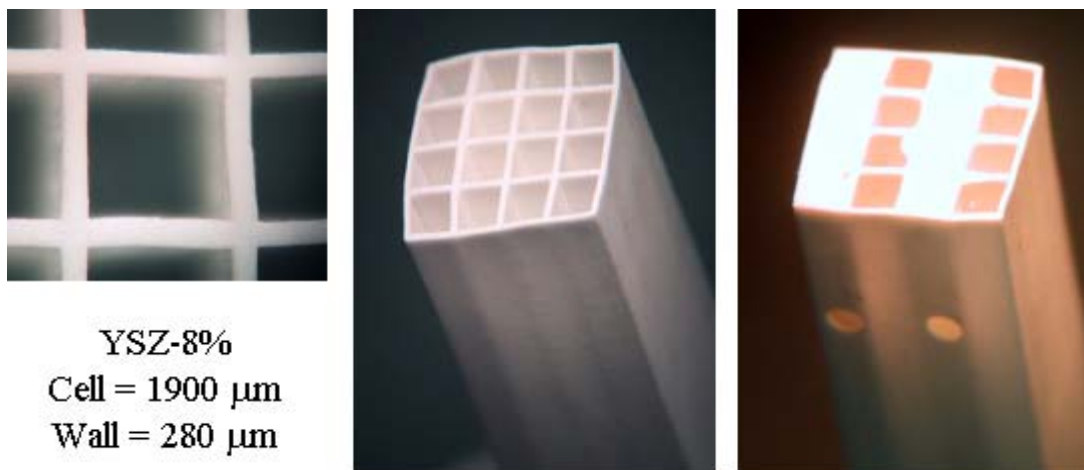
Figure C2. Hermetic YSZ-8% square cell honeycomb sintered at 1400°C. Note the translucency of the impervious walls as shown in (c).

When the hybrid extruded, see below, was developed, several large batches of YSZ monolithic fuel cells were processed because of the availability of the new die, which allowed fabrication of 180 μm thick layers in the extruded state. For fuel cell operation, ceramic honeycombs require a series of ports and hermetic end caps, i.e. manifolds and

techniques were improved to achieve hemeticity. Originally, porting was accomplished by drilling 1.6 mm holes in the green (as-extruded) honeycomb. There was evidence that in some cases, the cell walls (electrolyte layers) were damaged because the drill was too large for the 2.4 mm cell opening. Thus, the drill size was reduced to 0.8 mm and it appeared that the ports were in the middle of the cells and sufficiently removed from the walls not to cause damage. No firing cracks were observed around these ports, either on the exterior or the interior of the cell, Fig. C3. To fabricate electrolyte plugs for insertion into the ends of the cells, a die was machined containing four profiles: 2, 2.1, and 2.2 mm squares and a 2 mm diamond shape. Excess paste of the same material as the bulk honeycomb was extruded through this die. The extrudate is dried and cut into sections approximately 2mm in length and fitted into the channels to be sealed. The honeycomb was then dipped into a 15 v/o suspension of the electrolyte (YSZ) which was dispersed by adjusting the pH to <4 using HNO3 and adding Darvan 821A as the high charge anionic dispersant. This treatment results in the glassy appearance of the end cap. The dried honeycomb adsorbed water from the suspension and deposited a dense layer of YSZ on the ends, Fig. C3.
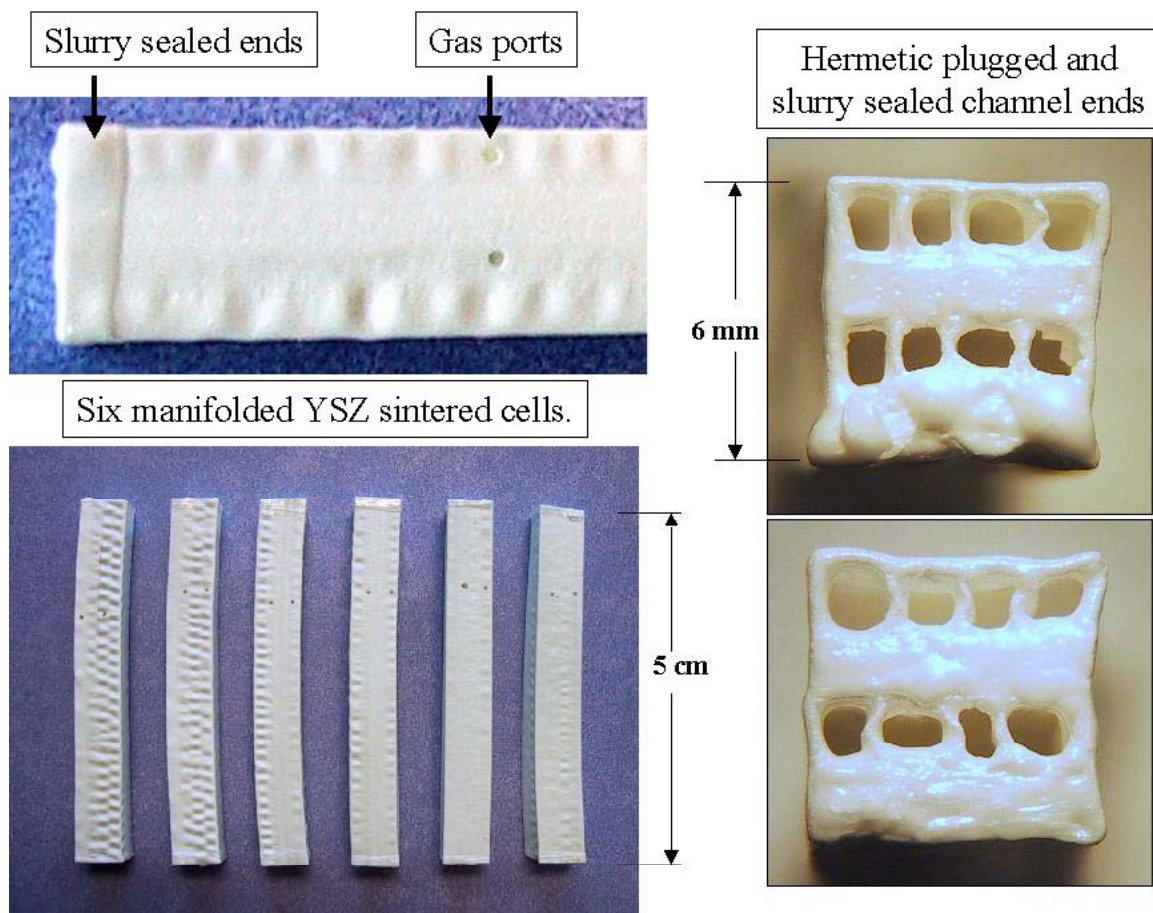
Figure C3. YSZ honeycomb fuel cells, manifolded and sintered to 1350°C, ready for application of electrodes.

3. Extrusion of Hybrid Structures

For layered extrusions, a hybrid extruder and fabricated at a local machine shop. The extruder consists of three parts:

- A barrel 8" in length having 5 paste cavities, of 5/8" diameter and o-ring sealed rams for each cavity. Each cavity feed a different layer in the honeycomb die, Figure C4.

- A reducer, made via EDM, which changes the cross section continuously from the 5/8" diameter cavities to the 0.08"x 0.50" rectangle that supplies each layer of feedholes in the die, Figure C5.

- A die that matches the profile of the reducer, with slot and feedhole sizes tailored to ensure equivalent volumetric flow rates, Figure C6. This die was also compatible with preexisting extrusion equipment to permit extrusion of monolithic electrolyte honeycomb.

Rams   Barrel   Reducer   Die
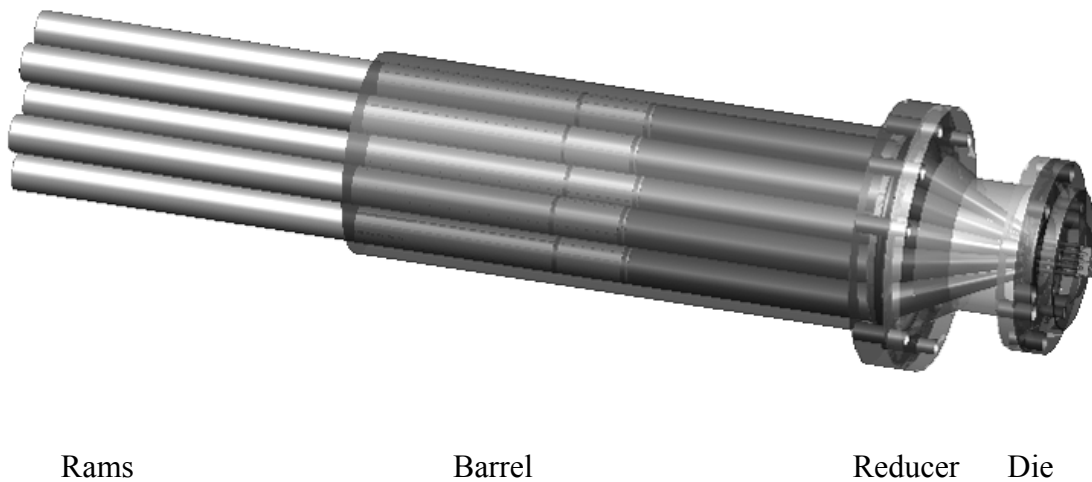
Figure C4. Multi-cavity hybrid extruder assembly.
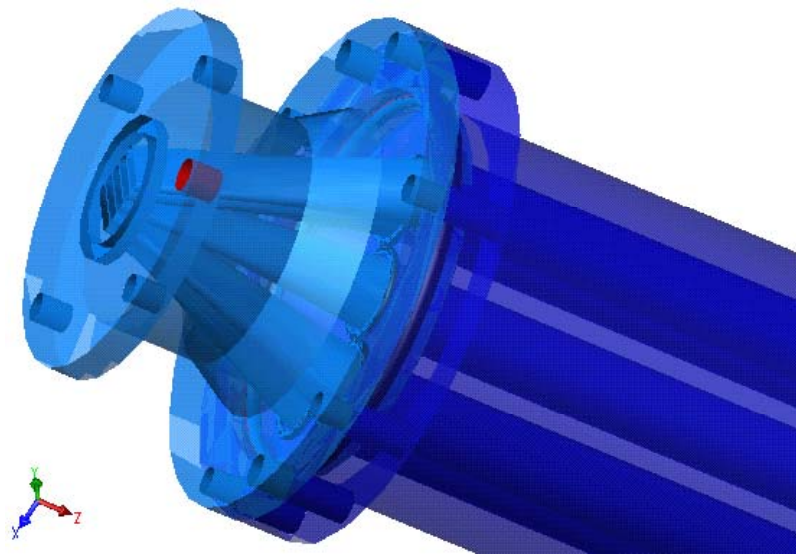
Figure C5. Reducer that connects the multi-cavity barrel to the
feedholes of the honeycomb extrusion die.
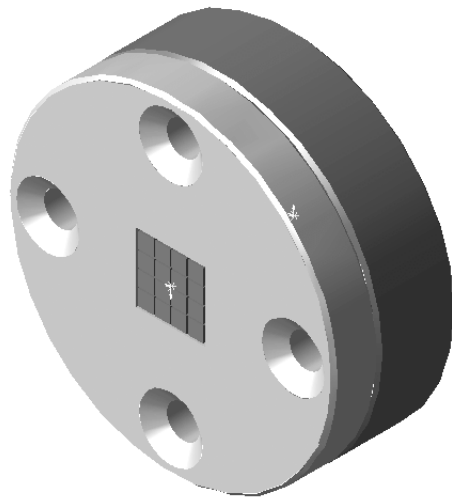
Redesigned die, 3-D rendering   *Die side view, cut away*
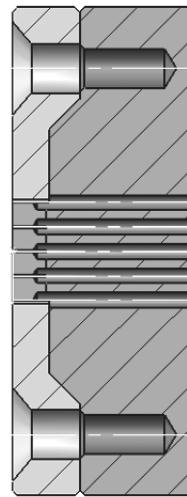
Figure C6. Honeycomb extrusion die for 4x4 square cell hybrid structures.

4. Hybrid Extrusion Dimensions and Quality

The 4 x 4 square cell honeycomb die for the hybrid extruder was quantified with a comparator by the die shop and the webs slots had a thickness of 187 ± 2.5 μm. This is a better tolerance than originally specified. Because of shrinkage, the final electrolyte thickness will be ~110 μm.

Program managers made a request to estimate electrolyte thickness dimensions that should be achievable with extrusion technology. This is provided in Table C1. As can be seen, the new die described above will produce electrolyte thickness of ~110 μm. Routine wire electro-discharge machining (EDM) can produce slots 100 μm wide, i.e. 60 μm webs after sintering, and state of the art EDM is 50 μm slots or 30 μm after sintering. Thus, extrusion technology will provide electrolyte thickness sufficiently thin to provide high current density.

Table C1. Fuel Cell Dimensions Based on Honeycomb Die Dimensions

Die Model	Skin Thickness Extruded (μm)	Skin Thickness Sintered (μm)	Web Thickness Extruded (μm)	Web Thickness Sintered (μm)	Tolerance (μm)	Technology
2002	300	180	200	120	10	Current
2003	150	90	100	60	10	Current
2004	75	45	50	30	?	State-of-Art

As we gained experience with the extruder, out techniques improved and significant improvements were also made to paste processing. For hybrid extrusion, the paste for the interconnect and the electrolyte were matched and the yield strength of both the interconnect paste and the electrolyte paste were adjusted to be in the range of 300-500 KPa as measured by a capillary rheometer. In addition, the compounded pastes were extruded in 10 mm rods to serve as feedstock for the hybrid extruder, which has 14 mm diameter cavities. The extrusion step consolidates the paste into an easily handled geometry, reduces porosity, and makes the paste more uniform. As can be seen Fig. C7, there is a significant increase to the straightness to the extrusions as evidenced by the 17 cm long section, which has very little curvature. In addition, the electrolyte interconnect interfaces are all centered approximately half way between the layer, which helps prevent shorting across the electrolyte. Also, note again the good web thickness uniformity through out the extrusion.
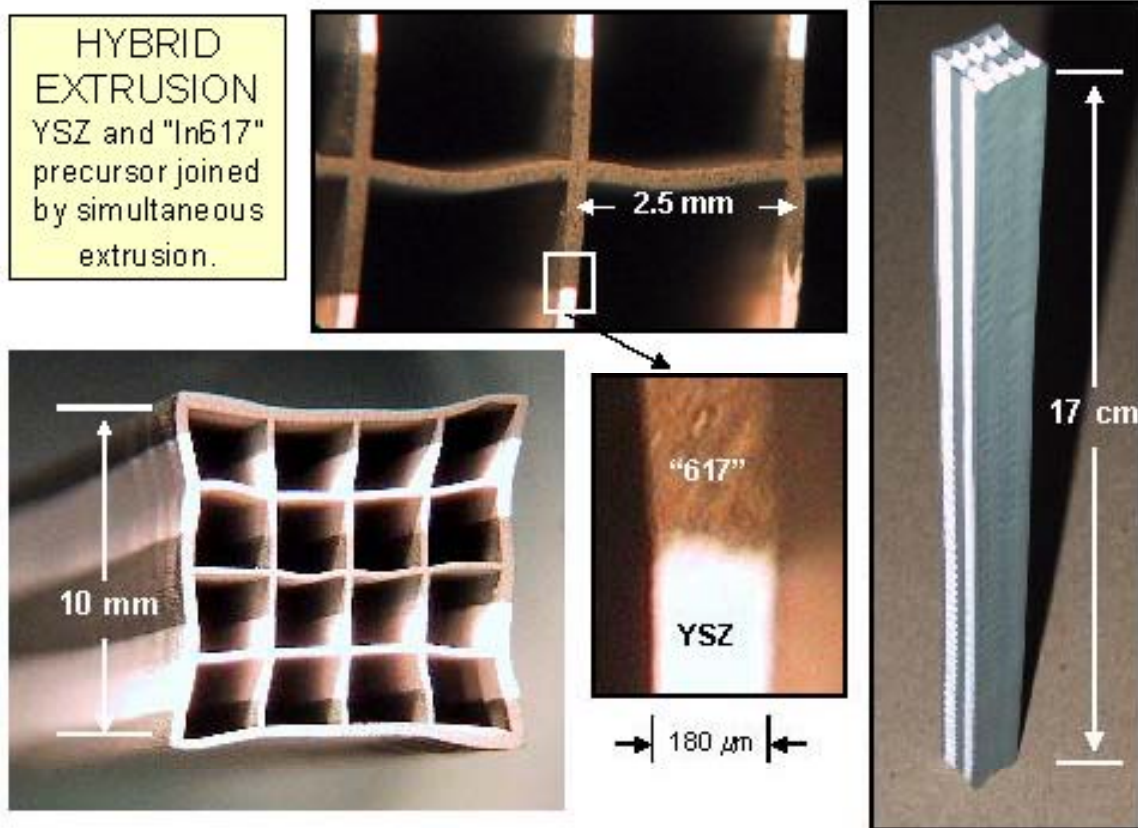
Figure C7. Layered structure of YSZ and In617 fabricated with the hybrid extruder.

5. Final Hybrid Sintered Structure

From results in the last few months of the program, it is apparent that the multilayer extrusion hybrid was close to being a workable approach. On the positive side, the platform could be fired to an impervious state and due to expansion matching, the structure is of sufficiently low residual stress that it can be cut with a diamond saw and polished without cracking the ends as shown in Fig. C8. Furthermore, EDS elemental analysis shows hermetic interfaces with no diffusion between the ceramic electrolyte and the metal interconnect, Fig. C9. With this accomplished one of the more difficult tasks is effectively introducing electrodes with ease of chemical flexibility. It was structures such as this which were tested as operating SOFCs as described above.
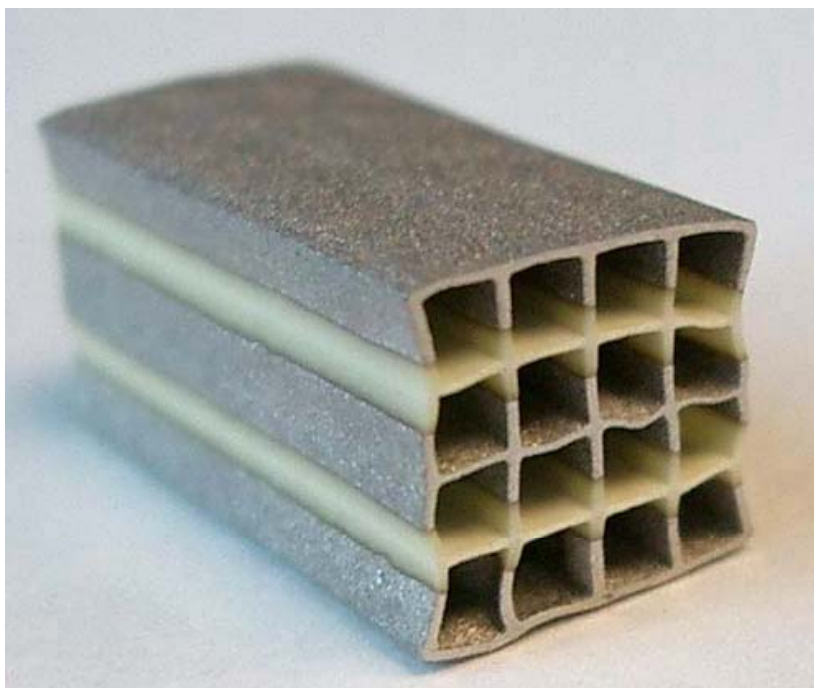
Figure C8. Impervious hybrid SOFC platform after diamond saw cutting and polishing.
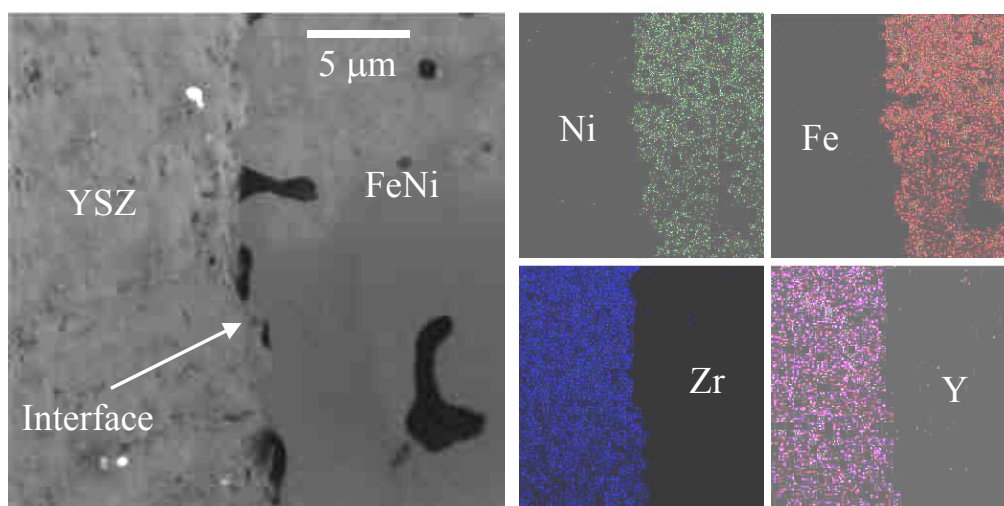
Figure C9. Hermetic YSZ/FeNi interface with no detectable interdiffusion.

6. Paste Processing and Characterization

6.1 Paste Properties for Hybrid Extrusion - Extrusion efforts concentrated on characterizing the rheology of both YSZ and FeNiCrO pastes to allow forming a hybrid feed stock with two pastes of the same rheology. As part of this effort, parameters for maximum solids content and hydrodynamic coefficients were determined for the Dougherty-Krieger model to allow prediction of rheology. In one study, four compositions were extruded using the hybrid extruder. The electrolyte was a 300 kPa yield stress YSZ paste with $\phi = 28.4$ vol.% in all cases. The Bagley plot used to measure the yield stress of this YSZ paste is shown in Fig. C10. The YSZ composition extruded extremely well and served as the basis for the ScSZ electrolyte paste explored later in the program. The composition of these interconnects are as specified in Fig. C11. Interconnect compositions were all between 300-400 kPa yield stress and, with the exception of composition 2, formed large sections (on the order of ten 20 cm sections) of high quality hybrid honeycomb. Shown in Fig. C12 are the extruded green hybrid honeycombs.

Extrusion Pressure vs. L/D
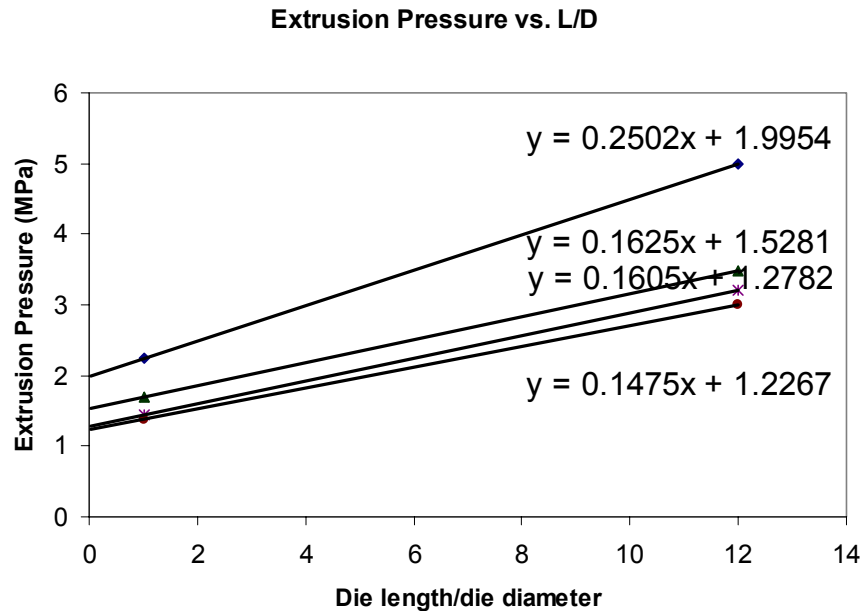
Figure C10. Bagley plot of YSZ paste at $\phi = 28.4$ vol.% used to extrude hybrid honeycomb.

1300C Isotherm
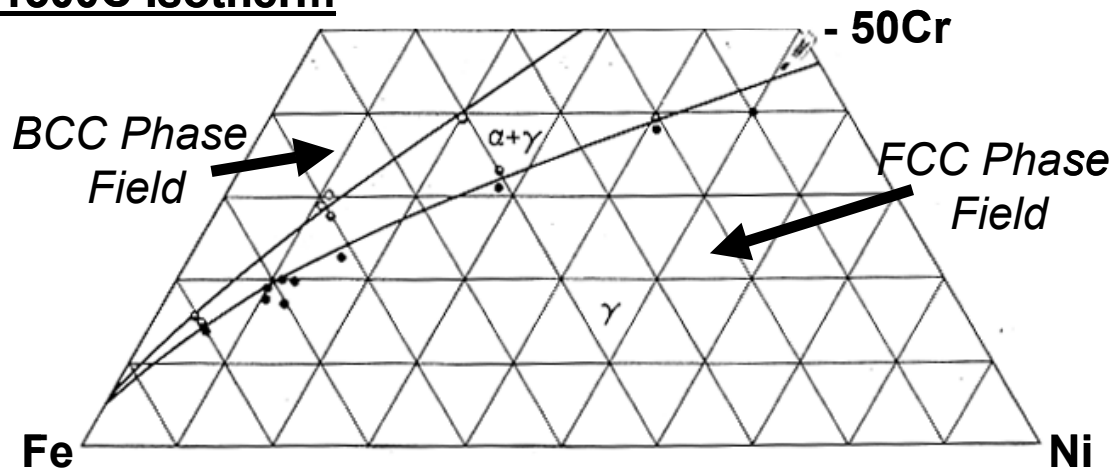
Figure C11. A section of the Fe-Ni-Cr ternary phase diagram at 1300°C (from *The Making, Shaping and Treating of Steels*, United States Steel, 9th edition, 1970, p. 1167). The compositions of the 4 interconnect materials are (1) Fe39Ni8Cr, (2) Fe15Cr, (3) Fe10Cr15Ni, and (4) Ni18Cr10Co5Mo.

Figure C12. Extruded hybrid honeycombs of YSZ and different interconnect: (1) Fe39Ni8Cr, (2) Fe15Cr, (3) Fe10Cr15Ni, and (4) Ni18Cr10Co5Mo.

6.2 Polymer Segregation in Extruded Paste – Extrusion efforts also concentrated on defect reduction in the electrolyte and demonstrated that large scale porosity resulted from polymer segregation in the paste. We demonstrated that binder inhomogeneity is from a combination of non-uniform binder hydration and incomplete mixing. A small scale mixer used early in the program resulted in porosity in the 50 μm size range, Figure C13. A solution was provided by compounding large batches of paste in a high-shear mixer, which eliminated most of the segregation. Significantly reduced porosity was seen after one pass and even more after three passes. The effects are clearly seen in

Figure C13 where porosity is reduced to pores less than a few microns in size. By reducing segregation further, porosity may be eliminated to an inconsequential level.
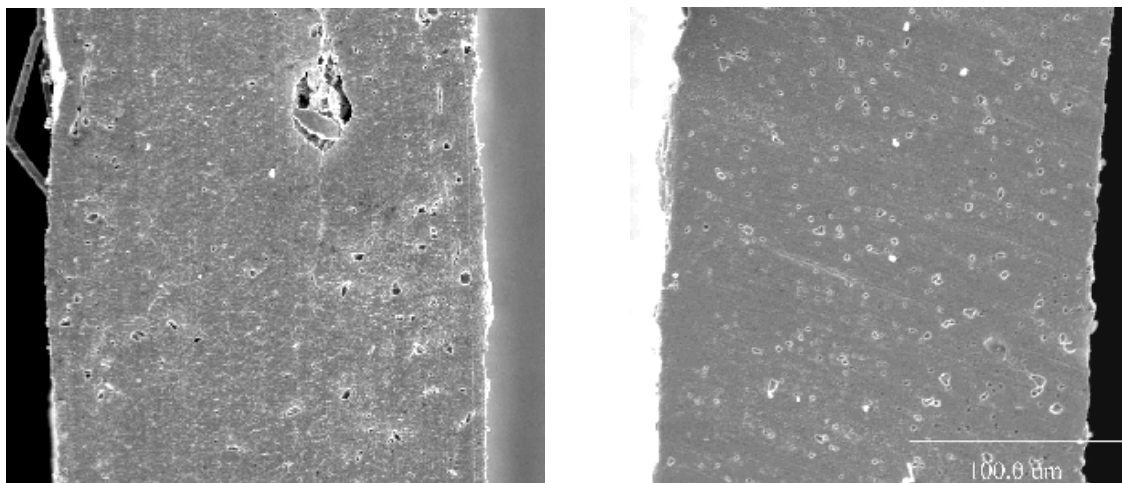
Figure C13.   Porosity produced from polymer segregation in a low shear mixer on the left and a high shear mixer on the right. Note the reduction in pore sized and uniformity.

7. Sintering of Electrolyte and Interconnect Materials:

7.2 Sintering of YSZ and Sc10Ce1SZ - Co-sintering of metals and ceramics requires good knowledge of the sintering characteristics of the ceramic phase in order to force the metal phase to match the sintering of the ceramic. Consequently, sintering of YSZ (8 mole % Y) with a surface area of 6-8 m^2/g was measured and presented below. In addition, $Sc_{0.10}Ce_{0.01}Zr_{0.89}O_{1.95}$ (ScCeSZ) has an oxygen ioic conductivity a factor of 5 greater than YSZ and a sintering study of ScCeSZ powder (10-14 m^2/g) was conducted to determining relative density and shrinkage as a function of temperature, Figures C14 and C15. For this study, ScCeSZ was extruded in the form of rods and honeycomb. Both geometries were sintered in air from 700 to 1400°C. As shown in Figure C14, ScCeSZ sinters in air at temperatures approximately 150^{0}C lower than that of YSZ. This is not surprising since the surface area for ScCeSZ is approximately twice that of YSZ (~13 m^2/g versus ~7 m^2/g). This is not necessarily positive or negative at this time but the difference in sintering temperature will certainly have an impact on the metal composition. A more important value is the total shrinkage at full densification as shown in Figure C15. The value for ScCeSZ matches that of YSZ at a value of ~25%. The total shrinkage of the reduced metal interconnects is also about 25% and the total shrinkage of the two hybrid components must be similar. Thus, this ScCeSZ powder is an acceptable candidate from total shrinkage considerations. It should be noted in Figure C15 that YSZ has the same sintering characteristics when it is sintered in hydrogen as when it is sintered in air. As seen below, this is not true for ScCeSZ.
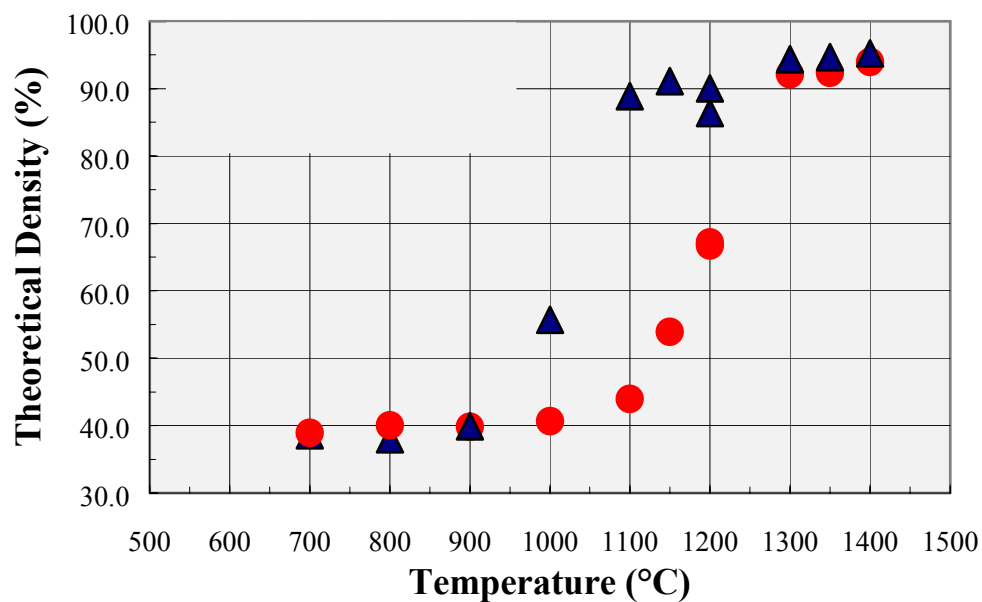
Figure C14. Sintering of extruded ScCeSZ in air and YSZ in air and H_2 based on relative density.
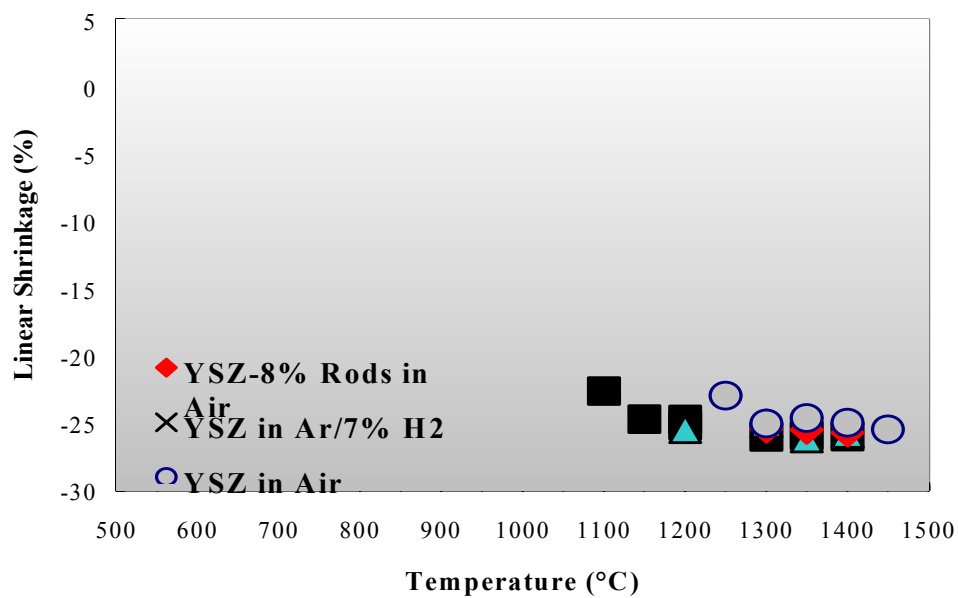
Figure C15. Sintering of extruded ScCeSZ in air and YSZ in air and H_2 based on shrinkage.

Sintering behavior (linear shrinkage v. temperature) of scandium stabilized zirconia in hydrogen and in air has been determined, Figure C16. Unlike YSZ, the furnace atmospheres to which the extruded honeycomb samples are exposed affect the path of linear shrinkage. In air, sintering starts at ~800 C (with shrinkage rate peaking at 1000 C) and reaches final dimensional change of –26.0 % at >1200 C. In hydrogen, sintering starts at ~900 C (with shrinkage rate peaking at 1100 C) and reaches final dimensional change of –24.0 % at >1250 C.

The appearances of ScCeSZ honeycombs fired in hydrogen and in air are also very different. For ScSZ fired in air, its appearance is very similar to YSZ. For ScSZ fired in hydrogen, it is brown in color with a metallic toning similar to copper. When the hydrogen fired samples are refired in air, additional shrinkage is measured that moves the data point back to the shrinkage curve for air firing.

The metallic tone is not due carbon residue as one might suspect due to incomplete binder burn off. In a controlled experiment, with and without prior binder burn off in air, the same appearance is present for hydrogen-fired samples. However, upon reheating in air (as low as 600^0C), the color of ScSZ reverts to white or beige. By firing the whitened samples again in hydrogen (to 1300° C), the copper color appearance will re-appear. The appearance change is found to be totally reversible without any measurable weight and dimensional changes. The preliminary conclusion is that the appearance is strictly a function of reduction potential of the environment, resulting a slight sub-stoichiometric composition of the oxides.
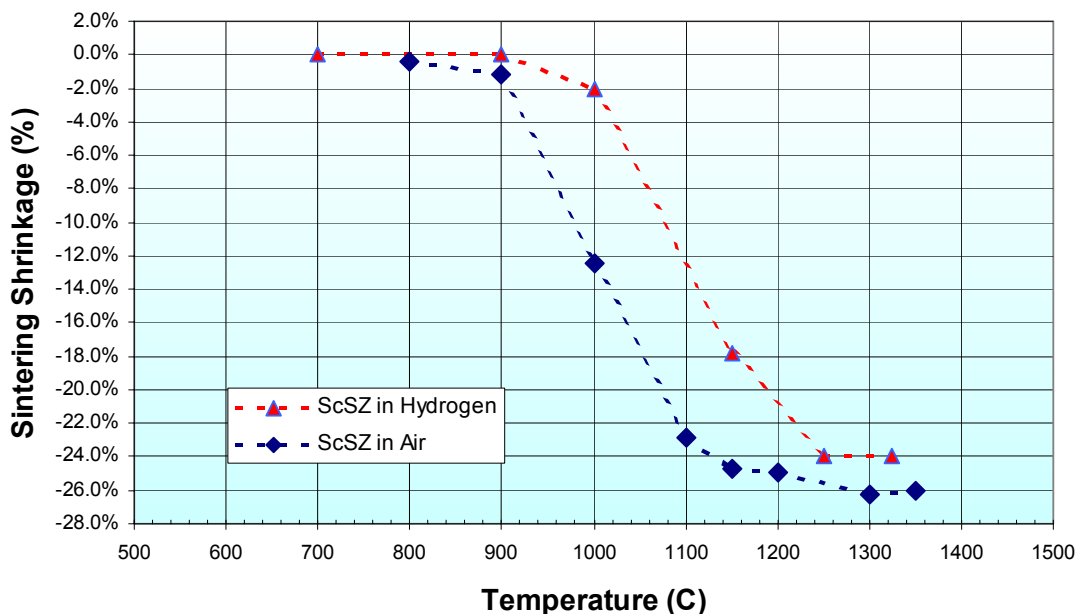
Figure C16. Sintering characteristics of ScCeSZ sintered on hydrogen and in air.

7.2 Extrusion and Sintering of Sc10Y1SZ –During this program have studied 10Sc1CeSZ for more than a year because of it high ionic conductivity but the high surface area and small particle size of this powder has proved difficult to extrude in spite of a great deal of effort. Thus, efforts have been ongoing for several months to find a Sc stabilized zirconia where the conductivity is acceptable with both good extrusion and sintering characteristics. A scandia-stabilized zirconia (10Sc1YSZ) powder with particle size and surface area close to that of YSZ provided encouraging results. This powder was compounded with the method described for paste preparation above, which resulted in a more homogenous paste. This material extruded well as monolithic honeycomb and was given to the electrochemical group for fuel cell fabrication. To look at sintering characteristics, the extruded structures were fired in air at 1200 and 1300°C and then pressure under water tested and samples from both temperatures were determined to be hermetically sound. The shrinkage observed from the newly processed electrolyte is compared with that of the HSY8 in Figure C17. The 10Sc1YSZ electrolyte sintered at a temperature approximately 50-75°C lower than the YSZ. This is actually desirable since the interconnect shrinkage is below that of the electrolyte.
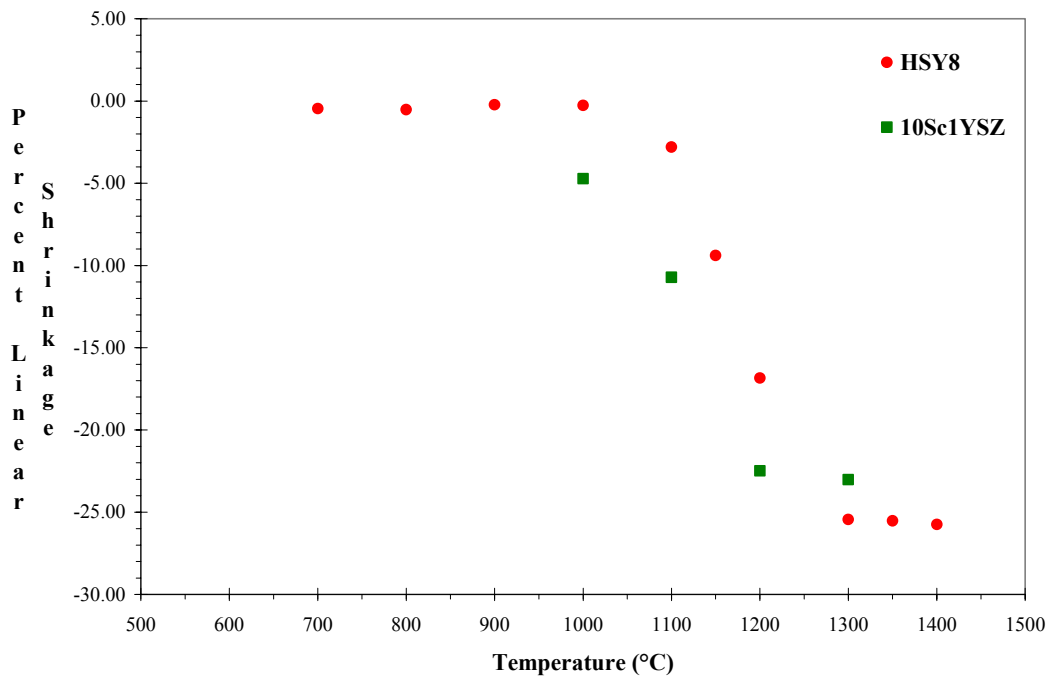
Figure C17. Comparison of air sintering characteristics of 10Sc1YSZ and YSZ

Appendix D
Sintering & Reduction of Hybrid Electrolyte Honeycomb

1. Strategy, Developmental Evolution & Final Results

The main objective of "Co-sintering and Reduction" task was to develop the methodology of successfully rendering the co-extruded hybrid honeycomb to its respective functional states, which are compatible with fuel cell operation. The foundation of this methodology consists of database of material properties (electrolytes & interconnect), tools (processing equipment, diagnostic apparatus, and hybrid sintering model), and rules (guideline for strategic planning and technical approach). By the end of 7th quarter of this three-year (12 quarters) effort, a co-sintering & reduction process was put together and operational in demonstrating the feasibility of this hybrid honeycomb fuel cell concept. At the end of 10th quarter, hybrid honeycomb with fully dense electrolyte and interconnect by final adjustment of metallic interconnect composition. Subsequently, this co-sintering & reduction process was transferred to a industrial-sized vacuum furnace to be production ready of large number of honeycomb substrates.

The timeline proposed for various subtasks of co-sintering is 1) to set up co-sintering & reduction of Hybrid Honeycomb by Q4; 2) to carry out co-sintering & reduction of Hybrid Honeycomb in Q5 to Q7; and 3) co-sintering & reduction of Hybrid Honeycomb with Reduced Dimension (Q10). Under the first subtask the work involved studying sintering behavior of all candidate electrolyte and interconnect material, chemical reactions between electrolyte-interconnect pairs, and setting up non-contact dilatometer measurement capability. Under the second subtask, the work involved developing control algorithm of both temperature and atmosphere (gas species and flow rates), matching thermal properties and response for chosen material pair, and studying kinetics of sintering and reactions (mainly reduction).

The overall strategy has three main emphases. First, it is to establish material system (electrolyte & metallic interconnect pair) and process condition for in-situ formation of electrolyte-interconnect bond. Secondly, it is to engineer their properties that are compatible (e.g., total shrinkage & CTE) to the jointed member. And thirdly, it is to match the sintering behavior or narrow the gap by process condition manipulation.

Many electrolyte-interconnect pairs were co-extruded into hybrid honeycomb for sintering. Examples of successfully so-sintered specimens are shown in Figures D1-D2. It has been a long evolution path leading to implementation of this methodology. Some the tasks or subtasks are discussed in details under descriptive heading in the following sections, along with noteworthy difficulties encountered and solution discussed. The success of this co-sintering task is based on satisfactory execution of the many sub-tasks and solving all the associated or incidental problems.
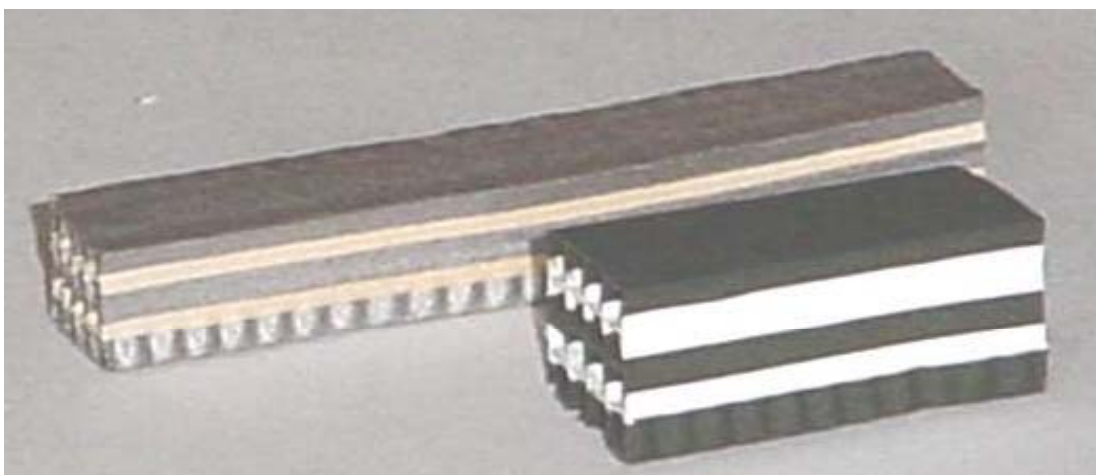
Figure D1. Fe39Ni8Cr-ScSZ hybrid honeycomb structure, reduced and sintered (top) and as-extruded (bottom).
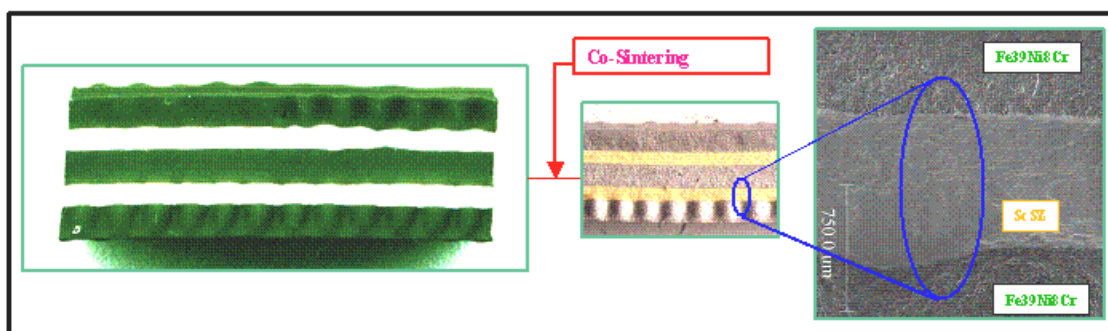

Figure D2. Layered hybrid structure with Fe39Ni8Cr interconnect and ScSZ electrolyte showing continuous hermetic, interconnect-electrolyte interface after reduction and sintering.

Also demonstrated was a rather long hermetic honeycomb, which is 27 and 22 cm long before and after sintering, Figure D3. To have this hybrid honeycomb sintered in one piece without obvious defect, all the critical matches of the two very dissimilar materials were managed well during sintering (strain rate, total shrinkage, CTE and stress relaxation). A more significant implication of achieving sintered honeycomb of a high aspect ratio is that this may enable "cold" interface for gas manifolds and electric connections as in a tubular SOFC configuration.
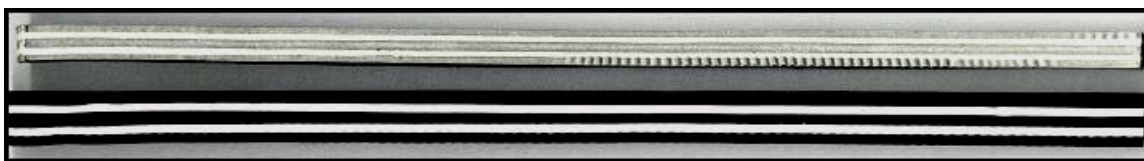
Figure D3. Hybrid SOFC platform with Fe50Ni interconnect and YSZ electrolyte sintered in hydrogen at 1350oC for 8 hours and annealed on cooling.

2. Non-Contact Dilatometer

A non-contact dilatometer was constructed for studying the sintering behavior of various electrolytes (YSZ, ScSZ, GDC) and metallic interconnects, Figure D4. Due to the construction of this apparatus, samples can be heated at a wide range of heating rates, gas composition and flow rates. Productivity of experiment was improved by a factor of more than 10, since an entire sintering cycle can be carried out in one day with automatic data acquisition comparing to manual data generation of one data point per day. The apparatus was also used for measuring reduction and sintering kinetic data for input into a hybrid sintering model.
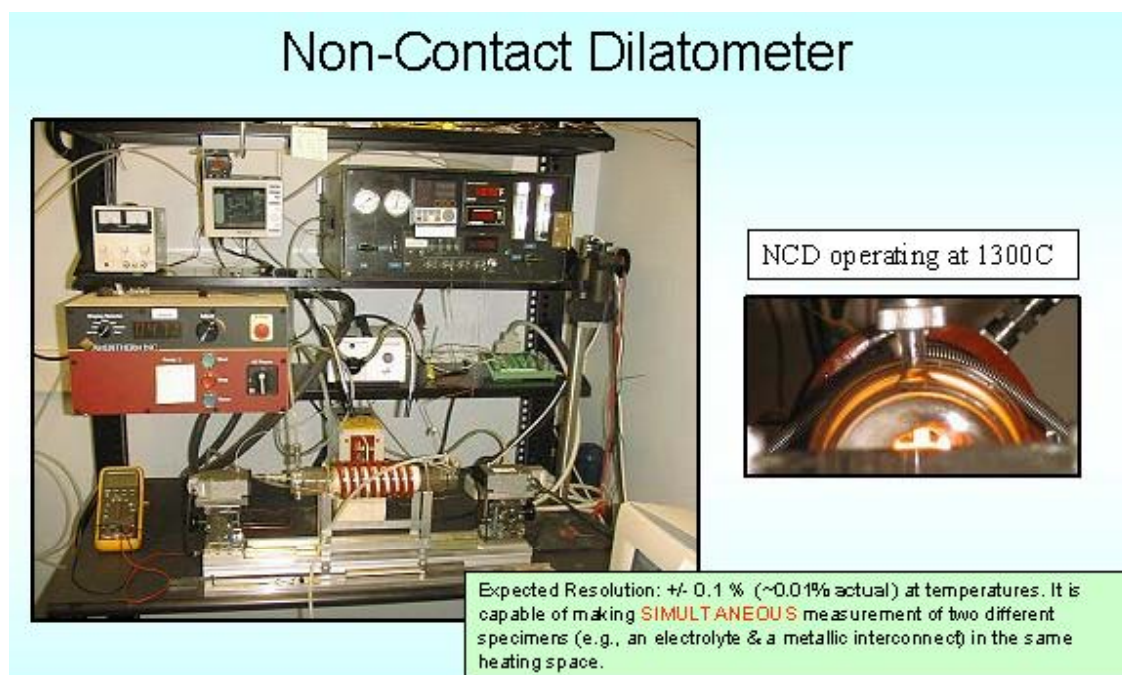
Figure D4. Photographs of non-contact dilatometer and furnace operating at 1300°C.

4. Sintering Behavior of Electrolytes & Interconnects

Sintering behavior (linear shrinkage v. temperature) of any given metallic interconnect needs to match up with those of electrolyte (YSZ or ScSZ) in order to maintain structure integrity. The different response in the sintering behavior for the metallic interconnect is due to various dynamic reaction of the body under manipulative heat treatment schedules (temperature, heating rate, environment condition mainly available hydrogen for reduction, etc.). Manipulation of interconnect sintering cuves by varying heating rates and hydrogen partial pressure is shown in Figure D5.
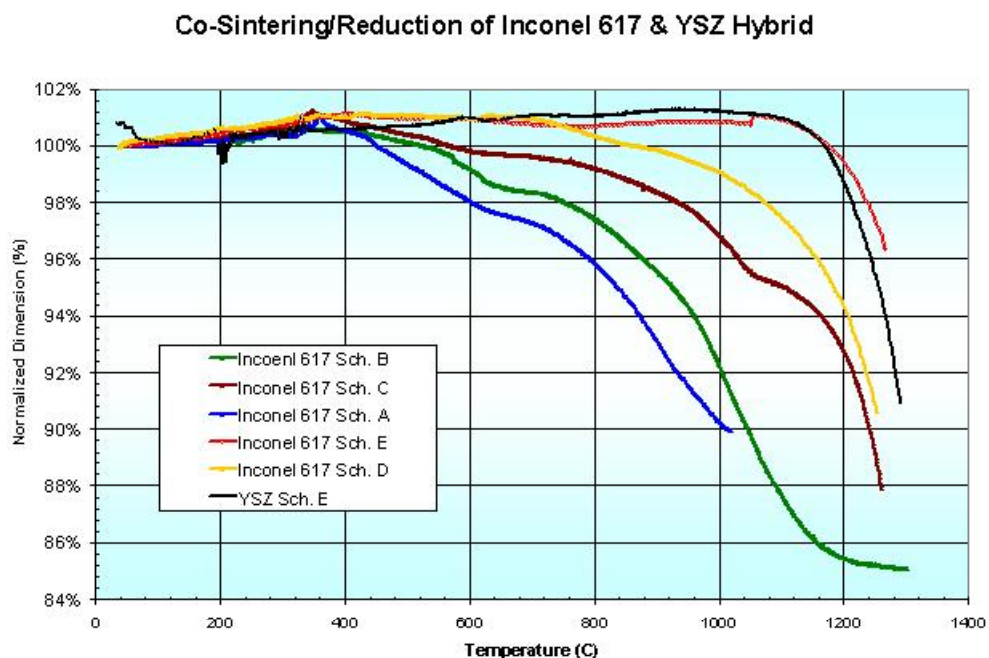
Figure D5.   Co-sintering and reduction of Inconel 617 and YSZ Hybrid.

5. Characterization of Interfaces (Microstructure, Reaction Zone, Interface Integrity)

The interface of YSZ-Fe39Ni8Cr after co-sintering/reduction was examined under SEM/EDAX, Figure D6. The results was for a sample sintered at 1300C, in the non-contact dilatometer with a larger steel susceptor tube (0.85 inch ID). The larger micrograph showed the details of microstructural features of the electrolyte interconnect and interface. However, full densification of the interconnect was not achieved due to incomplete reduction of Cr_2O_3. The full size honeycomb sample, of which the micrograph was taken, was shown as the smaller inlaid picture, Figure D6.
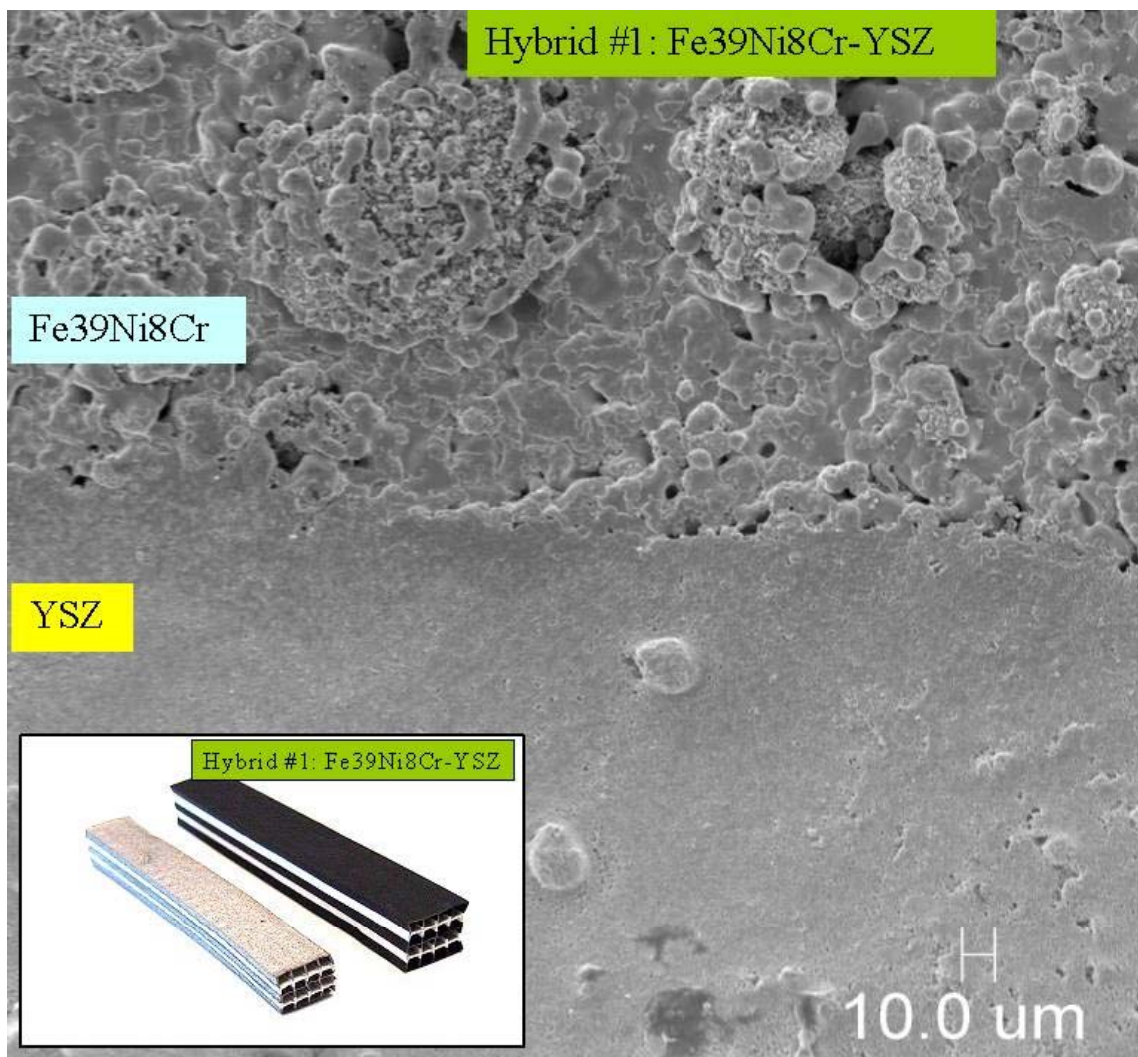
Figure D6. Micrograph of Co-sintered interface of Fe39Ni8Cr interconnect joined to YSZ at 1300°C.

The spatial distribution of elements, mapped with EDS, is shown in a collage of intensity images for all participating elements with an actual image of the interfacial region Figure D7. Good uniformity is apparent. The sample is YSZ-Inconel 617. The presence of Mo in the electrolyte side indicates a certain degree of reaction with or diffusion into the ceramic phase. The depth of penetration is about 300 to 500 micron from the interface. This reaction zone has also been observed as a darkened layer, whose was noticed on a 900C sample. The thickness of this reaction zone remained constant at subsequently higher processing temperatures of 1100, 1200, and 1325 C. This zone can be regarded as a cermet buffer layer with Mo being present in a low level (possibly at ~2%).

A line scan of elements across the interface shows a good definition of interfacial boundary and the transition of elemental distribution for 1200°C reduction joining, Figure D7. A similar set of micrographs for the 1325°C sample is included for comparison Figure D8. Basically, the observed features on the 1200°C are repeated for the higher temperatures, except for there are more delaminated regions on the repeatedly heat treated sample.
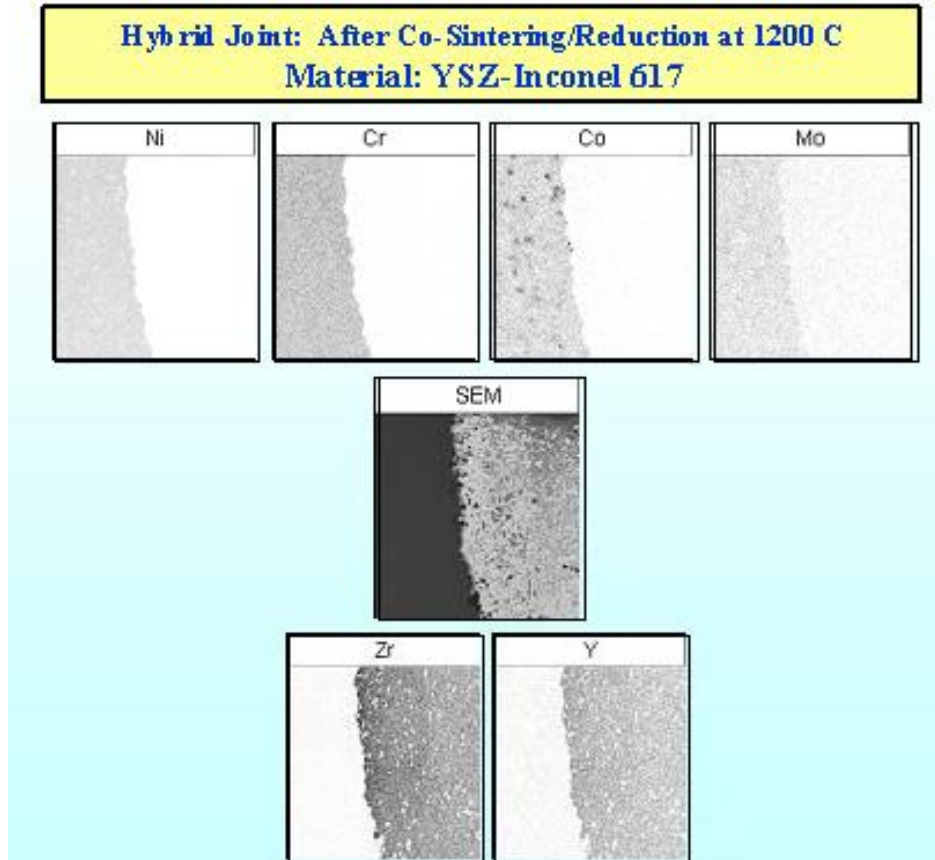
Figure D7. Elemental distribution across an interface of In617 joined to YSZ showing a lack of interdiffusion between the metal and ceramic elements when sintered in a H_2 atmosphere.

Hybrid Joint: After Co-Sintering/Reduction at 1200 C
Material: YSZ-Inconel 617
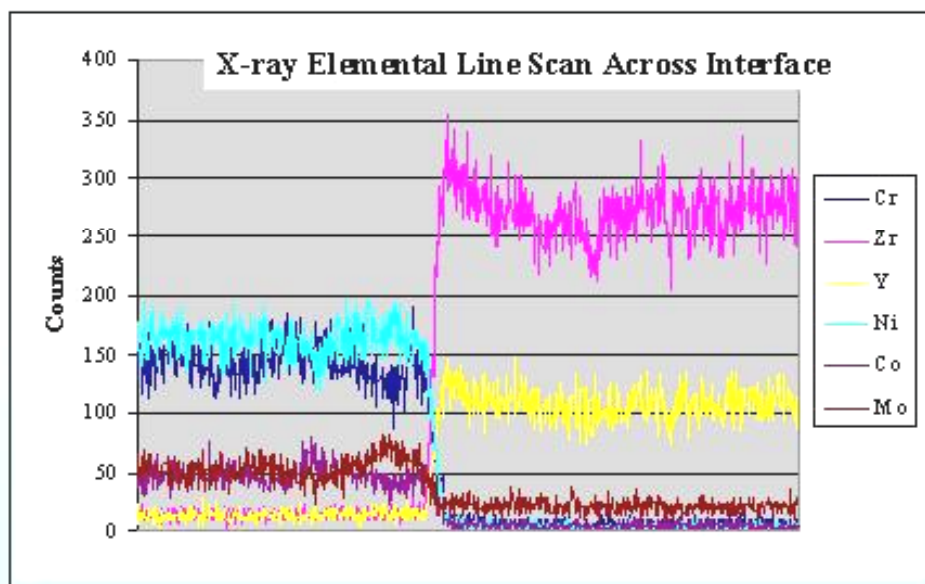
Figure D8. Elemental distribution across an interface of In617 joined to YSZ showing a lack of interdiffusion between the metal and ceramic elements when sintered in a H_2 atmosphere.

6. Potential Manufacturing Technology Transfer

In order to prepare for transferring this technology to production readiness, an industrial sized vacuum furnace was rebuilt to the specification that allows co-sintering to be done under tight temperature and atmosphere control Figure D9.   This furnace has volume to handle a very large number of samples. In addition to modern automatic process control features, hydrogen-handling safety is emphasized with built in triple-bypass and exhaust gas burn off. Near the end of this program, five reduction/sintering thermal treatment were carried out with ~20 hybrid structures in each run. The furnace performed well sand fraction of hermetic samples increased to ~ 80% in the last two runs.

Figure D9. Large volume hydrogen furnace rebuilt for reduction of significant numbers of hybrid SOFC structures.

Design and Thermo-mechanical Analysis of LCMs for SOFC Applications

Lead Faculty: David L. McDowell
Graduate Students:
Benjamin Dempsey (thermal-fluid and electronic performance modeling)
Prescott Eisele (experiments and modeling of SOFC sintering and reduction processes)
Jason LeMasters (finite difference codes for fluid flow, thermal stresses and fracture resistance)
Post Doctoral Fellows:
Aijun Wang (supported work on thermal stresses and process modeling)
Rajesh Kumar (supported work on systems design model for LCM SOFCs)

1. Thermal-Fluid and Electronic Performance of Hybrid SOFCs

Sizing Stack Geometry and Flow Rates for Steady State 20W Operation --Determination of the steady state temperature distribution of the operating hybrid fuel cell is a vital element in sizing the stack and understanding thermal gradients that may affect output. Both chemical reaction rates and thermal stresses are dependent on the temperature distribution in the fuel cell. The temperature field can be manipulated by altering the geometry of the fuel cell and the airflow rate. Modifying the fuel flow rate is an additional means of controlling the temperature field, but fuel will be a limited resource in the actual application, thus it is not a viable option for temperature field control. The FLUENT CFD code is used to compute the steady state temperature distribution of the fuel cell with fixed velocities for the hydrogen fuel and the air.

Figure 1 shows the stack component fuel cell configuration examined. The length of the fuel cell is 10 cm, the uniform wall thickness is 120 microns, and the interior dimension of the square cell is 2 mm. The particular geometry analyzed has four rows and four columns with eight active power generation zones. The electrolyte is assumed to be YSZ and the metallic interconnect is assumed to be Inconel 617. The fuel is assumed to be hydrogen, H_2, and the oxidant is assumed to be ambient air. The joule heating in the metal interconnect is assumed to be small in comparison to the heat generation rate in the electrolyte. Hence, the heat generation is assumed to take place in the electrolyte between the fuel and air channels. Counter-flow is assumed in this analysis. The four outer walls, inlet walls, and outlet walls are assumed adiabatic; thus the heat generated can only be removed by the flowing gases. The inlet fuel and air temperatures are 300 K. For all fuel cell temperature fields presented in this report, the boundary conditions and loads are fixed to constant values. The air mass flow rate, $\dot{m}_{air}$, is 1.021e-6 kg/s, and the fuel mass flow rate, $\dot{m}_{fuel}$, is 3.412e-8 kg/s. These numbers are based on an approximate flow rate of 50 cc/min for each channel, and are not intended at this stage to be optimal values. The volumetric heat generation rate of q''' = 3.82e7 W/m^3 is based om experiments performed by Dr. Liu's group on actual electrolytes. This value is assumed to be constant for purposes of this preliminary this analysis, and should be considered temperature dependent in future generation models. Figure 2 shows the temperature field of the fuel cell under steady-state conditions.
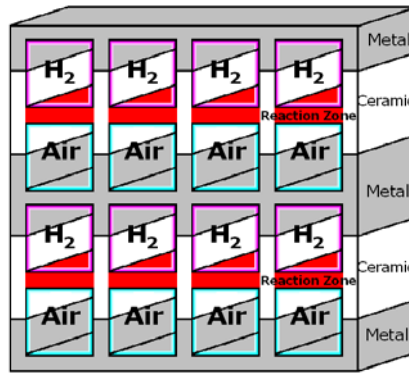
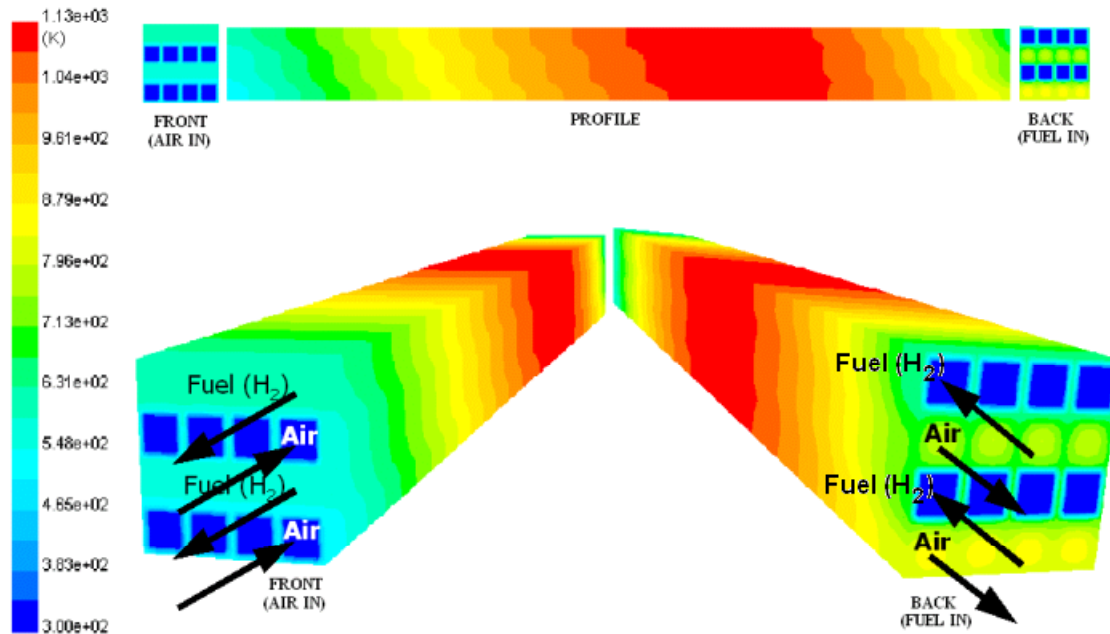Figure 1: Geometry of fuel cell analyzed.

Figure 2: Temperature field from front, back, profile, and 3-D.

High air flow rate relative to the fuel flow rate contributes to the maximum wall temperature being closer to the fuel inlet. This maximum temperature, ~856°C, can be reduced by increasing the airflow rate or shortening the length of the fuel cell. Future efforts will explore and model the effects of airflow rate and fuel cell length on the location and value of the maximum temperature in the fuel cell. To support a design exercise with the objective of maintaining steady state operating temperature within a specified range (e.g. 550°C to 650°C), it is necessary to consider the stack element width,

length and air flow rates as variables to be selected to optimize performance within these constraints. This work is presently underway and will continue this spring.

Steady State Heat Generation (Dissipation) in LCA SOFCs - Work continues using FLUENT CFD code to compute the steady state temperature distribution of the fuel cell as a function of fuel cell stack length for fixed flow rates of the hydrogen fuel and the air, with inlet temperature at ambient level. The aim of this study is to determine optimal flow rates and lengths of each stack element to maintain steady state temperature within a desired range and mean. These preliminary results are based on a fixed heat generation rate. Figure 3 shows the CFD contour plots of the temperature distribution for a 10 cm long LCM fuel cell.
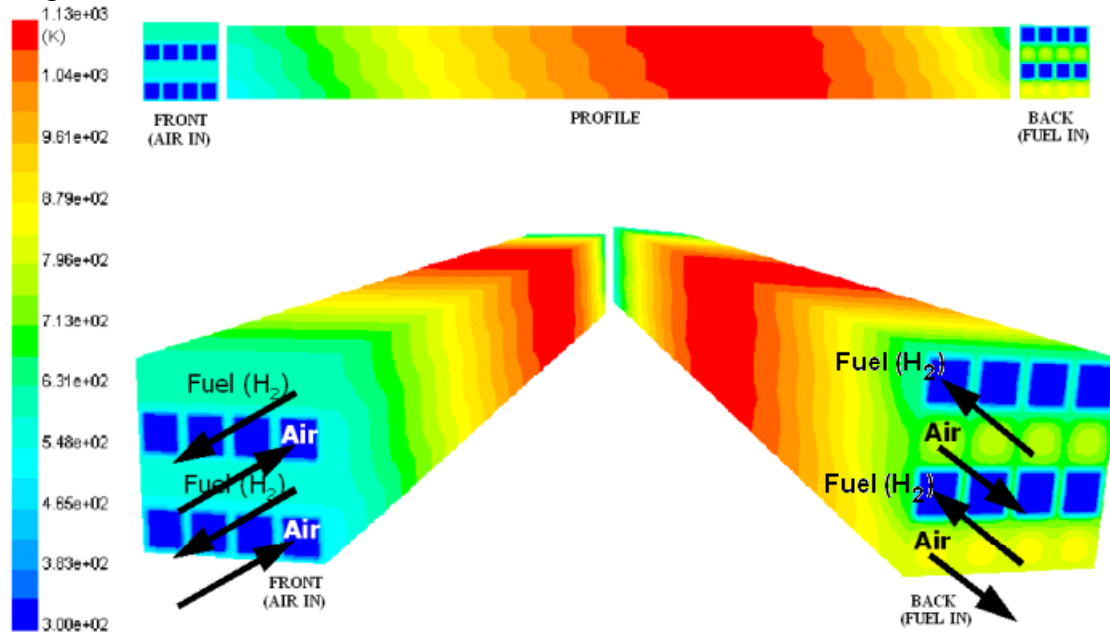
Figure 3. Temperature field for front, back, profile and 3-D
perspectives for 10 cm length SOFC.

High air flow rate relative to the fuel flow rate was shown to contribute to the maximum wall temperature being closer to the fuel inlet. This maximum temperature, ~856°C, can be reduced by increasing the airflow rate or shortening the length of the fuel cell. Figure 4 shows a preliminary exploration of the temperature field as a function of the length. Clearly, the longest cell has approximately 80% of its volume above 500°C, with about 40% of that in the range of 500°C to 650°C; about 20% of the volume is at 850°C. The middle cell, 7.5 cm length, has approximately 60% of its volume in the temperature range of 500°C to 650°C. The bottom length is insufficient to produce temperatures above about 400°C, and is therefore unacceptable for the given fuel-air flow rates. Clearly, adjustment of air flow rate can be explored to achieve the two-fold aim of more uniform temperatures within the range of 550°C to 650°C, as well as fuel and/or air pre-heating. It is evident that without pre-heating, lower air flow rate and shorter length is a necessary direction.

10 cm length

7.5 cm length

5 cm length
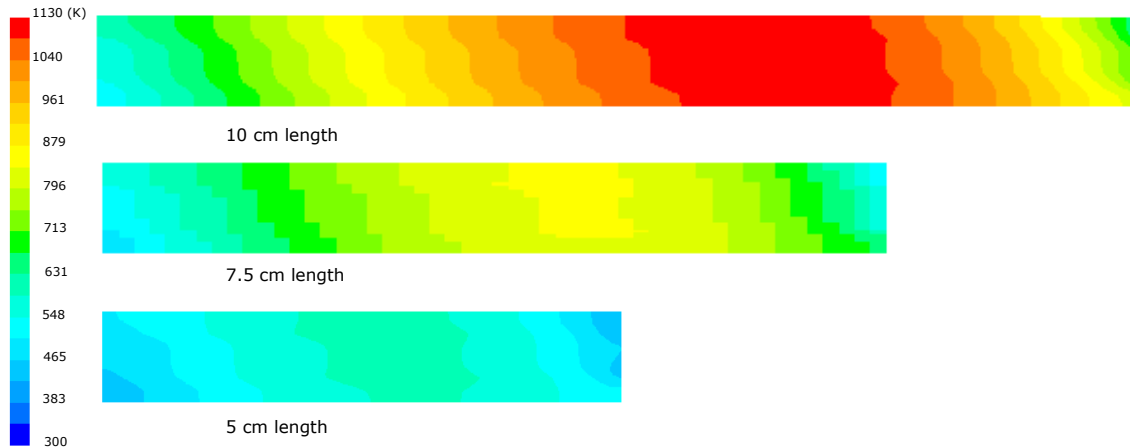
Figure 4. Temperature distribution as a function of length; boxed regions indicate zones where temperature is within the range of 500°C to 650°C.

Figure 5 shows the low, high and average temperatures within each 4x4 cell segment as a function of length, and indicates via dashed horizontal lines the target operating range of 500°C to 650°C. Clearly, for the given flow rates, only lengths of 8-10 cm have average temperatures in the desired range.   However, the effects of much lower minimum temperatures may mitigate against desired electrical performance.   In next generation calculations that appear later, we admitted temperature dependence of overvoltage and internal heat generation for a given current density to derive more accurate bounds on geometry.

For design purposes, the key variables are cell size, shape and wall thickness (all three fixed in this study), stack width, stack length, air flow rate, and extent of preheating of air and fuel. A design of experiments methodology will be utilized to serve as a basis for parametric analysis over these variables to achieve optimal stack geometry.

LCM Fuel Cell Temperature as a Function of Length Only
Fixed Boundary Conditions: Wall Thickness = 120 microns,
Interior Dimension of the Square Cell = 2 mm, 4 rows, 4 columns,
electrolyte = YsZ, interconnect = Inconel 617
H_2 mass flow rate = 3.412e-8 kg/s, Air mass flow rate = 1.021e-6 kg/s
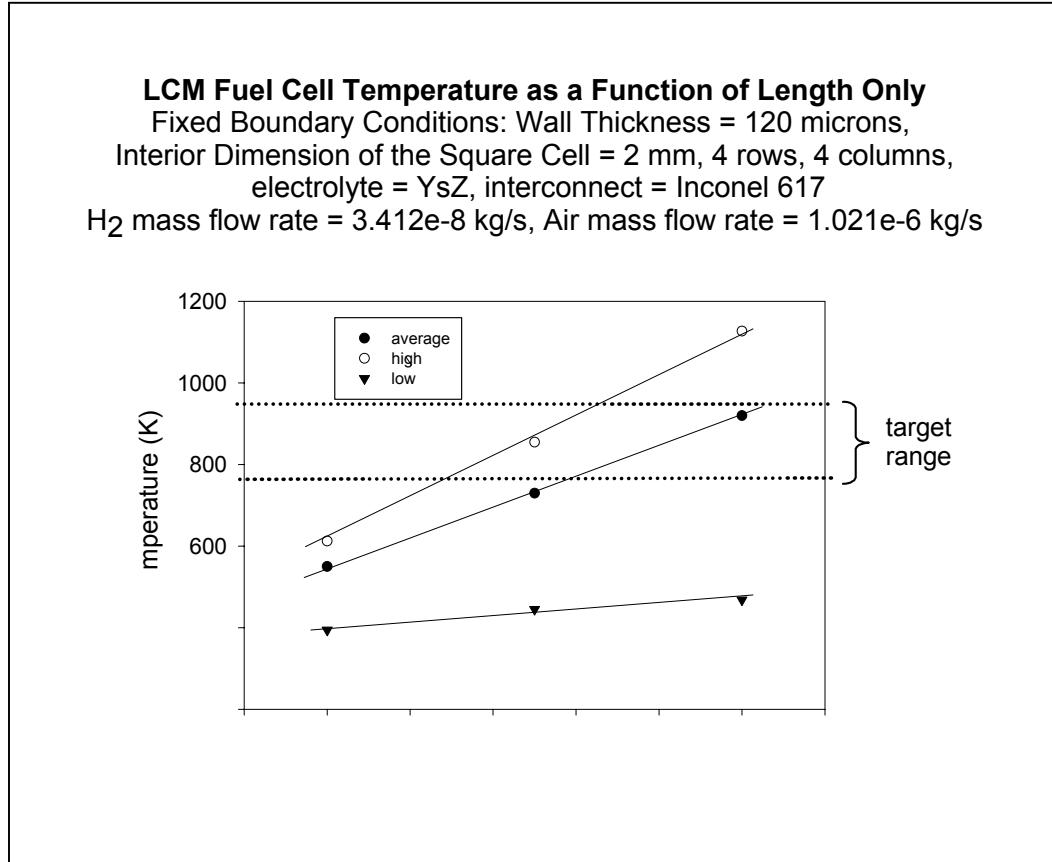
Figure 5. LCM fuel cell temperature as a function of
length for fixed air and fuel flow rates.

Steady State Heat Generation (Dissipation) in LCA SOFCs - The effect of the internal heat generation rate on the temperature field has been considered under steady state fuel cell operation. In previous CFD models up to this point, the heat generation rate has been modeled as constant. In reality, the heat generation rate depends on temperature.

The following results significantly advance the state-of-the-art in determination of the configuration required to maintain the specified power output and structural integrity of the fuel cell. This work utilizes the FLUENT and a temperature-dependent volumetric heat generation rate UDF. The steady state distribution of temperature is explored for three fuel cell lengths: 10 cm, 7.5 cm, and 5 cm. A uniform wall thickness of 120 microns is used in all three cases. The interior dimension of the square cell is 2 mm. The particular geometry analyzed has four rows and four columns with eight active power generation zones. The electrolyte is assumed to be ScSZ and the metallic interconnect is assumed to be Inconel 617. The fuel is assumed to be hydrogen, H_2, and the oxidant is assumed to be ambient air. The joule heating in the metal interconnect is assumed to be small in comparison to the heat generation rate in the electrolyte. Hence, the heat generation is assumed to take place in the electrolyte between the fuel and air channels. Counter-flow is assumed in this analysis. The four outer walls, inlet walls, and outlet walls are assumed adiabatic; thus the heat generated can only be removed by the flowing

gases. The inlet fuel and air temperatures are 300 K. For all fuel cell temperature fields presented in this report, the boundary conditions and loads are fixed to constant values. The air mass flow rate, $\dot{m}_{air}$, is 1.021e-6 kg/s, and the fuel mass flow rate, $\dot{m}_{fuel}$, is 3.412e-8 kg/s. These numbers are based on an approximate flow rate of 50 cc/min for each channel, and are not intended at this stage to be optimal values. Figure 6 shows the temperature distribution of the 10 cm long fuel cell with an assumed constant heat generation rate. Figure 6 is included to provide a baseline for the comparisons to follow in **Error! Reference source not found.**7.
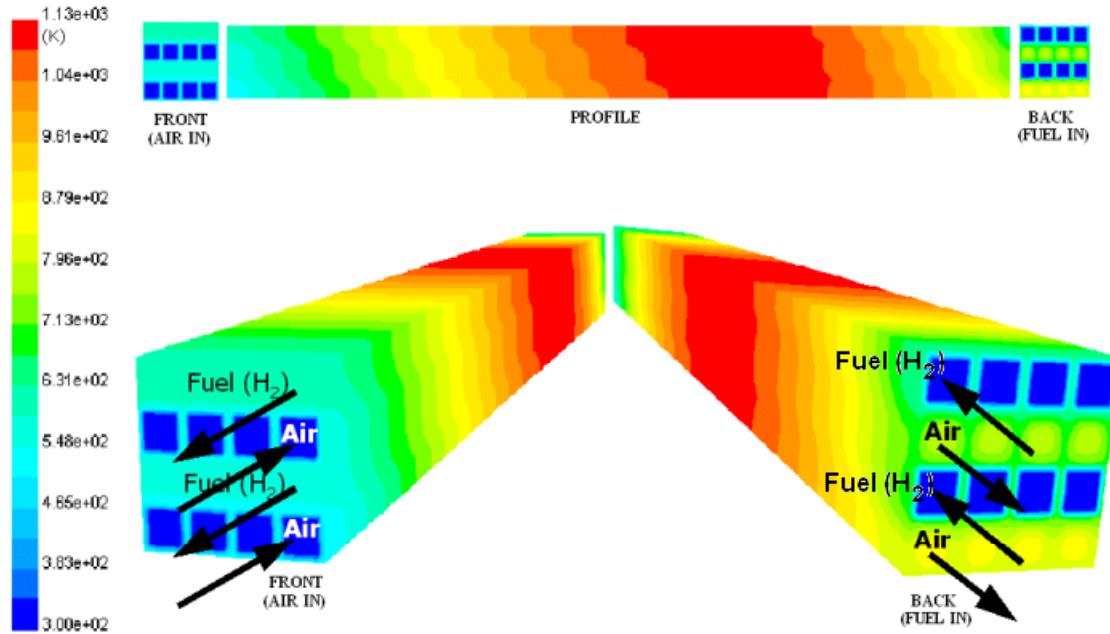
Figure 6. Temperature field from front, back, profile, and 3-D for 10 cm long fuel cell; simplified constant heat generation rate assumption.

The temperature-dependent heat generation rate analysis predicts an overall average temperature higher than that predicted using the simple constant heat generation rate approximation. From the above plots, it is apparent that for the assumed air and fuel flow rates, a length of approximately 7.0 cm provides steady state temperatures that average approximately 600°C, and range between about 400°C and 650°C. Clearly, preheating the air would assist in promoting more uniformity of the steady state temperature distribution. The model is capable of exercising comprehensive examination of effects of air preheating, air/fuel flow rates, and fuel cell length on the steady state temperature distribution, power generation, and efficiency. The increased complexity of the fuel cell model provides a more realistic prediction tool for the design of the Palm Power device.
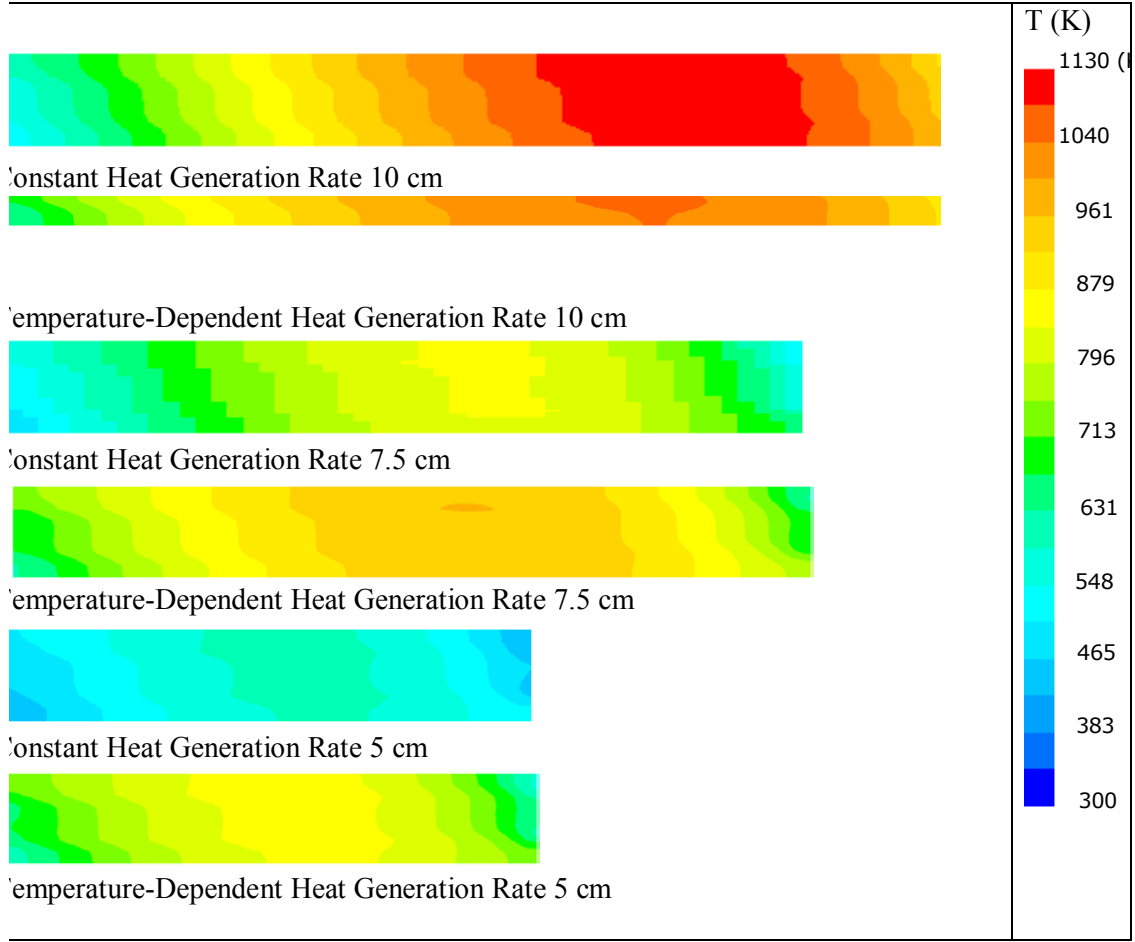
Figure 7. Steady state fuel cell temperature fields for temperature-dependent heat generation relations and simple constant heat generation rate assumption**.**

Steady State Heat Generation (Dissipation) in LCA SOFCs – All of the predictions of heat generation rate in this report are based on the experimental results generated by Dr. M. Liu's group. The total voltage available, $V_{available}(V)$, can be expressed as

$$V_{available} = n_{vert} ocv_{percell} - \eta - I\rho_e \tag{1}$$

where

$$I = 0.001 \cdot J A_{electrolyte} \tag{2}$$

and

$$A_{electrolyte} = n_{wide} w_{cell} l_{cell} \tag{3}$$

Here, n_{vert} is the number of active cell zones vertically, $ocv_{percell}(V)$ is the open cell voltage per active cell zone, I (A) is the current, J (mA/cm^2) is the current density, $A_{electrolyte}$ (cm^2) is the cross-sectional area, n_{wide} is the number of cells across the fuel cell,

$w_{cell}(cm)$ is the internal width of each cell, $l_{cell}(cm^2)$ is the length of the fuel cell. $\eta(V)$ is the activation overpotential and was defined in the previous report as

$$\eta(T,J) = 0.001 \cdot e^{\left(-0.0109 \cdot T + 0.0006 \cdot J + 15.026\right)} \tag{4}$$

where T (K) is the temperature and J (mA/cm^2) is the current density. The resistance, $\rho_e(\Omega)$ in Equation (1), can be expressed as

$$\rho_e = \frac{t_{electrolyte}}{A_{electrolyte}} \cdot T \cdot 10^{\left(\frac{2769.7}{T} - 4.1806\right)} \tag{5}$$

where $t_{electrolyte}(cm)$ is the thickness of the electrolyte and all other terms are as previously defined. Once the total available voltage is determined, the total usable power, $P_{total,usable}(W)$, can be expressed as

$$P_{total,usable} = V_{available} I . \tag{6}$$

The Palm Power project requirement specifies that 20 W of external power, $P_{external}(W)$, should be available. The total usable power should exceed 20 W by the amount of power that will be required to run internal mechanisms, $P_{internal}(W)$, such as fans, pumps, etc. This is written as

$$P_{total,usable} = P_{internal} + P_{external} . \tag{7}$$

By comparing the total usable power to the total power generated the percent of power that is usable is obtained as

$$\%usable = \frac{P_{total,usable}}{P_{total,usable} + P_{heat}} \times 100 . \tag{8}$$

where $P_{heat}(W)$ is the power generated in the form of heat.

For a given current, the required minimum mass flow rates of hydrogen, $\dot{m}_{H_2}(kg/s)$, and air, $\dot{m}_{air}(kg/s)$, can be obtained from Equations (9) and (10), i.e.,

$$\dot{m}_{H_2} = \frac{I}{F}\frac{1}{2}M_{H_2}\frac{1}{1000}\frac{1}{(\%_{utilization})} \tag{9}$$

$$\dot{m}_{air} = \frac{I}{F}\frac{1}{4}M_{air}\frac{1}{1000}\frac{1}{(\%_{utilization})} \tag{10}$$

Where F (C/mol) is Faraday's Constant, M is the atomic mass, and $\%_{utilization}$ is the percent of fuel/oxidant that is being converted.

The following results are based on a square cell geometry with internal cell dimension of 2 mm, wall thickness of $120\,\mu m$, 4 cells high by 4 cells wide, hybrid construction, with a 400 mA/cm^2 current density.

Table 1 contains results obtained from Equations (1) through (8). The temperatures in Table 1 are obtained from FLUENT simulations.

Table 1: Power density of hybrid fuel cells for various lengths.

Length (cm)	10.00	7.50	5.00
Power density (W/cc)	0.69	0.56	0.27
Average Active Electrolyte Zone Temperature (^{o}C)	669.84	605.57	530.56
60% Utilization Mass Flow Rate of H$_2$ (kg/s)	5.57E-08	4.18E-08	2.79E-08
60% Utilization Mass Flow Rate of Air (kg/s)	3.99E-07	3.00E-07	2.00E-07
% Usable Power	62.65	50.18	23.00

Pressure Drop through LCA with Electrolytic Fibers - Due to manufacturing constraints, the design of the fuel cell electrodes has been modified. The previous design was based on a thin electrode coating that covered the internal walls of the fuel cell channels. In an effort to increase the performance, a new concept utilizes a porous electrolyte fiber extension that fills each channel. This design is shown in Figure 1. At issue is whether the pressure drop of fuel and air passing through these filled channels is prohibitively high for required reactant flow rates.

The electrode coating is deposited on fiber in each channel of the fuel cell. This configuration should encourage reactions along interfacial regions of the fibers and flow. This is shown in Figure *1*9, where δ is the boundary layer depth into the flow stream that the majority of the reactions occur. An approximation of δ will be valuable for determining the temperature field in the interconnect, electrolyte, and porous electrolyte filler.
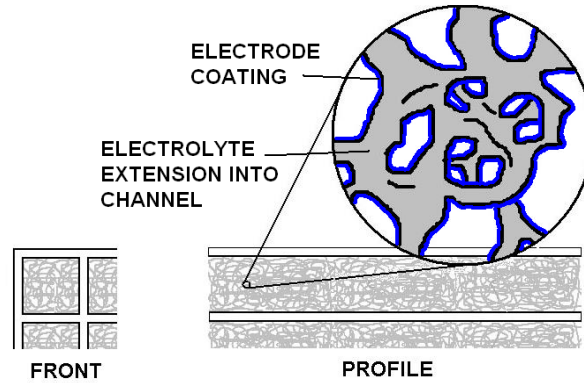
Figure 8. Schematic for new design of electrolyte and electrode.

The pressure drop through a fiber-filled LCA was measured at various flow rates. The experimental apparatus is shown in Figure 10. Helium flowed at a constant rate through the filled LCA, and the pressure drop down the length of the LCA was measured. Specifically, the pressure drop was measured between the gas inlet of the LCA, and the atmosphere. To ensure that all the gas was traveling through the LCA, the glue seal was submerged in water during the experiment so that leaks could easily be detected. No leaks were detected at pressures less then 6.5" H_2O, which was the upper limit of the pressure transducer. The measured results are shown in Figure 11.
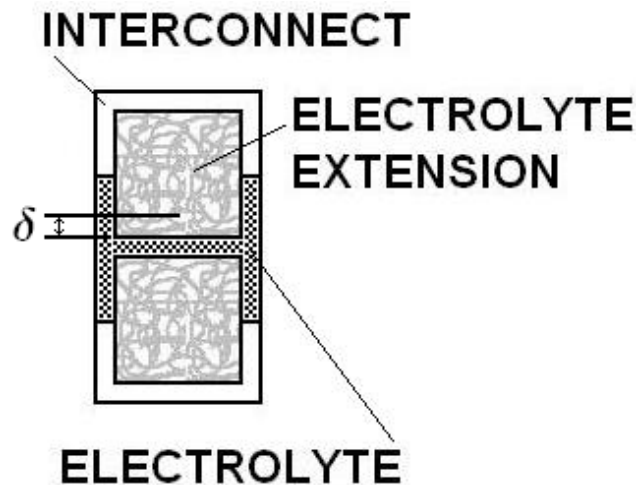
Figure 9. Single cell schematic of the reaction depth into the flow stream.
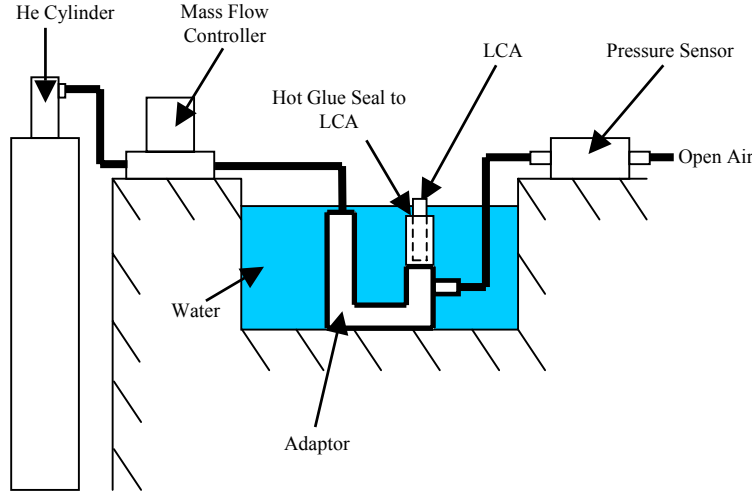
Figure 10. Experimental set up.

The experimental results were compared to analytical predictions based on Equations (11) through (13) (Richardson et al., 2000), i.e.,

$$\frac{\Delta P}{L} = a_0 V + a_1 V^2 \tag{11}$$

where $\Delta P / L$ is the pressure drop per unit length, V is the superficial velocity, and a_0 and a_1 are defined by

$$a_0 = \frac{\alpha S_v^2 \mu (1-\varepsilon)^2}{\varepsilon^3} \quad , \quad a_1 = \frac{\beta S_v \rho (1-\varepsilon)}{\varepsilon^3} \tag{12}$$

Here, α and β represent parameters that reflect the geometry and packing of the porous medium. The universal values recommended for these parameters are 5.00 and 0.300 respectively. In equations **Error! Reference source not found.**, μ is the viscosity of the fluid, ρ is the density of the fluid, ε is the porosity, and S_v is defined as

$$S_v = \frac{4\varepsilon}{d_p (1-\varepsilon)} \tag{13}$$

where d_p is the pore diameter. The specimen has a pore diameter of ~50 microns, a porosity of 70%, a length of 4.42 cm, and an internal square cell diameter of 1.5 mm. Experimental results for this sample are compared to predictions in Figure 11 and 12. The experimental results and analytical prediction are in good agreement. The analytical model is now extrapolated to the problem specific to the palm power research.
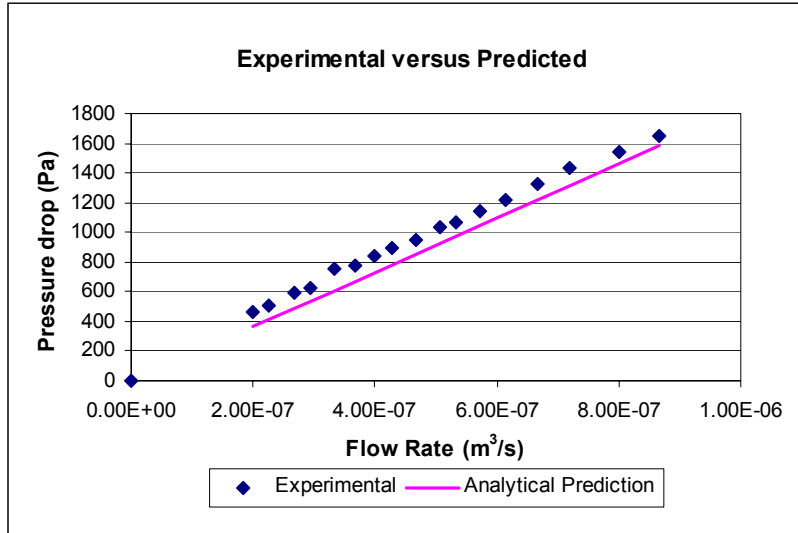
Figure 11. Experimental pressure drop compared with analytical prediction for a 4x4 monolithic SOFC structure with fiber filled channels and no electrode coating.
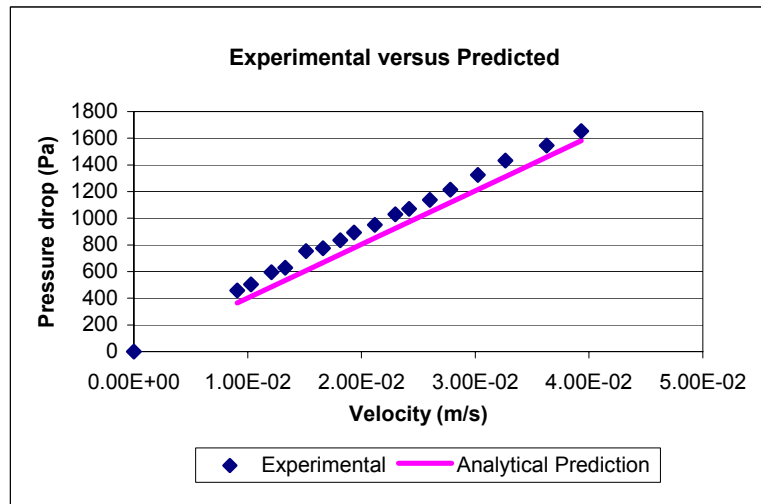
Figure 12. Experimental pressure drop plotted as a function of velocity.

The proposed fuel cell uses a stack of five 4x4 fuel cells. This results in an effective fuel cell 20 rows high and 4 columns across. The analyses in Figure 13 and 14 are based on the requirement of 0.2 sccm H_2/0.5 sccm air per cm length and per channel for 100 mA/cm^2 and 0.5 sccm H_2/2.25 sccm air per cm length and per channel for 250 mA/cm^2 (specific by W. Rauch). Figure 16 shows the pressure drop for the hydrogen and air sides of the fiber filled fuel cell for the two levels of current density.
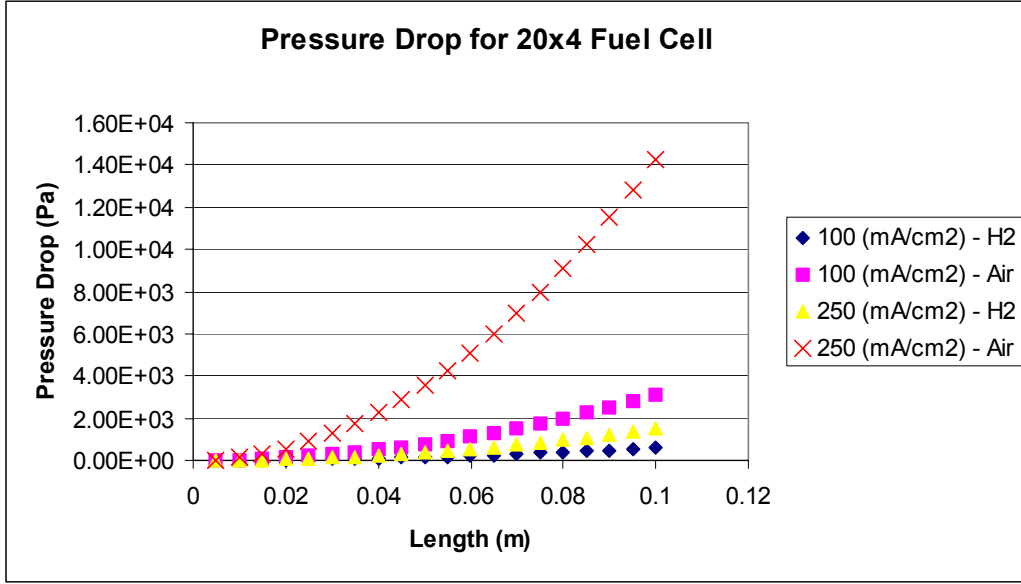
Figure 13: Predicted pressure drop for a 20x4 cell SOFC at various lengths and at two levels of current density, 100 mA/cm^2 and 250 mA/cm^2.
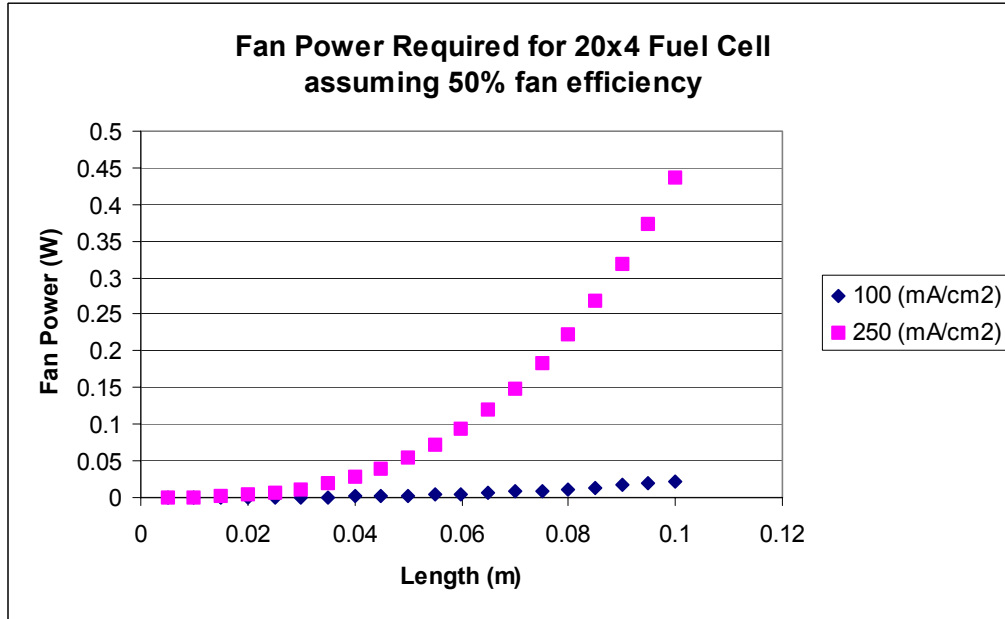
Figure 14: Predicted fan power required for a 20x4 fuel cell at various lengths and at two levels of current density, 100 mA/cm^2 and 250 mA/cm^2 with a 50% efficient fan.

Figure 14 combines the pressure drop from the fuel and air side for each level of current density and presents the mechanical power,

$$W_{mech} = \int_S P \underset{\sim}{V} \cdot d\underset{\sim}{A} = \Delta P_{air} A_{air} \bar{V}_{air} + \Delta P_{hyd} A_{hyd} \bar{V}_{hyd} \quad , \tag{14}$$

that is required to drive a fan with 50% efficiency. In Equation (14), A_{air} and A_{hyd} are the respective total areas of cells with flowing air and hydrogen, and the subscripted pressure drop and mean velocity terms are similarly associated with air and hydrogen flow. The predicted required power needed to deliver enough reactants to a 10cm long, 20 x 4, fuel cell with a power density of 250 mA/cm^2 is approximately 0.5 W. Hence, very little power must be drawn from the SOFC to meet this requirement and feasibility is established, although a fan is required to move the working fluids.

REFERENCE

Richardson, T. J., Peng, Y., Remue, D., 2000, "Properties of ceramic foam catalyst supports: pressure drop," *Applied Catalysis A: General*, **204**, 19-32.

Consideration of Fiber Based Electrode Configuration - Due to manufacturing constraints, the design of the fuel cell electrodes has been modified. The previous design was based on a thin electrode coating that covered the internal walls of the fuel cell channels. In an effort to increase the performance, the new design utilizes porous electrolyte fiber that fills each channel. This design is shown in Figure 15.
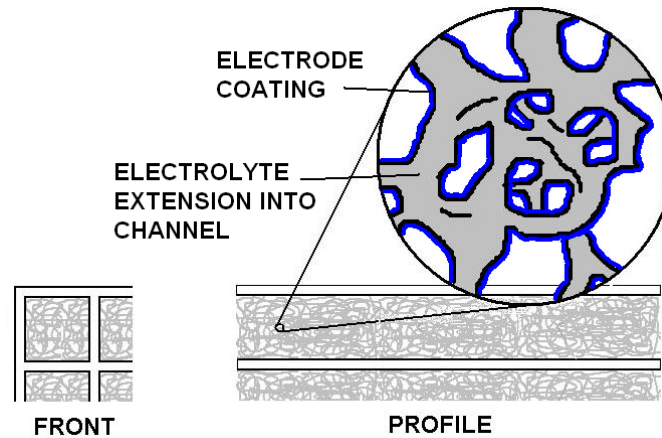
Figure 15. Schematic for new design of electrolyte and electrode.

The electrode coating is deposited on fiber in each channel of the fuel cell. This configuration should encourage reactions that occur in the gas flow streams. This is visually represented in Figure 15. In Figure 16, δ is the depth into the flow stream that the majority of the reactions take place. An approximation of δ will be valuable for determining the temperature field in the interconnect, electrolyte, and porous electrolyte extension. Even though the design has been slightly modified, the effects of the temperature field on the structural integrity of the fuel cell will continue to be a critical aspect for operation and will be explored in future efforts. The fluid flow in this new configuration will now be governed by Stokes flow (Kaviany, 1995), i.e.,

$$-\frac{dp}{dx} = \frac{\mu}{K} u_D \quad , \tag{15}$$

where dp is the pressure difference across the porous medium, dx is the distance between pressure measurements, μ is the viscosity, K is the permeability, and u_D is the filter (or Darcy) velocity. A schematic of this one-dimensional flow is shown in Figure 17.
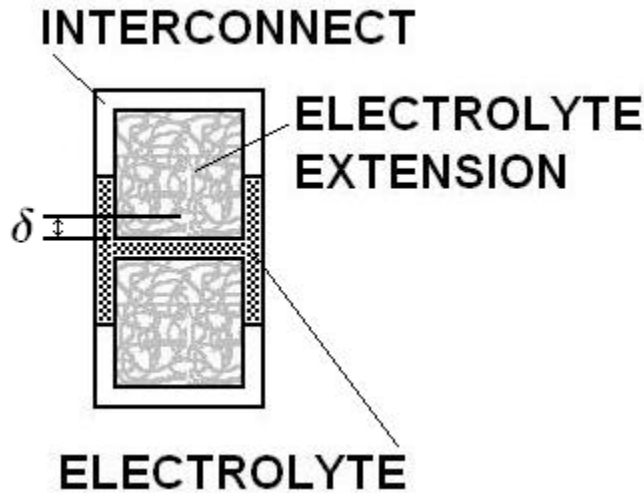
Figure 16. Single cell schematic of the reaction depth into the flow stream.
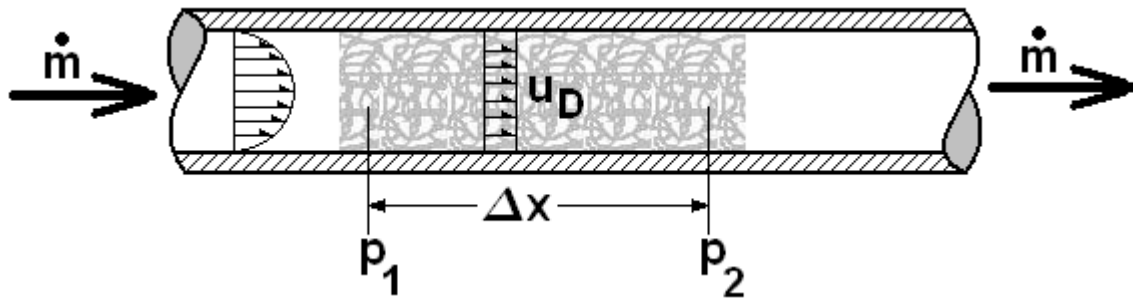
Figure 17. One-dimensional steady-state determination of filter velocity.

The permeability accounts for the hydrodynamic characteristics of the porous medium and is generally determined experimentally, but various analytical permeability approximations do exist. FLUENT simulations will incorporate porosity and radiation to better predict the performance and temperature field of this new design.

REFERENCE

Kaviany, M., Principles of Heat Transfer in Porous Media, Springer-Verlag, New York, 1995.

Design of SOFC Cell for Polymer Tube Tubing Attachments- The case of a LCM hybrid fuel cell with cooled ends is simulated in order to determine the effects of cooling on the temperature distribution and the electrical output of the fuel cell. Cooled ends yield less fabrication restraints on the fuel and air flow manifolding. While cooling the ends of the fuel cell will greatly reduce the power density of the fuel cell, it does allow preliminary measurements to be taken on manufactured hybrid specimens, which serves the short-

term purposes of the project. The case simulated with CFD (FLUENT) is shown in Figure 18.
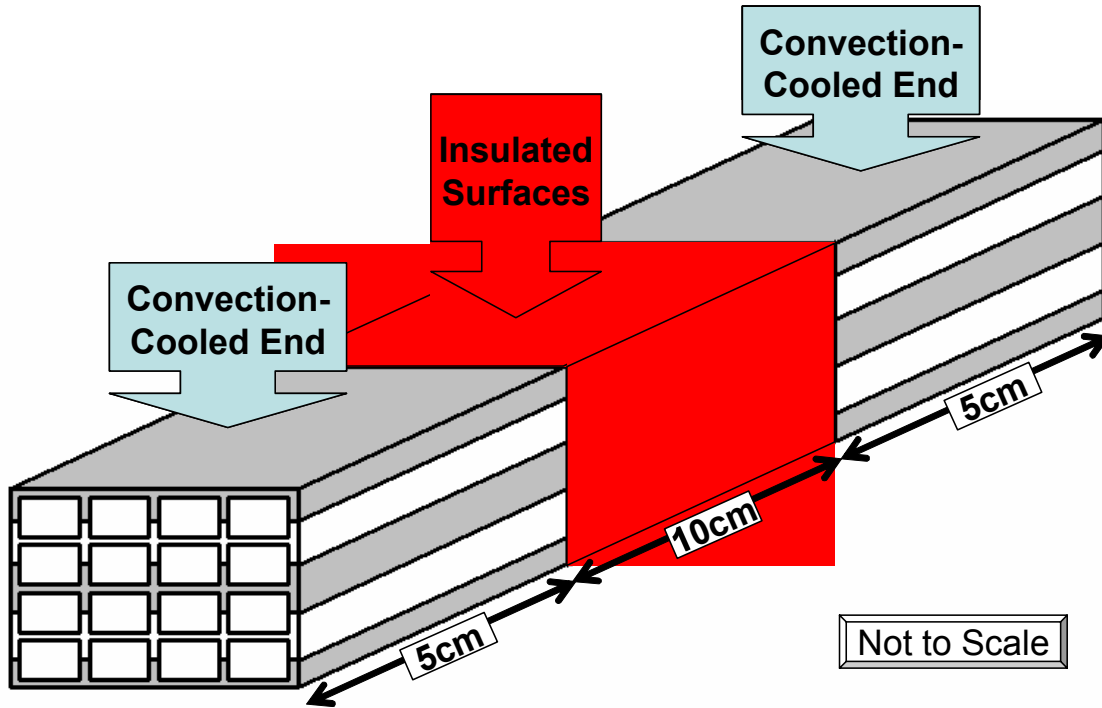
Figure 18. Schematic of hybrid fuel cell with cooled ends.

A 4x4 hybrid fuel cell with 5 cm of cooled length on each end is analyzed. The middle section of 10 cm length is insulated. The electrical generation is assumed to come from only the middle section. The fuel cell has two active electrolyte layers. The case examined here is for open cells with no porous filling, i.e. a thin electrode coating is assumed to coat the interior of the channels. Figure 19 shows the temperature distribution in one of the realizations calculated from the CFD simulations.
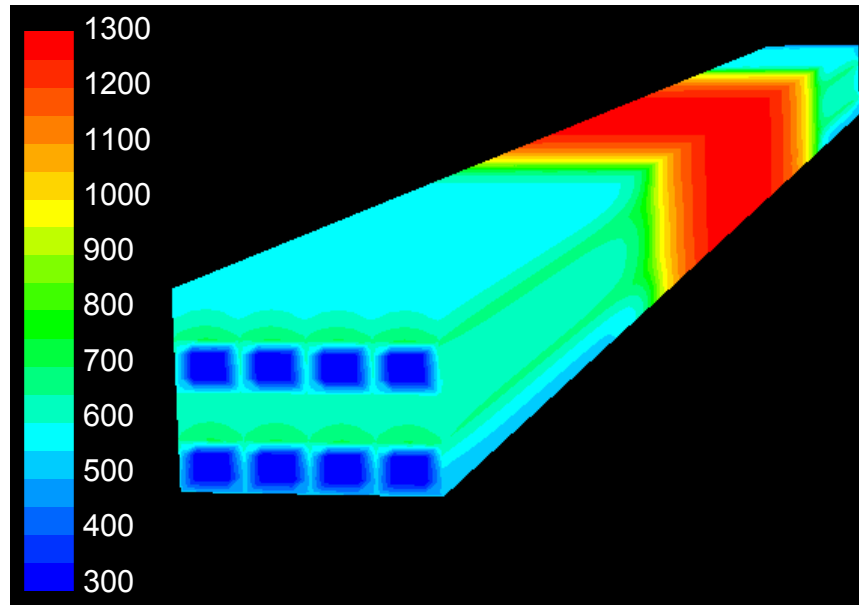
Figure 19. Typical temperature field for hybrid fuel cell with cooled ends.

The temperature of the ends shown in Figure 19 is slightly above the required temperature of 150ºC (423 K). If the temperature of the ends is relatively cool, a large range of materials can be used to manifold the fuel and air flows.   Table 22 contains the results from several CFD analyses.

Table 2. CFD results of various cooled end simulations.

Air Mass Flow Rate (kg/s)	Convective Heat Transfer Coefficient (W/(m^2·K))	Approximate Cooled End Temperature (K)	Maximum Temperature in Insulated Region (K)	Average Electrolyte Temperature in Insulated Region (K)	Predicted Power for 4x4 cells by 10 cm Fuel Cell (W)
7.97e-04	74.54	490.9261	721.55	691.72	0
3.50e-05	74.54	570.4745	902.30	839.79	0
7.97e-06	74.54	588.7372	1128.12	1018.842	4.76
7.97e-07	74.54	588.447	1305.92	1172.10	6.56
7.97e-06	228.96	535	1099.739	979.4396	4.04

In the case analyzed, there are two means that can be used to reduce the temperature of the ends. The first is to increase the flow rate of the air. A minimum air mass flow rate of approximately 4.00E-07 kg/s is required for operation of the 10 cm long 4x4 hybrid fuel cell assuming 60% fuel utilization. Any flow rate that is used above this flow rate will produce a temperature drop of the ends such that materials with relatively lower melting temperatures can be used for manifolding the flow. The disadvantage of this approach is that the electrolyte temperature is reduced.   The reduced electrolyte temperature causes the power output to be reduced as well. The second means that can be used to reduce the end temperature is forced convective cooling. The convective heat

transfer coefficient of 74.54 W/(m²·K) is approximate for free-convection while the last value listed in the convective heat transfer coefficient column is for a moderate forced convection (air at a velocity ~ 10m/s). The last case listed in Table 22 used a forced convective heat transfer coefficient. This allows cooling of the ends while maintaining the temperature of the electrolyte. The optimal configuration for this case will likely need to use forced convective cooling on the ends to prevent overheating. For maximum power output, the electrolyte should be at as high of a temperature as possible that doesn't cause failure. A combination of relatively low airflow rates (beyond the amount required for reaction) and forced convection cooled ends will best solve the problem described here.

Design of SOFC Cell for Polymer Tube Tubing Attachments - The previous report contained simulations relating to LCMs with cooled ends. This case was explored to determine the effects of cooled ends on the temperature field and electronic performance. The goal of the cooled end design is to facilitate low temperature manifolding. Table 3 contains several results previously reported. Additional runs that bracket electrolyte temperature within the desired operational range are also included in Table 3.

Table 3. CFD results of various cooled end simulations.

Air Mass Flow Rate (kg/s)	Convective Heat Transfer Coefficient (W/(m²·K))	Approximate Cooled End Temperature (K)	Maximum Temperature in Insulated Region (K)	Average Electrolyte Temperature in Insulated Region (K)	Predicted Power for 4x4 cells by 10 cm Fuel Cell (W)
7.97e-06	228.96	535.00	1099.74	979.44	4.04
7.97e-07	74.54	588.45	1305.92	1172.10	6.56
7.97e-06	74.54	588.74	1128.12	1018.842	4.76
1.50E-05	74.54	585.25	1019.27	932.31	2.90
2.50E-05	74.54	577.66	943.25	872.40	0.68
2.98E-05	74.54	574.11	920.97	854.77	0
3.19E-05	74.54	572.63	912.95	848.35	0
3.50e-05	74.54	570.47	902.30	839.79	0
7.97e-04	74.54	490.93	721.55	691.72	0

The results in Table 3 are for a 4x4 hybrid fuel cell with 5 cm of cooled length on each end. The middle section of 10 cm length is insulated. The electrical generation is assumed to come from only the middle section. The fuel cell has two active electrolyte layers. The case examined here is for open cells with no porous filling, i.e., a thin electrode layer is assumed to coat the interior of the channels.

The temperature of the ends of the fuel cell modeled above are still too high for the low temperature manifolding, so the same design is analyzed with a slight modification. In this second design, the fuel and air are dumped from the fuel cell after each stream passes the reaction zone of the fuel cell. This configuration is shown in Figure 20.
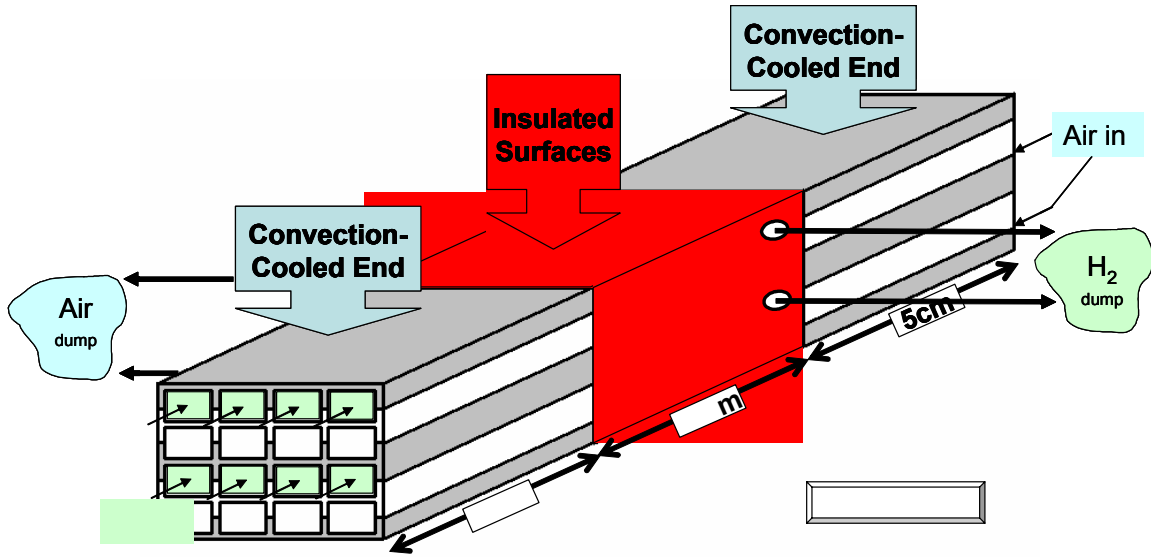
Figure 20. New configuration with hydrogen and air rejection at the end of the reaction zone.

Results of the corresponding CFD analysis that is based on the boundary conditions seen in Figure 20 are given in Table 4.

Table 4. Results for LCM fuel cell with hydrogen and air dumped after passing the reaction zone.

Air Mass Flow Rate (kg/s)	Convective Heat Transfer Coefficient (W/(m²·K))	Approximate Cooled End Temperature (K)	Maximum Temperature in Insulated Region (K)	Average Electrolyte Temperature in Insulated Region (K)	Predicted Power for 4x4 cells by 10 cm Fuel Cell (W)
1.00E-05	74.54	373.10	1041.75	926.02	2.71
1.50E-05	74.54	372.20	971.01	872.61	0.69
2.98E-05	74.54	370.28	880.84	805.73	0.00

Dumping the fuel and air after passing the reaction zone causes the maximum and average electrolyte temperatures to drop. This reduction in temperature confers a reduction in the predicted power. However, this reduction in the maximum temperatures in the electrolyte active area is linked to a much lower cooled end temperature. Because the hot gases leaving the reaction zone are not allowed to heat up the cooled ends, the end temperatures can be maintained at a much lower temperature. Figure 21 is an example of the temperature field predicted in the cooled ends analyzed.
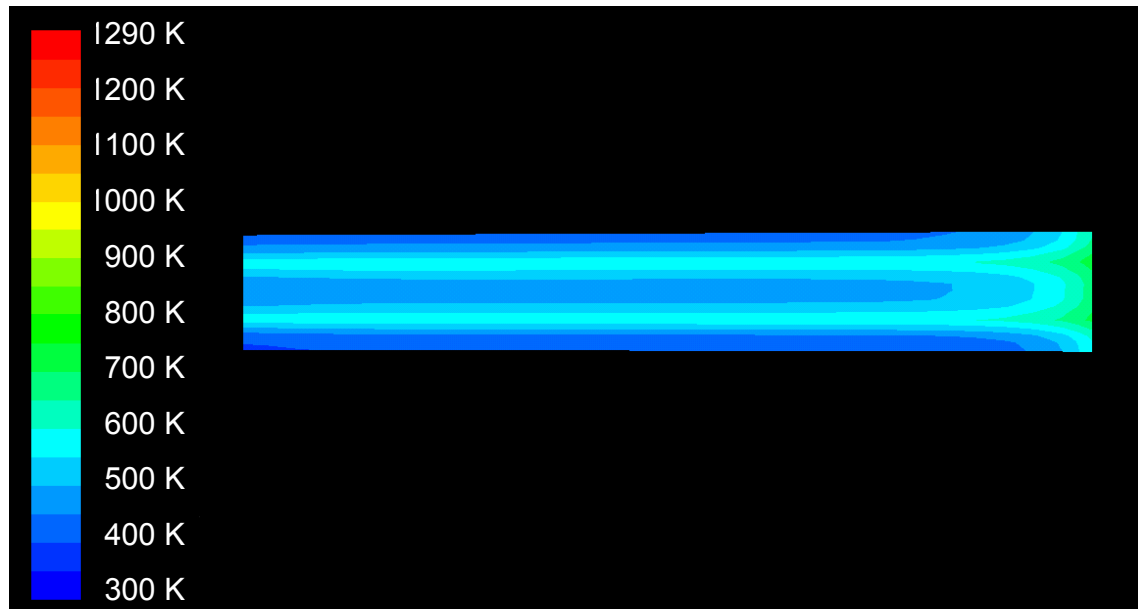
Figure 21. Cooled end temperature contours (total length shown 5 cm).

The temperature field shown in Figure 21 suggests that the entire 5 cm of cooled ends is not necessary for manifolding; 2 cm of cooled ends may be all that is required for low temperature manifolding.

Effects of Fiber Filled Channels on SOFC Performance - Subjects covered below include a discussion on the reaction zone in the electrolyte extension and metallic extension and the permeability and other properties of the electrolyte extension. Two basic fuel cells were developed using the square cell honeycomb configuration. The first is the hybrid structure that is based on the concept of alternating rows of electrolyte and metallic interconnect. This configuration is shown in Figure 22a. The second configuration is a monolithic structure that has a base structure consisting of only electrolyte. This configuration is shown in Figure23a.

Figures 22b and 23b show the proposed fiber-filled channels. Figure 22b shows the hybrid structure filled with both electrolyte extension (on the left) and metallic current collector extension (on the right). Figure 23b shows the monolithic design filled with the metallic current collector extension. All of the filled channels will be coated with an electrode made from a mixed ionic-electronic conductor (MIEC). In all cases the MIEC electrodes are possible pathways for both oxygen-ion vacancies and electrons. There are two types of triple-phase boundaries (TPBs) shown in Figures 22b and 23b. TPB1 is at the intersection of the electrolyte (or electrolyte extension), the MIEC, and O_2 gas (Liu, 1998). TPB2 is at the intersection of the current collector (or metallic current collector extension), the MIEC, and the O_2 gas (Liu, 1998). The TPBs highlighted in the diagrams are at voids in the MIEC electrode coating. Whether these voids are a byproduct of the fabrication process or intentional, they increase the number of sites that TPBs can occur. Because the electrode is formed from an MIEC, the reaction sites are not limited to just the TPBs. The reactions can also take place along the MIEC/gas interface (Liu, 1998).
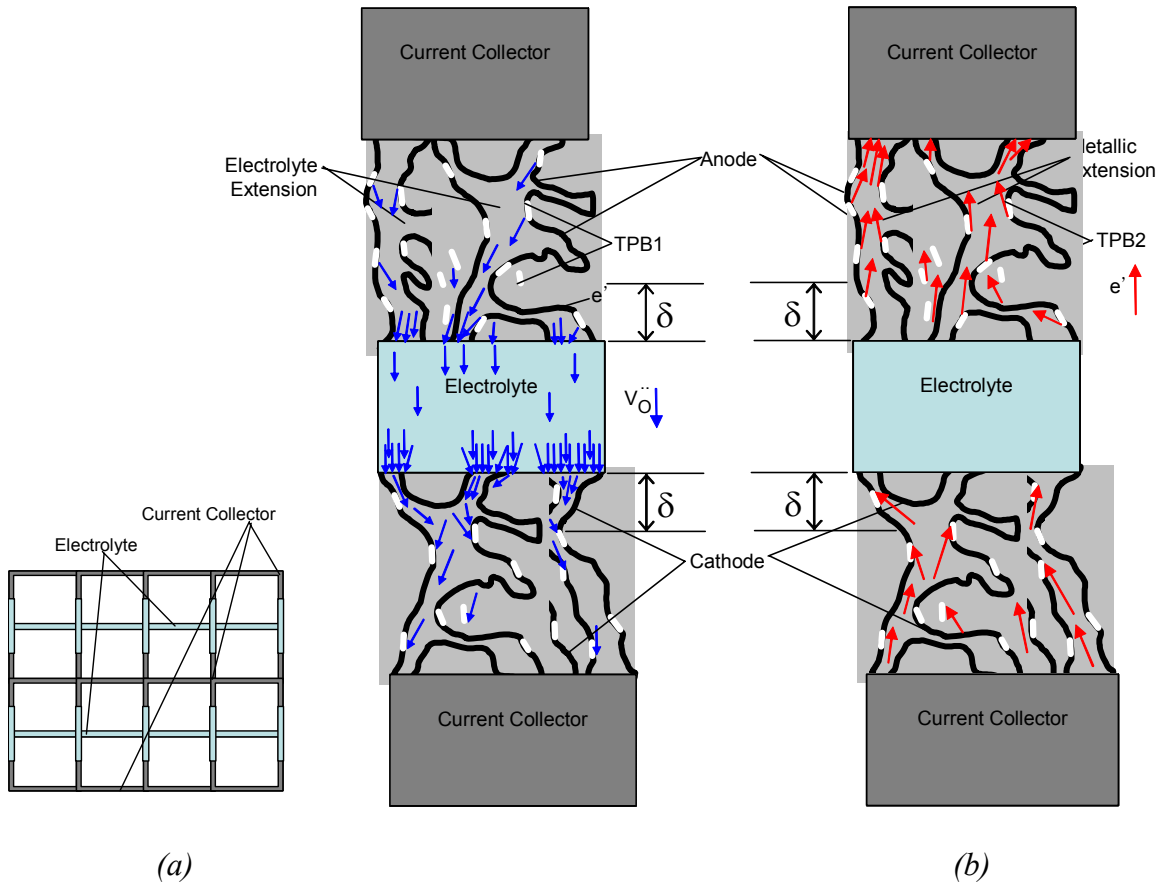
Figure 22: Schematic of hybrid fuel cell with fiber filled channels.

The metallic fiber-filled channel provides a high conductivity path for the electrons to flow. This configuration is particularly advantageous in the monolithic design, as it lacks the alternating metallic layers seen in the hybrid structure. Because of the inherent resistance of the system, the zone where most of the reactions will take place will be near the electrolyte. The zone is denoted by δ in Figures 3b and 4b. Reactions can occur at any TPBs in this reaction zone or along the MIEC/gas interface in this region. The goal of all of the configurations is to increase the overall performance of the fuel cell.

Flow in these fiber-filled channels can be modeled as flow through a porous media. Based on previously reported measurements and calculations, the predicted required fan power needed to deliver enough reactants to a 10cm long, 20x4, fuel cell with a power density of 250 mW/cm^2 is approximately 0.5 Watt. These same experiments provided the pressure drop that is required for determining the permeability, K, of the electrolyte extension in the fuel cell channel.
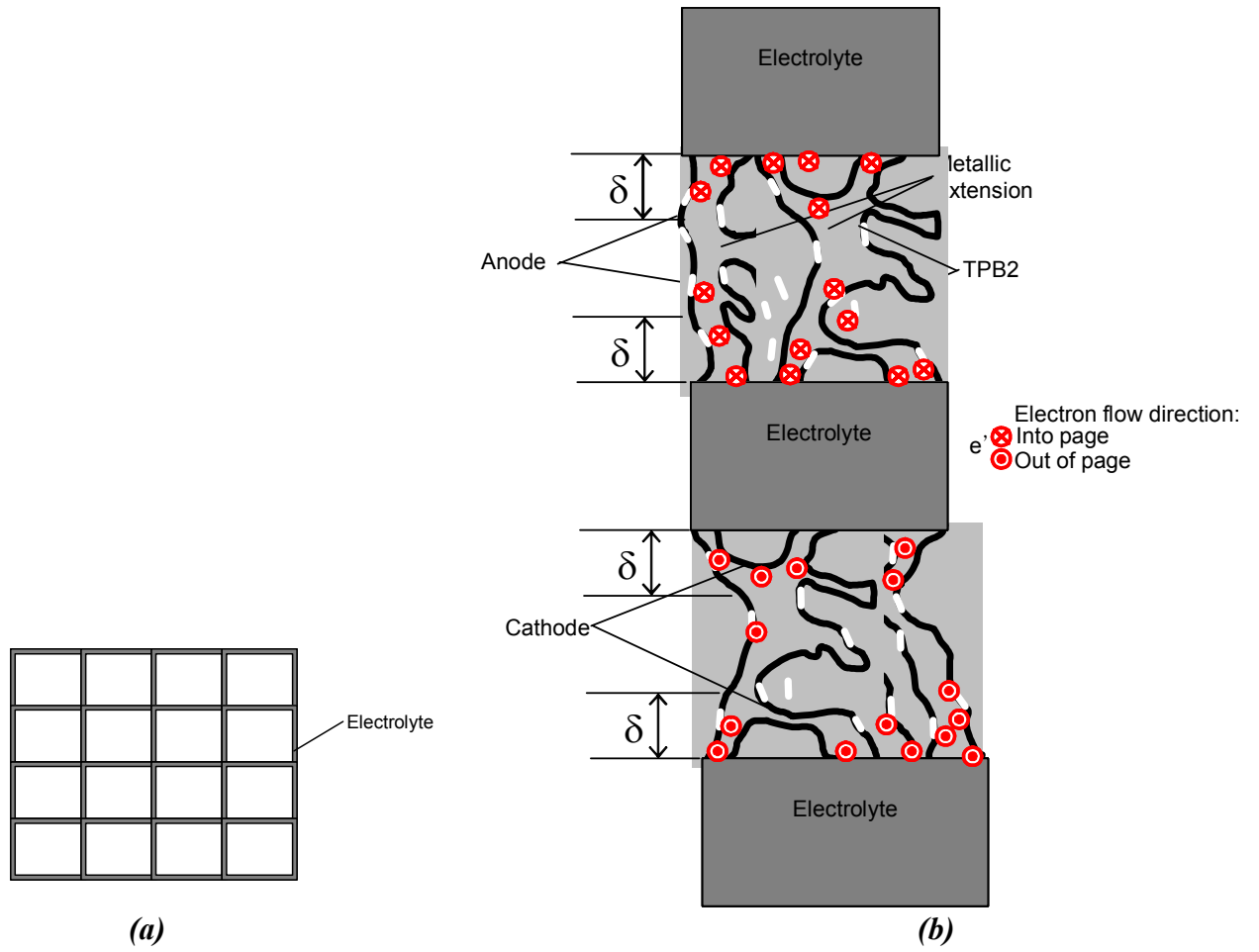
Figure 23. Schematic of monolithic fuel cell with fiber-filled channels.

The permeability can be calculated based on the following equation (Kaviany, 1995):

$$-\frac{dp}{dx} = \frac{\mu}{K} u_D \qquad (16)$$

Where dp is the pressure change over a distance, dx, μ is the dynamic viscosity of the fluid, and u_D is the filter velocity. The specimen examined had a pore diameter, d_p, of approximately 50 microns, a porosity of 70%, and an internal cell dimension of 1.5 mm. Via Equation (1), the permeability of the specimen was determined to be 1.92e-11 m². The internal resistance factor, C_2, can be approximated by (Fluent, 1998)

$$C_2 = \frac{3.5}{d_p} \frac{(1-\varepsilon)}{\varepsilon^3} \qquad (17)$$

where ε is the porosity and d_p is the pore diameter. Currently, CFD models are being run that use these porous flow relations.

REFERENCES

FLUENT User's Guide, Release 6.0.20. FLUENT Inc., 1998.

Kaviany, M., Principles of Heat Transfer in Porous Media, 2nd ed., Springer-Verlag, New York (1995).

Liu, M., "Equivalent Circuit Approximation to Porous Mixed-Conducting Oxygen Electrodes in Solid-State Cells", *Journal of Electrochemical Society*, 145 (1998) 142-154.

Transient CFD Simulations of Hybrid SOFCs - Modeling the transient behavior of the fuel cell is a vital component in preventing the mechanical failure of the fuel cell. FLUENT was utilized for transient analysis of the fuel cell (FLUENT, 1998). A 4 x 4 cell fuel cell 10 cm long has cell wall thicknesses of 120 microns and 2 mm internal cell wall dimensions. The fuel cell is at an initial condition of room temperature and pressure (300K, 1 atm). The fuel (hydrogen) and oxidant (air) are then forced through the fuel cell at a mass flow rate of 7.24e-4 kg/s for the air and a mass flow rate of 2.78e-8 kg/s for the fuel. The inlet temperature of the air is 475 K, and the inlet temperature of the fuel is 300 K. Assuming fully insulated walls and the preheated air, the model reached steady state conditions at approximately 90 seconds. Figures 24 through 28 show the temperature contours for the fuel cell at various times of operation.
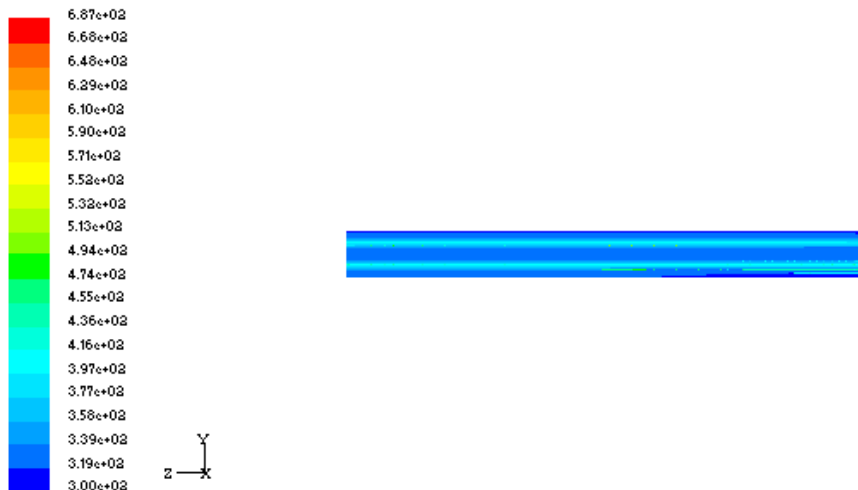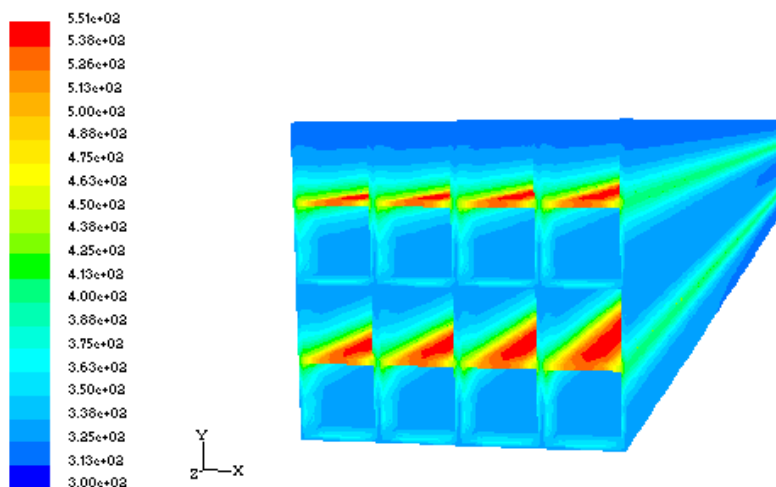

Figure 24.Temperature (Kelvin) contours of the fuel cell at 1 second.
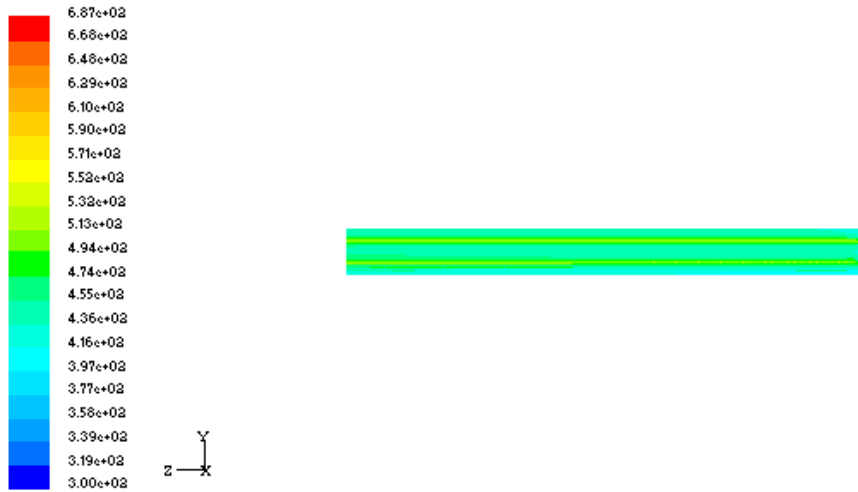
Figure 25. Temperature (Kelvin) contours of the fuel cell at 5 seconds.
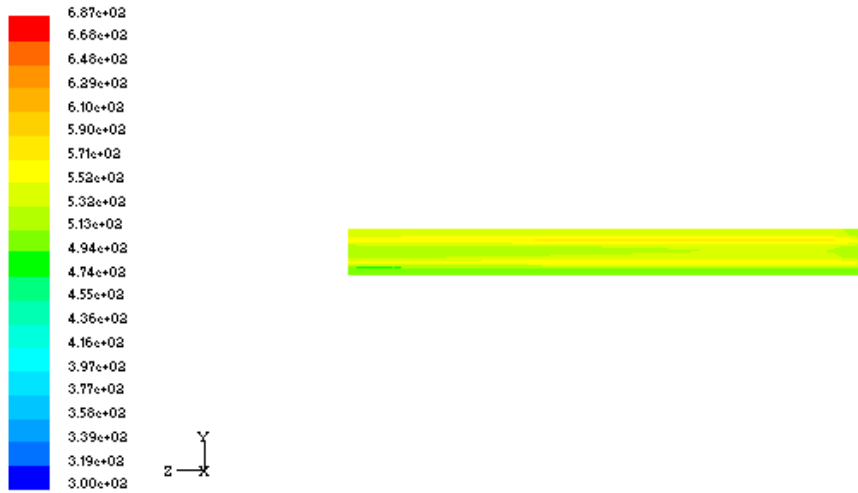
Figure 26. Temperature (Kelvin) contours of the fuel cell at 15 seconds.
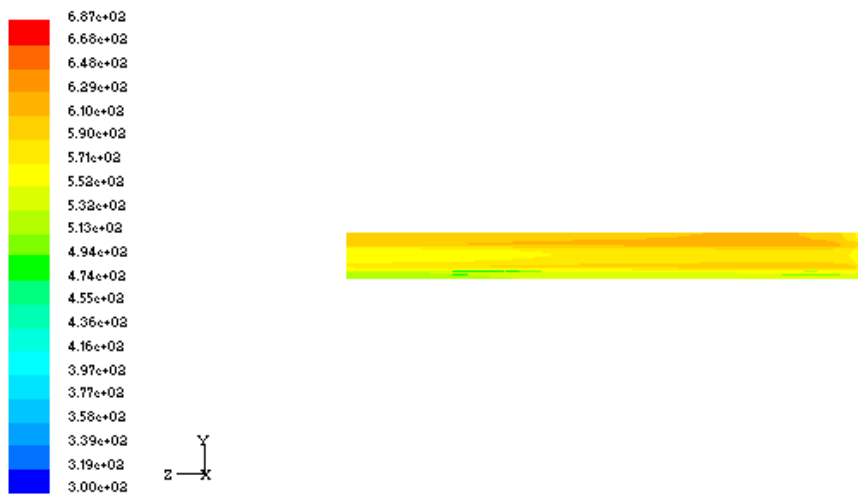
Figure 27. Temperature (Kelvin) contours of the fuel cell at 25 seconds.
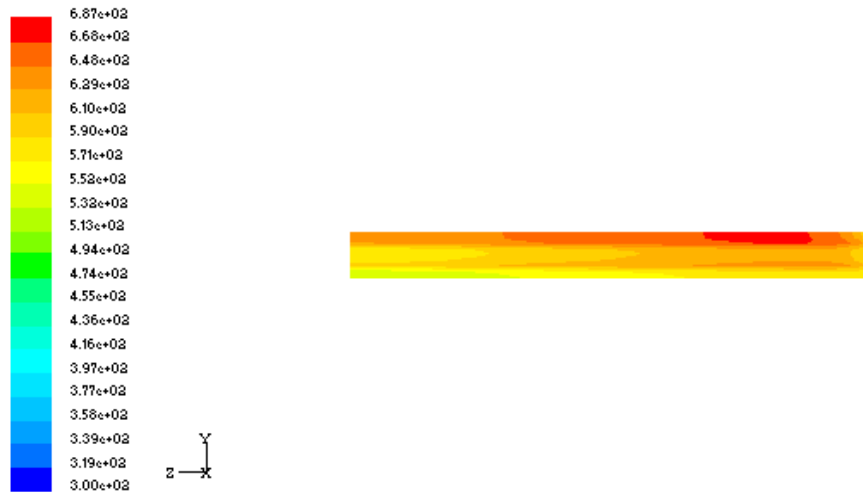
Figure 28. Temperature (Kelvin) contours of the fuel cell at steady state.

In Figures 24 through 28, fuel enters from the right and air enters from the left. The increase in temperature begins very uniformly with respect to the z axis from initial startup. At 15 seconds the non-uniformity of the temperature distribution (with respect to the z-axis) begins to become much more visible. At 25 seconds the basic shape of the final steady-state temperature gradient is reached. Finally, at approximately 75 seconds the steady state temperature distribution is reached. Again, this relatively short time required to reach steady state is for a fuel cell with perfectly insulated walls, preheated incoming air, and for a fuel cell that is at temperatures that would be too low for good power production. However, this model does illustrate the value of transient analysis as shown in Figures 29 and 30, which illustrate the large temperature gradients that will exist during the initial stages of startup.

Figure 29. Temperature (Kelvin) contours of the fuel cell at 1 second.
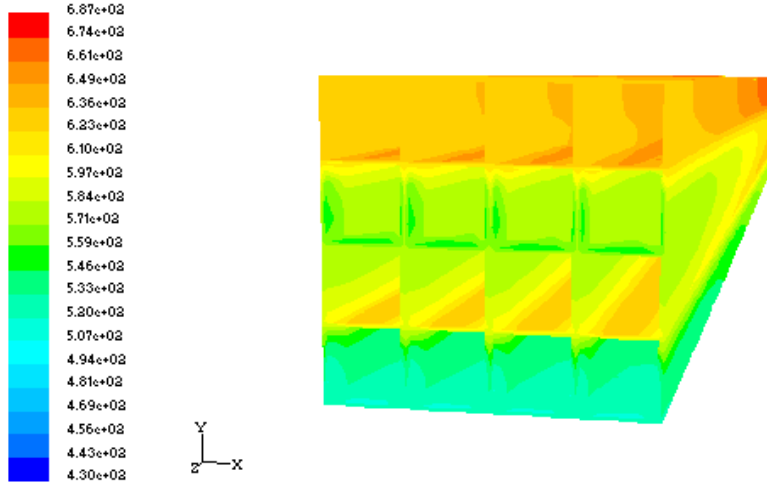
Figure 30. Temperature (Kelvin) contours of the fuel cell at steady state.

For the best comparison of the fuel cell temperature gradients at the different times, both Figures 29 and 30 are presented with temperature scales that range over 250 degrees Kelvin. The early stages of transient operation provide some of the greatest temperature gradients. These temperature gradients will likely serve to provide limits for mechanical failure of the fuel cell. Preheating the fuel cell or fuel itself are means to avoid these possible complications.

REFERENCE

FLUENT User's Guide, Release 6.0.20. FLUENT Inc., 1998.

Constant Voltage Fuel Cell Heat Generation Model **-** The total heat transfer generation rate and its derivative are required for FLUENT CFD simulations. These terms have been expressed previously for constant current cases, but have not been reported for constant voltage. As shown previously, the total heat generation rate can be expressed as:

$$
\begin{aligned}
\dot{Q} =\ & \frac{t_{ele,cm}}{A_{ele,cm}} T 10^{\left(\frac{2.7697 \cdot 1000}{T} - 4.1806\right)} \left(J \frac{A_{ele,cm}}{1000}\right)^2 \\
& + \frac{e^{(-0.0109 \cdot T + 0.0006 \cdot J + 15.026)}}{1000} \left(J \frac{A_{ele,cm}}{1000}\right) \\
& - \frac{\left(J \cdot \frac{A_{ele,cm}}{1000}\right)}{2F} \Delta H_{H_2O} - \frac{RT}{4F} \ln\left(\frac{p_{o_2,(c)}}{p_{o_2,(a)}}\right)\left(J \frac{A_{ele,cm}}{1000}\right)
\end{aligned}
\tag{18}
$$

86

where $t_{ele,cm}$ (cm) is the thickness of the electrolyte and $A_{ele,cm}$ (cm) is the cross-sectional area of the electrolyte parallel to the fluid flow in the Linear Cellular Material (LCM) fuel cell, T (K) is the temperature of the electrolyte, J (mA/cm^2) is the current density, ΔH_{H_2O} (J/mol) is the enthalpy of H_2O formation, F (C/mol) is the Faraday constant, R $\left(\dfrac{J}{mol \cdot K}\right)$ is the universal gas constant, $p_{O_2,(c)}$ is the partial pressure of the oxygen at the cathode, and $p_{O_2,(a)}$ is the partial pressure of the oxygen at the anode. When a constant operational voltage of 0.7 V is assumed one can use Equation (19) to derive the current or current density (Minh and Takahashi, 1995).

$$E = E_r - IR_e - \eta \tag{19}$$

where E(V) is the operating voltage and all other terms are previously defined. Note that R_e and η are simplified for this case. Only the resistance of the electrolyte and the overpotential of the cathode are being considered. The terms in Equation **Error! Reference source not found.** contain I (or J since I = JA) inside and outside of an exponential function, thus I cannot be expressed explicitly as a function of temperature. Solving for the root of this equation at various temperatures generates a set of points. When these points are fit to a curve, we arrive at

$$J\left[\frac{mA}{cm^2}\right] = 0.01633T^2 - 26.85T + 10940 \qquad for\,925K - 1115K \tag{20}$$

$$J\left[\frac{mA}{cm^2}\right] = 0.0292T^2 - 56.6T + 28170 \qquad for\,1115K - up \tag{21}$$

For temperatures below 925 K, the current in the system is zero. According to experimental results, at temperatures below 925 K the system cannot overcome the resistance to start the reaction process. By inserting Equations (20) and (21) into Equation (19) and plotting the results, Figure 31 is generated.
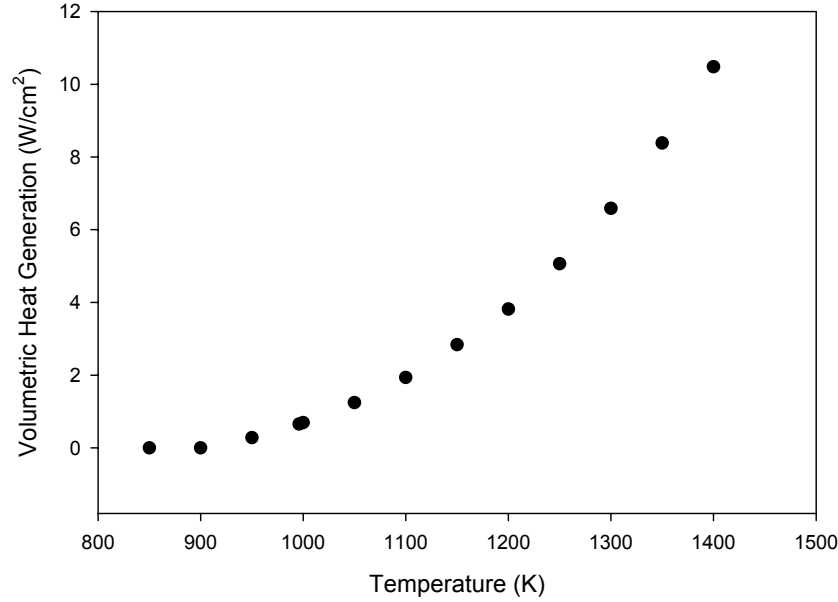
Figure 31: Volumetric heat generation of the fuel cell versus temperature

Equation (18) is expressed on a per unit volume basis, so that the curve in Figure 31 is valid for all geometries. Equation (18) obviously depends on the size of the fuel cell, i.e., the larger the fuel cell the larger the total rate of heat generation. When Equation (21) is inserted in to Equation (18), the latter is written as

$$
\begin{aligned}
\dot{Q} &= \frac{t_{ele,cm}}{A_{ele,cm}} \cdot T \cdot 10^{\left(\frac{2.7697 \cdot 1000}{T} - 4.1806\right)} \cdot \left(\left(0.0292 \cdot T^2 - 56.6 \cdot T + 28170\right) \cdot \frac{A_{ele,cm}}{1000}\right)^2 \\
&+ \frac{e^{\left(-0.0109 \cdot T + 0.0006 \cdot \left(0.0292 \cdot T^2 - 56.6 \cdot T + 28170\right) + 15.026\right)}}{1000} \cdot \left(\left(0.0292 \cdot T^2 - 56.6 \cdot T + 28170\right) \cdot \frac{A_{ele,cm}}{1000}\right) \\
&- \frac{\left(\left(0.0292 \cdot T^2 - 56.6 \cdot T + 28170\right) \cdot \frac{A_{ele,cm}}{1000}\right)}{2F} \Delta H_{H_2O} \\
&- \frac{RT}{4F} \ln\left(\frac{p_{O_2,(c)}}{p_{O_2,(a)}}\right) \cdot \left(\left(0.0292 \cdot T^2 - 56.6 \cdot T + 28170\right) \cdot \frac{A_{ele,cm}}{1000}\right)
\end{aligned}
\tag{22}
$$

By expanding the terms in Equation (22) one arrives at

$$
\begin{aligned}
\dot{Q} = & \left(t_{ele,cm} \cdot A_{ele,cm} \cdot 8.5264E-10 \cdot 10^{\left(\frac{2.7697E3}{T} - 4.1806 \right)} \right) \cdot T^5 \\[4pt]
& + \left(-t_{ele,cm} \cdot A_{ele,cm} \cdot 3.30544E-6 \cdot 10^{\left(\frac{2.7697E3}{T} - 4.1806 \right)} \right) \cdot T^4 \\[4pt]
& + \left(\begin{aligned} & t_{ele,cm} \cdot A_{ele,cm} \cdot 4.848688E-3 \cdot 10^{\left(\frac{2.7697E3}{T} - 4.1806 \right)} \\ & -7.3E-6 \cdot \frac{R}{F} \ln\left(\frac{p_{O_2,(c)}}{p_{O_2,(a)}} \right) \cdot A_{ele,cm} \end{aligned} \right) \cdot T^3 \\[4pt]
& + \left(\begin{aligned} & -t_{ele,cm} \cdot A_{ele,cm} \cdot 3.188844 \cdot 10^{\left(\frac{2.7697E3}{T} - 4.1806 \right)} \\ & +2.92E-8 \cdot A_{ele,cm} \cdot e^{\left(1.752E-5 \cdot T^2 - 4.486E-2 \cdot T + 3.1928E1 \right)} \\ & -1.46E-5 \cdot \frac{A_{ele,cm} \cdot \Delta H_{H_2O}}{F} + 1.415E-2 \cdot \frac{R}{F} \ln\left(\frac{p_{O_2,(c)}}{p_{O_2,(a)}} \right) \cdot A_{ele,cm} \end{aligned} \right) \cdot T^2 \\[4pt]
& + \left(\begin{aligned} & t_{ele,cm} \cdot A_{ele,cm} \cdot 7.935489E2 \cdot 10^{\left(\frac{2.7697E3}{T} - 4.1806 \right)} \\ & -5.66E-5 \cdot A_{ele,cm} \cdot e^{\left(1.752E-5 \cdot T^2 - 4.486E-2 \cdot T + 3.1928E1 \right)} \\ & +2.83E-2 \cdot \frac{A_{ele,cm} \cdot \Delta H_{H_2O}}{F} - 7.0425 \cdot \frac{R}{F} \ln\left(\frac{p_{O_2,(c)}}{p_{O_2,(a)}} \right) \cdot A_{ele,cm} \end{aligned} \right) \cdot T \\[4pt]
& + 2.817E-2 \cdot A_{ele,cm} \cdot e^{\left(1.752E-5 \cdot T^2 - 4.486E-2 \cdot T + 3.1928E1 \right)} \\[4pt]
& - 1.4085E1 \cdot \frac{A_{ele,cm} \cdot \Delta H_{H_2O}}{F}
\end{aligned}
\tag{23}
$$

Equation (23) is required for any simulation that is intended to simulate the total heat generation rate in the fuel cell for a constant voltage application. However, incorporation of the heat generation rate in to a FLUENT model requires the derivative of the heat generation rate with respect to temperature (FLUENT, 1998). When Equation (23) is differentiated with respect to temperature, the result is given by

$$\frac{d\dot{Q}}{dT} = \left(t_{ele,cm} \cdot A_{ele,cm} \cdot 8.5264E-10 \cdot 10^{\left(\frac{2.7697E3}{T}-4.1806\right)} \ln(10)\frac{-2.7697E3}{T^2} \right) \cdot T^5$$

$$+ \left(t_{ele,cm} \cdot A_{ele,cm} \cdot 8.5264E-10 \cdot 10^{\left(\frac{2.7697E3}{T}-4.1806\right)}{}_5 \right) T^4$$

$$+ \left(-t_{ele,cm} \cdot A_{ele,cm} \cdot 3.30544E-6 \cdot 10^{\left(\frac{2.7697E3}{T}-4.1806\right)} \ln(10)\frac{-2.7697E3}{T^2} \right) \cdot T^4$$

$$+ \left(-t_{ele,cm} \cdot A_{ele,cm} \cdot 3.30544E-6 \cdot 10^{\left(\frac{2.7697E3}{T}-4.1806\right)}{}_4 \right) \cdot T^3$$

$$+ \left(t_{ele,cm} \cdot A_{ele,cm} \cdot 4.848688E-3 \cdot 10^{\left(\frac{2.7697E3}{T}-4.1806\right)} \ln(10)\frac{-2.7697E3}{T^2} \right) \cdot T^3$$

$$+ \left(t_{ele,cm} \cdot A_{ele,cm} \cdot 4.848688E-3 \cdot 10^{\left(\frac{2.7697E3}{T}-4.1806\right)}{}_3 \right) \cdot T^2 + \left(-7.3E-6 \cdot \frac{R}{F}\ln\left(\frac{p_{o2,(c)}}{p_{o2,(a)}}\right) \cdot A_{ele,cm}3 \right) \cdot T^2$$

$$+ \left(-t_{ele,cm} \cdot A_{ele,cm} \cdot 3.188844 \cdot 10^{\left(\frac{2.7697E3}{T}-4.1806\right)} \ln(10)\frac{-2.7697E3}{T^2} \right) \cdot T^2$$

$$+ \left(+2.92E-8 \cdot A_{ele,cm}(1.752E-5\cdot 2 \cdot T - 4.486E-2) \cdot e^{\left(1.752E-5\cdot T^2 - 4.486E-2\cdot T + 3.1928E1\right)} \right) \cdot T^2$$

$$+ \left(-t_{ele,cm} \cdot A_{ele,cm} \cdot 3.188844 \cdot 10^{\left(\frac{2.7697E3}{T}-4.1806\right)}{}_2 \right) \cdot T$$

$$+ \left(+2.92E-8 \cdot A_{ele,cm} \cdot e^{\left(1.752E-5\cdot T^2 - 4.486E-2\cdot T + 3.1928E1\right)}{}_2 \right) \cdot T$$

$$+ \left(\left(-1.46E-5 \cdot \frac{A_{ele,cm}\cdot \Delta H_{H2O}}{F} + 1.415E-2 \cdot \frac{R}{F}\ln\left(\frac{p_{o2,(c)}}{p_{o2,(a)}}\right) \cdot A_{ele,cm} \right) \cdot 2 \right) \cdot T$$

$$+ \left(t_{ele,cm} \cdot A_{ele,cm} \cdot 7.935489E2 \cdot 10^{\left(\frac{2.7697E3}{T}-4.1806\right)} \ln(10)\frac{-2.7697E3}{T^2} \right) \cdot T$$

$$+ \left(-5.66E-5 \cdot A_{ele,cm}(1.752E-5\cdot 2 \cdot T - 4.486E-2) \cdot e^{\left(1.752E-5\cdot T^2 - 4.486E-2\cdot T + 3.1928E1\right)} \right) \cdot T$$

$$+ t_{ele,cm} \cdot A_{ele,cm} \cdot 7.935489E2 \cdot 10^{\left(\frac{2.7697E3}{T}-4.1806\right)} - 5.66E-5 \cdot A_{ele,cm} \cdot e^{\left(1.752E-5\cdot T^2 - 4.486E-2\cdot T + 3.1928E1\right)}$$

$$+ 2.83E-2 \cdot \frac{A_{ele,cm}\cdot \Delta H_{H2O}}{F} - 7.0425 \cdot \frac{R}{F}\ln\left(\frac{p_{o2,(c)}}{p_{o2,(a)}}\right) \cdot A_{ele,cm}$$

$$+ 2.817E-2 \cdot A_{ele,cm} \cdot (1.752E-5\cdot 2 \cdot T - 4.486E-2)e^{\left(1.752E-5\cdot T^2 - 4.486E-2\cdot T + 3.1928E1\right)}$$

(24)

For verification, Equation (24) is compared to the slope of the line generated from Equation (23) in Figure 32. In Figure 32, the scope of the heat generation rate is evaluated at the midpoint before it is plotted. The final output of the derivative and the estimation of the slope at the midpoint agree, verifying that the derivative is correct. Both the total heat transfer rate and its derivative must be expressed on a per unit volume basis and then written into the user defined subroutine that interacts with FLUENT. The volumetric heat transfer rate is included in the APPENDIX to this section.
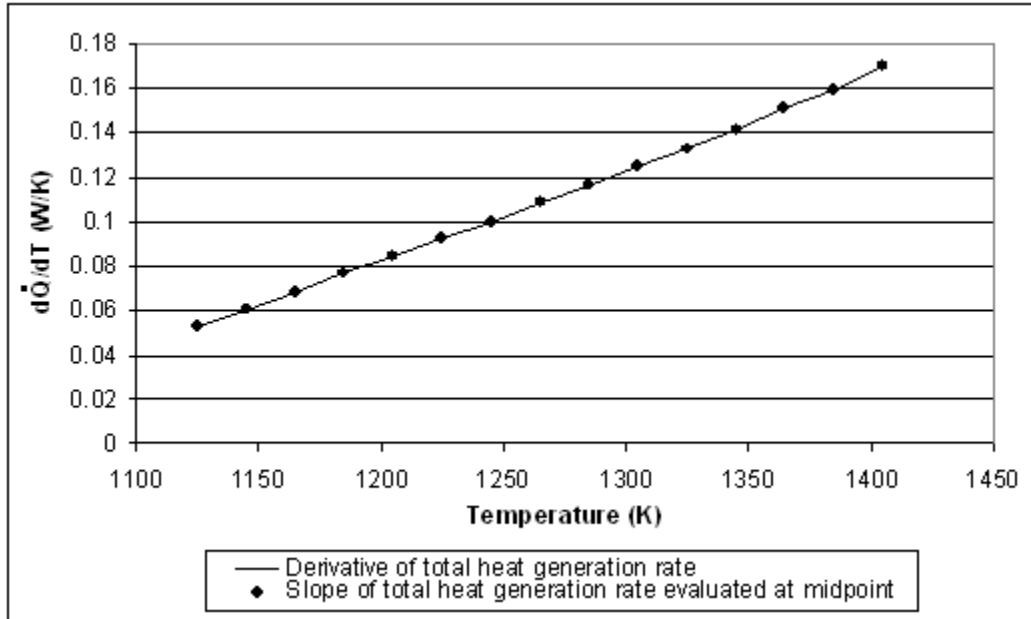
Figure 32: Verification for derivative of heat generation rate.

REFERENCES

FLUENT User's Guide, Release 6.0.20. FLUENT Inc., 1998.

Iwata, M., Hikosaka, T., Morita, M., Iwanari, T., Ito, K., Onda, K., Esaki, Y., Sakaki, Y., Nagata, S., "Performance analysis of planar-type unit SOFC considering current and temperature distributions," Solid State Ionics, Diffusion & Reactions, v 132, n 3-4, 2000, p 297-308.

Minh, N. Q. and Takahashi, T., Science and Technology of Ceramic Fuel Cells, Elsevier Science, Amsterdam, 1995.

APPENDIX

Total volumetric heat transfer rate as expressed in user defined function for FLUENT:

source = ((t_cell_cm*0.00000000085264
*pow(10,(2769.7/C_T(CELL,THREAD)-4.1806)))*pow(C_T(CELL,THREAD),5.0)
+(-t_cell_cm*0.00000330544*pow(10,(2769.7/C_T(CELL,THREAD)-4.1806)))
*pow(C_T(CELL,THREAD),4.0)+(t_cell_cm*0.004848688
*pow(10,(2769.7/C_T(CELL,THREAD)-4.1806))-
0.0000073*R/Faraday*LOG(0.21/1.0e-20))*pow(C_T(CELL,THREAD),3.0)
+(-t_cell_cm*3.188844*pow(10,(2769.7/C_T(CELL,THREAD)-4.1806))
+0.0000000292*EXP(0.00001752*pow(C_T(CELL,THREAD),2.0)
-0.04486*C_T(CELL,THREAD)+31.928)-0.0000146*Del_H2O/Faraday
+0.01415*R/Faraday*LOG(0.21/1.0e-20))*pow(C_T(CELL,THREAD),2.0)
+(t_cell_cm*793.5489*pow(10,(2769.7/C_T(CELL,THREAD)-4.1806))
-0.0000566*EXP(0.00001752*pow(C_T(CELL,THREAD),2.0)
-0.04486*C_T(CELL,THREAD)+31.928)+0.0283*Del_H2O/Faraday
-7.0425*R/Faraday*LOG(0.21/1.0e-20))*C_T(CELL,THREAD)
+0.02817*EXP(0.00001752*pow(C_T(CELL,THREAD),2.0)
-0.04486*C_T(CELL,THREAD)+31.928)-14.085*Del_H2O/Faraday)*10000/t_cell_m

Pressure Drop of Filled Versus Unfilled LCM SOFCs – Here, the pressure drop of the filled LCM is compared to that of the unfilled channel. The filled channel may be needed for either electronic current (in the case of a metal fiber filled channel of a monolith LCM) or ionic current (in the case of the hybrid fuel cell with poor or limited usable electrode area). If the filled channel is selected over the unfilled channel, by necessity or choice, the difference in power required and pressure drop in the two cases should be known.

Previous sections have proved that we have a good approximation of the fiber pore diameter (50 microns), porosity (70%), and internal cell dimension (1.5 mm). We were able to closely correlate experimental results to predictions based on these approximations. The experimental results were compared to analytical predictions based on Equations (25) through (28) (Richardson et al., 2000):

$$\frac{dP}{L} = a_0 V + a_1 V^2 \tag{25}$$

where $\frac{dP}{L}$ is the pressure drop per unit length, V is the superficial velocity, a_0 and a_1 are defined by

$$a_0 = \frac{\alpha S_v^2 \mu (1-\varepsilon)^2}{\varepsilon^3} \tag{26}$$

$$a_1 = \frac{\beta S_v \rho (1-\varepsilon)}{\varepsilon^3} \tag{27}$$

where α and β represent parameters that reflect the geometry and packing of the porous medium. The universal values recommended for these parameters are 5.00 and 0.300 respectively. In Equations (26) and (27), μ is the viscosity of the fluid, ρ is the density of the fluid, ε is the porosity, and S_v is defined as

$$S_v = \frac{4\varepsilon}{d_p(1-\varepsilon)} \tag{28}$$

where d_p is the pore diameter. The experimental results for this sample are plotted along with the analytical prediction in Figure 33.
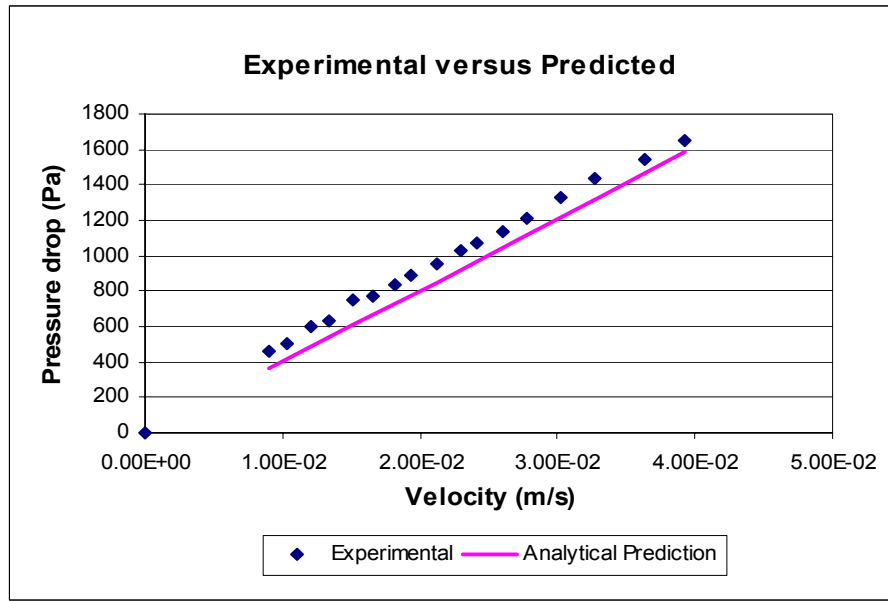
Figure 33. Experimental pressure drop plotted as a function of velocity.

The experimental results and analytical prediction are in good agreement. The solution to the non-filled channel can be expressed as (Roberson and Crowe, 1997),

$$\frac{dP}{L} = f\left(\frac{\rho\,\bar{v}^2}{2\,D_h}\right) \quad , \quad f = \frac{57}{Re} \tag{29}$$

and,

$$Re = \frac{\rho\,\bar{v}\,D_h}{\mu} \quad . \tag{30}$$

Combining Equations (29) and (30),

$$\frac{dP}{L} = \frac{57\,\mu\,\bar{v}}{2\,D_h^2} \quad , \tag{31}$$

where f is the friction, $\bar{v}$ is the average velocity per channel factor, D_h is the hydraulic diameter and is equal to the base dimension for a square, Re is the Reynold's number, and all other terms have been previously defined. The analytical models are now extrapolated to the problem specific to the palm power research.

The proposed fuel cell uses a stack of five 4x4 fuel cells. This results in an effective fuel cell 20 rows high and 4 columns across. The analysis in Figure and Figure is based on the requirement of 0.2 sccm H_2/0.5 sccm air per cm length and per channel for 100 mW/cm^2 and 0.5 sccm H_2/2.25 sccm air per cm length and per channel for 250 mW/cm^2 (Rauch).
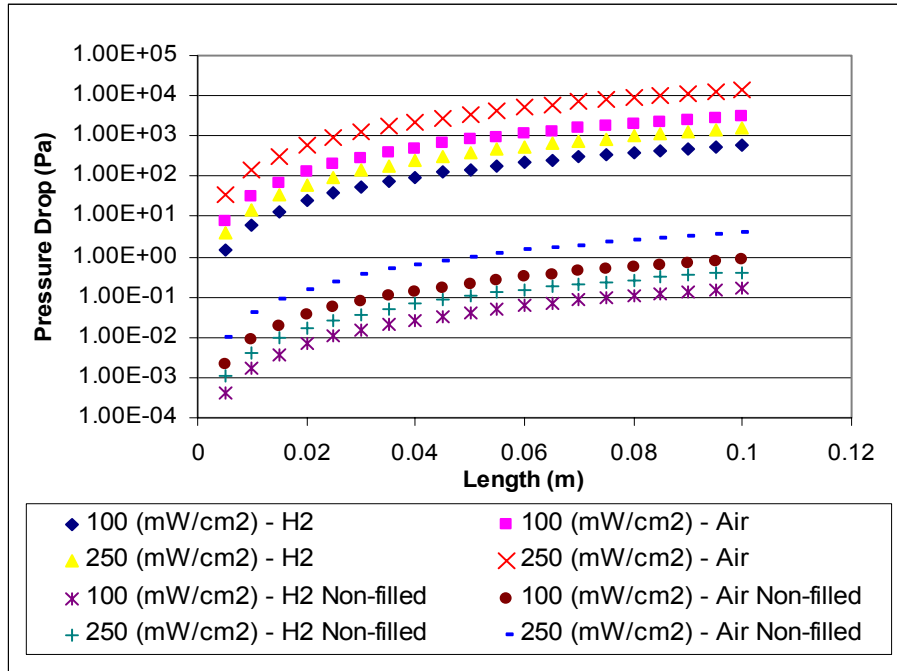

Figure 34. Predicted pressure drop for a 20x4 fuel cell at various lengths, for filled and non-filled channels, and at two levels of power density - 100 mW/cm^2 and 250 mW/cm^2.

Figure 34 shows the pressure drop for the hydrogen and air sides of the fiber-filled and non-filled fuel cell channels for the two levels of power density. As expected, the pressure drop for both power density levels is substantially lower than the pressure drop of the fiber filled case. The difference in pressure drop between the fiber filled and non-filled cases is over three orders of magnitude.

Figure combines the pressure drop from the fuel and air side for each level of power density for both the fiber filled and non-filled channels and calculates the flow work power that is required to drive a 50% efficient fan. Because of the dependence of the fan power required on the pressure drop, the power required differs by the same amount as the pressure drop for the fiber filled and non-filled cases. The predicted required power needed to deliver enough reactants to a 10cm long, 20x4, fiber filled, fuel cell with a power density of 250 mW/cm^2 is approximately one half of a Watt. The power required for a non-filled channel is only 0.1 mW. Clearly, the non-filled channel has a huge advantage with respect to the fan power required to drive the flow. If the non-filled channel can be fabricated, it would be the most likely candidate for successful operation.

However, in the absence of a functional non-filled fuel cell, the fiber-filled fuel cell may be a viable option.
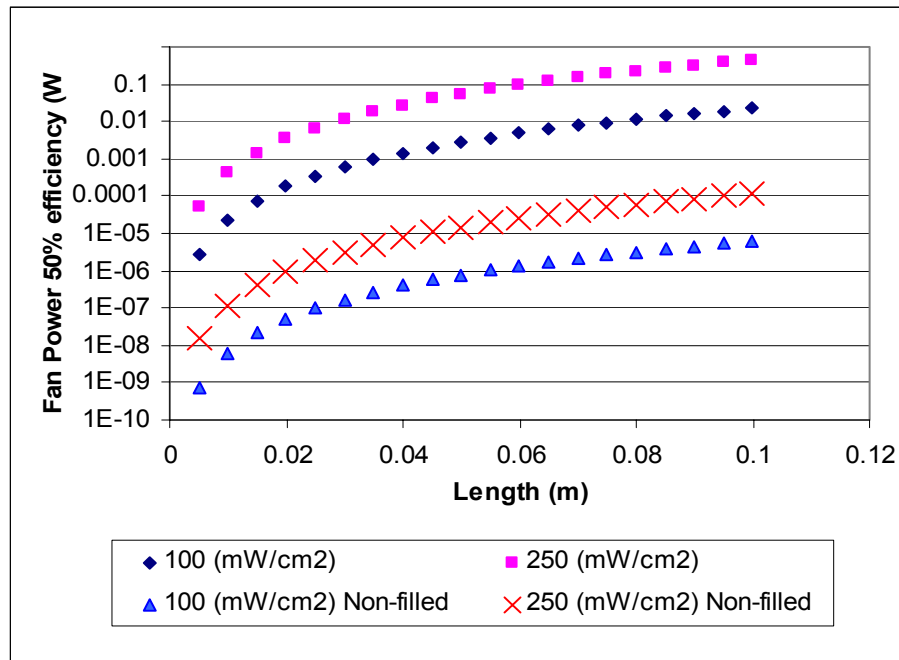

Figure 35. Predicted fan power required for a 20x4 fuel cell at various lengths, for filled and non-filled channels, and at two levels of power density - 100 mW/cm^2 and 250 mW/cm^2 with a 50% eff. fan.

REFERENCES

Richardson, T. J., Peng, Y., Remue, D., 2000, "Properties of ceramic foam catalyst supports: pressure drop," *Applied Catalysis A: General*, **204**, 19-32.

Roberson, J. A. and Crowe, C. T., Engineering Fluid Mechanics, 6th ed., John Wiley & Sons, New York, 1997.

2. Thermo-Mechanical Stress Modeling and Heat Transfer

Solid State Process Designs for SOFCs - Preliminary finite element analysis has shown that the thermal expansion stresses in the out of plane direction (longitudinal direction) can be reduced by approximately 20% through the alteration of the 2-d in-plane (cross sectional) geometry. Specifically, by adding 45-degree offsets shown in Figure 36, a more compliant structure than the square cell design is produced. The added compliancy results in the general reduction of longitudinal stresses on the order of 20%. The reduction of thermal cycling stress is very important because of its non-linear relationship with crack formation.
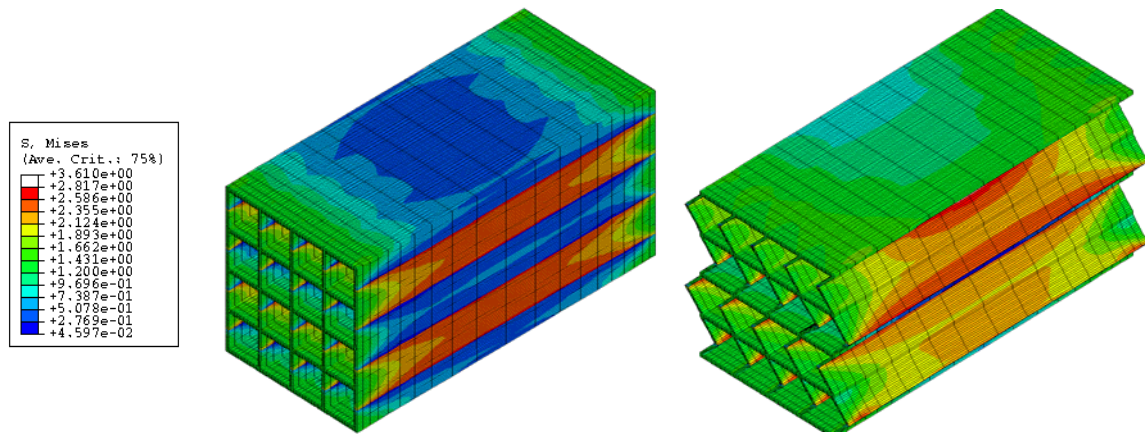
Figure 36. In-plane 45-degree joints can produce a more compliant honeycomb design.

Comparison of in-plane crack propagation in various fuel cell configurations – Numerical computation (Finite Element Approach) was used to study the driving force for in-plane crack propagation, the elastic energy release rate, for realistic size scale LCM cross sections. Different cell shapes were considered for the LCM. Due to the differences in expansion coefficient, stiffness and strength of the metallic and ceramic phases, cracking may occur due to high temperature gradients and thermal expansion/property mismatches at the interconnected interfaces during the manufacture and application of LCM fuel cell assemblies. The literature does not address crack problems for these kinds of bimaterial cellular structures. These calculations consider thermoelastic fracture mechanics problem with assumption of no changes of material properties with the temperature.

Two-dimensional (in-plane) solid element FEM models have been established for square cell and zigzag cell LCMs cross sections. The size of the structure is 4x4 mm^2, the cell wall thickness is 0.2 mm for the square cell and 0.166 mm for the zigzag cell, so the relative densities of both two models are the same, i.e., 20.0%. Every cell wall has four layers of quadratic 8-noded plane-strain elements. Considering the heat exchange within fuel cell structure, one can envision a transient temperature field state for start-up and shutdown phases of operation, and steady state otherwise. In this initial study, we consider the steady state phase and assign constant temperature boundary conditions. A

thermal analysis was performed to determine the temperature field distribution in the fuel cell structure, and the temperature distribution was subsequently coupled with a thermal stress calculation. Finally the cracks (cell-wall fracture) are inserted in areas of maximum stress concentration and cell walls were removed one by one to model progressive fracture of cell walls along the interface of two materials. In this way, we calculate the strain energy release rate of the structure with crack extension, the crack driving force.

In the FE calculation, the material properties parameters are: (1) ceramic phase, Young's modulus = 190.0 GPa, Poisson's ratio = 0.22, thermal expansion coefficient = 0.0001, specific heat = 5.0×10^8 J/kg-K, conductivity = 3.1 W/m-k; (2) metallic phase (steel), Young's modulus = 210.0 GPa, Poisson's ratio = 0.28, thermal expansion coefficient = 0.0003, specific heat = 20×10^8 J/kg-K, conductivity = 25.0 W/m-K. The boundary conditions are: - stress/displacement analysis, four sides traction free, thermal analysis-left side and right side have imposed temperature and top side and bottom side are insulated. The results for square cell layered hybrid structures are shown in Figure 37. Because only elastic properties are considered and the interface is assumed to be perfectly-connected, the computed stress level exceeds expected actual levels, perhaps significantly. Yielding of the metallic phase will be considered in future work and the interface fracture strength will also will be introduced into models to portray the actual situation more realistically. The crack development indicates that the crack initiation and propagation may grow primarily in mode II due to the shear thermal stress near interface areas. Because of the stress concentration in irregular zigzag structure (not shown), the elastic energy release rate and strain energy density are much higher than that of square cell.
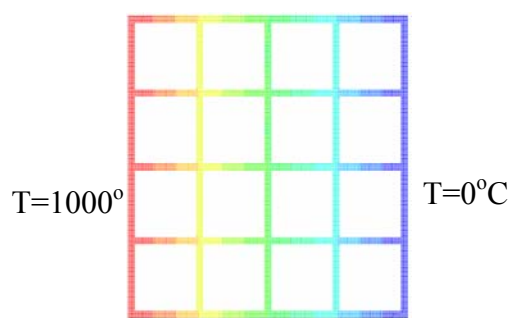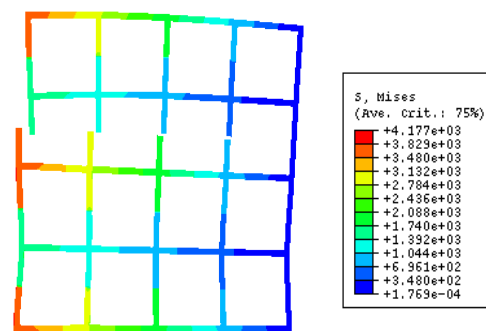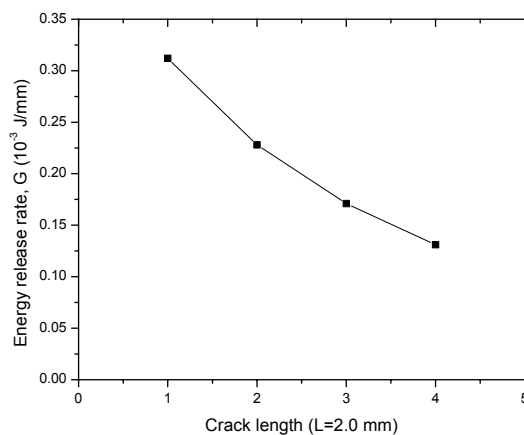
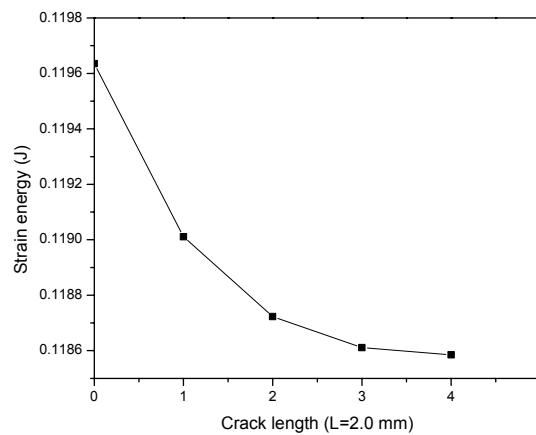(a) Temperature distribution
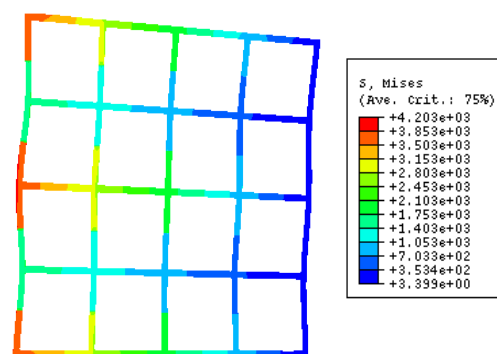
(b) Thermal stress in intact case
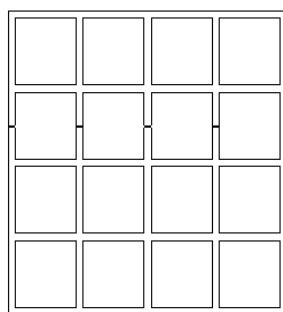
(c) Introduction of crack

(d) Deformation after damage

(e) Energy release rate during crack propagation

(d) Strain energy change

Figure 37. FEM calculations for in-plane cracks in square cell fuel cell LCM structures with temperature gradients.

CTE Mismatch Effects for LCM Fuel Cell Stacks - During design and manufacture of SOFC stacks, minimization of thermal stress should be undertaken to avoid exceeding the strength limits of LCM ceramic and metallic components, as well as their interfaces. In this work we use finite element modeling to predict the residual stress levels due to different Coefficient of Thermal Expansion (CTE) of YSZ ceramic and interconnect alloys. The purpose is to estimate thermal stress magnitudes for slowly varying temperature histories due to CTE mismatch between ceramic and interconnect fuel cell components.

Sets of alloys are considered for metallic interconnect materials sandwiched between ceramic electrolytes in order to reduce the CTE mismatch between them. They are alloys with primary elements Ni, Fe, Cr, e.g. Fe(5-15%)Cr(0-15%)Ni and Fe(30-40%)Ni(5-10%)Cr and Ni(10-20%)Cr(10-15%)Co(5-10%)Mo. We expect them to exhibit similar CTE to that of YSZ ceramic. Experiments are being conducted for the purposes of measuring CTE and various alloy mechanical properties. In this study, we use finite element models to study the thermal stress distribution due only to CTE mismatch for an assumed 4x4 hybrid fuel cell stack. Since we consider cool-down from the stress-free state, this study may provide information relevant to potential for residual thermal stress during the manufacturing process, with the proviso that here we use very simple, linearly temperature dependent material properties for the thermoelastic calculations.

Table 5. Material properties of interconnect alloys and ceramic electrolyte from the literature.

Material	Young's Modulus	Poisson's Ratio	CTE	Temperature
In 617 (metal-1)	*210 000*	*0 31*	**11 6 x10^{-6} /^{o}C**	**25 ^{o}C**
	129,000	*0.31*	**16.3 x10^{-6} /^{o}C**	**1200 ^{o}C**
Invar 36 (metal-2)	*150,000*	*0.3*	**1.0 x10^{-6} /^{o}C**	**25 ^{o}C**
	100,000	*0.32*	**4.0 x10^{-6} /^{o}C**	**1200 ^{o}C**
YSZ (ceramic)	*200,000*	*0.23*	**8.0 x10^{-6} /^{o}C**	**25 ^{o}C**
	200,000	*0.23*	**10.0 x10^{-6} /^{o}C**	**1200 ^{o}C**

Having assigned the above material properties for constituents of a co-extruded LCM fuel cell stack component with 4x4 cells and assuming a perfect structure with perfect bonding of metal-ceramic interfaces, the thermal stresses were calculated using the finite element code ABAQUS [1] and plotted as contours (stress unit: Pa) in Figures 38 and 39 for Inconel-YSZ and Invar-YSZ stacks. The temperature is reduced from a value of 1200°C to room temperature within the entire LCM structure (uniform temperature through entire LCM structure at each stage of cool-down). The specimen model size is assumed at 6mm x 6mm x 60mm, with a cell wall thickness of 120 microns.

In Figures 38 and 39, contours of various components of stress are plotted for hybrid LCMs. As expected, the stress component σ_{33} along the cell longitudinal direction is

highest among all the normal stress components. The shear stress component σ_{23} along the cell wall interfaces near the ends of the stack (edge effect) is largest among the shear stress components. It is noted that the stress may becomes larger at the cross-joints within same materials, which is because those areas thermal deformation is limited by connected structures and they are out of our interest for the study of metal/ceramic CTE mismatch. However, all these stress components are below 1 MPa, which indicates that in the absence of temperature gradients (e.g. slow heating or cooling) the thermal residual stresses that might drive fracture are minimal. Of course, the caveat here is that we have not considered shrinkage due to reduction and sintering of the constituents in this simple study, which are likely to introduce much more significant levels of residual stress and damage into the structure as it cools down during processing; indeed, this work is underway but is much more complex. We can say that in terms of the operation of an as-processed LCM stack, these calculations suggest that only the thermal shock during the heat-up or cool-down phases or presence of intense thermal gradients under steady state operation (which can be addressed in stack design) are of much more concern from the standpoint of mechanical integrity and durability.
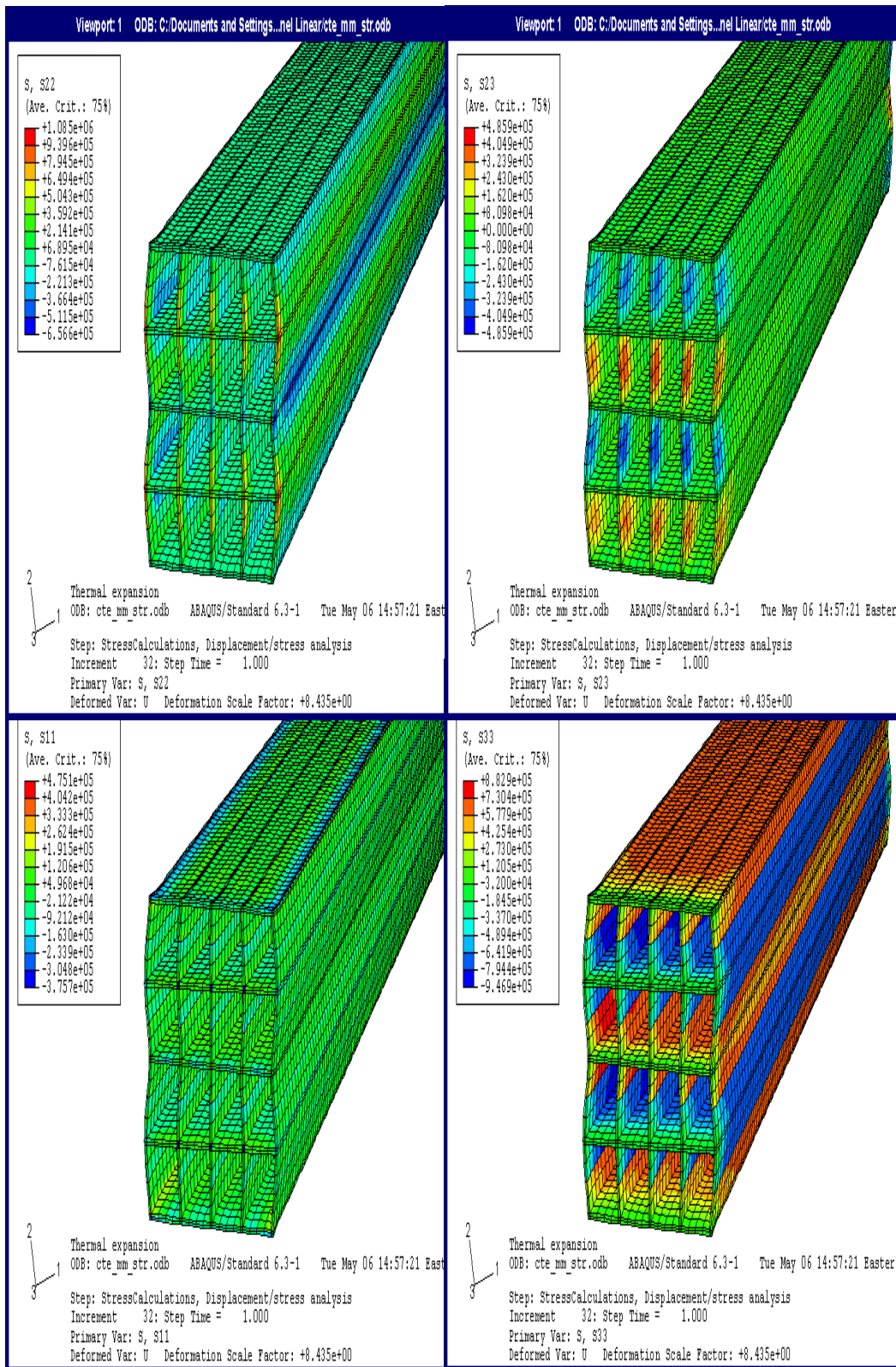
Fig. 38 Distribution of various thermal stress components within In617-YSZ LCM Fuel cell stack.
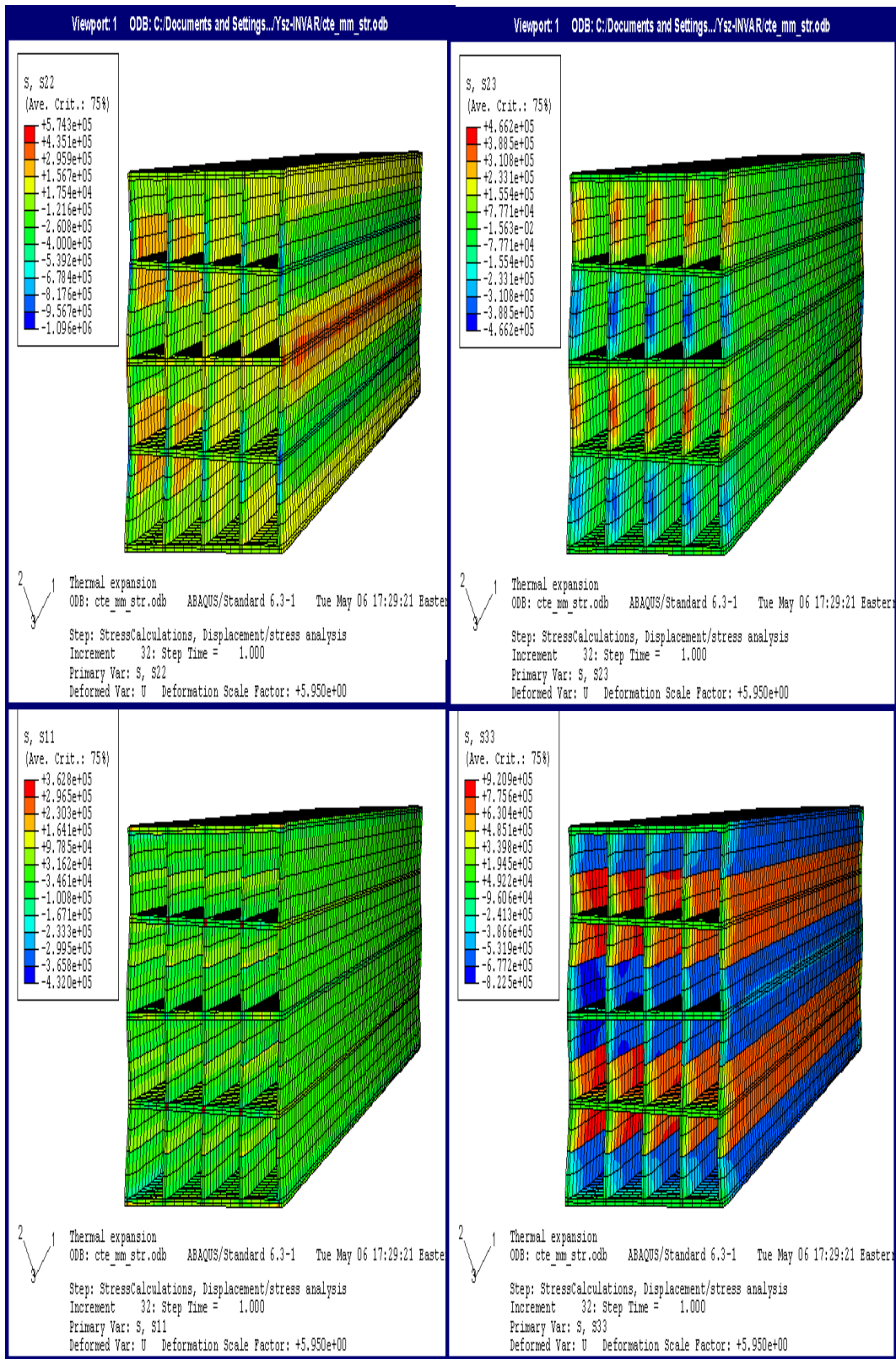
Fig. 39 Distribution of various thermal stress components within Invar36-YSZ LCM Fuel cell stack.

We next select some particular positions within the YSZ ceramic cross-section of the LCM fuel cell stacks, as shown in Figure 40, at which to plot selected stress components along the length to aid visualization of the stress distribution, as shown in Figures 41 and 42.
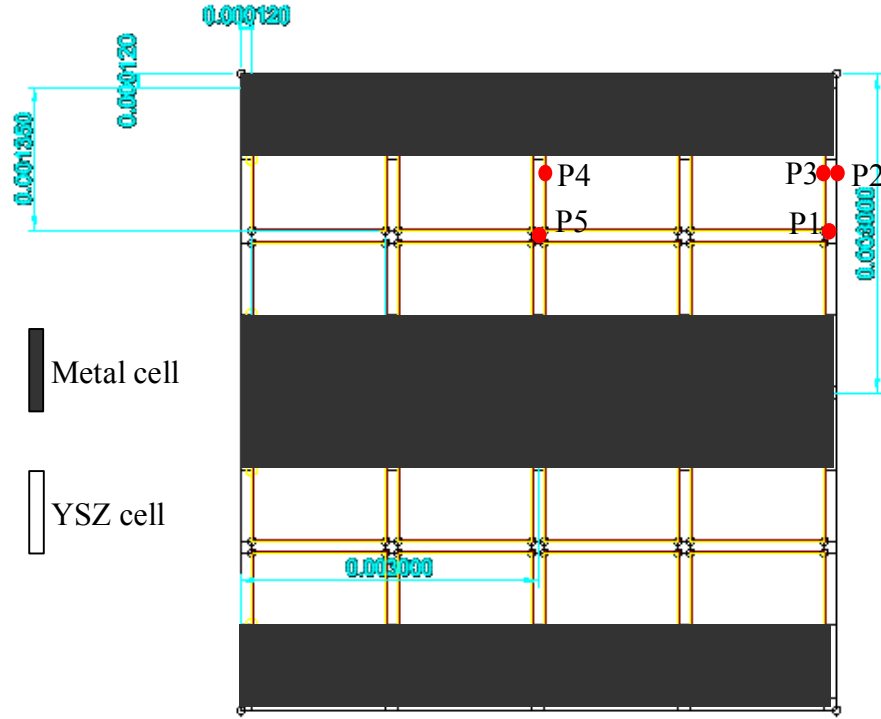

Figure 40. Location of selected positions in LCM cross-section for plotting stress components along the length in Figs. 10-11.

In Figures 41 and 42, we focus on the stress distribution along the length for points 2, 3 and 4 and points 1 and 5 for reference. For points 2-4, the shear stress σ_{23} shows exactly the same distribution with maxima at the ends. For the axial stress σ_{33}, the stress distribution is mainly affected by structural constraint, so the interior points exhibit somewhat higher stress levels. It bears emphasis that sign of stress is opposite between Figure 41 and 42, in particular negative (compressive stress) σ_{33} within YSZ/In617 LCM, and positive (tensile stress) σ_{33} within YSZ/Invar36 LCM. The same effects are observed for the shear stress. This arises because the CTE of In617 is larger than that of YSZ while the CTE of Invar 36 is smaller than that of YSZ.
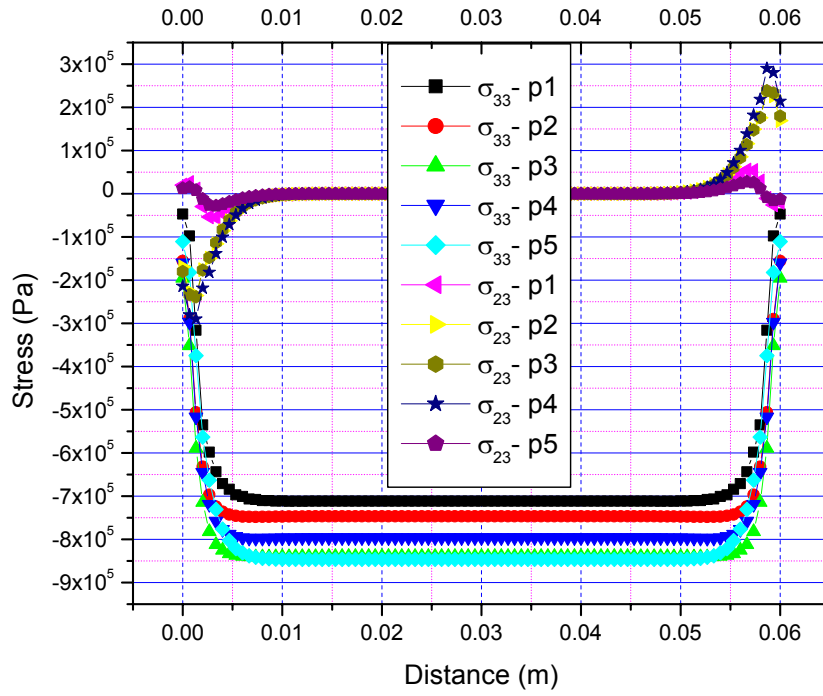
Figure 41. Thermal stress components versus distance along the stack length for five points. IN617-YSZ LCM fuel cell stack.
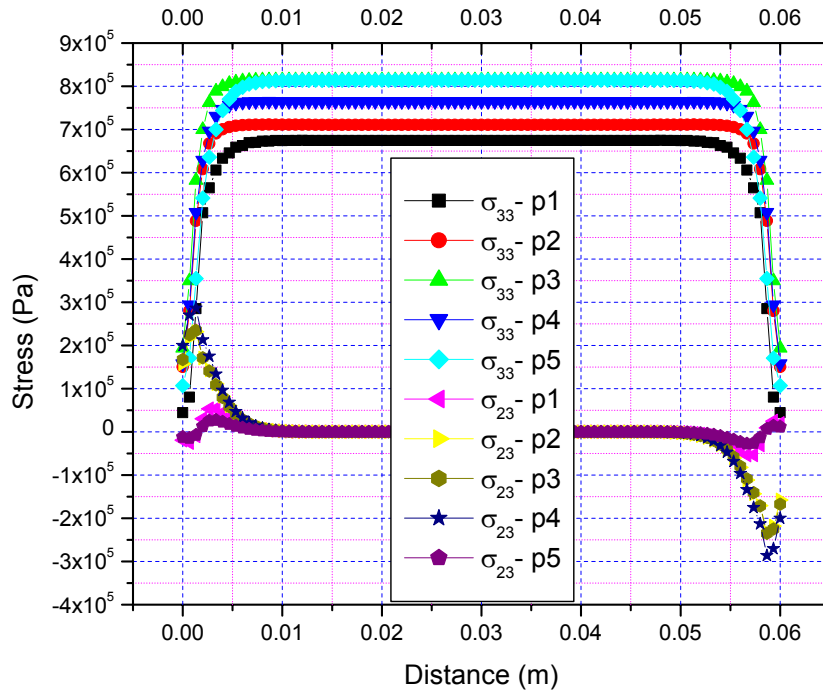

Figure 42. Thermal stress components versus distance along the stack length for five points. Invar36-YSZ fuel cell stack.

Improved estimates of residual stresses from cool-down during fabrication of hybrid honeycomb structure - Several improvements have been made to the simple elastic model of the residual manufacturing stresses. Previously, the cool down period after manufacturing had been modeled as a totally elastic stress problem, beginning at the sintering temperature of 1000°C and ending at room temperature. However, the elastic model produces unrealistically high stresses in the ceramic. Of course, the metal would yield and the ceramic would likely also fracture at these high stresses. Plasticity was implemented in the model to more accurately reflect metal deformation at high stress. Also, practical variations in geometry of the model were explored to determine the effect on residual stresses. Finally, due to test results obtained by Scott Eisle (discussed later in this report), more accurate material properties were used.

Previous analysis showed much of the CTE mismatch stress was due to bending forces in the honeycomb structure. Therefore, reductions in the residual stresses are possible by changing material properties or by optimizing the honeycomb structure. The residual stresses due simply to CTE mismatch of the two materials can be modeled as a long rectangular laminate structure.

The stress in Figure 43 is about half the maximum stress in a complete honeycomb structure. Bending in the ceramic section accounts for the high stresses. Since the measured yield stress of Fe39Ni8Cr is around 64MPa, plasticity must be modeled.
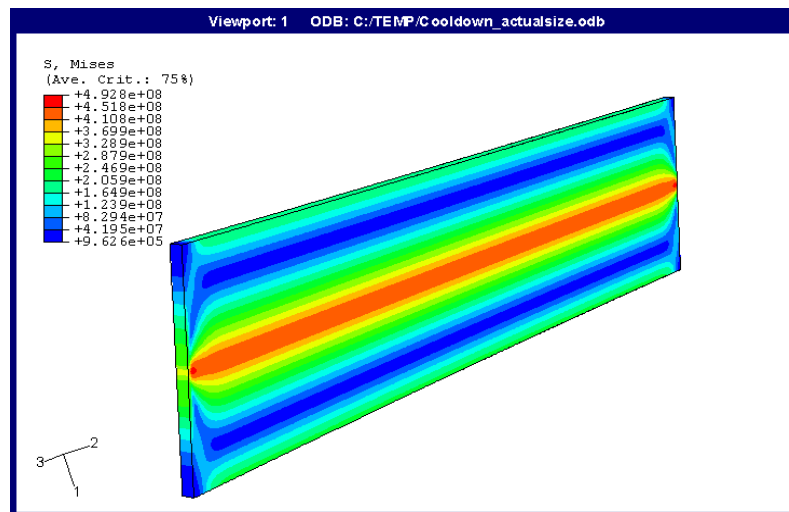

Figure 43: Stress from elastic strain in a laminate of YSZ and Fe39Ni8Cr

Several different cases were devised to explore the effects structure on fuel cell residual stresses. They are all 4x4 cell structures. Material used in the interconnect of the model was changed from earlier analyses to Fe39Ni8Cr, to reflect the latest manufacturing specimens. The cases examined are as followed:

Case 1: Control case with dimensions: 4x4, 8.6mm x 8.6mm overall, 2mm x 2mm cell, 120μm wall thickness
Case 2: Amount of ceramic was reduced
Case 3: Amount of ceramic was increased
Case 4: 4.6mm x 12.6mm overall, 1mm x 3mm cell
Case 5: 12.6mm x 4.6mm overall, 3mm x 1mm cell
Case 6: Graded cell width of 1mm, 3mm, 3mm, 1mm. Overall dimensions unchanged.

The maximum stresses in different parametric results are presented in Table 6. The models used YSZ and Fe39Ni8Cr data from a combination of sources, including recent stress vs. strain and CTE data from testing at Georgia Tech.

Table 6: Peak stresses obtained for different geometric cases.

Model Case	ELASTIC		PERFECTLY PLASTIC		STRAIN HARDENING	
	Peak Stress (MPa)		Peak Stress (MPa)		Peak Stress (MPa)	
	Fe39Ni8Cr	YSZ	Fe39Ni8Cr	YSZ	Fe39Ni8Cr	YSZ
Case 1	656	1034	66.4	365	88.1	278
Case 2	656	856	66.4	170.5	89.2	224
Case 3	645	751	66.4	196	87.5	225
Case 4	549	745	66.4	237	81.7	258
Case 5	913	1345	66.4	383	102.6	453
Case 6	568	874			88	287

The objective of these models was to evaluate easily manufactured alternatives to the current square honeycomb configuration. However, as Table 6 shows, moderate variations in geometry do not appear to have much impact on peak stress levels. The ductility of the metal most likely distributes the stress well in each case. Most importantly, the inclusion of plasticity for the metallic constituent has led to results much closer to the actual strength of the ceramic. Instead of exceeding 1GPa, the stress is 200 MPa. The residual stress after plastic strain hardening can be used in combination with operating stresses to better determine the life of the fuel cell under operating conditions.

Process-Induced Residual Stresses and Thermal Shock - When a ceramic-metal laminate is cooled to room temperature, residual stresses are present due to the thermal expansion mismatch between the two materials. The origin of most fracture events, due to CTE mismatch, is cracking at either end of the laminate (He, 1991). The high probability of edge flaws, combined with the elevated stresses due to edge effects, contribute to fracture in this region. For cracking near the interface or near the edge, Mode I and Mode II fracture are most important (He, 1991). The dominant stress contributors for these cases are σ_{22}, for Mode I (opening), and σ_{23}, for Mode II (in-plane shear).
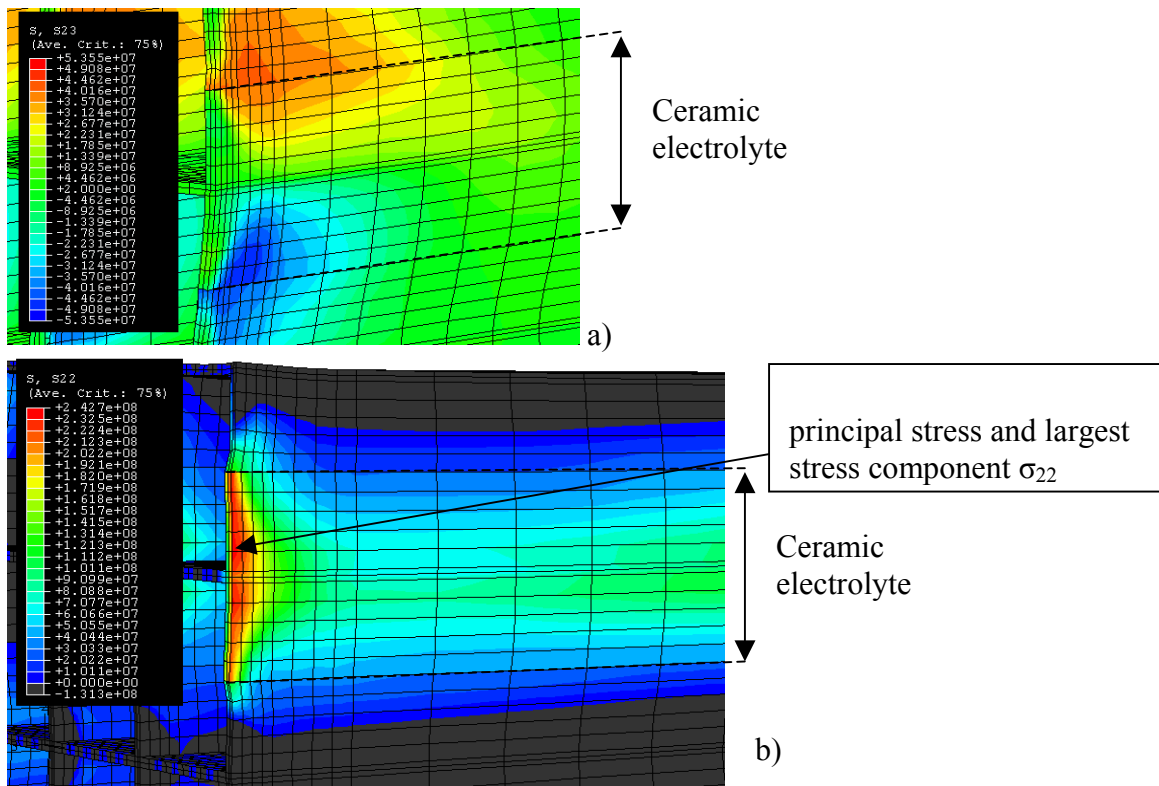
Figure 44. ABAQUS model showing residual stresses at the edge of the ceramic for a 4x4 cell array, 3 cm long honeycomb, cooled from stress-free temperature (1000°C) to room temperature (25°C): (a) In-plane shear stresses contributing to Mode II failure (Pa), (b) Tensile normal stresses that would contribute to crack opening (Pa)

The dominant stress in the ABAQUS model is the normal stress, σ_{22}. The location of the maximum stress, shown in Figure 44, suggests that fracture within the ceramic, as opposed to at the joint, is a distinct possibility. However, elevated stresses exist all throughout the edge of the ceramic. The quality of the joint and the distribution of flaws in the ceramic would determine the location of crack initiation for a particular case. Also, metal plasticity and CTE substantially influence the driving forces of crack initiation (He, 1991).

During the operation of the fuel cell, rapid start-up and shut-down may be necessary. Rapid temperature change leads to a large temperature difference between the surface of a material and the mean body temperature. If the surface is much cooler than the body, the surface is in a state of tension. For rapid heating, the surface is in a state of compression. Since tension leads to crack growth, and heating to crack closure, rapid cooling is more severe than heating.

Thermal shock is more important in the ceramic than in the metal because of the high temperature gradients in the ceramic on startup (observed in the finite difference thermal

model).   Also, ceramics typically have low resistance to thermal shock and brittle behavior. Resistance to thermal shock can be estimated by (Hasselman, 1970)

$$R = \frac{\sigma_t (1-\nu)}{\alpha E}$$
(32)

where σ_t is the tensile strength, ν is Poisson's ratio, E is Young's modulus, and α is the coefficient of thermal expansion. The R value measures the instantaneous difference between the surface temperature and the core temperature at which initiation of small cracks would be expected.

A separate equation has been derived for the maximum rate of cooling for a flat plate before failure (Hasselman, 1970):

$$\left(\dot{T} \right)_{max} = \frac{3\sigma_t (1-\nu) d}{\alpha E b^2}$$
(33)

where b is the thickness of the plate and d is the thermal diffusivity of the ceramic. By this approximation, the thin walls of the honeycomb result in a very large acceptable rate of cooling.

Of course, evaluation of thermal shock in the honeycomb requires finite element analysis that provides tensile stresses in the ceramic electrolyte and metal interconnect-electrolyte bond region, which are presently underway.

REFERENCES

He, M.Y. and Evans, A.G., "The Strength and Fracture of Metal/Ceramic Bonds," Acta Metallurgica et Materialia, 39 (1991) 1587-1593.

Hasselman, D.P.H., "Thermal Stress Resistance Parameters for Brittle Refractory Ceramics: A Compendium," Ceramic Bulletin, 49 (1970) 1033-1037.

Transient Thermal Stress Analyses

I. Model Setup - A transient thermal-stress analysis was performed on a 4x4 unit celled hybrid SOFC, composed of a YSZ electrolyte and an $Fe_{39}Ni_8Cr$ interconnect. The overall dimensions were 0.86 x 0.86 x 3cm. The temperature necessary to initiate the electro-chemical reaction is about 910K. Therefore, the inlet air temperature was pre-heated to 980K for this example (at 6.24e-5 kg/s total flow). The fuel inlet temperature remained at 300K at a mass flow rate of 2.784e-8 kg/s (total flow). The resulting power output was 1.16W at a power density of 0.52W/cc.

II.1. Finite difference transient temperature field - To analyze the finite difference results, the average electrolyte element temperature at the fuel inlet is plotted over a

range of time, Figure 45. The side of the electrolyte nearest the cold fuel inlet should take more time to heat-up compared to the front of the electrolyte.

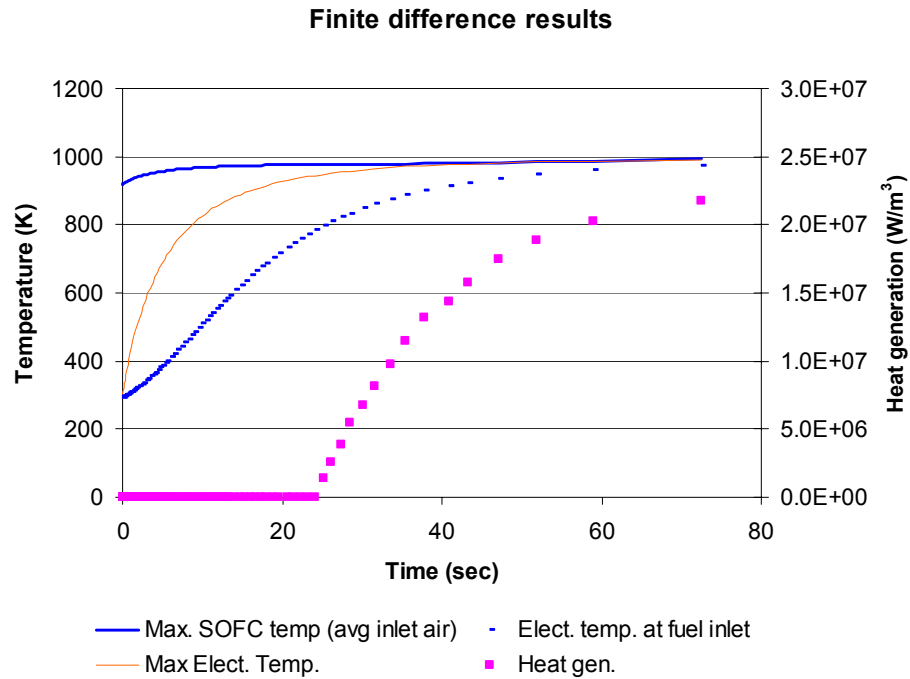**Finite difference results**

Figure 45. The temperature of the bottom electrolyte, near the fuel inlet, represents heating in the electrolyte during startup.

The finite difference results are interpolated by ABAQUS. Note that air is flowing in the front face as shown Figure 46. Also, to capture the subtle temperature contour, the maximum and minimum spectrum values in each slide are recalculated.
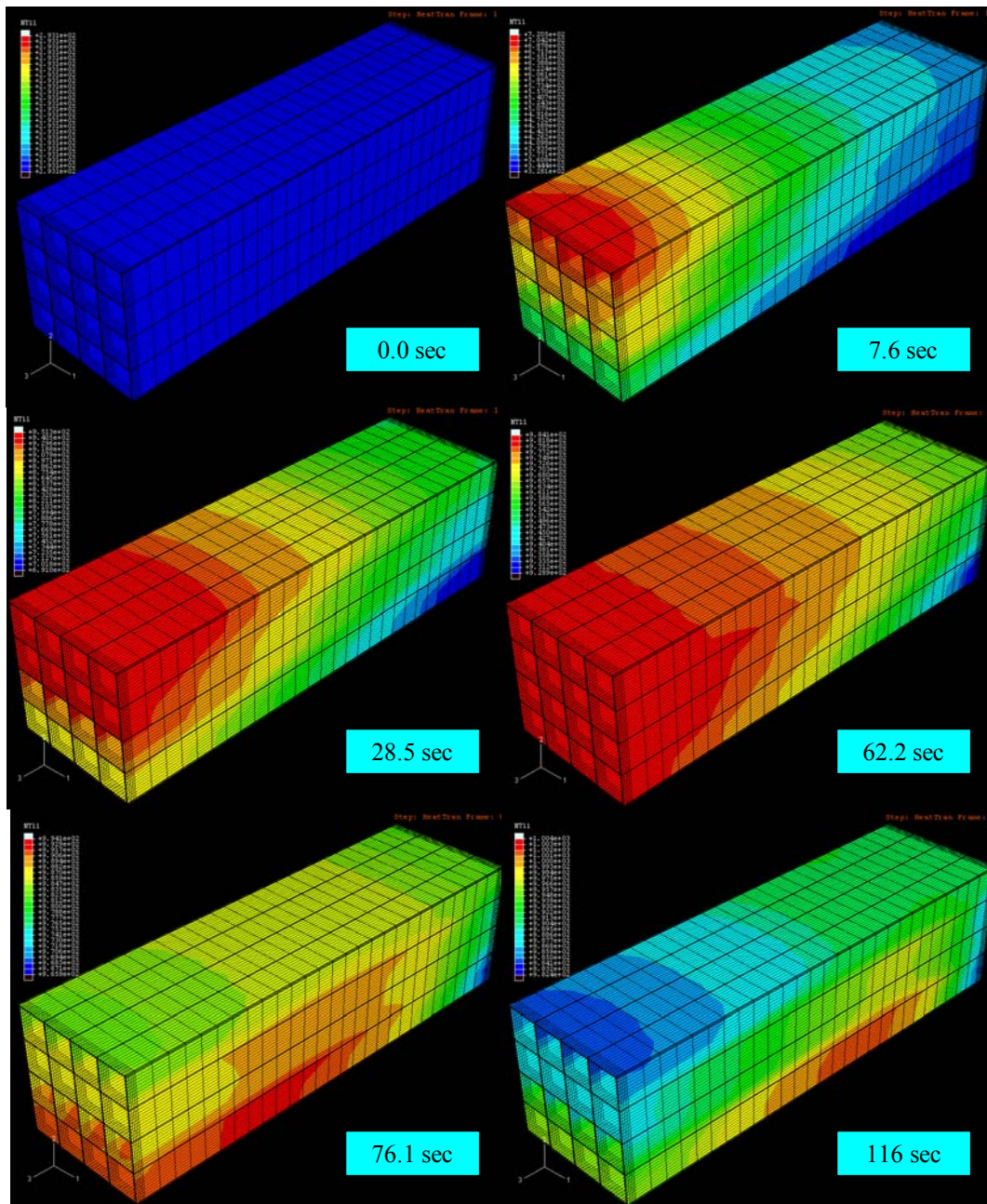
Figure 46. The temperature distribution at start-up is interpolated from the results of the finite difference code. Moving left to right and top to bottom: 1) The fuel cell begins at RT. 2-3) Hot inlet air heats the structure. 4) The chemical reaction begins to heat the electrolyte. 5-6) The air temperature is now below the operating temperature, resulting in convective cooling.

II.2. Contour plots of stresses - For simplicity, the edge of the ceramic will be presented, Figures 47 and 48, since the critical stresses rely on the edge effects in the honeycomb. Stress in the y-direction is most important because in general, the largest component of stress is at the edge and it is the most important for cracking in the ceramic. The maximum stress during cool down occurs slightly above room temperature because at lower temperatures, the CTE of the metal is lower than the ceramic, thus relieving stress upon further cooling.
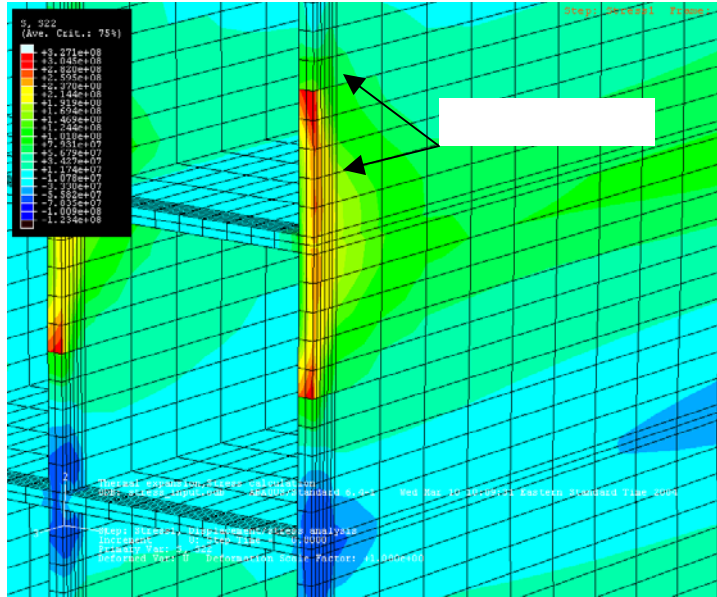
Figure 47. During cool down, maximum stress (tensile) occurs at two spots in the ceramic at around 400K.
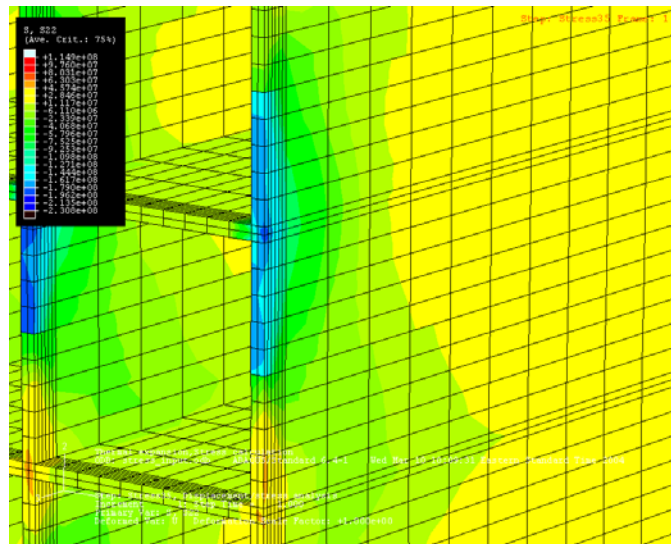
Figure 48. At steady state operating temperature, the ceramic is put in compression due to the plastic deformation of the metal.

II.3. Line graphs of stresses - A line graph, Figure 49, shows the path of stress including cool down and transient start-up. Again, one particular node is evaluated for simplicity. The node chosen is on the joint of the ceramic and metal, as shown in Figure 49.
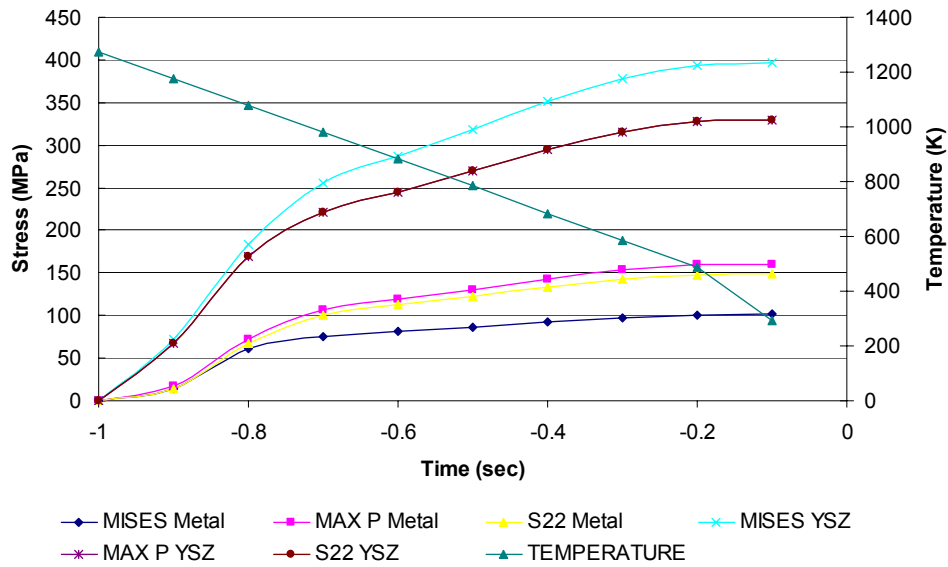
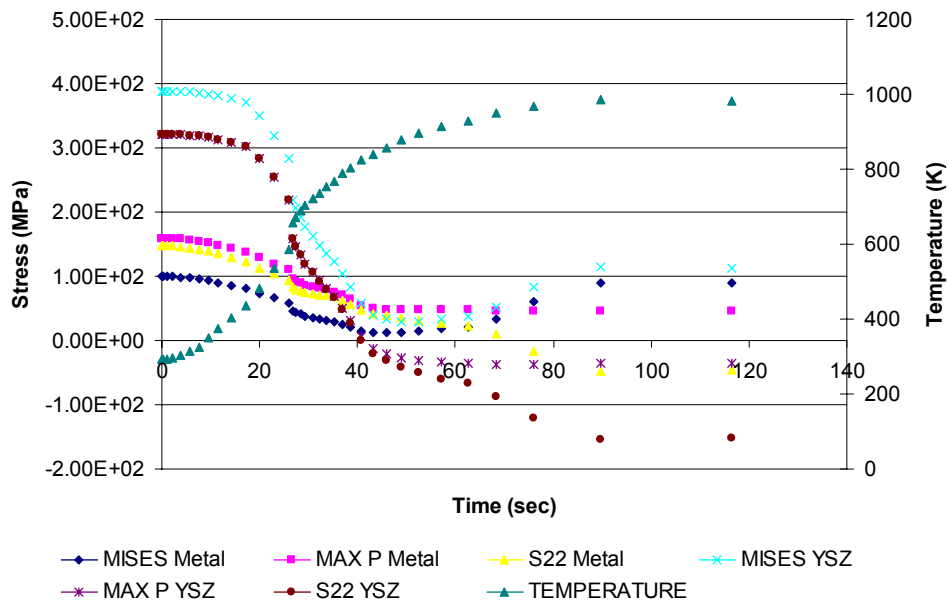**Stress/temp vs. time at the joint of an operating SOFC**

Figure 49. Stress during operation of hybrid SOFC.

III. Failure - The metal in this first cycle does pass the UTS as measured by Scott Eisle (250 MPa). MOR data has been recorded for very dense 8% YSZ (Du, Sammes et al. 2003). The corresponding MOR for porous YSZ, such as the kind currently fabricated in the hybrid SOFC, should be substantially lower. However, even using MOR data from very dense YSZ, the ceramic fails as it is cooled from relaxation temperature, Figure 50.
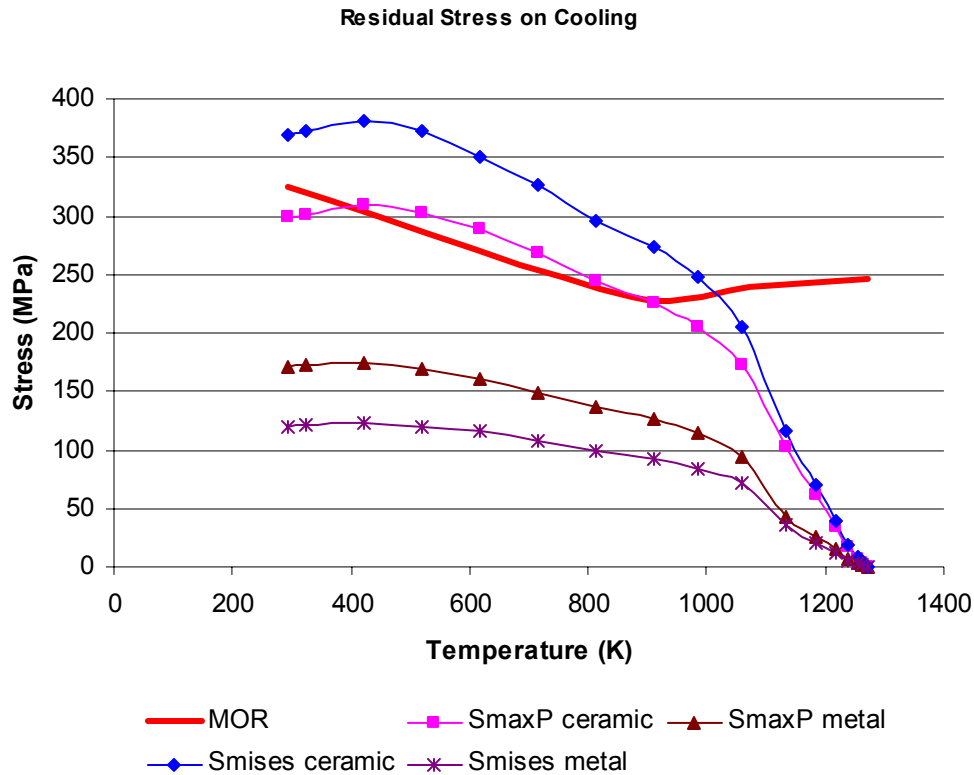

Residual Stress on Cooling

Figure 50. First signs of failure occur above 900K during cooling directly following manufacturing.

II.2 Example with no CTE mismatch - One of the focuses of manufacturing is to eliminate CTE mismatch by customizing the metal expansion. However, even under these ideal conditions, the temperature gradients during start-up cause a build up of stresses. The same conditions were used from earlier analysis with the exception that the metal CTE was set equal to the ceramic. The most severe stresses occur during the rapid heating by the inlet air, Figure 51. Gradual heating may be used to mitigate these stresses, instead of an instantaneous injection of 980K air.

REFERENCES

Du, Y., N. M. Sammes, et al. (2003). "Extruded Tubular Strontium and Magnesium-Doped Lanthanum Gallate, Gadolinium-Doped Ceria, and Yttria-Stabilized Zironia Electrolytes: Mechanical and Thermal Properties." Journal of the Electrochemical Society **150**(1): A74-A78.

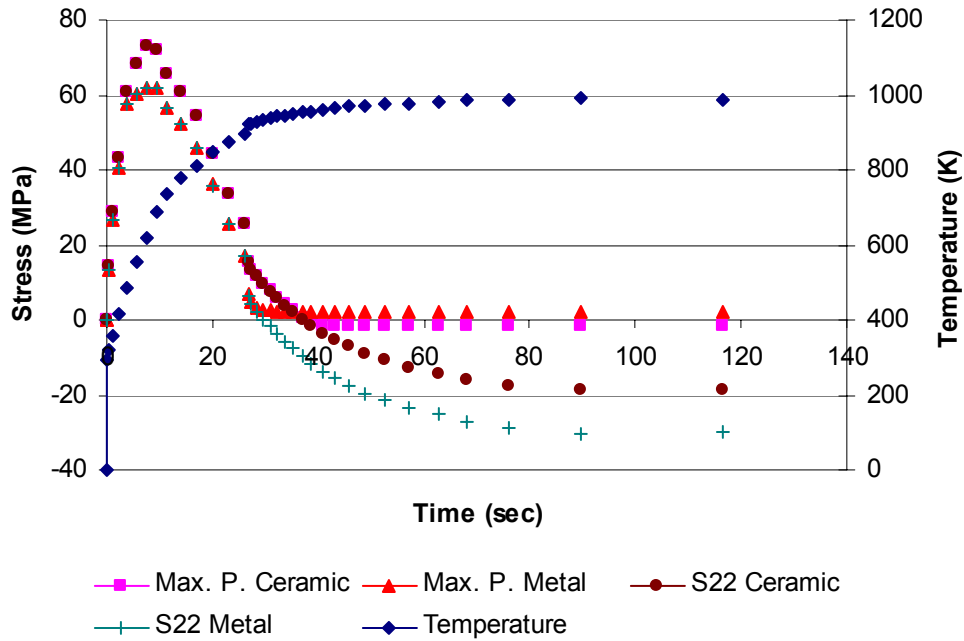**Transient stresses during operation for materials with identical CTEs**

Figure 51: Stress in the joint at the air inlet.

Modifications to the Hybrid LCM Geometry to Mitigate End Effects - Prior thermal stress analysis of the rectangular-celled hybrid LCM SOFC has revealed stress concentrations near the joint at the free ends. In manufacturing, it was noticed that delamination and cracking of samples appeared to be reduced by machining the front and back ends of the honeycomb at an angle. To support and understand these observations, the residual stress of a sample with a 45° cut was analyzed using the finite element code ABAQUS to determine how the stress concentration at the joint may be effected with the elimination of 90° edges at the joints. The original SOFC model ends were machined to two different angles shown in Figure 52. Fe39Ni8Cr and YSZ material properties were used.
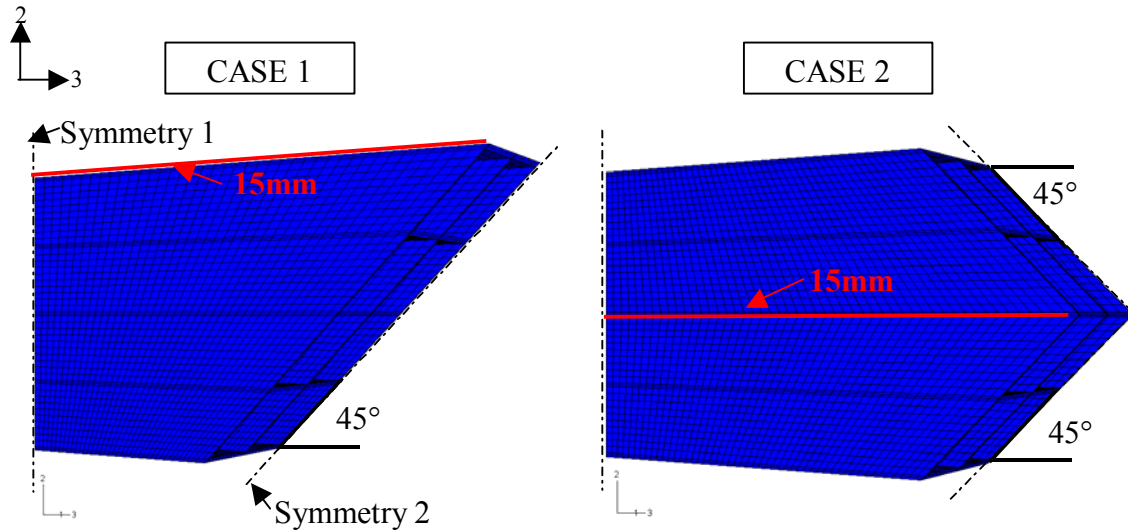
Figure 52: The end of the honeycomb model was cut at a 45° angle. The models used reduced integration quadratic elements. Two planes of symmetry were used to reduce the number of elements in the residual stress model to a quarter of the original mesh.

As expected, the stress concentration at the joint was changed due to the 45° angled intersection of the ceramic and metal. Case 1 is a non-symmetric laminate and case two is symmetric, i.e., Case 1 will bend concave up (2-direction). As a result, the residual stress contours arising from cool down with temperature dependent elastic and plastic properties (neglecting viscous relaxation) will differ significantly. Figure 53 shows the residual stress results.

Close inspection of the results reveals that both of the angled models appear to eliminate the singularity present in the original model at the free end near the joint of the ceramic and metal. However, a stress concentration was present in the top ceramic layer of Case 1 near the front end. The concentration is localized to the edge and does not extend up to the joint. Case 2 appears to redistribute the stress more equally (due to symmetry) than Case 1. Please note that the different cases are not rendered using the same color coded scale for stress level. The maximum principal stress along the joint is shown graphically for the three cases in Figure 54.
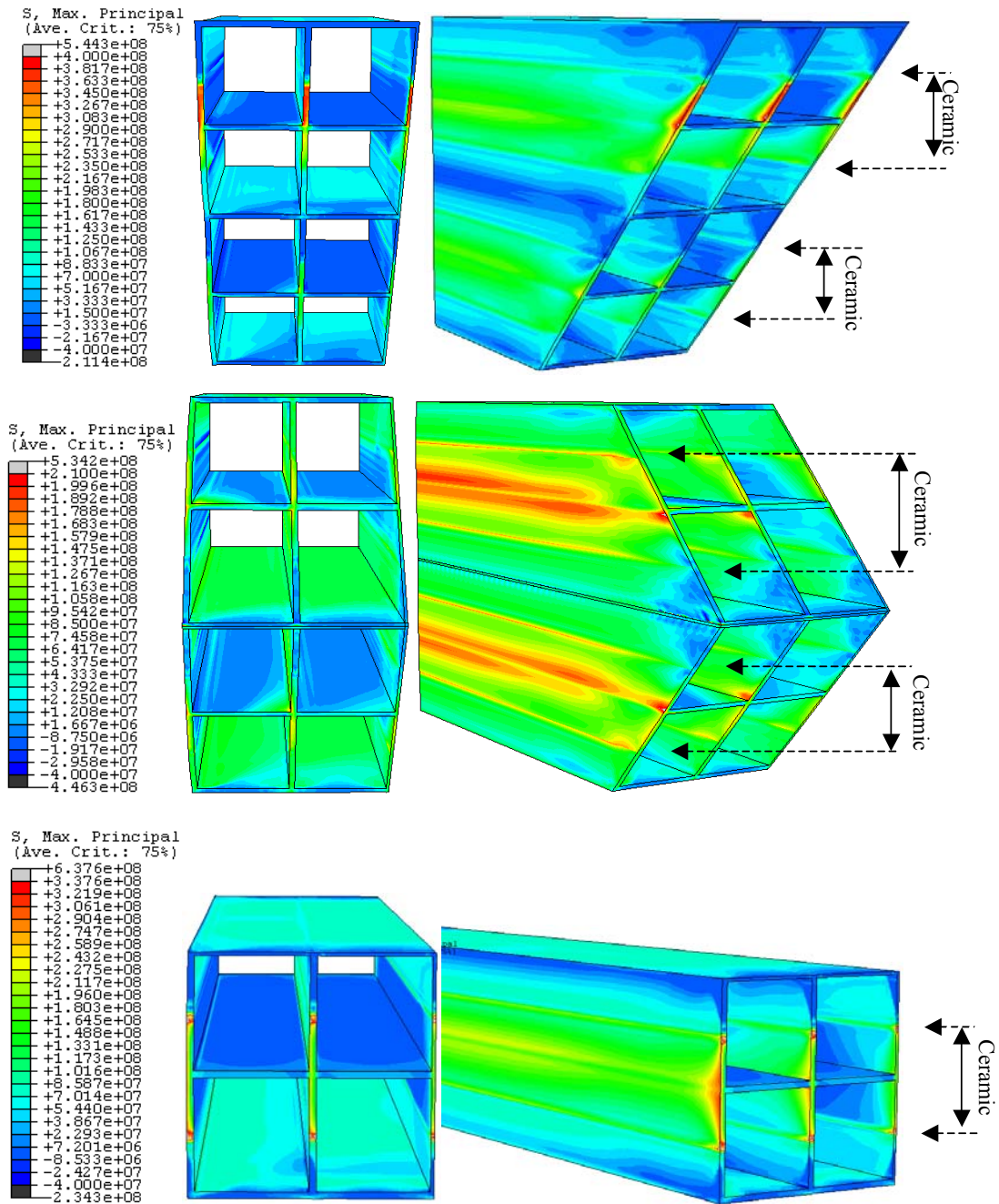
Figure 53: Residual maximum principal stress for Case 1 (TOP), Case 2 (MIDDLE) and the original honeycomb model (BOTTOM). A different symmetry condition was used for the original model as evident by the 2x2 cell structure, and the overall length was only 20mm in the original case (compared to 30mm in Case1 and Case2).
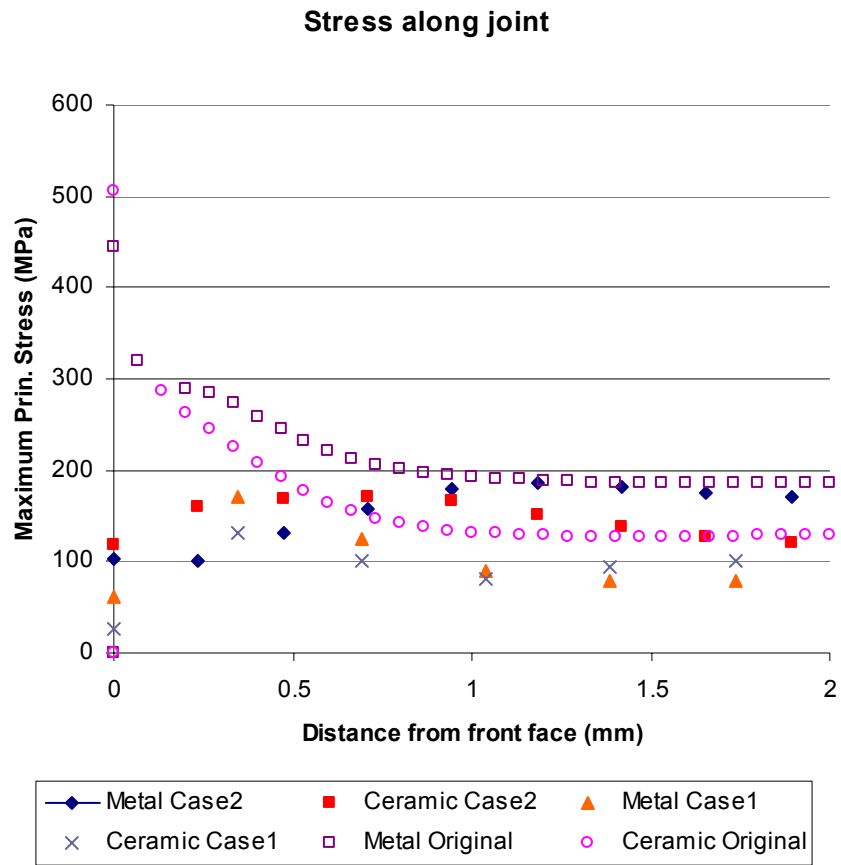
Stress along joint

Figure 54: Maximum principal stress along the joint in the entrance effects region (< 2 mm) for Cases 1-3.

## 3. Modeling Process Route: Reduction, Sintering and Residual Stresses

An effort was made to develop the complex, coupled set of constitutive equations for modeling sintering, hydrogen reduction and shrinkage effects on: (i) residual stress distribution, and (ii) driving forces for failure of hybrid LCM fuel cells. These models are intended to be implemented within the ABAQUS UMAT finite element code to provide a useful tool to guide process path and minimization of process-induced residula stresses.

Numerical Implementation of Constitutive Models for Sintering of Co-Extruded Metallo-Ceramic LCMs - The model written for nonisothermal conditions is fully coupled with the mechanical loading through a porosity dependent elastic stiffness. For implementing those Internal State Variable-based constitutive models, two numerical methods have been studied for coding the material models within UMAT: (i) semi-implicit integration scheme (Marin and McDowell, 1997) and (ii) a multi-level Newton-Raphson solution scheme (Hartmann, 2002). We use generalized midpoint scheme for the constitutive models, which is implicit in the stress increment and important internal variable, mass density increment, but is explicit in the other less important ISVs (e.g., material work hardening rate). For solving the implicit equations and the continuity equation, a Multilevel Newton-Raphson (two-level) iteration method is applied respectively for determining the stress increments in a system of nonlinear algebraic equations; the convergence of this particular Newton-Raphson method is quadratic.

Sintering and Reduction Studies - The sintering and reduction processes must be understood to support process modeling developments in this program and understand limits of manufacturability of hybrid LCM SOFCs. Until recently, only reduction/sintering studies based on shrinkage had been performed because of the inability to experimentally monitor the reduction process. However, with the acquisition of a capacitive film type hygrometer, the emission of water from a sample could be detected during reduction, lending valuable insight into kinetics of the hydrogen reduction process. The hygrometer was inserted into a T in the exhaust line approximately 18 inches from the reducing sample. Figure 55 shows the sintering and reduction curve obtained from a typical Fe39Ni8Cr sample being heated with a relative slow ramp rate of 0.85 C/min. Figure 55 has two sets of curves, measured from two similar samples in a similar environment to demonstrate the repeatability of the experiments. The left vertical axis shows the relative humidity of the exhaust gas, while the right vertical axis plots temperature. The hygrometer output was corrected for differences in the initial mass of the sample. The elevated hygrometer readings that occurred before 100 minutes are attributed to residual water vapor in the chamber from when the system was opened up to the outside environment. The increasing hygrometer signal after 1000 minutes is interference noise between the hygrometer and the high frequency heater. From the results shown in Figures 56 and 57, we interpret that the first hygrometer peak represents the reduction of nickel oxide, while the second shorter broader peak represents the reduction of various iron species. The iron peak is much broader then the nickel oxide peak, which could be due to the more complicated reduction process arising from the presence of various iron alloys. Additionally, because

there is substantially more iron than nickel, and it is possible that the iron reduction is being starved of hydrogen, which would result in the reduction occurring over a longer period of time. Qualitative analysis of samples heated to 600-775ºC indicated that reduction was complete, but sintering had not yet taken place. Specifically, samples heated to 600ºC lost the same mass fraction as samples heated to 1250ºC. This indicates that all the oxygen associated with reduction left the sample before reaching 600ºC. Furthermore, after heating a sample to 775ºC and holding it for 4 hours, the sample did not shrink further during the isothermal hold. Upon removal of the sample, the sample could easily be crushed between fingers, indicating that sintering had not yet taken place. Instead, it is hypothesized that the dimensional shrinkage measured up to 775ºC is due to the structure filling in the voids left by the binder that burned out. Electron microscopy will be used to more accurately determine when the structure first starts to sinter.

For modeling purposes the reduction and sintering behavior of various materials must be investigated in non-isothermal temperature environments. Figure 58 shows the sintering and reduction curves for the same material being heated at different ramp rates. There appears to be a general trend, with reduction and sintering occurring at higher temperatures as the ramp rate increases. The higher ramp rate curves appear broader, which is merely a result of plotting the hygrometer output versus temperature, and not time. The broader peaks do not necessarily represent a greater water output. The very first hygrometer peak present in some of the faster ramp rates is attributed to water

Sintering & Reducing data for Fe39Ni8Cr
Ramp Rate 0.85 C/min, 500 sccm Ar + 4% H$_2$
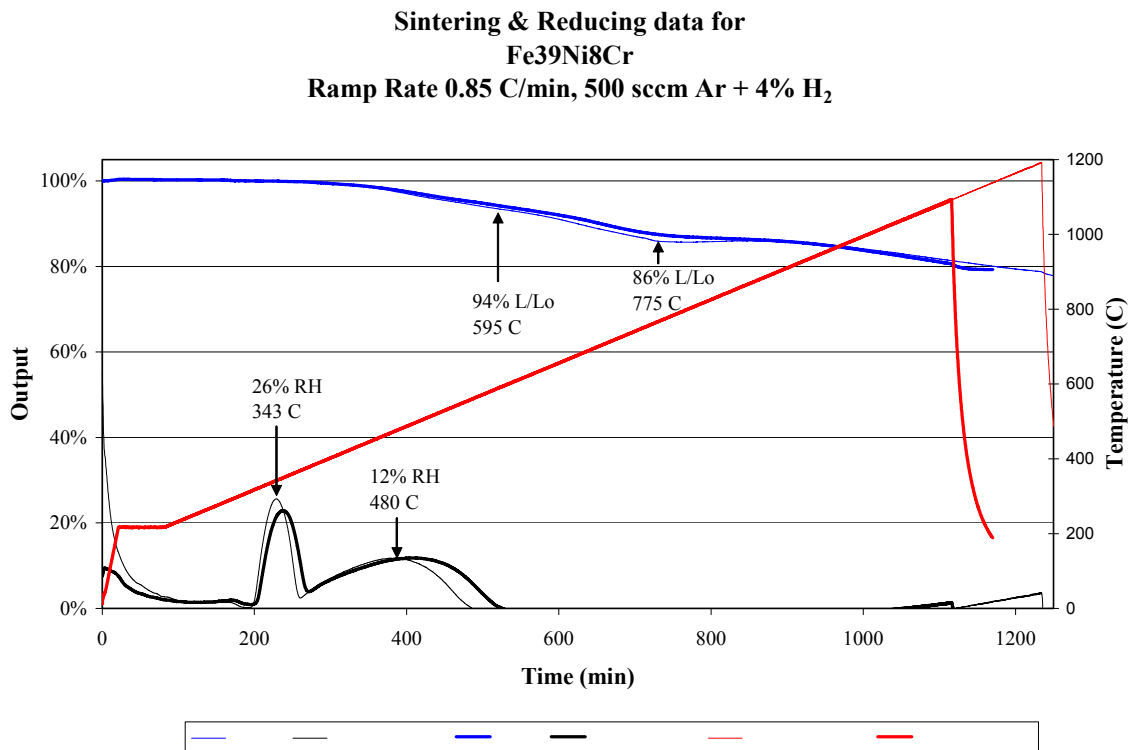
released during the binder burnout phase, not associated with reduction.

Figure 55. Sintering and reduction for Fe39Ni8Cr.

Sintering & Reducing data for
NiO
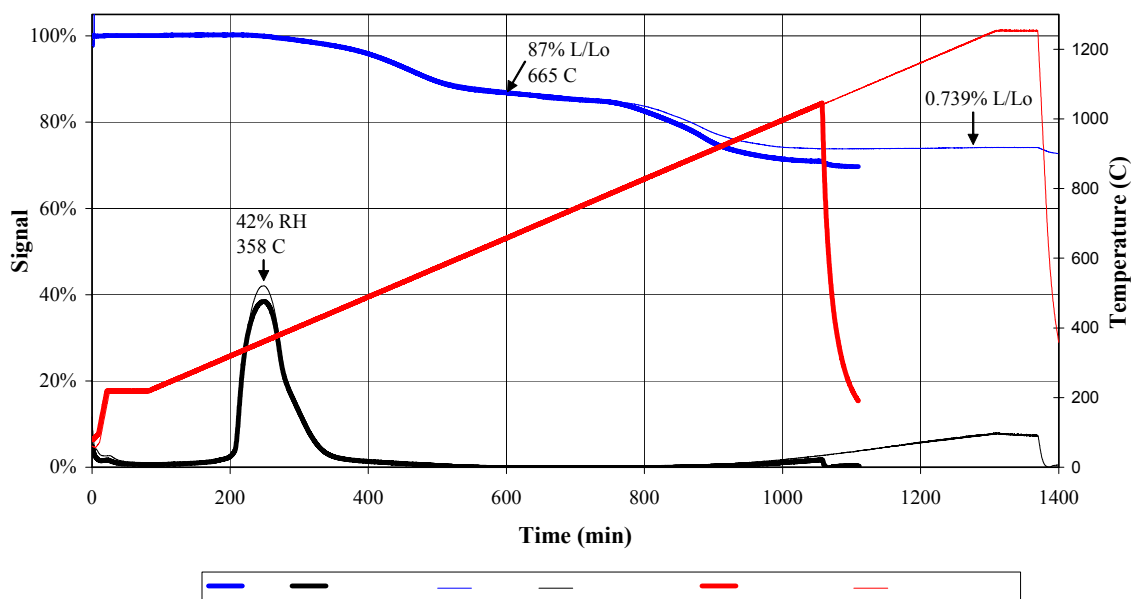**Ramp Rate 0.85 C/min, 500 sccm Ar + 4% H$_2$**

Figure 56. Sintering and reduction for NiO.

Sintering & Reducing data for
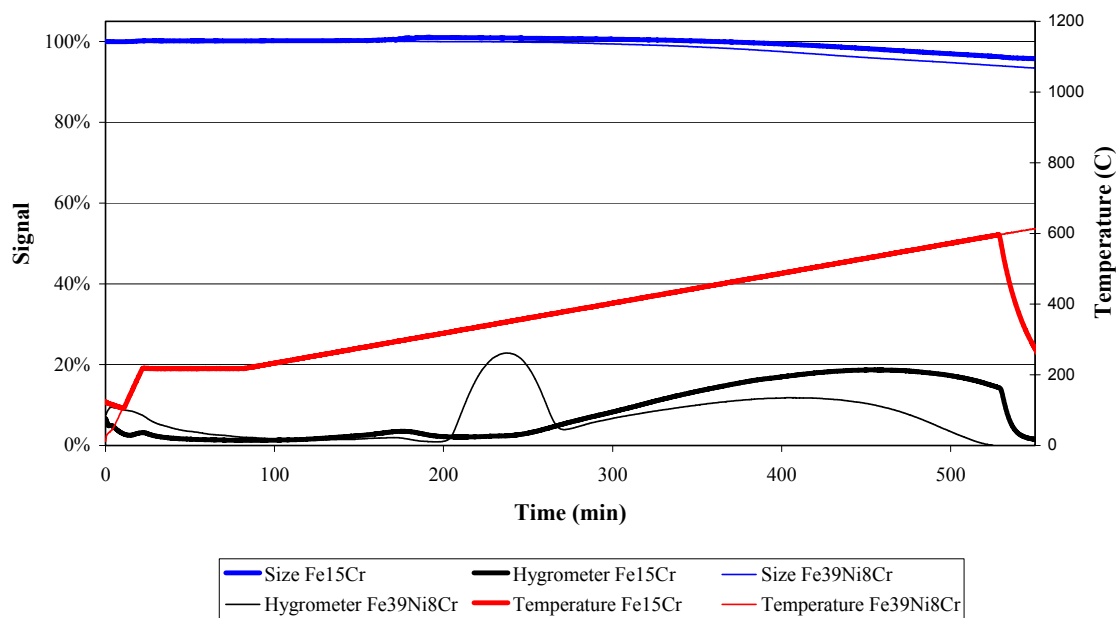**Fe15Cr & Fe39Ni8Cr,**
Ramp Rate 0.85 C/min, 500 sccm Ar+4% H2

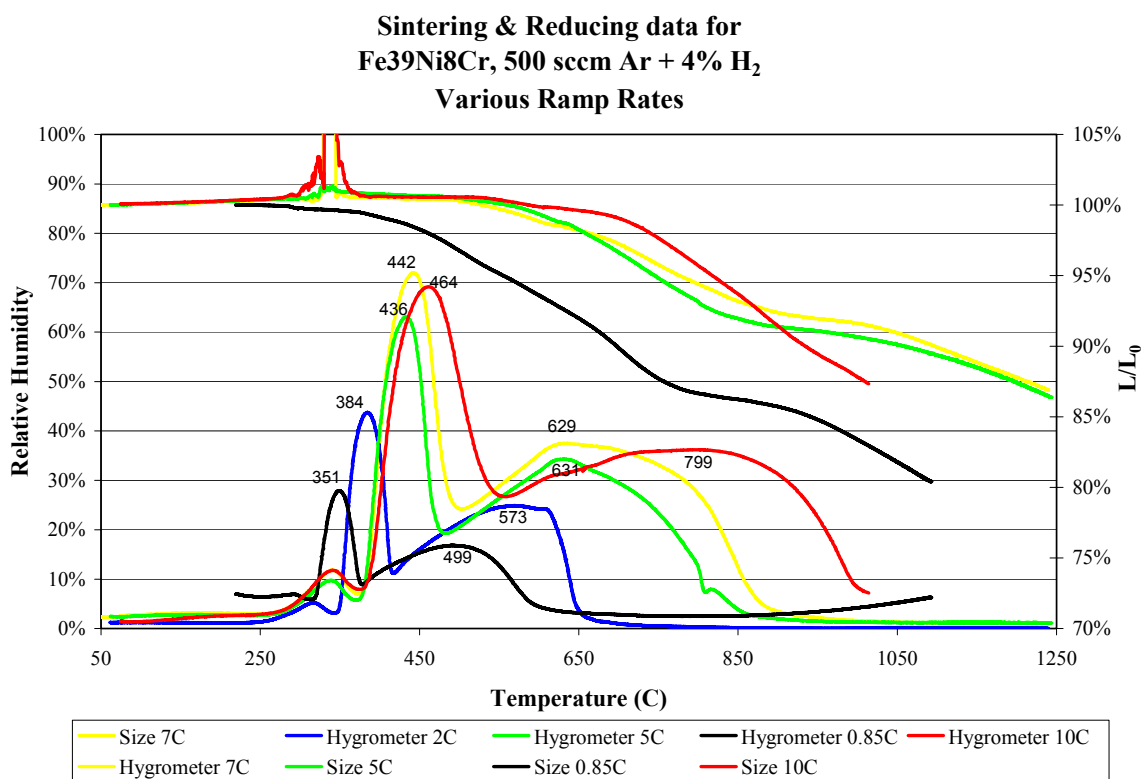Figure 57. Sintering and reduction for Fe15Cr and Fe39Ni8Cr.

Figure 58. Sintering and reduction for Fe39Ni8Cr.

Sintering and Reduction Studies -A substantial effort was made this month to characterize the sintering behavior of Scandia-stabilized Zirconia. Hsueh et al. (1986) proposed the density variation of a stress free sintering compact, i.e.,

$$\rho = \left[1 - \frac{1 - \rho_o/\rho_f}{\left(1 + \dfrac{t}{\tau(T)}\right)^{\beta(T)}} \right] \rho_f \tag{34}$$

where
         t = time elapsed
         $\beta(T)$ = temperature dependent fitting parameter
         $\tau(T)$ = temperature dependent fitting parameter
         ρ_o = initial density in green state = ~2.3 g/cc
         ρ_f = solid density = ~6 g/cc

The β and τ parameters were obtained by fitting Eq. (34) to the measured isothermal hold data shown in Figure 59. The red lines in Figure 59 are the predicted relative density at a given temperature using the fitted parameters. Figure 60 shows the variation of β and τ with temperature. An empirical correlation relating β to temperature (Celcius) is given by

$$\beta(T) = 0.06 \times 2.4 + 0.06 \times \arctan\left(1.2 \times \left(\frac{T\text{-}1133}{30} \right) \right) \tag{35}$$

Several lower temperature experiments have to be performed to create a similar correlation for τ.

Preliminary investigation into the sintering behavior of Fe39Ni8Cr indicates that sintering does not occur before 600ºC, as shown in Figure 61. Figure 61 shows 8 different SEM micrographs taken from 4 different samples that were heated to a given temperature and then held nearly isothermally for an hour. The dimensional shrinkage that occurs after the reduction of NiO, but before 600ºC is believed to be the consolidation of the structure from oxygen vacancies being removed.

Reference: C.-H. Hsueh, A.G. Evans, R.M. Cannon and R. J. Brook, "*Viscoelastic Stress and Sintering Damage in Powder Compacts,*" Acta Metal., **34** [5] 927-36 (1986).
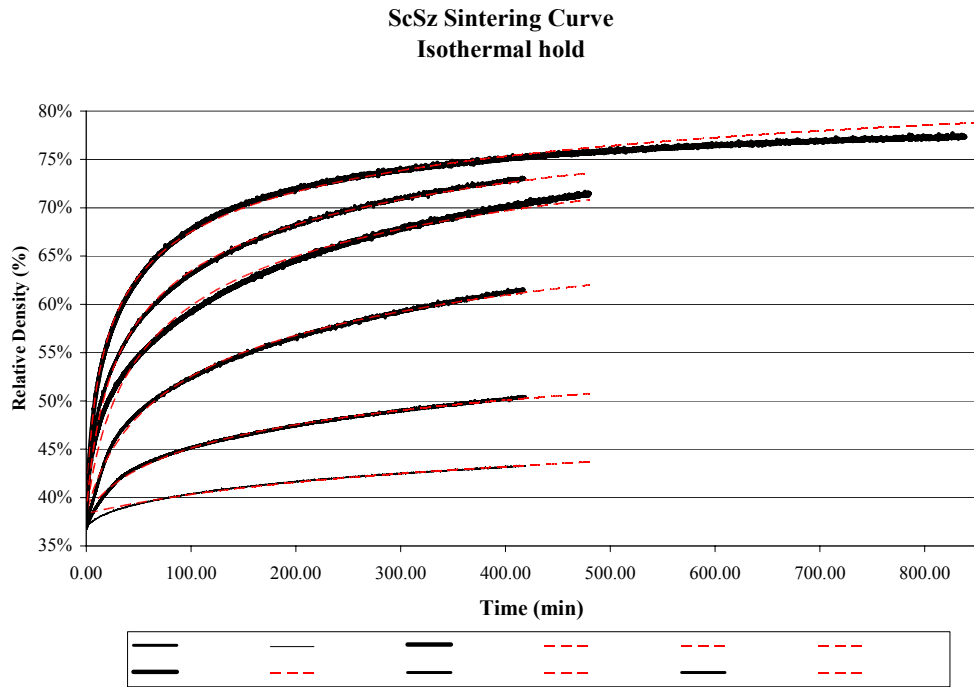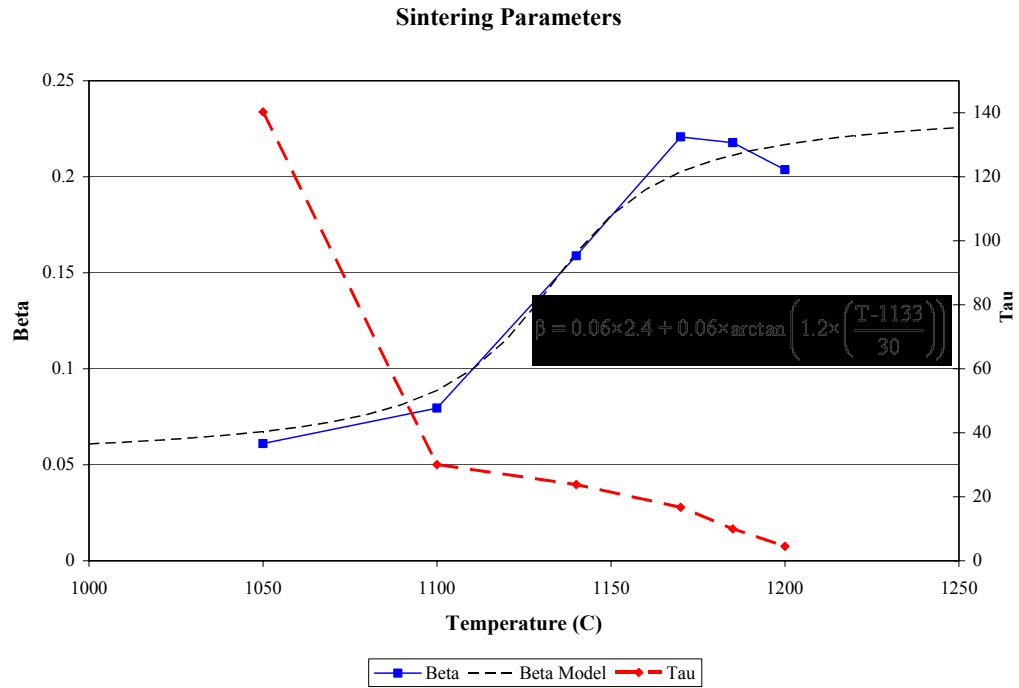
ScSz Sintering Curve
Isothermal hold

Figure 59. ScSZ Sintering Curve for Isothermal Holds.

Sintering Parameters

$$\beta = 0.06 \times 2.4 + 0.06 \times \arctan\left(1.2 \times \left(\frac{T-1133}{30}\right)\right)$$

Figure 60. Parameters for ScSZ.

Green Compact

300 ℃

~600 ℃

5,000 X

~850 ℃

Green Compact

300 ℃

~600 ℃

10,000 X

~850 ℃
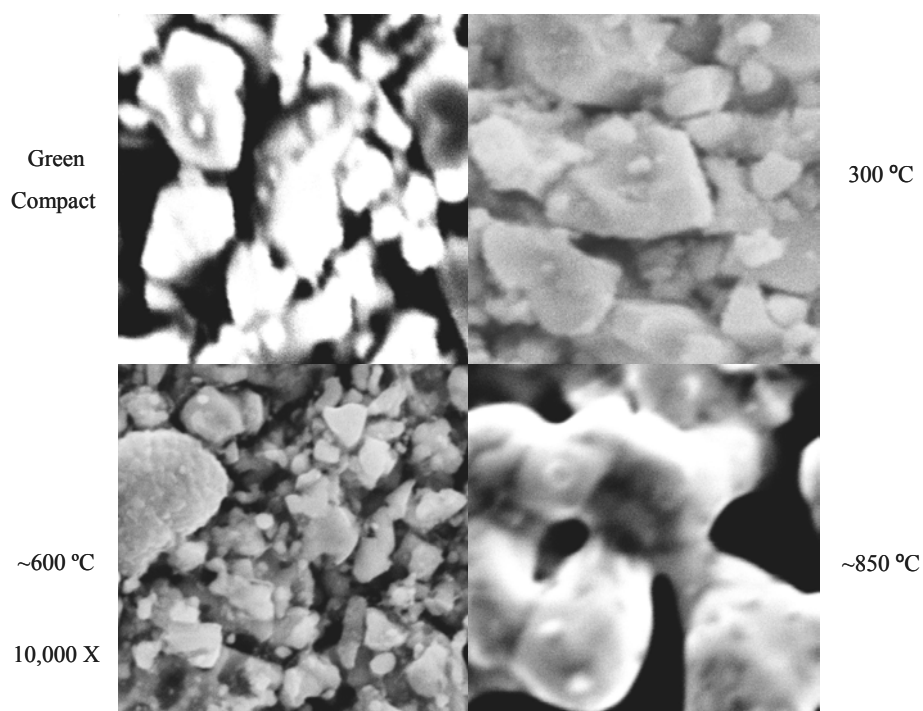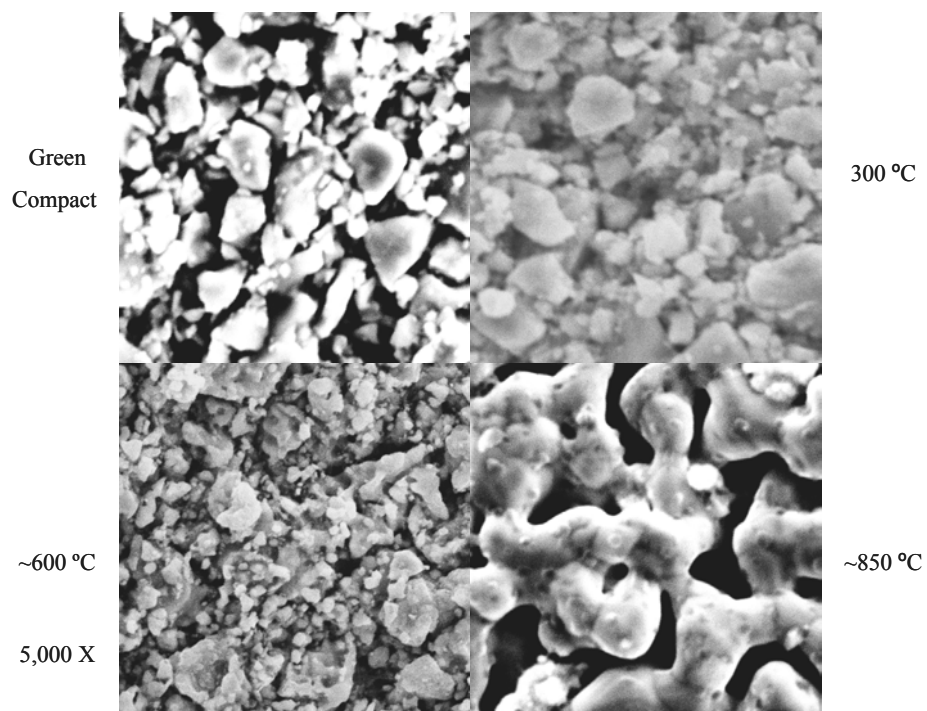
Figure 61. Fe39Ni8Cr heated in H_2 and held for one hour at the specified temperature.

Sintering and Reduction Studies - Several modifications were made to the constitutive equations governing the ceramic model. Specifically, the viscoelastic and sintering portions of the equations were modified. The viscoelastic equations were modified to a form suggested by Bordia and Scherer (1988), i.e.,

$$\dot{\varepsilon}_{ij}^{v} = \frac{S_{ij}}{2G_p} + \frac{\sigma_m}{K_p}\delta_{ij}$$

$$G_p = \frac{3\eta\bar{\rho}}{6 - 4\bar{\rho} + \left(3\bar{\rho} - 2\bar{\rho}^2\right)^{\frac{1}{2}}}$$

$$K_p = \frac{\left(\dfrac{3\eta\bar{\rho}}{3 - 2\bar{\rho}}\right)}{3\left[1 - \left(\dfrac{\bar{\rho}}{3 - 2\bar{\rho}}\right)^{\frac{1}{2}}\right]}$$

$$\eta = 9 \times 10^{-13} \times \exp\left(\frac{100}{0.001987 \times T}\right) \quad , \quad T = \text{Temperature in K}$$

where

$$S_{ij} = \sigma_{ij} - 1/3\sigma_{kk}\delta_{ij}.$$
$$\sigma_m = 1/3(\sigma_{11} + \sigma_{22} + \sigma_{33})$$
$$G_p = \text{Shear viscosity of porous body}$$
$$K_p = \text{Bulk viscosity of porous body}$$
$$\eta = \text{Shear viscosity of solid material}$$
$$\bar{\rho} = \frac{\rho}{\rho_f} = \text{relative density}$$

The sintering potential term was modified in the sintering equation in accordance to the model suggested by Bordia and Scherer (1988). The modified equations are shown below.

$$\dot{\rho}_{stressed} = \dot{\rho}_{stress\_free}\left(1 - \frac{\sigma_m}{\Sigma}\right)$$

$$\Sigma = 3K_p\dot{\varepsilon}_{stress\_free}^{sintering}$$

$$\rho_{stress\_free} = \left[1 + \frac{\rho_o/\rho_f - 1}{\left(1 + \dfrac{t}{\tau(T)}\right)^{\beta(T)}}\right]\rho_f$$

where

$$\sum = \text{Sintering potential}$$

$K_p = \text{Porous bulk viscosity of compact}$

$$\dot{\varepsilon}_{\text{stress\_free}}^{\text{sintering}} = -\frac{\dot{\rho}_{\text{stress\_free}}}{3\rho_{\text{stress\_free}}}$$

Additionally, further experiments were performed to get a better correlation between sintering parameters β and τ, and temperature. The correlations for β and τ are given as (see Figure 62)

$$\beta = 0.06 \times 2.4 + 0.06 \times \arctan\left(1.2 \times \left(\frac{T\text{-}1133}{30}\right)\right), \quad \tau = 2\text{E-}13 \times \exp\left(\frac{90}{0.00199 \times T}\right)$$
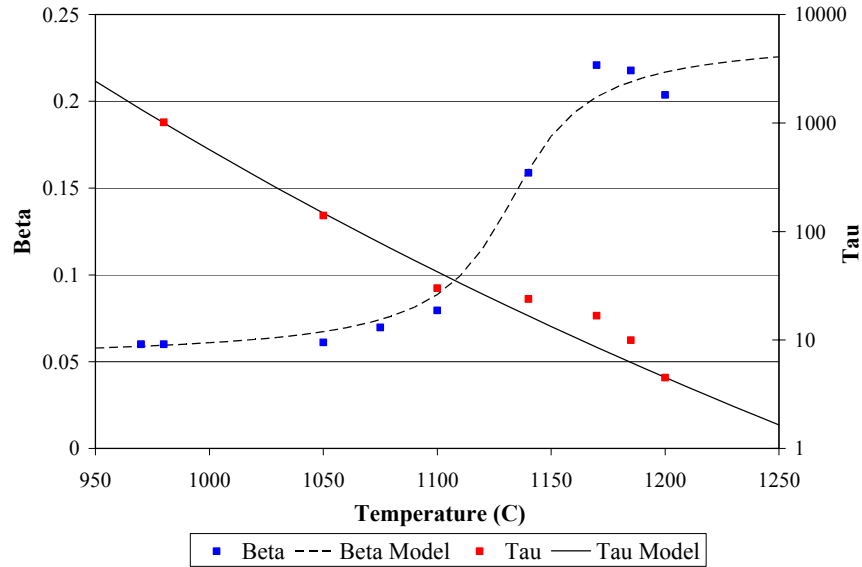
Figure 62. Beta and tau as a function of temperature.

The powder compact ceramic model is now complete and ready for implementation. The equations and parameters needed for the metallic powder reduction, sintering and viscoplasticity models are now being refined.

REFERENCE

R. K. Bordia and G. W. Scherer, "On Constrained Sintering – II Constitutive Model for a Sintering Body," *Acta Metal*, 36 [9] 2393-2397

Sintering and Reduction Studies - Work continues on development of constitutive equations for reduction, sintering, ceramic powder viscoelasticity and metallic porous viscoplasticity. This month, several additional experiments were performed to check the accuracy of the stress-free sintering model. Specifically, the dimensional change of two identical ScSZ compacts were monitored over two different temperature histories. The experimental results were then plotted against the predicted model results, and can be seen in Figure 63a and 63b. It should be noted that the model deviates substantially more for the very slow ramp rate, because the system spends more time at low temperatures where the model parameters have greater uncertainty. At modest ramp rates however, the model is in good agreement with the experimental results. Based on Figures 63a and 63b, it was determined that the current stress-free sintering model is adequate for our modeling purposes.

After completing the ceramic model, additional effort was spent on characterizing the reduction process of the metal interconnect (Fe39Ni8Cr). First an attempt was made to more accurately determine the temperature at which sintering begins in the Fe39Ni8Cr system. To do this, SEM pictures were taken of two different samples that were heated to 700ºC and 750ºC and held isothermally for 2 hours. As evident both in the SEM pictures shown in Figure 64, and the properties of the resulting structure, no sintering had taken place at 700ºC, but sintering was just beginning to take place at 750ºC. From previous experiments, it was determined that reduction of NiO and Fe_3O_4 is completed by ~600ºC at a quasi-static ramp rate of 0.85ºC /min. Therefore, it is assumed that any dimensional change taking place below 750ºC is due to consolidation of oxygen vacancies, and the shrinkage above 750ºC is attributed to sintering of the particles. It is important to realize that both the reduction temperature and sintering temperature appear to shift upwards with higher temperature ramp rates due to the thermal inertia of the structure.

Preliminary attempts have been made at characterizing the shrinkage of the metal oxide in the temperature region between 360ºC and 750ºC, which is associated with oxygen vacancy consolidation. Figure 65 shows the measured shrinkage at various isothermal hold temperatures. The trends of the shrinkage appear very similar to the trends in the sintering ceramic. Therefore, the current idea is to model the shrinkage with the same equation used to model the sintering of ScSZ, but with different fitting parameters τ, and β. On a side note, it is important to realize that the driving force for oxygen vacancy consolidation is probably small, so the importance of accurately characterizing its associated shrinkage in a constrained system is diminished. Furthermore, it is believed that the sintering of Fe39Ni8Cr can modeled in a manner similar to that used for ScSZ.

In an attempt to more accurately quantify the relaxation mechanisms of the metal interconnect, 10 uniaxial strip specimens have been prepared for uniaxial tests. The tests will be conducted over a range of temperatures, and strain rates, and will include relaxation tests at fixed strain. Information regarding plastic flow and relaxation of Fe39Ni8Cr will be backed out of the experiments, and used in the current plastic deformation model.
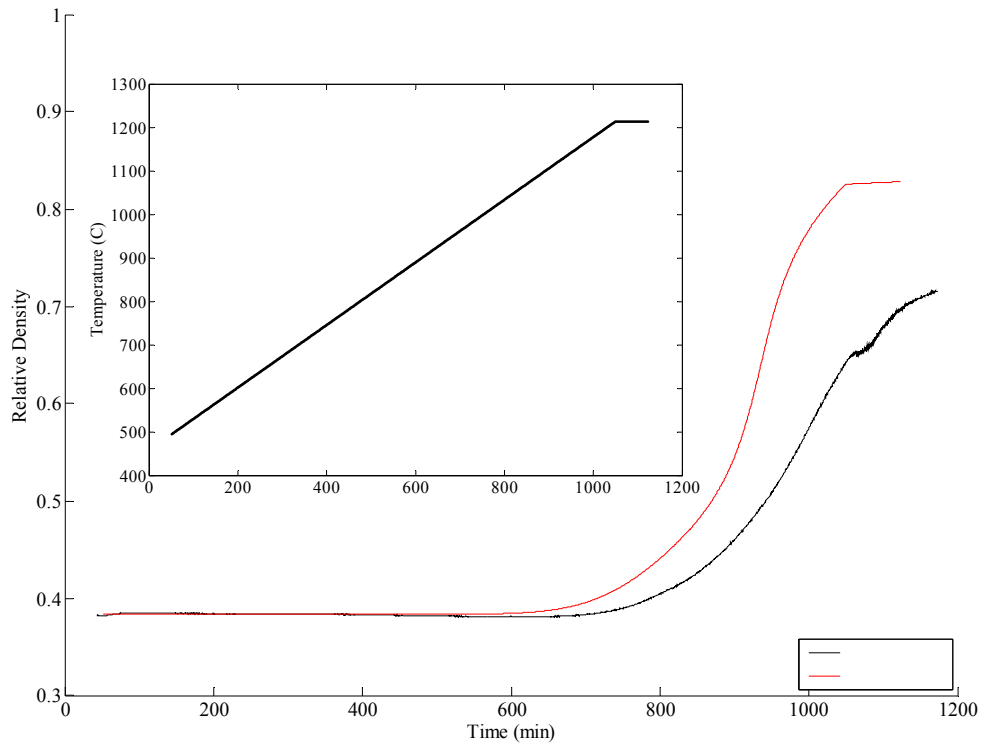
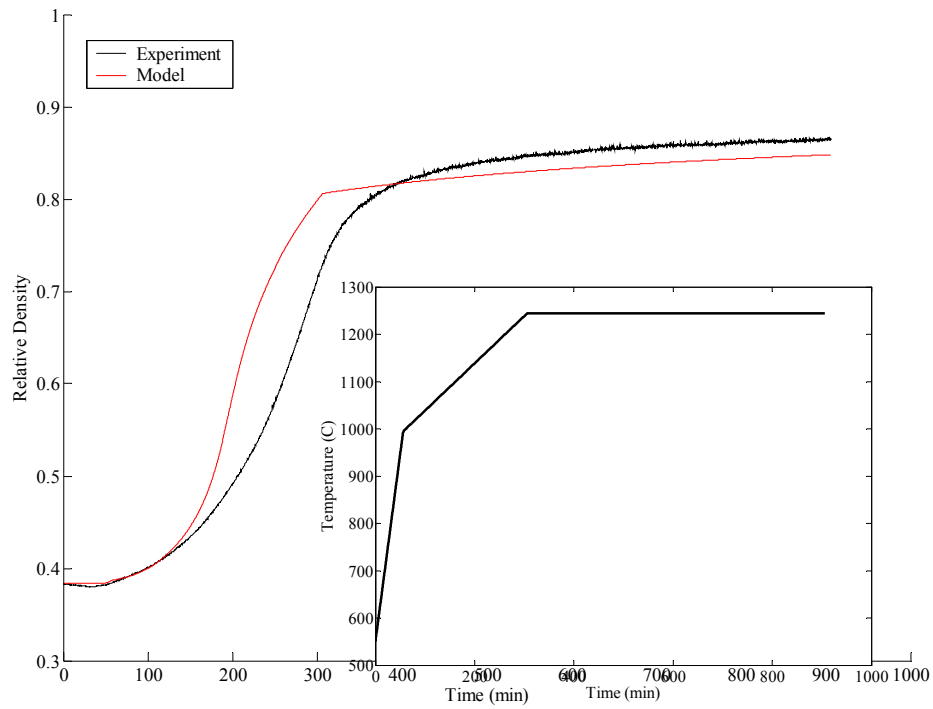Figure 63a: Comparison of model to experimental results for very slow ramp rate (0.75C/min)

Figure 63b: Comparison of model to experimental results for current manufacturing temperature profile.
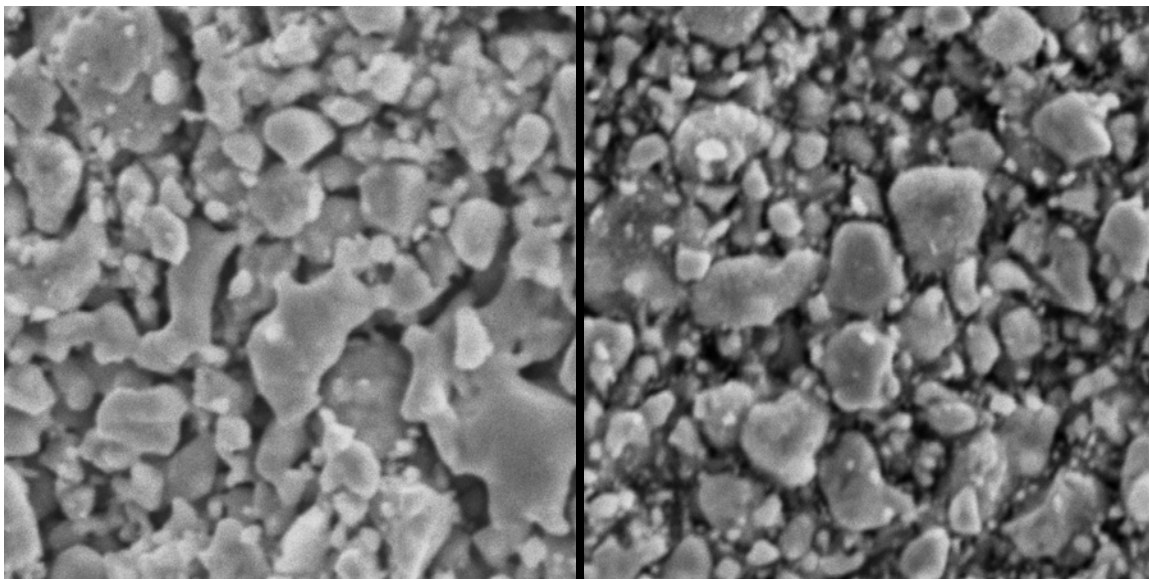
Figure 64: SEM picture of two different Fe39Ni8Cr samples held isothermally at 750 C (left) and 700 C (right) for 2 hours. The left picture is at a magnification of 3500 X, and the one on the right is at a magnification of 3000 X.
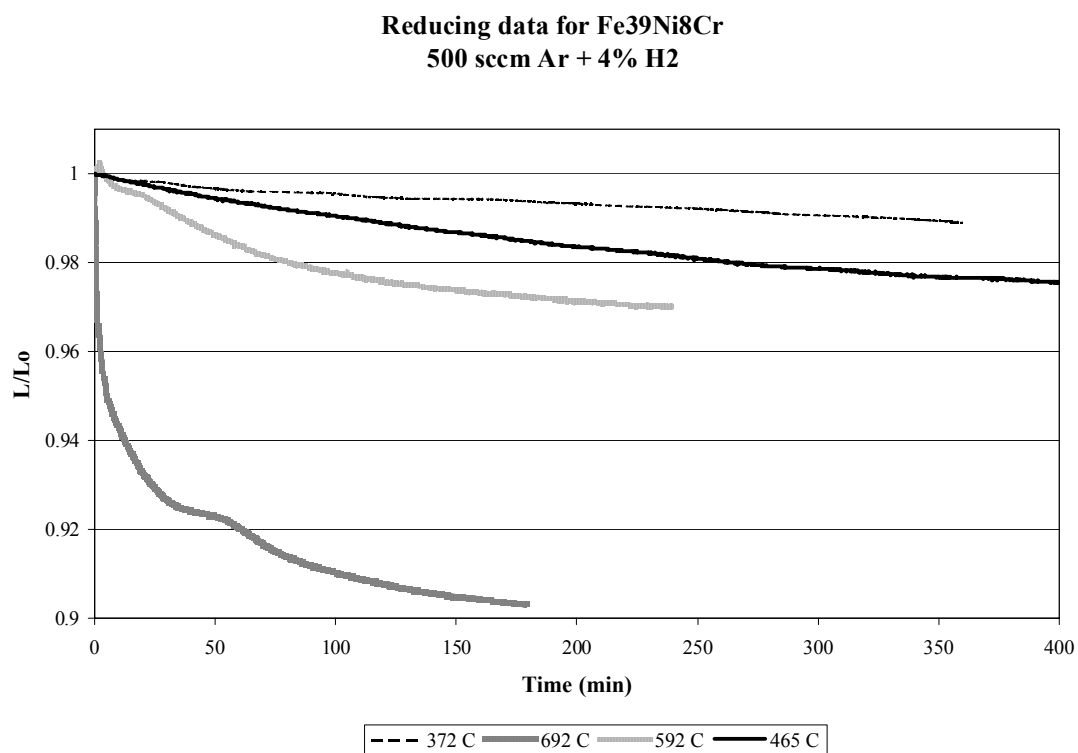

Figure 65: Linear shrinkage of various Fe39Ni8Cr samples at different isothermal hold temperatures.

Sintering and Reduction Studies - During the previous month the reduction process of Fe39Ni8Cr was studied. A precise knowledge of the reduction kinetics of the material will give more insight into desirable manufacturing temperature profiles. Additionally, a precise knowledge of the state of reduction allows for the evolution of density of the structure to be tracked so that a more accurate porosity level can be input into the plasticity model.

During the reduction process: $NiOFe_3O_4Cr + 5H_2 \rightarrow NiFeCr + 5H_2O$. There is a dimensional shrinkage associated with oxygen vacancy consolidation and crystallographic rearrangement, as well as a mass loss from oxygen leaving the structure. The dimensional change seems to follow a classical sintering model of the form:

$$\frac{L}{L_o} = \frac{L_o}{\left(\left[1 + \frac{L_0^{1/3}/L_f^{1/3} - 1}{\left(1 + \frac{t}{\tau(T)} \right)^{\beta(T)}} \right] L_f^{1/3} \right)^{1/3}}$$

$$L_f \approx 0.82 L_o$$

More experiments are needed to accurately determine the values of the parameters.

The mass flux of oxygen molecules leaving the structure during reduction is governed by two different mechanisms, depending on whether reduction is taking place for the NiO species or the Fe_3O_4 species. Based on this separation, the proposed mass of oxygen leaving the structure can be written as

$$mass_{\substack{\text{total oxide} \\ \text{reduced}}} = 0.072 \left[\eta_{Ni}(T,t)\, mass_{initial} \right] + 0.138 \left[\eta_{Fe}(T,t,P,m_{ini})\, mass_{initial} \right],$$

where the 0.072, and 0.138 are the mass percents of oxygen in NiO and Fe_3O_4 for the Fe39Ni8Cr composition in the green state with binder. From experimental observations, it was determined that the rate of reduction for NiO is independent of the partial pressure of water vapor and initial mass of sample assuming the reaction is not limited by stoichimetery. After several experimental runs, the dependence of η on temperature was determined to be

$$\eta = \int_0^t \dot{\eta}_{NiO} dt , \quad \dot{\eta}_{NiO} = a(T) \times exp\left(-0.5 \left(\frac{\ln\left(\frac{t}{x_o(T)} \right)}{b(T)} \right)^2 \right)$$

$$a(T) = 0.0013T - 0.418 \text{ for } 350 < T < 450$$

$$b(T) = 0.0032T - 0.738 \text{ for } 350 < T < 450$$

$$x_o(T) = -0.22T + 100.47 \text{ for } 350 < T < 450$$

To get the best estimate of the reduction time, the above equation must be integrated over the given temperature profile. However, for simplicity, the reduction time has been tabulated for several constant temperatures below.

Temperature (C)	Approximate Reduction Time for NiO (min)
250	~infinite
350	65
380	35
450	12
450+	~12

The reduction of Fe_3O_4 is substantially more complicated. The reduction of the iron species is dependent on the partial pressure of water vapor in the system, temperature, and initial mass of iron oxides. Additionally, the reduction of iron oxide seems to have at least two different reduction processes, one acting between 350ºC -700ºC and another over 700ºC. Below 700ºC, the reduction takes place at approximately a constant rate for a constant temperature until ~75% of the total iron oxide mass has reduced. More experimental results are needed to quantify the observed relation. Further examination into the reduction of iron species should allow for a correlation to be drawn between the time necessary for reduction of a specimen and the specimen's mass and current temperature.

In addition to characterizing the reduction process of the metal oxides, several room temperature uniaxial tests were run on Fe39Ni8Cr strip specimens to get accurate stress strain curves. Figure 66 shows the results from the uniaxial tests. Four tests were run, two tests at two different strain rates. Part of the variation in measured strain to failure is due to local defects specific to the sample. Specifically, 2 of the 4 samples fractured at internal defects large enough to be seen by the naked eye.
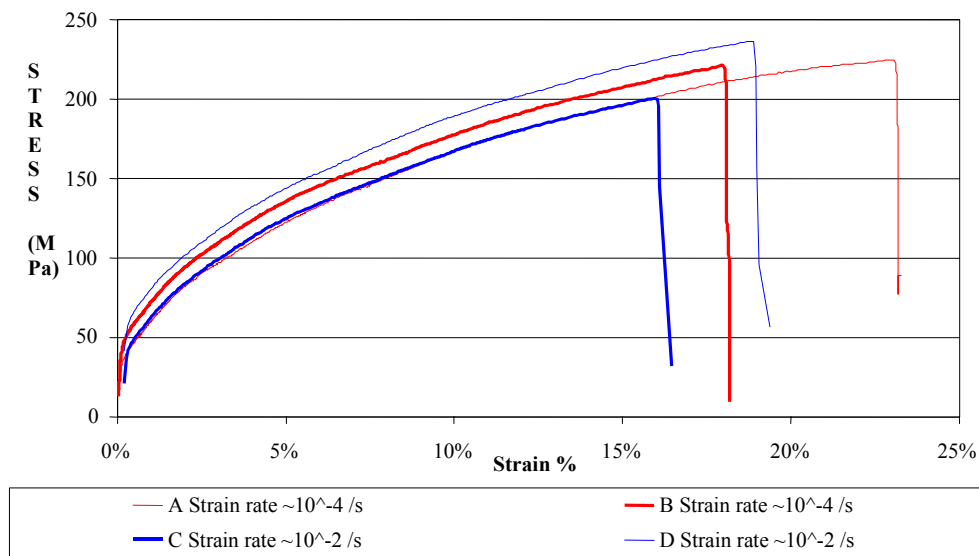
Figure 66. Uniaxial Test data for at Room Temperature, ~3% Porosity Fe39Ni8Cr

Creep-Plasticity Model for Interconnect Material - High temperature uniaxial tests were performed on several flat dog-bone Fe39Ni8Cr specimens. The tests were run to characterize the yielding and relaxation behavior of a surrogate material, for use in a plasticity model. The elastic modulus could not be determined because the experimental setup did not permit the use of an extensometer. However, the experiments did provide insight into the yielding behavior of the material. The results of the uniaxial tension test appear in Figure 67. The results stress relaxation during a strain hold test at ~2.25% strain are plotted in Figure 68.
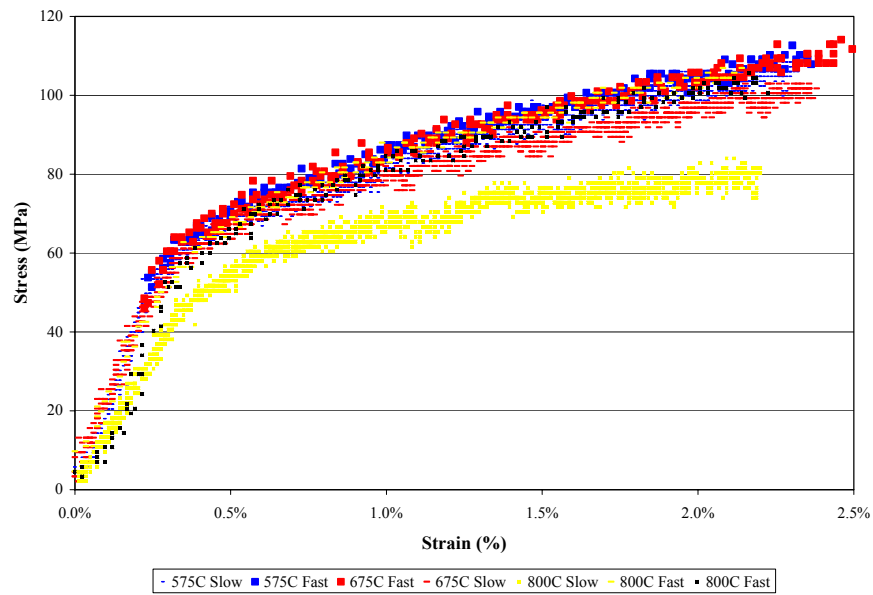
Figure 67. Uniaxial tension tests on flat dog-bone specimens of Fe39Ni8Cr. Two different strain rates were tested, 10^{-2} per second, and 10^{-4} per second. The specimens had a porosity of 15%.
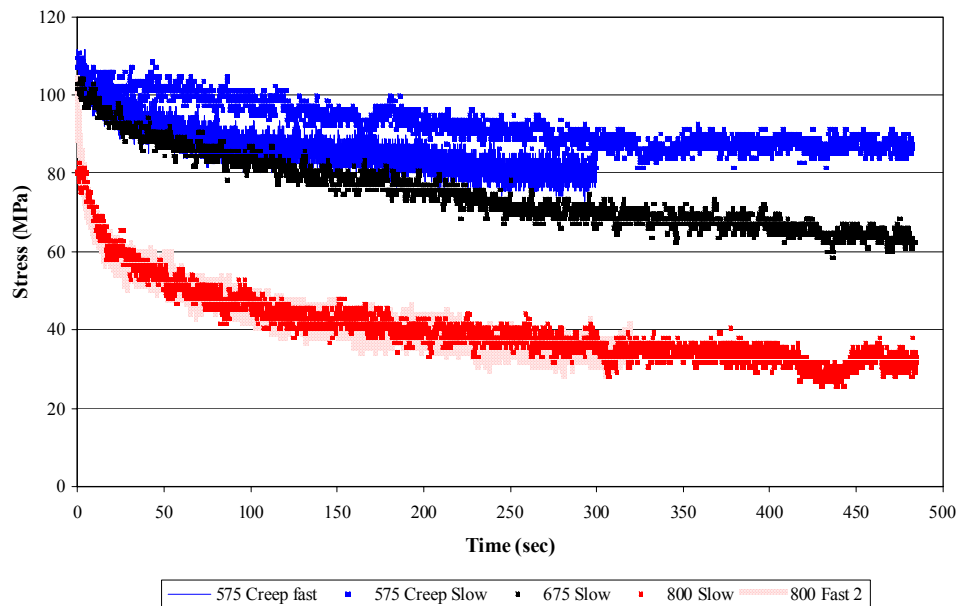

Figure 68: Stress relaxation during uniaxial tensile strain hold for specimens subjected to a 2.25% strain prior to hold period.

133

Metal Interconnect Model - The model that simulates the behavior of the metal interconnect during the manufacturing process was developed more fully. The model and its associated parameters were checked by comparing model predictions to an independent set of experimental results. The results of the comparison are shown in Figure 69 below. The model captures the trends of behavior well, but some of the material parameters still need to be adjusted. The primary reason for the discrepancy between the model and experiments is that the sintering parameters were characterized after reduction had been completed. Hence, sintering occurs more rapidly in the model, resulting in a faster predicted densification. Unfortunately, the sintering behavior cannot easily be characterized in-situ in parallel with reduction; however, other adjustments can be made to the model to alleviate the current error.

The usefulness of manufacturing models also requires knowledge of the failure criteria for the materials at various steps in the process. Therefore, uniaxial compression tests were performed on samples from three different periods of the manufacturing process. Specifically, compression tests were run on the Fe39Ni8Cr green compact, the Fe39Ni8Cr compact after the binder had burned out, and the Fe39Ni8Cr compact after the binder had burned out and the structure was reduced. Figure 70 shows the results of the compression tests. The compression tests were repeated twice for consistency except for the green compact test, which was only performed once. The stress plateau exhibited in Figure 70 for the binder burn-out and reducing stages is indicative of material failure. The experimental setup did not allow the green compact to be tested to failure. The electrolyte should exhibit similar behaviors to the green compact and binder burnout. Cyclic loading of the green compact and binder burnout specimen gave insight into the elastic nature of the materials. Figure 71 shows the stress-strain curves for cyclic loading of the materials. The green compact seemed to only elastically deform, whereas the binder burnout structure was permanently deformed.
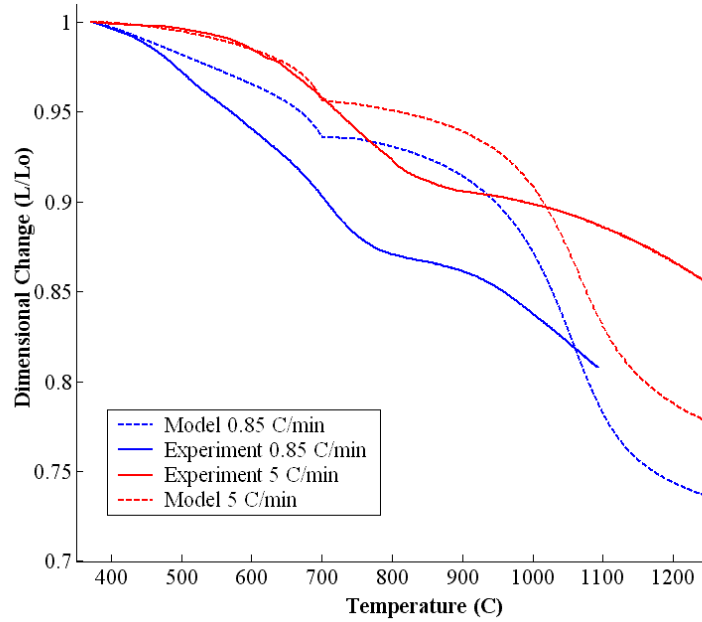
Figure 69.   Comparison of predicted and observed shrinkages undergone by the Fe39Ni8Cr system when being heated from 370 C to 1270 C at two different ramp rates.
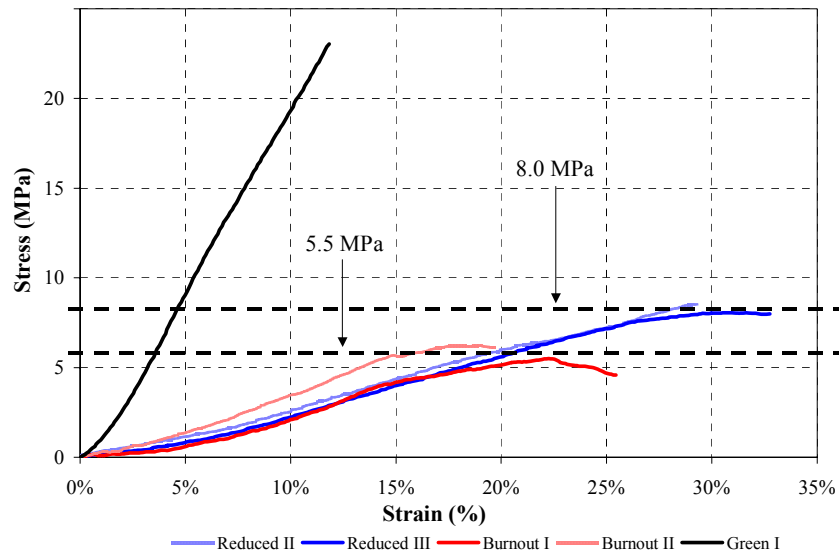

Figure 70. Uniaxial compression tests on Fe39Ni8Cr compact from three different stages in the manufacturing process. The green compact was tested (Green I), the compact after the binder had burned out, but before reduction had occurred was tested (Burnout I &II),

and the compact after the binder had burned out, and after reduction had finished was tested (Reduced II &III). Most runs were repeated twice for consistency.
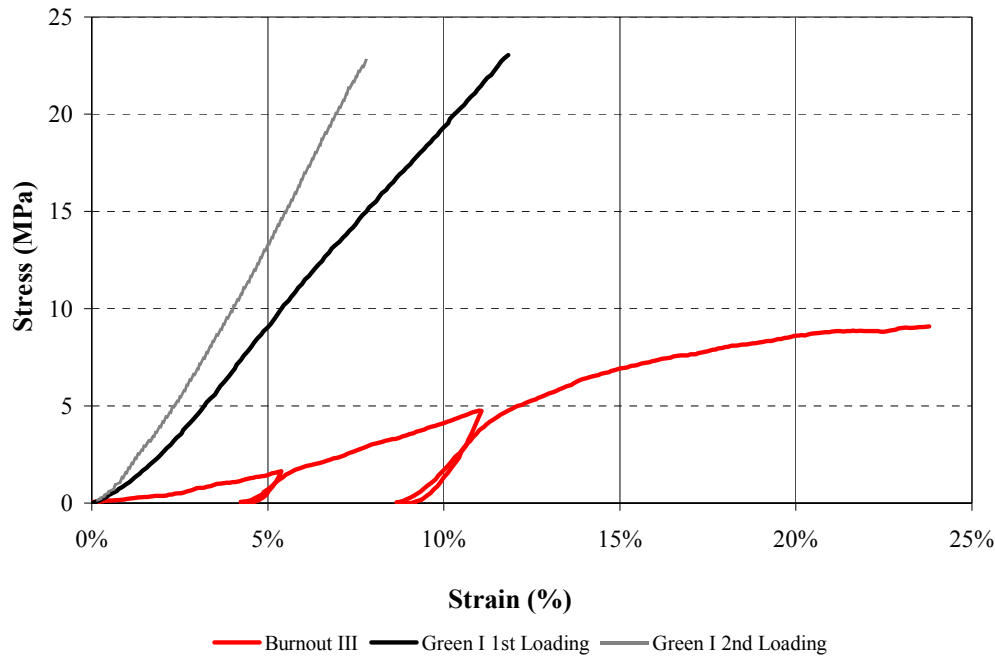

Figure 71. The Fe39Ni8Cr green compact and the compact with the binder burned out were cyclically loaded to determine the level of inelastic deformation.

Constrained Hybrid LCM Shrinkage - Dilatometry experiments were performed this past month on the constrained Fe39Ni8Cr / ScSz system. Figure 72 compares the same hybrid structure before and after firing to 1250°C. The deformation in the metal phase after firing indicates substantial compliance, which helps resist fracture. Figures 73 and 74 compare shrinkage of the constrained Fe39Ni8Cr / ScSz system relative to each of the unconstrained monolithic components. The difference in the time at which a fixed amount of shrinkage occurs at for the two different heating schedules is shown in Figures 73 and 74, indicating that constrained sintering will occur in the actual hybrid LCM SOFC structure.

The previously developed viscosity model was then used to estimate the high temperature behavior of the ScSz system. Specifically, two cases were considered: (i) the length of time required at high temperatures to anneal the sintering stresses in a constrained hybrid system, and (ii) the cool down temperature at which the ScSz system began to substantially lose its ability to relax stresses in a viscous manner. For simplicity, only the effects of bulk viscous flow were considered for both cases. In order to determine the duration of the high temperature isothermal hold required to relax the stresses in the system, a constant driving stress of 1 MPa (on the same order as the sintering potential)

was chosen and a total sintering mismatch strain of 2% was assumed between the ceramic and metal interconnect. The length of time required for the structure to relax could then be expressed as a function of the temperature of the isothermal hold and the final relative density of the structure, as shown in Figure 73. The hold times shown in Figure 73 are greater then the actual hold time required to relieve the stresses because of the assumptions made to generate the Figure. Likewise, several simplifying assumptions were made to approximate the cool down temperature at which the ScSz system loses the ability to relax stresses in a constrained hybrid system. First of all, it was assumed that the isothermal hold period was long enough so that prior to cool down, the hybrid structure was in a stress-free state. Secondly, it was assumed that the only source of residual stress during cool down was the mismatch of thermal expansion coefficients between the metal interconnect and ScSz, which was assumed constant with temperature for simplicity. Finally, the relaxation temperature was defined as the temperature at which the stress in the ScSz system first exceeded 1 MPa. The resulting relaxation temperature was then found to be a function of temperature cool down rate (dT/dt) and final relative density of the structure, as shown in Figure 75. Again, the assumptions made will result in a higher relaxation temperature then would be observed in the actual system. Furthermore, it is extremely important to understand that the information shown in Figures 75 and 76 assumes that the metal interconnect behaves as a rigid body in the hybrid structure, and that only the ScSz system has the ability to undergo viscous relaxation. In reality it is believed that the metal interconnect is substantially more compliant then the ScSz system, which would result in substantially shorter annealing temperatures and a lower relaxation temperature.
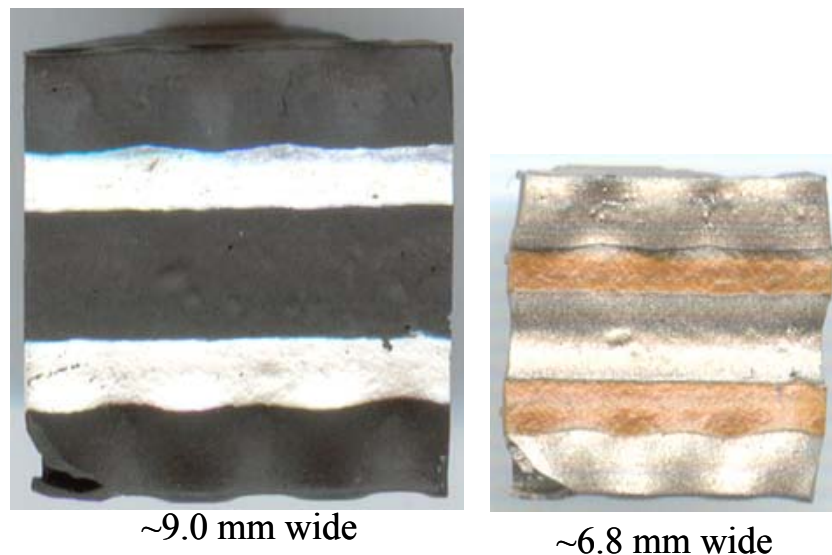

~9.0 mm wide   ~6.8 mm wide

Figure 72: Extruded Fe39Ni8Cr / ScSz system before and after firing. Notice the deformation in the once parallel sides of the specimen after firing.
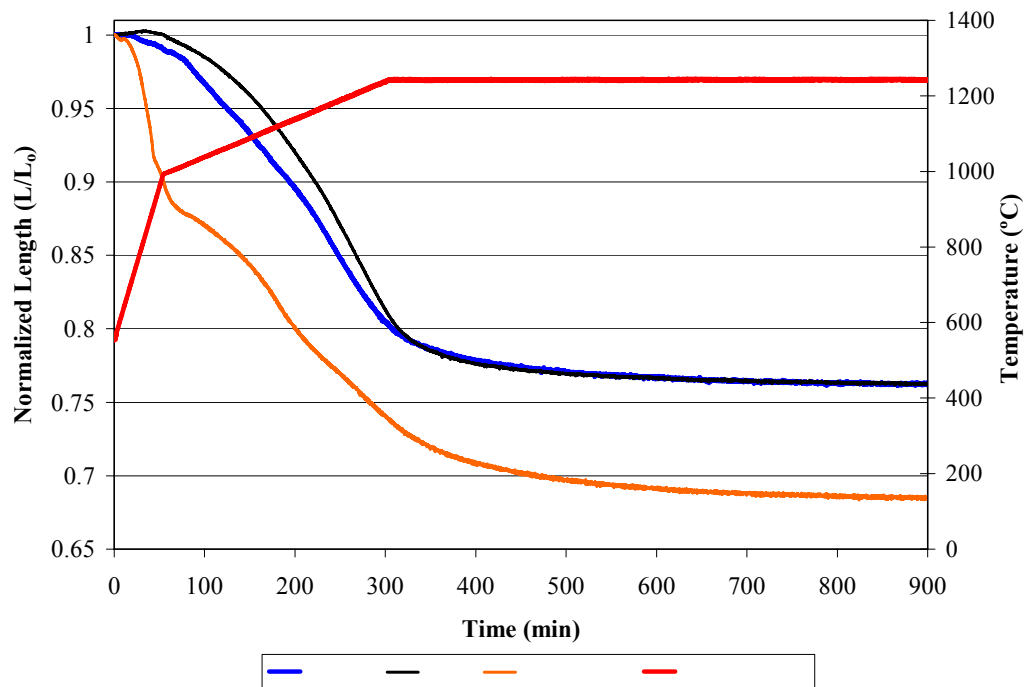
Figure 73: Comparison of the shrinkage of the constrained hybrid structure with the unconstrained monolithic shrinkages of its two components.
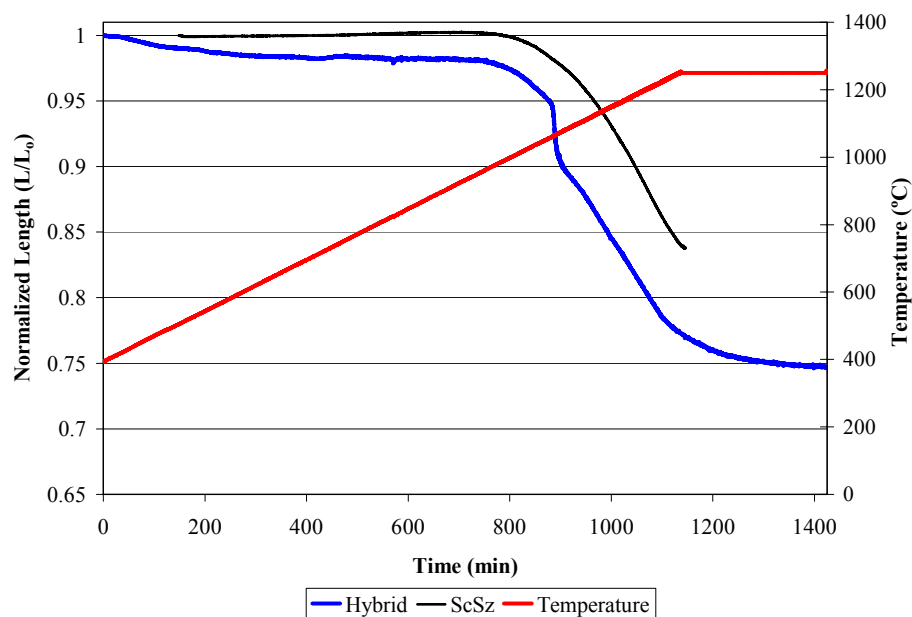

Figure 74: Comparison of the shrinkage of the constrained hybrid structure with the unconstrained monolithic shrinkage of the ScSz system at a much slower heating rate.
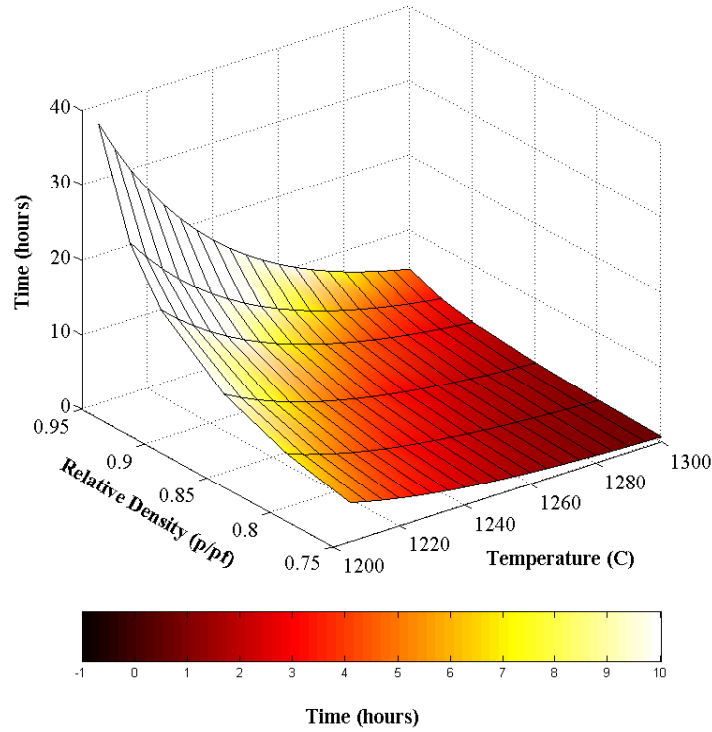
Figure 75: Approximate time required for ScSz system to relax 2% strain under 1 MPa hydrostatic driving stress (from sintering potential) at a constant temperature, assuming only bulk viscous flow.
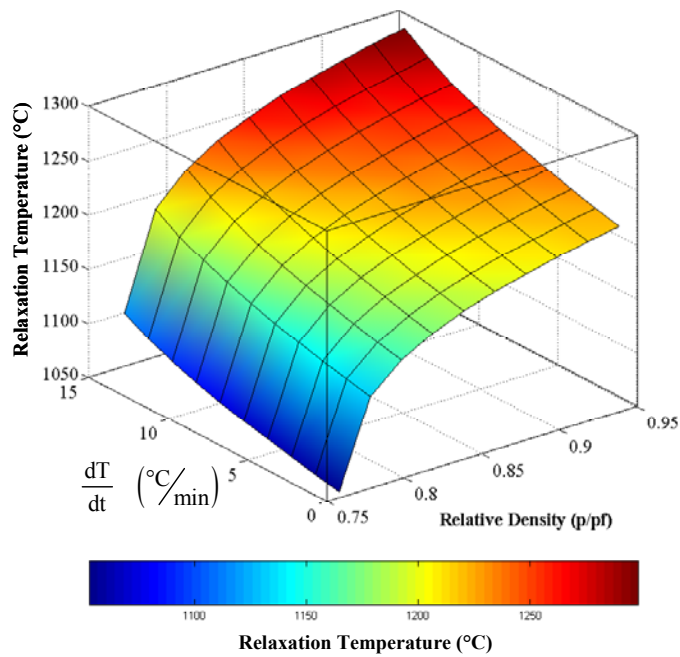

Figure 76: Approximate relaxation temperature of ScSz as a function of cool down temperature ramp rate and final relative density, assuming a mean hydrostatic stress of 1 MPa is 'relaxed'.

4. Theses

Benjamin Dempsey, completed M.S. Thesis Summer Semester 2002 "Thermal Properties of Linear Cellular Alloys"

Jason LeMasters, completed M.S. Thesis Spring Semester 2004; "Thermal Stress Analysis of LCA-Based Solid Oxide Fuel Cells"

Prescott Eisele, completed M.S. Thesis Spring Semester 2004; "Characterization of Material Behavior During the Manufacturing Process of a Co-Extruded Solid Oxide Fuel Cell"